OCRWM	MODEL COVER SHEET	1. QA: QA
		Page 1 of 168

2. Type of Mathematical Model

☒ Process Model ☐ Abstraction Model ☐ System Model

Describe Intended Use of Model

The purpose of the site-scale saturated zone transport model is to simulate transport in saturated porous rock and alluvium.

3. Title

Site-Scale Saturated Zone Transport

4. DI (Including Rev. No. and Change No., if applicable):

MDL-NBS-HS-000010 REV 01

5. Total Attachments	6. Attachment Numbers - No. of Pages in Each
4	I – 64 pages, II – 3 pages, III – 14 pages, IV – 3 pages, V – 3 pages

	Printed Name	Signature	Date
7. Originator	S. Kelkar	SIGNATURE ON FILE	12/19/03
8. CSO	M. Zhu	SIGNATURE ON FILE	12/15/03
9. Checker	B. Kalinina	SIGNATURE ON FILE	12-18-03
10. QER	J. Graff	SIGNATURE ON FILE	12/22/2003
11. Responsible Manager/Lead	S. P. Kuzio	SIGNATURE ON FILE	12/22/2003
12. Responsible Manager	P. R. Dixon	SIGNATURE ON FILE	12/22/03

13. Remarks

FINAL.

Contributing authors include A. Meijer, R. Pawar, H. Viswanathan, B. A. Robinson, and B. W. Arnold. S. Altman contributed to the CSO reviews of this document.

TER-02-0061 was written to be addressed in the revision of ANL-NBS-HS-000031. However, Attachment II of this report addresses the colloid-facilitated transport issues contained in the TER.

All files containing calculations are not attached to this report because of their size, but will reside in the TDMS.

OFFICE OF CIVILIAN RADIOACTIVE WASTE MANAGEMENT
MODEL REVISION RECORD

2. Model Title:
Site-Scale Saturated Zone Transport

3. DI (including Rev. No. and Change No., if applicable):

MDL-NBS-HS-000010 REV01

4. Revision/Change No.	5. Description of Revision/Change
REV 00	Initial issue.
REV01	Revision includes additional data and parameters. No change bars were used because of the extensive nature of the changes.

CONTENTS

CONTENTS (Continued)

CONTENTS (continued)

CONTENTS (continued)

FIGURES

FIGURES (continued)

INTENTIONALLY LEFT BLANK

TABLES

TABLES (continued)

ACRONYMS AND ABBREVIATIONS

3-D	three-dimensional
ACM	alternative conceptual model
AMR	analysis/model report
AP	administrative procedure
ATC	(Nye County) Alluvial Testing Complex
BSC	Bechtel/SAIC Company
CDF	cumulative distribution function
CRWMS M&O	Civilian Radioactive Waste Management System Management and Operating Contractor
DIRS	Document Input Reference System
DOE	U.S. Department of Energy
DTN	data tracking number
ER	environmental restoration
ESF	Exploratory Studies Facility
FEHM	finite-element heat and mass transfer numerical analysis computer code
FEPs	features, events, and processes
LA	license application
LANL	Los Alamos National Laboratory
NRC	U.S. Nuclear Regulatory Commission
NTS	Nevada Test Site
NC-EWDP	Nye County Early Warning Drilling Program
OCRWM	Office of Civilian Radioactive Waste Management
PA	Performance Assessment
QA	quality assurance
REV	revision
SPGM	Scientific Processes Guidelines Manual
STN	software tracking number
SZ	saturated zone

ACRONYMS AND ABBREVIATIONS (continued)

TSPA   Total Systems Performance Assessment
TSPA-LA   Total Systems Performance Assessment for the License Application
TSPA-SR   Total Systems Performance Assessment for Site Recommendation
TWP   technical work plan

UMTRA   Uranium Mill Tailings Remedial Action
USGS   U.S. Geological Survey
UZ   unsaturated zone

V   version

YMP   Yucca Mountain Project
YMRP   Yucca Mountain Review Plan

1.   PURPOSE

This work provides a site-scale transport model for calculating radionuclide transport in the saturated zone (SZ) at Yucca Mountain for use in the abstractions model in support of Total System Performance Assessment (TSPA). The purpose of this model report is to provide documentation for the components of the site-scale saturated-zone transport model in accordance with administrative procedure (AP)-SIII.10Q, *Models*. This report:

- Revises the analysis/model report (AMR) *Saturated Zone Transport Methodology and Transport Component Integration* (CRWMS M&O 2000 [146962]).

- Provides an update to the advection-dispersion transport model including matrix diffusion (Sections 6.3 and 6.5).

- Provides a description and validation of the transport model (Sections 6.3 and 7).

- Describes the numerical methods for simulating radionuclide transport (Section 6.5).

- Documents the parameters (sorption coefficient, K_d) and their uncertainty distributions used for modeling radionuclide sorption (Attachment I and III).

- Documents the parameters used for modeling colloid-facilitated radionuclide transport (Table 4-1, Section 6.5.2.6, and Attachment II).

- Describes alternative conceptual models (ACM) and their dispositions.

The intended use of this model is to simulate transport in saturated fractured porous rock (double porosity) and alluvium. The particle-tracking method of simulating radionuclide transport is incorporated in the FEHM computer code, Version (V) 2.20 (software tracking number STN: 10086-2.20-00 [161725]) and described in Section 6.5 of this report.   FEHM is a three-dimensional (3-D), finite-volume, finite-element, heat and mass flow-and-transport code.

This report documents the features and capabilities of the site-scale transport model for calculating radionuclide transport in the SZ at Yucca Mountain in support of the TSPA. Correlative flow-model calculations using FEHM V 2.20 (STN: 10086-2.20-00 [161725]) are being carried out and documented in the model report *Site-Scale Saturated Zone Flow Model* (BSC 2003 [162649]). The velocity fields are calculated by the flow model independent of the transport processes and supplied as a part of the output package from the flow model, which is then used as inputs to the transport model.

The geohydrologic setting to be modeled is complex with multifaceted and diverse geochemical interactions possible between the groundwater, solutes, and the geological materials. Also, the intended use by the TSPA requires a computationally efficient model that is amenable to repeated runs for stochastic simulations. The approach taken in this report is to construct a plausible conceptual model of transport that represents the important SZ transport processes and also supports the TSPA. Alternate conceptual models and the implications of these models for transport predictions are evaluated relative to the base-case model. A number of relevant features, events, and processes (FEPs) are included in this report (Section 6.2). The manner of

their inclusion is described in various sections of this report. The excluded FEPs are discussed in a separate report, *Features, Events, and Processes in SZ Flow and Transport*, which will be a revision of CRWMS M&O (2001 [153931]).

The transport of chemical species in groundwater generally leads to retardation of the migration of transported species with respect to the bulk movement of the groundwater. The radionuclide transport times can be several orders of magnitude longer than those for the bulk water. The processes of importance to the SZ are radionuclide dispersion, diffusion into the rock matrix and subsequent radionuclide adsorption onto matrix surfaces, and colloid-facilitated radionuclide transport. These processes are included in the site-scale SZ transport model (Sections 6.3 and 6.5). The sorption of radionuclides onto fracture surfaces is not included in this model as a conservative approach.

The process of radionuclide adsorption within rock matrix surfaces is represented using a sorption coefficient (K_d) approach, which is presented in this report with justification for its use (Sections 6.3, 6.4, 6.5, and Attachment I). Probability distributions for the K_d values for radionuclides of interest are derived based on data from the field, laboratory, literature, and models of sorption reactions. The probability distributions are designed to include expected variations in environmental parameters that can influence the sorption behavior of the radionuclides of interest. To make the transport calculations more efficient computationally, an abstraction is developed in which two separate single-valued sorption coefficients are used to calculate transport rates in both the volcanic and alluvial portions of the flow path in the SZ. The justification for this abstraction is provided in this report (Attachment I). Also, the process of colloid-facilitated radionuclide transport is represented using the colloid sorption coefficient (K_c) approach. This modeling approach and its justification are presented in this report (Sections 6.3, 6.4, 6.5, and Attachment II).

The methodology for computing the transport of radionuclides within the SZ has been revised to capture a variety of different processes with accuracy. This document presents a radionuclide transport mathematical and computational model that satisfies the requirement of the Yucca Mountain Project (YMP), which is to produce scientifically defensible transport predictions. The numerical techniques required to implement the method are described in Section 6.5.

Model validation activities presented in this report provide increased confidence that the model is a reasonable representation of the transport likely to occur at Yucca Mountain in the vicinity of the proposed repository site (Section 7). Due to the time and spatial scales involved and the fact that radionuclides cannot be used as tracers in field experiments, confidence building activities during model development as well as post-development validation are documented in this report. Recognizing that the model is being used to perform probabilistic calculations in which parameter uncertainties are propagated through the model, the intent of this validation is to confirm that radionuclide parameters and processes included in the SZ site-scale transport model are adequately represented with sufficient accuracy. Confidence building during model development (Section 7.1) is carried out by a series of different approaches that include: (1) comparisons to analog sites, (2) submodel-data comparisons, (3) model-data comparisons, and (4) comparison with data published in refereed journals. The data used in confidence building for the relevant transport parameters (e.g., sorption coefficients), submodel processes (e.g., advection, sorption), and site-scale model processes (e.g., flow pathways, transit times)

are based on laboratory testing, field tests, natural analog sites, and expert elicitations. Post-development validation (Section 7.2) is carried out by comparison of model predictions with inferences based on geochemical data. By demonstrating that the parameters and processes selected have an experimental or observational basis, the model is validated for use in a stochastic analysis that establishes ranges of potential behavior of the SZ transport system.

The technical output of this report is comprised of (a) the SZ site-scale transport model and associated input and output files (base-case transport files); and (b) SZ Distribution Coefficients (K_ds) data for U, Np, Pu, Cs, Am, Pa, Sr, Th, Ra, C, Tc, and I (Table III-14). The output breakthrough curves and travel times will be integrated into the SZ flow and transport abstractions model for use in the TSPA calculations.

When using the SZ site-scale transport model for calculations, there are limitations that must be noted with regard to the following:

- *Input parameter values/ranges*. The transport model is intended for use with stochastic simulations using large uncertainty ranges for particular parameters such as specific discharge, fracture spacing and aperture, diffusion coefficient, and sorption coefficients. Care should be exercised in interpreting individual simulations for single sets of parameter values. Also, care should be exercised if the parameters used fall outside the range of parameter values (Table 4-2) or outside the range established by model validation (Section 7.2).

- *Useable path-line distances*. The flow field underlying the SZ transport model is based on the dual-porosity, effective-continuum approach requiring large grid blocks that effectively average fracture, rock matrix, and alluvium properties. Also, the parallel fracture model used to model advection/diffusion in the volcanics is valid only for grid-block sizes much larger than the expected flowing-interval spacing of 21 m. It is recommended in the SZ flow model report (BSC 2003 [162649], Section 8) that to produce meaningful results, the flow path should be long compared to the grid-block size. Because the grid-block size is 500 m, a minimum distance of 2 kilometers is recommended for path lines used in PA calculations.

- *Sufficient number of input particles for particle tracking*. Radionuclide transport is implemented in the SZ transport model using particle tracking with a random walk method (Section 6.5.2.3 and 6.5.2.4). In order to obtain reproducible results, sufficient number of particles must be input to the model. The base case transport model utilizes 1000 input particles (Output Data Tracking Number (DTN): LA0306SK831231.001), visually judged to be sufficient for the purpose of obtaining a smooth breakthrough curve at the 18 km compliance boundary (Figure 6.6-1). However, a larger number of input particles may be required depending on the purpose of the model use.

This model report is governed by the Office of Civilian Radioactive Waste Management (OCRWM) *Technical Work Plan For: Saturated Zone Flow and Transport Modeling and Testing* (BSC 2003 [163965], Work Package ASZM04). All activities listed in the technical work plan (TWP) that are appropriate to the transport model are documented in this report.

(Note: In this report, the six-digit numerical identifier in brackets next to each reference callout is the YMP Document Input Reference System [DIRS] number, the purpose of which is to assist the reader in locating a specific reference in the reference list in Section 9 and in the DIRS database.)

2. QUALITY ASSURANCE

Development of this model report and the supporting modeling activities have been determined to be subject to the YMP quality assurance (QA) program (BSC 2003 [163965], Section 8, Work Package ASZM04). Approved QA procedures identified in Revision (REV) 01 of the technical work plan (BSC 2003 [163965], Section 4) have been used to conduct and document the activities described in this model report. The technical work plan also identifies the methods used to control the electronic management of data (BSC 2003 [163965], Section 8).

This model report provides calibrated values for hydrologic properties of the saturated zone natural barrier, which is important to demonstrate compliance with the postclosure performance objectives prescribed in 10 CFR 63.113 [156605]. Therefore, the saturated zone is classified on the *Q-List* (BSC 2003 [165179], Table A-2) as "SC" (Safety Category), reflecting its importance to waste isolation, as defined in AP-2.22Q, *Classification Analyses and Maintenance of the Q-List*. This report contributes to the analysis and modeling data used to support postclosure performance assessment; the conclusions do not directly impact preclosure engineered features important to safety, as defined in AP-2.22Q].

INTENTIONALLY LEFT BLANK

3. USE OF SOFTWARE

3.1 SOFTWARE TRACKED BY CONFIGURATION MANAGEMENT

The computer software code used as the basis to model SZ transport in this report is FEHM (Finite Element Heat and Mass Transport code) V 2.20 (STN: 10086-2.20-00 [161725]). This version of the code includes the particle-tracking algorithm described in this report and was obtained from Software Configuration Management. The other codes listed in Table 3-1 were used in the analysis described in the Attachments. All were obtained from Software Configuration Management, used only within the range of validation as required by AP-SI.1Q, *Software Management*, and are appropriate for the application in this report. Input and output files for this report are listed in Section 8.2.2 and identified in the respective discussions in Sections 6, 7, and 8.

Table 3-1. Computer Software and Routines

Software Title/Version Number	Software Tracking Number (STN)	Code Usage	Computer: Type, Platform, and Location	References
FEHM V 2.20	10086-2.20-00	Used for calculations throughout this model report. The FEHM V 2.20 application is based on a finite-volume/finite-element heat- and mass-transfer code that simulates nonisothermal, multiphase, multicomponent flow and solute transport in porous media.	Sun, PC SUN OS 5.7 and 5.8, Windows 2000, Linux 7.1 Location: Los Alamos National Laboratory (LANL).	LANL 2003 [161725]
cr8sptr.c V 2.0	10927-2.0-00	Used to create an input file for sptr macro in FEHM.	Sun, Sun OS 5.7, Location: LANL	SNL 2002 [163836]
calc_cdf.c V 1.0	10924-1.0-00	Used to calculate the cumulative distribution function (CDF) of the stochastic distributions of K_d.	Sun, Sun OS 5.7, Location: LANL	SNL 2000 [149117]
gs2fehm.c V 1.0	10923-1.0-00	Used to create an input file for the perm macro in FEHM.	Sun, Sun OS 5.7, Location: LANL	SNL 2002 [163837]
GSLIB V1.0GAMV3V1.201	10398-1.0GAMV3V1.201-00	Used to calculate a three-dimensional (3-D) variogram of input data.	Sun, Sun OS5.5.1, Location: LANL	LBNL 2000 [153099]
GSLIB V2.0MSISIMV2.0	10098-2.0MSISIMV2.0-00	Used to generate a stochastic distributions of parameters, such as K_d and permeability.	Sun, UNIX, Location: LANL	SNL 2000 [149114]
PHREEQC V 2.3	10068-2.3-00	Calculates surface complexation reactions for radionuclides.	PC, Location: LANL	BSC 2001 [155323]
FRACT_p V1.0	11009-1.0-00	Calculates data that correlate concentrations with time for transport in the fractured media.	Sun, UNIX, Location: LANL	LANL 2003 [164509]

3.2 EXEMPT SOFTWARE

Commercial, off-the-shelf software used in support of this model report is listed in Table 3-2. This software is exempt from the requirements of AP-SI.1Q, *Software Management*.

Table 3-2. Exempt Software

Software Name and Version (V)	Description	Computer and Platform Identification
Microsoft Excel, 2000	The commercial software, Microsoft Excel, 2000, was used for preparing spreadsheets of data and plotting graphs. No data analysis was done with this software. Only built-in standard functions in this software were used. No software routines or macros were used with this software to prepare this report. The output was visually checked for correctness.	PC, Windows 2000/NT
FORTNER SUN PLOT	The commercial software, FORTNER SUN PLOT, was used for plotting graphs. No data analysis was done with this software. Only built-in standard functions in this software were used. No software routines or macros were used with this software to prepare this report. The output was visually checked for correctness.	SUN with UNIX OS, FORTRAN
SURFER V6.03	The commercial software, SURFER V 6.03, was used for plotting and visualization of analysis results in figures shown in this report. No data analysis was done with this software. Only built-in standard functions in this software were used. No software routines or macros were used with this software to prepare this report. The output was visually checked for correctness.	PC, Windows 2000/NT

4. INPUTS

4.1 DATA AND PARAMETERS

This section identifies all input data and parameters that are used in this modeling activity.

4.1.1 Data and Technical Information

The data providing input for the development of parameters used in the modeling activities documented in this report are listed in Table 4-1. The base case flow model (DTN: LA0304TM831231.002 [163788]) forms the starting point data for this transport model. The development of this flow model, including the conceptual model, various alternate conceptual models, the choice of parameter values for base case flow model, and the appropriateness of data and technical information used in this model are discussed in detail in BSC 2003 ([162649], Sections 4, 5 and 6). For a number of parameters that are needed in the transport model, the selection of ranges of values and uncertainty distributions are presented in BSC 2003 ([164870], Section 6.5.2; DTN: SN0306T0502103.007 [163946]). Where available, sorption coefficient data for radionuclides of interest on rock and water samples from Yucca Mountain were used for developing the K_d distributions that are used in this model report, as described in detail in Attachment I of this report. These sorption coefficient data were augmented by technical information available in the literature on systems with similar geochemical characteristics. Mineralogic composition data are available on core samples taken from boreholes in the Yucca Mountain area. Since these data are site specific, they were considered to be the most appropriate data for use in stochastic analysis of K_d distributions described in Attachment III of this report. These input data and technical information, and their sources are given in Table 4-1. Parameters needed for modeling colloid facilitated transport (Table 4-2) were obtained from BSC (2003 [162729] Sections 6.4, 6.5, and 6.6) and BSC (2003 [161620] Tables 5, and 10). Justification for the choice of data and technical information for selecting the range of values (presented in Table 4-2) of all other parameters needed for the SZ transport model is given in detail in (BSC 2003 [164870] Section 6.5.2). The qualification status of the input sources is provided in the Technical Data Management System. A discussion of the selection of the range of values for each model parameter using the available data is presented in Section 4.1.2.

Table 4-1. Input Data and Technical Information

Data and Technical Information for Uncertainty Distribution of Parameters		
Data Description	**Source**	**Data Tracking Number**
Uncertainty distribution for parameters used in the SZ transport abstractions model	BSC 2003 [164870], Section 6.5.2	SN0306T0502103.007 [163946]
Data and Technical Information for Base Case Flow Model		
Data Description	**Source**	**Data Tracking Number**
FEHM V2.20 files for base case flow model	BSC 2003 [162649], entire document	LA0304TM831231.002 [163788]

Table 4-1 (continued). Input Data and Technical Information

Data and Technical Information for Sorption Coefficient Data		
Data Description	**Source**	**Data Tracking Number**
Input data file (LLNL.DAT) for thermodynamic data software code PHREEQC, Version 2.3.	N/A	MO0309THDPHRLL.000 [165530]
Input data file (PHREEQC.DAT) for thermodynamic data software code PHREEQC, Version 2.3.	N/A	MO0309THDPHRQC.000 [165529]
Am, Pa, Pu, and Th sorption coefficients on silica and surface area for silica sample	Allard et al. 1983 [162982], pp. 6, 9, 10, 12; Allard et al. 1980 [104410], p. 478; Beall et al. 1986 [162983], entire document.	Technical Information
Density of sorption sites,on the solid surface, U and Np surface complexation binding constants on silica	Pabalan et al. 1998 [162987], p. 124; Bertetti et al. 1998 [162984], entire document	Technical Information
Cs, Sr, Ba, Ra, Am, Th, Pu, and Pa sorption coefficients on Yucca Mountain tuffs in J-13 water	Thomas 1987 [101361], entire document	LA000000000042.001 [162791]
Ba sorption coefficient on devitrified tuff	N/A	LA0010JC831341.001 [162476]
Surface areas for Yucca Mountain tuffs	Triay et al. 1996 [101023], p. 62	LA0311SK831341.001 [166195]
Np, U, Pu, Ba, Sr, Cs sorption coefficients on Yucca Mountain tuffs	N/A	LA0010JC831341.002 [153321], LA0010JC831341.003 [153322], LA0010JC831341.005 [153320], LA0010JC831341.006 [153318], LA0010JC831341.007 [153319], LA0305AM831341.001 [163789], LA0302MD831341.003 [163784], LA0302MD831341.004 [163785]
Eh-pH field measurements on Nye County EWDP wells	N/A	LA0206AM831234.001 [160051]
Geochemical field measurements on Nye County EWDP wells.	N/A	LA0206AM831234.002 [163852]
The elutions of radionuclides through columns of crushed rock from the Nevada Test Site	Treher and Raybold 1982 [125967], entire document	LA000000000010.001 [162788]
Transport of Np through Yucca Mountain tuffs	Triay et al. 1993 [144693], entire document	LA000000000035.001 [162789]
Np retardation with tuffs and groundwater from Yucca Mountain	Triay et al. 1993 [125972], entire document	LA000000000035.002 [162790]
Sorption of Np, Pu, and Am on rock samples from Busted Butte, NV	N/A	LA0004WS831372.002 [149399]
Radionuclide retardation measurements of sorption distribution coefficients for Ba	N/A	LA0010JC831341.001 [162476]
Radionuclide retardation measurements of sorption distribution coefficients for Se	N/A	LA0010JC831341.004 [153323]

Table 4-1 (continued). Input Data and Technical Information

Data Description	Source	Data Tracking Number
Np sorption onto clinoptilolite-rich tuff in J-13 water under atmospheric conditions	N/A	LA0012AM831341.002 [163042]
Uranium sorption coefficients for minerals and tuffs under oxidizing conditions in J-13 water	N/A	LA0101AM831341.001 [163043]
Static batch sorption coefficients and retardation coefficients	N/A	LA0108TV12213U.001 [161525]
Adsorption of Np-237 in three types of alluvium as a function of time and stratigraphic position	N/A	LA0109MD831341.001 [156870]
Adsorption of Tc-99 in three types of alluvium as a function of time and stratigraphic position	N/A	LA0109MD831341.002 [156871]
Batch sorption coefficient data for Ba on Yucca Mountain tuffs in representative water compositions	N/A	LA0309AM831341.002 [165523]
Batch sorption coefficient data for Cs on Yucca Mountain tuffs in representative water compositions	N/A	LA0309AM831341.003 [165524]
Batch sorption coefficient data for Np on Yucca Mountain tuffs in representative water compositions	N/A	LA0309AM831341.004 [165525]
Batch sorption coefficient data for Pu on Yucca Mountain tuffs in representative water compositions	N/A	LA0309AM831341.005 [165526]
Batch sorption coefficient data for Sr on Yucca Mountain tuffs in representative water compositions	N/A	LA0309AM831341.006 [165527]
Batch sorption coefficient data for U on Yucca Mountain tuffs In representative water compositions	N/A	LA0309AM831341.007 [165528]
Water chemistry for J-13 water and pH in p#1 water	N/A	MO0007MAJIONPH.013 [151530]
Water chemistry for p#1 water	N/A	MO0007MAJIONPH.010 [151523]
CO_3^{2-} and F^- data for p#1 water	Benson and McKinley 1985 [101036], entire document	GS920408312321.003 [105937]
CO_3^{2-} and F^- data for J-13 water	Benson et al. 1983 [100727], entire document	GS930308312323.001 [145530]
Deprotonation constants and binding constants for Al on silica	Dixit and Van Cappellen 2002 [162985], p. 2565	Technical Information
Binding constants for Na on silica	Marmier et al. 1999 [162986], p. 228	Technical Information
Binding constants for Np on silica	Turner et al. 1998 [162989], p. 264	Technical Information
Binding constants for K and Ca on silica	Triay et al. 1997 [100422], p. 169	Technical Information
18-km regulatory compliance boundary		
18-km regulatory compliance boundary	10 CFR 63.302 [156605]	Technical Information

Table 4-1 (continued). Input Data and Technical Information

Data and Technical Information for Stochastic Analysis Scaling for K_d		
Data Description	**Source**	**Data Tracking Number**
XRD data describing mineralogic composition of core samples from wells	Chipera et al. 1995 [111081], entire document	LA000000000086.002 [107144]
XRD data describing mineralogic composition of core samples from wells	N/A	LAJC831321AQ98.005 [109004], LADV831321AQ97.001 [107142], LASC831321AQ98.001 [109047], LADV831321AQ99.001 [109044]
XRD data describing mineralogic composition of core samples from wells	Steinborn 2002 [160702], entire document)	MO0101XRDMINAB.001 [163796], MO0106XRDDRILC.003 [163797], MO0101XRDDRILC.002 [163795]
Values of diffusion coefficients used for scaling.	N/A	LA0003JC831362.001 [149557]
Hydraulic gradient used in stochastic modeling on a 550 m block	CRWMS M&O 2000 [152259], pp. 14, Sec. 5.2.	Product Output
Data and Technical Information for FEP		
Data Description	**Source**	**Data Tracking Number**
LA FEPs list	N/A	MO0307SEPFEPS4.000 [164527]

4.1.2   Parameters and Parameter Uncertainty

The range of values for each input parameter is presented in Table 4-2 and discussed in Sections 4.1.2.1 through 4.1.2.18 and in Attachment I of this report. The ranges of sorption coefficient values presented in Table 4-2 encompass all the radionuclides of interest since the intent of this AMR is to present an SZ transport model that can be used by the TSPA with any of these radionuclides. The distributions for individual radionuclides are presented in Table III-14. Base case values for most parameters were chosen to be the median values for the distributions except for sorption coefficients, which were taken to be 0 to represent a nonsorbing radionuclide such as [14]C.

Table 4-2. Input Parameters and Range of Values for the SZ Transport Model

Parameter	Base-Case Value(s)	Uncertainty Range	Units	Variable Type	Source/DTN
Specific discharge multiplier [a]	1 [b]	1/30–10	-	stochastic	BSC (2003 [164870]) SN0306T0502103.007 [163946]
Permeability horizontal anisotropy ratio	4.2 [c]	0.05–20	-	stochastic	SN0306T0502103.007 [163946]
Bulk density in alluvium	1910 [c]	1669–2151 [d]	kg/m^3	stochastic	BSC (2003 [164870]) SN0306T0502103.007 [163946]
Sorption coefficient in alluvium	0.0 [e]	0–10000	mL/g	stochastic	Attachment I and III

Table 4-2 (continued). Input Parameters and Range of Values for the SZ Transport Model

Parameter	Base-Case Value(s)	Uncertainty Range	Units	Variable Type	Source/DTN
Effective porosity in the alluvium, fraction	0.18 [b]	0. 02–0.3	-	stochastic	BSC (2003 [164870]) SN0306T0502103.007 [163946]
Colloid retardation factor in alluvium for irreversible colloids	0 [g]	7.9–5188	-	stochastic	BSC (2003 [162729]) LA0303HV831352.004 [163559]
Flowing interval porosity, fraction [i]	0.01 [f]	0.00001–0.1	-	stochastic	BSC (2003 [164870]) SN0306T0502103.007 [163946]
Flowing interval spacing	20 [b]	1.22–417	m	stochastic	SN0306T0502103.007 [163946]
Matrix porosity in volcanics, fraction	0.15–0.25 [h]	N/A	-	Assigned value for each unit; not a stochastic parameter	BSC (2003 [164870]) SN0306T0502103.007 [163946]
Effective diffusion coefficient in volcanics	5.0×10^{-11} [b]	5.0×10^{-12}– 5.0×10^{-10}	m^2/s	stochastic	BSC (2003 [164870]) SN0306T0502103.007 [163946]
Matrix sorption coefficient in volcanics	0.0 [e]	0–10000	mL/g	stochastic	Attachments I & III
Colloid retardation factor in volcanics for irreversible colloids	0 [g]	6.0–794	-	stochastic	BSC (2003 [162729]) LA0303HV831352.002 [163558]
Groundwater concentration of colloids	0 [g]	10^{-9}– 2.5×10^{-4}	g/mL	N/A	BSC (2003 [161620])
Sorption coefficient onto colloids	0 [g]	10^{1}–10^{7}	mL/g	N/A	BSC (2003 [161620])
Fraction of colloids transported unretarded	0 [g]	0.00034– 0.0017	-	stochastic	BSC (2003 [162729])
Dispersivity, longitudinal	10.0	0.10–2000	m	stochastic	Section 4.1.2.16
Dispersivity, transverse, horizontal	0.05	0.0005–10	m	stochastic	Section 4.1.2.17
Dispersivity, transverse, vertical	0.0005	0.000005– 0.1	m	stochastic	Section 4.1.2.18

[a] The boundary fluxes, recharge rates and permeabilities were multiplied by this factor to vary the specific discharge, which has a base case value of 0.67 m/yr from the repository to the 5-km boundary (BSC 2003 [162649] Section 6.6.2.3).

[b] Median value, given as the 0.5 probability value in the source DTN

[c] Median value, interpolated to the 0.5 probability from the data given in the source DTN

[d] Range derived from the normal distribution given in BSC (2003 [164870] Figure 6-16)

[e] Base case is taken to be the value for nonsorbing radionuclides.

[f] Base case value taken at 0.8 probability

[g] Base case colloid parameters are set to 0 to simulate the base case of nonsorbing radionuclide.

[h] Each hydrostratigraphic unit was assigned a fixed value within this range.

[i] Flowing interval porosity is referred to as the "Fracture porosity in volcanic units" in SN0306T0502103.007 [163946].

4.1.2.1   Specific Discharge Multiplier

Field values of groundwater specific discharge in the SZ have been estimated from the tracer testing at the Alluvial Testing Complex (ATC) (BSC 2003 [162415], Section 6.5) to be in the range of 1.2 m/yr to 9.4 m/yr. This information is combined with the recommendations from the SZ expert elicitation project (CRWMS M&O 1998 [100353], pp. 3-43) to create a distribution of the specific discharge multiplier in the range of 1/30 to 10 (DTN: SN0306T0502103.007 [163946]). More details of this analysis are presented in BSC 2003 ([164870], Section 6.5.2.1). All the permeabilities in the base-case flow model are multiplied by this factor, and all the recharge values and boundary fluxes input to the model are also multiplied by this factor to preserve the calibration of the base case SZ flow model (BSC 2003 [162649], Section 6.6 and DTN: LA0304TM831231.002 [163788]). The effect of the range of uncertainty in this parameter on the output breakthrough curves is presented in Section 8.3.2.1. The base case multiplier for the SZ transport model is chosen to be 1, corresponding to the value used in the base case SZ flow model.

4.1.2.2   Horizontal Anisotropy in Permeability

Field estimates of the horizontal permeability anisotropy ratio in the north-south/east-west direction were obtained from the long-term pumping test conducted at the C-wells complex (BSC 2003 [162415], Section 6.2.6). These data were used to obtain a distribution of the anisotropy ratio in the range of 0.05 to 20 with a median value of 4.2 (DTN: SN0306T0502103.007 [163946]). More details of this analysis are presented in BSC (2003 [164870], Section 6.5.2.10). The effect of the range of uncertainty in this parameter on the output breakthrough curves is presented in Section 8.3.2.2. The base case ratio is chosen to be the median value of 4.2.

4.1.2.3   Bulk Density in Alluvium

Borehole gravimeter data (DTN: MO0105GPLOG19D.000) [163480] from the well NC-EWDP-19D1 was used in conjunction with laboratory grain-density measurements (USGS n.d. [154495]) in estimating the uncertainty distribution of the bulk density. These data yielded a normal distribution with a mean of 1910 kg/m^3 and standard deviation of 78 kg/m^3 (SN0306T0502103.007 [163946]). More details of this analysis are presented in BSC (2003 [164870], Section 6.5.2.7) and are presented graphically in (BSC 2003 [164870], Figure 6-16). From this graph, a lower bound of 1669 kg/m^3 and an upper bound of 2151 kg/m^3 are estimated. The effect of the range of uncertainty in this parameter on the output breakthrough curves is presented in Section 8.3.2.3. The base case value is chosen to be the median value of 1910 kg/m^3.

4.1.2.4   Sorption Coefficient in Alluvium

Sorption coefficient measurements for Np and U on core samples from the alluvium to the south of the Yucca Mountain are available (Section I.8.3.3 and Section I.8.9.3 of Attachment I). For the radionuclides of Am, Cs, Pu, Pa, Ra, Sr and Th, the data on devitrified tuff samples from the Yucca Mountain area are used, since devitrified tuff makes up a major portion of the alluvium (Sections I.8.1.3, I.8.2.3, I.8.4.3, I.8.5.3, I.8.6.3, I.8.7.3 and I.8.8.3 of Attachment I). These data

and the analysis to obtain stochastic uncertainty distributions for the sorption coefficient are presented in detail in Attachment I of this report. Uncertainty distributions with wide ranges were selected to account for the uncertainty in the sorption coefficient rising from the uncertainties associated with the conceptual model (Section 6), geochemical conditions, and the in situ rock mineralogy (Output DTN: LA0310AM831341.002). The sensitivity of the breakthrough curves for each radionuclide to the uncertainty in its K_d values is presented in BSC (2003 [164870], Section 6.6). In this report only the overall uncertainty range that encompasses all the radionuclides, 0 to 10,000 mL/g (Table 4-2), is considered. The effect of the range of uncertainty in this parameter on the output breakthrough curves is presented in Section 8.3.2.4. A base-case value of 0 is chosen to represent the case of nonsorbing radionuclides.

4.1.2.5   Effective Porosity in Alluvium

The study of Bedinger et al. (1989 [129676], p. A18, Table 1) on the hydraulic characteristics of alluvium within the Southwest Basin and Range Province appears relevant to the local basin fill conditions and provides an uncertainty distribution for effective porosity. Further information is available from the following sources: (1) single-point, site-specific, effective porosity data from the well NC-EWDP-19D1 (BSC 2003 [162415], Section 6.5) with a value of 0.1; (2) total porosity data from the CAMBRIC study (Burbey and Wheatcraft 1986 [129679], pp. 23-24) with an average value of 0.34; and (3) total porosity data from the DOE (1997 [103021], Tables 8-1 and 8-2) with values of 0.36 and 0.35. All these data are used as supporting information to develop an uncertainty distribution with an upper bound of 0.3, median value of 0.18 and lower limit of 0 (DTN: SN0306T0502103.007 [163946]) for the effective porosity. More details of this analysis are presented in BSC (2003 [164870], Section 6.5.2.3). The lower limit given in this work (Table 4-2 and Table 6.5-2) is 0.02, which is slightly greater than 0. This is a conservative choice and helps to avoid any potential numerical problems with the value 0. The effect of the range of uncertainty in this parameter on the output breakthrough curves is presented in Section 8.3.2.5. The base case value is chosen to be the median value of 0.18.

4.1.2.6   Retardation Factor in Alluvium for Irreversible Colloids

The development of colloid retardation factors based on experimental data specific to Yucca Mountain as well as field studies of bacteriophage transport in alluvial material is presented in BSC (2003 [162729], Section 6.5). An uncertainty distribution with a range of 7.9 to 5188 and a median value of 33.9 is presented. More details of this analysis are presented in BSC (2003 [164870], Section 6.5.2.11). The effect of the range of uncertainty in this parameter on the output breakthrough curves is presented in Section 8.3.2.6. The base case value is set to 0 to simulate the transport of nonsorbing radionuclides.

4.1.2.7   Flowing Interval Porosity

At Yucca Mountain, a flowing interval is defined as the region in which significant groundwater flow occurs at a well. The fracture porosity then characterizes these flowing intervals rather than individual fractures. Data from tests in unsaturated tuff in the Exploratory Studies Facility (ESF) using gas flow (BSC 2003 [161773], p. 42), water flow (BSC 2003 [161773], p. 64), cross-hole tracer tests at the C-Wells complex (CRWMS M&O 1997 [100328], pp. 2 to 4 and 28), Nevada Environmental Restoration Project tests (DOE 1997 [103021], pp. 5-14), and laboratory measurements on core from the wells USW G-1, USW GU-3, USW G-4, and UE-25 a#1, where

parallel-plate fracture geometry model is used (Wilson et al. 1994 [100191], Volume 1, Chapter 7, Table 7-19, p. 7-30) were used to estimate the uncertainty distribution with a range of 0.00001 to 0.1 and a median value of 0.001 More details of this analysis are presented in BSC (2003 [164870], Section 6.5.2.5). The flowing interval porosity enters the transport model indirectly through the flowing interval aperture parameter, which is computed as a product of the porosity and the spacing. The effect of the range of uncertainty in the flowing interval aperture on the output breakthrough curves is presented in Section 8.3.2.8. The base case value of the flowing interval porosity is taken to be .01, which is greater than the median value of the distribution. This is because, as discussed in BSC 2003 [164870], Section 6.5.2.5, the median value of .001 is at the lower limit of the values obtained from field data acquired after TSPA Site Recommendations (SR) calculations were done—0.01 is more representative of the average of this data.

4.1.2.8   Flowing Interval Spacing

An uncertainty distribution with a range of 1.22 m to 417 m and a median value of 20 m was developed in BSC (2003 [164870], Section 6.5.2.4). The borehole flow meter survey data and analysis presented in *Probability Distributions for Flowing Interval Spacing* (BSC 2001 [156965], p. 84) were used in the above referenced analysis. The flowing interval spacing enters the transport model indirectly through the flowing interval aperture parameter, which is computed as a product of the porosity and the spacing. The effect of the range of uncertainty in the flowing interval aperture on the output breakthrough curves is presented in Section 8.3.2.8. The base case value of the flowing interval spacing was taken to be the median of the distribution, 20 m.

4.1.2.9   Matrix Porosity in Volcanics

The matrix porosity in volcanic units is treated as a nonstochastic parameter, although it is allowed to vary from unit to unit (DTN: SN0306T0502103.007 [163946]). It is acceptable to treat this parameter as a nonstochastic parameter because it enters the SZ transport model through a combination with the distribution coefficient (Equation 57, Section 6.5.2.4.1 of this report) or with the diffusion coefficient (Equations 64 and 74, Section 6.5.2.4.1 of this report), and both these coefficients are being treated as stochastic variables with wide ranges (Sections 4.1.2.10 and 4.1.2.11 of this report). Values are assigned on a unit-by-unit basis. These values are in the range 0.15 to 2.5. Values were chosen based on the *Rock Properties Model* (BSC 2002 [159530], Table 13, p. 52) and porosity data from boreholes UE-25 p#1, USW H-3, USW SD-7, USW G-3, USW H-1, USW G-4, USW H-5, and USW H-6 (DTN: SN0004T0501399.003 [155045], MO0109HYMXPROP.001 [155989], and MO0010CPORGLOG.002 [155229]). More details of this analysis are presented in BSC (2003 [164870], Section 6.5.2.18).

4.1.2.10 Effective Diffusion Coefficient in Volcanics

Matrix diffusion is a process in which diffusing particles move, via Brownian motion, through both mobile and immobile fluids. Diffusion is a Fickian process, that is, diffusing species move from high to low concentrations. It is dependent on the free water molecular diffusion coefficient for individual constituents and the characteristics of the flow path in which the diffusing species passes. Because diffusion through porous media is less than free water

molecular diffusion, it is quantitatively defined as the effective diffusion coefficient, D_e. The variability in D_e in saturated media is caused by the variability in: 1) the individual constituents' size (atom, ion, or molecule) and charge; 2) fluid temperature; and 3) the unique properties of a porous media's lithology at a microscopic scale, including the tortuosity of the media.

Diffusion-cell measurements on numerous rock samples from the vicinity of Yucca Mountain have been reported by Reimus et al. (2002 [162956], Tables 3-2 through 3-8; 2002 [163008], Tables 2-4 and 2-5). These measurements give a correlation between the measured effective diffusion coefficient, sample porosity, and sample permeability. The range of values is corroborated by the site-specific values reported by Triay et al. (1993 [145123], Tables 1 and 2) and Rundberg et al. (1987 [106481]). The correlation given by Reimus et al. (2002 [163008]) Equation 2.5, p. 2.25) was used to develop a range of values appropriate for the porosities and permeabilities of various units as reported in Flint (1998 [100033], p. 89). These were scaled to account for the uncertainty and variation in the effective diffusion coefficient based on the species size and charge, leading to the final uncertainty range of 5 x 10^{-12} to 5 x 10^{-10} m^2/s, with a median value of 5.0 x 10^{-11} m^2/sec (DTN: SN0306T0502103.007 [163946]). Details of this analysis are presented in BSC (2003 [164870], Section 6.5.2.6). The effect of the range of uncertainty in this parameter on the output breakthrough curves is presented in Section 8.3.2.9. The median value of 5.0 x 10^{-11} m^2/sec was taken to be the base case value.

4.1.2.11 Matrix Sorption Coefficient in Volcanics

Sorption coefficients were measured on devitrified and zeolitic tuff samples from the Yucca Mountain area for the radionuclides Am, Ba, Cs, Np, Pu, Pa, Ra, Sr, Th and U (Attachment I). These data and analyses were used to obtain stochastic uncertainty distributions for the sorption coefficients presented in detail in Attachment I of this report. These measurements represent a spatial scale on the order of centimeters. A stochastic scaling procedure was used to obtain from these distributions the uncertainty distributions on the scale of 500 m, which is the scale of the grid blocks used in the SZ transport model. This stochastic analysis is presented in detail in Attachment III of this report. Stochastic analysis was combined with expert judgment (Attachment III, Sec III-2) to develop uncertainty distributions with wide ranges. These were selected to account for the uncertainty in the sorption coefficient rising from the uncertainties associated with the conceptual model (Section 6), geochemical conditions, and the in situ rock mineralogy (Output DTN: LA0310AM831341.002). The resulting distributions for individual radionuclides are given in Table III-14 and Output DTN: LA0310AM831341.002. The overall uncertainty range that encompasses all the radionuclides is 0 to 10,000 mL/g (Table III-14). The effect of the range of uncertainty in this parameter on the output breakthrough curves is presented in Section 8.3.2.10. A base-case value of 0 was chosen to represent the case of nonsorbing radionuclides such as C^{14}.

4.1.2.12 Retardation Factor in Volcanics for Irreversible Colloids

BSC (2003 [162729], Section 6.4) describes the development of colloid retardation factors for fractured tuff from field and experimental data. More details of this analysis are presented in BSC (2003 [164870], Section 6.5.2.11) leading to an uncertainty distribution with a range of 6 to 794 and a median value of 26 (DTN: LA0303HV831352.002 [163558]). The effect of the range of uncertainty in this parameter on the output breakthrough curves is presented in Section

8.3.2.11. Base case value for the SZ transport model is set to 0 to simulate the transport of nonsorbing radionuclides.

4.1.2.13 Groundwater Concentrations of Colloids

The uncertainty distribution was developed in BSC (2003 [161620], Table 5). A range of 10^{-9} to 2.5×10^{-4} g/mL with a median value of 10^{-7} g/mL is given. This parameter enters the SZ transport model indirectly through the coefficient for reversible sorption onto colloids (BSC 2003 [164870], Section 6.5.2.12). The effect of the range of uncertainty in this parameter on the output breakthrough curves is presented in Section 8.3.2.12. The value of this parameter in the base case transport model is set to 0 to simulate the transport of nonsorbing radionuclides.

4.1.2.14 Sorption Coefficient onto Colloids

The uncertainty distributions for the coefficient of sorption of Pu, Am, Th, Pa, and Cs onto colloids were developed in BSC (2003 [161620], Table 10). A range of 10^{1} to 10^{7} mL/g was used with a median value of 0.5×10^{7} mL/g. More details are presented in BSC (2003 [164870], Section 6.5.2.12). This parameter enters the SZ transport model indirectly through the coefficient for reversible sorption onto colloids. The effect of the range of uncertainty in this parameter on the output breakthrough curves is presented in Section 8.3.2.12. The value of this parameter in the base case transport model is set to 0 to simulate the transport of nonsorbing radionuclides.

4.1.2.15 Fraction of Colloids Transported Unretarded

A discussion of the fraction of colloids transported with no retardation is in BSC (2003 [162729], Section 6.6). The range of uncertainty distribution of this fraction is taken to be 0.00034 to 0.0017 with a median value of 0.0005. This parameter is applied in the TSPA calculations after the breakthrough curves are calculated from the SZ transport model; hence the influence of the uncertainty in this parameter on the breakthrough curves is not discussed in this AMR. The base case value is set to 0 to simulate the transport of nonsorbing radionuclides.

4.1.2.16 Dispersivity, Longitudinal

As explained in BSC (2003 [164870], Section 6.5.2.9), the uncertainty distribution for longitudinal dispersivity was taken to be truncated lognormal with the mean of 2 and the standard deviation of 0.75 (in the log space) (DTN: SN0306T0502103.007 [163946]). The basis used in BSC 2003 [164870] for this was expert elicitation (CRWMS M&O 1998 [100353], pp. 3-10, 3-11, and LG-12). Graphically the estimated range of this distribution is 1 m to 20000 m with a median value of 100 m (BSC 2003 [164870]), Figure 6-18). As explained in BSC 2003 ([164870]), Section 6.5.2.9 and Figure 6-19), these dispersivity values are on the scale of the SZ transport model and correspond to dispersivity values smaller by a factor of 10 when represented on the scale of 500 m, the scale of computational grid blocks. Hence the range of uncertainty for this parameter given in Table 4-2 is 0.1 m to 2000 m. More details of this analysis are presented in BSC (2003 [164870]), Section 6.5.2.9). The effect of the range of uncertainty in this parameter on the output breakthrough curves is presented in Section 8.3.2.13. The base case value is taken to be the median value on the 500-m scale, 10 m.

4.1.2.17 Dispersivity, Transverse, Horizontal

As explained in BSC (2003 [164870], Section 6.5.2.9), the basis for computing the transverse horizontal dispersivity values was determined by dividing the longitudinal dispersivity by a factor of 200. The basis used in BSC (2003 [164870]) for this was expert elicitation (CRWMS M&O 1998 [100353], pp. 3-11, LG-11, and LG-14). More details of this analysis are presented in BSC (2003 [164870], Section 6.5.2.9). The range of values is 0.0005 m to 10 m. The base case value is taken to be 0.05 m, calculated as the median value of the longitudinal dispersivity (Section 4.1.2.16) of 10 m divided by 200.

4.1.2.18 Dispersivity, Transverse, Vertical

As explained in BSC (2003 [164870], Section 6.5.2.9), the basis for computing the transverse vertical dispersivity values was determined by dividing the transverse horizontal dispersivity by a factor of 100. The basis used in BSC (2003 [164870]) for this was expert elicitation (CRWMS M&O 1998 [100353], pp. 3-11, LG-11, and LG-14). More details of this analysis are presented in BSC (2003 [164870], Section 6.5.2.9). The range of values is 0.000005 m to 0.1 m. The base case value is taken to be 0.0005 m, calculated as the base value of the transverse horizontal dispersivity (Section 4.1.2.17) of 0.05 m divided by 100.

4.1.3 Accuracy, Precision, And Representativeness

The SZ site-scale transport model is a theoretical framework involving a number of transport parameters that reflect the properties of the saturated zone, incorporated into a computer code using numerical methods. This model is intended for making TSPA predictions using stochastic methods with a wide range of values that reflect uncertainty in the input parameters. The accuracy and precision of the output results depend upon the accuracy and precision of the input parameter values, the theoretical model and the numerical model. As seen in Table 4-2, the uncertainty ranges for all input parameters (except the matrix porosity in volcanics, which is a deterministic value per each lithologic unit) are at least 25 % or more of the base case value, and in most cases they are several orders of magnitude larger than the base case value. The theoretical and mathematical methods selected for the computational transport model, as described in detail in Section 6 of this report, are well established in the literature and are sufficiently accurate to deal with these wide parameter ranges. The approach taken in this report is to select a range of values for each input parameter as described in Section 4.1.2 of this report and evaluate the propagation of this uncertainty range to the output breakthrough curves as described in Section 8. Confidence in the representativeness of the model output is developed through the validation activities of comparison against field data and independent models, and other confidence building activities described in detail in Section 7 of this report.

4.2 CRITERIA

The general requirements to be satisfied by the TSPA are stated in 10 CFR 63.114 [156605]. Technical requirements to be satisfied by the TSPA are identified in the Yucca Mountain *Project Requirements Document* (Canori and Leitner 2003 [161770]). The acceptance criteria that will be used by the Nuclear Regulatory Commission (NRC) to determine whether the technical requirements have been met are identified in the *Yucca Mountain Review Plan* (YMRP; NRC

2003 [163274]). The pertinent requirements and criteria for this report are summarized in Table 4-3.

Table 4-3. Project Requirements and YMRP Acceptance Criteria Applicable to This Model Report

Requirement Number[a]	Requirement Title[a]	10 CFR 63 Link[b]	YMRP Acceptance Criteria[c]
PRD-002/T-014	Performance Objectives for the Geologic Repository After Permanent Closure	10 CFR 63.113(a) and 63.115(a)–(c)	Criteria 1 to 3 for *System Description and Demonstration of Multiple Barriers*
PRD-002/T-015	Requirements for Performance Assessment	10 CFR 63.114 (a)–(c) and (e)–(g)	Criteria 1 and 2 for *Radionuclide Transport in the Saturated Zone*

NOTE: [a] from Canori and Leitner (2003 [161770])
[b] from 10 CFR 63 [156605]
[c] from NRC (2003 [163274])

The acceptance criteria identified in Section 2.2.1.1, *System Description and Demonstration of Multiple Barriers*, of the YMRP (NRC 2003 [163274] are given below, followed by a short description of their applicability to this model report.

- Acceptance Criterion 1, Identification of Barriers is Adequate:

  Barriers relied on to achieve compliance with 10 CFR 63.113(b), as demonstrated in the total system performance assessment, are adequately identified and are clearly linked to their capability. The barriers identified include at least one from the natural system. This model report describes the transport of radionuclides with the groundwater in the saturated zone of the natural system.

- Acceptance Criterion 2, Description of Barrier Capability to Isolate Waste is Acceptable:

  The capability of the identified barriers to prevent or substantially delay the movement of water or radioactive materials is adequately identified and described.

  1. The information on the time period over which each barrier performs its intended function, including any changes during the compliance period, is provided. This model report relates to the time period from the possible entry of the radionuclides into the SZ via the unsaturated zone (UZ) to the possible release of the contaminants at the compliance boundary. As shown in Sections 6, 7, and 8 of this report, this period can range from several hundreds of years to tens of thousands of years or longer after a potential release of the radionuclides.

  2. The uncertainty associated with barrier capabilities is adequately described in Section 8 of this report.

- Acceptance Criterion 3, Technical Basis for Barrier Capability is Adequately Presented.

  The technical bases are consistent with the technical basis for the performance assessment. The technical basis for assertions of barrier capability is commensurate with the importance of each barrier's capability and the associated uncertainties.

The acceptance criteria identified in Section 2.2.1.3.9, *Radionuclide Transport in the Saturated Zone*, of the YMRP (NRC 2003 [163274]) are given below, followed by a short description of their applicability to this model report.

- Acceptance Criterion 1, System Description and Model Integration are Adequate.

  The description of the aspects of hydrology, geology, geochemistry, design features, physical phenomena, and couplings that may affect radionuclide transport in the saturated zone is adequate.

- Acceptance Criterion 2, Data are Sufficient for Model Justification.

  Geological, hydrological, and geochemical values used in the safety case are adequately justified (e.g., flow path lengths, sorption coefficients, retardation factors, colloid concentrations, etc.). Adequate descriptions of how the data were used, interpreted, and appropriately synthesized into the parameters are provided.

4.3 CODES AND STANDARDS

No specific formally established codes or standards, other than those referenced in Section 4.2, have been identified as applying to this modeling activity. This activity does not directly support License Application (LA) design.

INTENTIONALLY LEFT BLANK

5. ASSUMPTIONS

A list of the assumptions used in this model report is provided in Table 5-1. Subsections where assumptions are used are identified in the table. The conceptual model of transport representing the important transport processes in the SZ is presented in Section 6.3 of this report. Alternative conceptual models and the implications of these models are discussed in Section 6.4. The theoretical framework of this model and its computational implementation is presented in Section 6.5. The simplifications necessary to develop a model amenable to efficient computations for stochastic simulations are also discussed in Sections 6.3 through 6.5.

Table 5-1. Assumptions

Number	Assumption	Rationale	Location in this Report
1	Sorption on individual fracture surfaces is not included in the SZ transport model.	Sorption on individual fracture surfaces can result in significant retardation of radionuclide transport even for small values of fracture sorption coefficients (Figure 6.7-1b; and Robinson 1994 [101154], Figure 7). However, the sorption coefficient onto fracture surfaces is a strong function of the minerals coating the fracture surfaces. Due to the lack of sufficient data, there is uncertainty about the nature of the fracture coatings in the volcanics along the potential transport pathways in the SZ. Hence, as a conservative approach, no credit is taken for sorption on individual fracture surfaces in the SZ. This assumption requires no further justification.	Section 6.3
2	The derivation of the probability distribution for the absorption coefficients assumes that conditions are oxidizing in the groundwater in the SZ.	Available measurements show that the waters in the SZ at the Yucca Mountain (Attachment I; and BSC 2003 [162657], Table 5) are in oxidizing conditions or in transition between oxidizing-reducing conditions. There is insufficient data to completely characterize in detail the oxidation state of the water along the expected transport pathways in the SZ. Further, the assumption of oxidizing conditions generally leads to predictions of lower values of sorption coefficients. Hence, as a conservative approach, it is assumed that conditions are oxidizing in the groundwater in the SZ. This assumption requires no further justification.	Attachment I-Section I.8

Table 5-1 (continued). Assumptions

Number	Assumption	Rationale	Location in this Report
3	For the radionuclides Am, Cs, Pu, Pa, Sr, and Th, sorption coefficients in alluvium are assumed to be those corresponding to the values measured on samples of devitrified crushed tuff.	There is insufficient data on the sorption coefficients of the radionuclides Am, Cs, Pu, Pa, Sr, and Th in alluvium. Alluvium along the potential transport pathways is composed largely of disaggregated tuffaceous materials. Sources of data on aquifer matrix compositions in the SZ are provided in Table III-3. These data have been incorporated into a site mineralogic model BSC 2002 [158730]. There are two dominant rock types in the SZ along potential flow paths in volcanics to the 18-km boundary: devitrified tuff and zeolitic tuff. Because devitrified tuff makes up a major portion of the volcanic units exposed at the surface, it should be a major component in alluvium. In addition, clays and other secondary minerals are enriched in alluvial materials. These characteristics would result in higher sorption coefficients for alluvial materials compared to intact devitrified tuff. Also, the sorption coefficients onto zeolitic tuffs are higher than those on devitrified tuffs. Hence, as a conservative approach, it is assumed that, for the radionuclides Am, Cs, Pu, Pa, Sr, and Th, sorption coefficients in alluvium are given by the corresponding values measured on samples of devitrified crushed tuff. This assumption needs no further justification.	Attachment I-Section I.8

6. MODEL DISCUSSION

This section presents a discussion of the SZ site-scale transport model. Section 6.1 summarizes the objectives of this modeling activity, a description of the problem, and model inputs and outputs. Section 6.2 lists the included FEPs specifically addressed by this model report and their disposition in the Total System Performance Assessment-License Application (TSPA-LA). Also given in Section 6.2 are FEPs for which supporting information is provided in this report. The base-case conceptual model is presented in Section 6.3. Alternative conceptual models are discussed and evaluated along with their dispositions in Section 6.4. The mathematical formulation of the base-case conceptual model is presented in Section 6.5, and the base-case model results are given in Section 6.6. In Section 6.7, a description of the SZ as a barrier to transport of radionuclides is given.

6.1 MODELING OBJECTIVES

As summarized in Section 1 of this report, the objective of the SZ transport model is to simulate the transport of radionuclides in the saturated, fractured volcanic rock and alluvium in the vicinity of Yucca Mountain. The geohydrologic setting to be modeled is multifaceted with complex and diverse geochemical interactions possible between the groundwater, solutes, and the geological materials. Also, the intended use requires a computationally efficient model that is amenable to repeated runs for stochastic simulations. The approach taken here is to construct a plausible conceptual model of transport that incorporates the main SZ transport processes and is amenable to efficient computation (Sections 6.3 and 6.5). Alternate conceptual models and the implications of these models for transport predictions are evaluated relative to this base-case model (Section 6.4). The relevant FEPs are included in this report (Section 6.2), and the rationale for their inclusion and their dispositions are described. The excluded FEPs will be discussed in a separate analysis report (Rev. 02) of CRWMS M&O 2001 [153931]).

This transport model takes the calibrated flow model (DTN: LA0304TM831231.002 [163788]) described in detail in BSC (2003 [162649] as the starting point and, using the steady-state flow-velocity field supplied by the flow model, incorporates the transport processes of advection, dispersion, diffusion, retardation, and colloid-facilitated transport to compute the downstream radionuclide concentrations. Input parameters to the transport model are radionuclide release locations, dispersivities in the volcanics, matrix porosity, matrix diffusion coefficient, the sorption distribution coefficient K_d in the matrix, flowing interval porosity, flowing interval spacing, retardation factor in the flowing interval, effective porosity of the alluvium, dispersivities in the alluvium, and the K_d value in the alluvium. These are listed along with the base case and range of values in Table 6.5-2 in Section 6.5.3 and in Table 4-2 in Section 4. The output from the transport model consists of radionuclide breakthrough curves at the compliance boundary for nonsorbing as well as reactive transport. The reactive transport includes aqueous and colloid-facilitated transport. Breakthrough curves for aqueous species are calculated including the retardation due to sorption onto rock surfaces (Section 6.5.2.5). Breakthrough curves are generated for transport of radionuclides attached reversibly to the colloids using modified transport parameters (Section 6.5.2.6.2). Breakthrough curves for the radionuclides attached irreversibly to the colloids are generated using retardation factors for colloids (Section 6.5.2.6.1). A small fraction of colloids travels with the groundwater unretarded and is handled using the same breakthrough curves as those for nonsorbing radionuclides.

A variety of laboratory and field data supports the understanding of the transport processes of importance included in the transport model. The cross-hole tracer tests conducted at the C-wells complex support the use of a dual-porosity fracture flow and transport model of advection and dispersion coupled with a matrix-diffusion and matrix-sorption model (BSC 2003 [162415], Sections 6.3.5.6 and 6.3.5.8). Additionally, several laboratory-scale colloid-facilitated Pu transport experiments conducted in fractured volcanic rocks support the use of a colloid-facilitated transport model in the volcanics (Kersting and Reimus 2003 [162421], Chapter 7, and DTNs LA0301PR831361.003 [162435] and LA0301PR831361.004 [162436]). The model of transport in the alluvium with advection, dispersion, sorption, and colloid-facilitated transport is validated by the single-well tracer tests at the Nye County ATC wells (BSC 2003 [162415], Section 6.5). Laboratory column transport experiments in Yucca Mountain alluvium have indicated that sorption is a valid process that should be included in the alluvium transport model (BSC 2003 [162415], Section 6.5.6). Likewise, colloid-facilitated Pu transport experiments in laboratory-scale columns packed with Yucca Mountain alluvium (DTN: LA0301AA831352.001 [162433]) have indicated that colloid-facilitated transport is a valid process to include in the alluvium transport mode. These models are supported also by information available from analog studies at the Nevada Test Site (NTS) (Sections 7.1.1.1 and 7.1.2.6.2 in this report). The overall site-scale model is validated by comparison against transit times and flow paths deduced from hydrochemistry data (Section 7.2).

The SZ site-scale transport model is used directly in the model report *SZ Flow and Transport Model Abstraction* (BSC 2003 [164870]) for generating a set of radionuclide breakthrough curves at the accessible environment for use in the TSPA simulations of radionuclide release to the biosphere. The outputs from the transport model are transit times, flow paths, and breakthrough curves at the compliance boundaries for various radionuclides of concern. The results for the base case are given in Section 6.6.

6.2 FEATURES, EVENTS, AND PROCESSES FOR THIS MODEL REPORT

A comprehensive list has been developed of FEPs potentially relevant to postclosure performance of the potential Yucca Mountain repository based on site-specific information, design, and regulations. The approach for developing an initial list of FEPs in support of the *Total System Performance Assessment for the Site Recommendation* (TSPA-SR; CRWMS M&O 2000 [153246]) was documented in Freeze et al. (2001 [154365]). The initial FEPs list contained 328 FEPs, of which 176 were included in TSPA-SR models (CRWMS M&O 2000 [153246], Tables B-9–B-17). To support the TSPA-LA, the FEPs list was re-evaluated in accordance with the *Enhanced Plan for Features Events and Processes (FEPs) at Yucca Mountain* (BSC 2002 [158966], Section 3.2). The list of SZ-related FEPs addressed in this report was extracted from the LA FEP list (DTN: MO0307SEPFEPS4.000 [164527]).

The included FEPs abstractions incorporated in the TSPA-LA model, which is implemented through specific process models or input parameters, are presented as TSPA-LA dispositions and are specifically addressed in SZ model reports (Table 6.2-1a). The rationale for excluding a FEP from the TSPA-LA model will be given in the upcoming revision (REV 02) of *Features, Events, and Processes in SZ Flow and Transport* (BSC 2003 [163128]). FEPs specifically addressed in

this report and those only supported by the results of the work documented in this report are listed in Tables 6.2-1b and 6.2-2, respectively. The included FEPs that are specifically addressed in this report, along with their dispositions, are given in Table 6.2-1b. The acronyms used in Table 6.2-1b are defined in Table 6.2-1c.

Table 6.2-1a. Included FEPs for the Saturated Zone TSPA-LA

FEP Number	FEP Name	Responsible SZ Report
1.2.02.01.0A	Fractures	*SZ Flow and Transport Model Abstraction*, MDL-NBS-HS-000021 (BSC 2003 [164870])
1.2.02.02.0A	Faults	*SZ Flow and Transport Model Abstraction*, MDL-NBS-HS-000021 (BSC 2003 [164870])
1.4.07.02.0A	Wells	*SZ Flow and Transport Model Abstraction*, MDL-NBS-HS-000021 (BSC 2003 [164870])
2.2.03.01.0A	Stratigraphy	*Site-Scale Saturated Zone Flow Model*, MDL-NBS-HS-000011 (BSC 2003 [162649])
2.2.03.02.0A	Rock Properties of Host Rock and Other Units	*SZ Flow and Transport Model Abstraction*, MDL-NBS-HS-000021 (BSC 2003 [164870])
2.2.07.12.0A	Saturated Groundwater Flow in the Geosphere	*Site-Scale Saturated Zone Flow Model*, MDL-NBS-HS-000011 (BSC 2003 [162649])
2.2.07.13.0A	Water-Conducting Features in the SZ	*SZ Flow and Transport Model Abstraction*, MDL-NBS-HS-000021 (BSC 2003 [164870])
2.2.07.15.0A	Advection and Dispersion in the SZ	This report
2.2.07.16.0A	Dilution of Radionuclides in Groundwater	*SZ Flow and Transport Model Abstraction*, MDL-NBS-HS-000021 (BSC 2003 [164870])
2.2.07.17.0A	Diffusion in the SZ	This report
2.2.08.01.0A	Chemical Characteristics of Groundwater in the SZ	This report
2.2.08.06.0A	Complexation in the SZ	This report
2.2.08.08.0A	Matrix Diffusion in the SZ	This report
2.2.08.09.0A	Sorption in the SZ	This report
2.2.08.10.0A	Colloid Transport in the SZ	*SZ Flow and Transport Model Abstraction*, MDL-NBS-HS-000021 (BSC 2003 [164870])
2.2.08.11.0A	Groundwater Discharge to Surface Within the Reference Biosphere	*SZ Flow and Transport Model Abstraction*, MDL-NBS-HS-000021 (BSC 2003 [164870])
2.2.10.03.0A	Natural Geothermal Effects on Flow in the SZ	*Site-Scale Saturated Zone Flow Model*, MDL-NBS-HS-000011 (BSC 2003 [162649])
2.2.12.00.0B	Undetected Features in the SZ	*SZ Flow and Transport Model Abstraction*, MDL-NBS-HS-000021 (BSC 2003 [164870])
3.1.01.01.0A	Radioactive Decay and Ingrowth	*SZ Flow and Transport Model Abstraction*, MDL-NBS-HS-000021 (BSC 2003 [164870])

Table 6.2-1b. FEPs Included in the TSPA-LA for Which This Model Report Provides the Technical Basis

FEP Number	FEP Name	Where Disposition Described	Summary of Disposition in TSPA-LA
2.2.07.15.0A	Advection and dispersion in SZ	Sections 6.3 (Items 2 and 6), 6.5.2.2, 6.5.2.3, 4.1.2.1, 4.1.2.16	These processes are explicitly included in the conceptual and mathematical models of transport and in the numerical implementation of the model FEHM (V 2.20 STN: 10086-2.0-00) [161725] through the use of the dispersion tensor and the random-walk particle-tracking method. The flow field and the dispersion tensor input to this model are dependent on the nature of the geologic material and the scale of the model.
			FEHM generates a mean 3-D specific discharge ("advection") flow field using calibrated permeability as input. The mean specific discharge field is output from the *Site-Scale Saturated Zone Flow Model* (BSC 2003 [162649], Section 6.6). The mean calibrated permeability field is scaled with the stochastically sampled scaling parameters GWSPD and HAVO (BSC 2003 [164870], Section 6.5.2.1) to produce 200 unique 3-D permeability fields. GWSPD scales permeabilities in both the volcanic and alluvium units. The range for the GWSPD scaling parameter is based on field-test analyses (discussed in *Saturated Zone In-Situ Testing* (BSC 2003 [162415], Section 6.4.2), calibration of the "mean" flow field to measured heads (discussed in *Site-Scale Saturated Zone Flow Model*, BSC 2003 [162649], Section 6.6), and expert elicitation (CRWMS M&O 1998 [100353], Section 3.2.3). The HAVO parameter determines the degree of anisotropy in permeability for only the volcanic units. HAVO is based on field-test analyses (discussed in *Saturated Zone In-Situ Testing*, BSC 2003 [162415], Sections 6.2.4 and 6.2.6) and numerical analysis (discussed in *Site-Scale Saturated Zone Flow Model*, BSC 2003 [162649], Sections 4.1.1.2, 6.4.3.2 and 6.8.3). The scaled permeability fields are used to generate 200 flow fields (advection fields). A more detailed discussion of GWSPD and HAVO implementation is described in *SZ Flow and Transport Model Abstraction* (BSC 2003 [164870], Section 6.5.2.1 and 6.5.2.10).
			Uncertainty in the dispersion tensor is modeled by varying the input longitudinal dispersivity value stochastically. This approach is done using the longitudinal dispersion parameter, LDISP. The range for the LDISP parameter is based on recommendations from the expert elicitation panel (CRWMS M&O 1998 [100353], pp. 3-10, 3-11, LG-12), which were used as the basis for determining the bounds on the longitudinal dispersivity. The transverse dispersion parameters are not varied independently but scaled from LDISP. More details are presented in BSC (2003 [164870], Section 6.5.2.9).
2.2.07.17.0A	Diffusion in the SZ	Sections 6.3 (Item 3), 6.5.2.4, 4.1.2.10	This FEP is meant to address diffusive transport (e.g., fracture diffusion), such as is modeled numerically as part of the hydrodynamic dispersion coefficient (part mechanical dispersion, part diffusion). Matrix diffusion (which contributes to retardation) is addressed in the FEP 2.2.08.08.0A later in this table. The dispersion tensor D' appearing in Equation 1 is the sum of the mechanical dispersion tensor (D) for the flow system and the coefficient of molecular diffusion (D_0) in porous media. The effects of molecular diffusion are explicitly included also in the displacement matrix given by Equation 55. The effects of molecular diffusion are thus explicitly included in the SZ transport model. These effects are significant only at low flow velocities (Bear 1972 [156269], p. 581). The specific discharge value of 0.67 m/yr reported in BSC (2003 [162649] Section 6.6.2.3) leads to fluid velocities on the order of 10^{-7} to 10^{-4} m/s. Combining this with the lower limit of the longitudinal dispersivity of 0.1 m given in Table 4-2, this leads to a lower limit of dispersion coefficient in excess of 10^{-8} m^2/s. The upper limit of effective diffusion coefficient for volcanics given in Table 4-2 is 5×10^{-10} m^2/s. Thus, the effects of molecular diffusion are overshadowed by advection and dispersion.

FEP Number	FEP Name	Where Disposition Described	Summary of Disposition in TSPA-LA
2.2.08.01.0A	Chemical characteristics of groundwater in the SZ	Section 6.3 (Items 4 and 7); Attachment I (I.4 and I.8)	Variations in temperature, pH, Eh, ionic strength, and major ionic concentrations in the groundwater affect sorption of radionuclides onto the rock surface and colloids, which in turn, affects the sorption coefficient K_d and, thus, the retardation factor R for each radionuclide. These coefficients are entered directly in Equations 56 and 57 (Section 6.5.2.4.1), which describe reactive transport through porous media. The effects of THC and dissolved gases within the SZ are implicitly included in the variations in temperature, pH, Eh, ionic strength, and major ionic concentrations in the groundwater. Appropriate ranges and distributions of values for K_d are chosen based on expert elicitation (CRWMS M&O 1998 [100353], Section 3.2.8) and laboratory and field studies for the sorption coefficient K_d (Attachment I). The parameter ranges incorporated in the model abstraction through the K_d variables are KDNPVO, KDRAVO, KDSRVO, KDUVO, KDNPAL, KDRAAL, KDSRAL, KDUAL, KD_AM_VO, KD_CS_VO, KD_PU_VO, KD_AM_AL, KD_CS_AL, KD_PU_AL, and effective colloidal retardation factors (CORAL and CORVO) (*SZ Flow and Transport Model Abstraction*, BSC 2003 [164870], Section 6.5.2.8).

Regarding the spatial and temporal dependencies of K_d, geochemical analysis indicates current SZ groundwater under the proposed repository and along the SZ transport path is paleoclimate recharge water (BSC 2003 [162657], Section 6.7.6.6). Spatial variability in the composition of the ground water reflects, in part, temporal variability in recharge when data from the Fortymile Wash are included. Uncorrected C^{14} groundwater ages range from a few thousand years in vicinity of the Fortymile Wash to values greater than 15,000 years under portions of the Yucca Mountain (BSC 2003 [162657], Table 16). Using the reasonable approach that spatial variability within the recharge domain brackets the temporal variability expected to occur at a given location within the domain, the observed variability in geochemistry among the wells in the model area brackets the temporal variations expected to occur in the water composition. Additionally, as discussed in Attachment V and BSC (2003 [162649], Section 6.4.5), significant water table rise is expected to have occurred under paleoclimatic conditions. Thus, the large influx of paleoclimate recharge waters, now underneath the proposed repository and along the transport path, include interactions with rock types overlying the current water table as well as the rock types along the expected transport pathways. Consequently, the range in each radionuclide K_d and effective colloidal retardation factor bracket the temporal and spatial variations in water composition. |
| 2.2.08.06.0A | Complexation in the SZ | Sections 6.5.2.4.1, 6.5.2.5, 6.5.2.6; Attachments I (I.8, I.9) and II | Organic complexing agents, such as humic and fulvic acids, as well as inorganic complexing agents, such as carbonates, can affect sorption of radionuclides onto the rock surface and colloids. The sorption coefficients K_d and K_c enter the SZ transport model via Equations 57, 77, and 78–81 (Sections 6.5.2.4.1 and 6.5.2.5), which describe reactive transport through porous media. These effects are included in the model by choosing appropriate ranges of values for the sorption coefficients K_d and K_c as described in Attachments I and II respectively. Available data are summarized in this model report, and K_d and K_c distributions are developed on the basis of these data. |

FEP Number	FEP Name	Where Disposition Described	Summary of Disposition in TSPA-LA
2.2.08.08.0A	Matrix diffusion in the SZ	Sections 6.3 (Item 3), 6.5.2.4, 4.1.2.10	Matrix diffusion is the process by which radionuclides transported in the SZ move into the matrix of the porous rock. This process can be a very effective retarding mechanism and is explicitly included in the conceptual model of transport in the mathematical model transport Equations 56 and 57, Section 6.5.2.4.1, and in the numerical implementation of the model FEHM (V 2.20 STN: 10086-2.0-00]) [161725] through the use of the diffusion coefficient and the random-walk particle-tracking method with a semianalytical solution.
			Matrix diffusion is included in the SZ transport model (*SZ Flow and Transport Model Abstraction*, BSC 2003 [164870], Table 6.8) through the matrix diffusion parameter DCVO. The semianalytical matrix diffusion equation obeys Fick's law and incorporates concentration gradients and the temporal and spatial changes in the gradient along the transport pathway. Matrix diffusion is modeled only in the matrix portion of the volcanic units (BSC 2003 [164870], Section 6.5.2.6). The cumulative distribution function (CDF) for the DVCO is based on:
			• field and laboratory diffusion experiments performed in and on volcanic tuffs located within the Yucca Mountain vicinity
			• a least-squares linear empirical equation fit to diffusion experiment results and measured values for matrix porosity and permeability.
			The effective matrix diffusion coefficients for diffusing radionuclides are stochastically sampled from this same CDF. A related FEP is 2.2.07.17.0A—Diffusion in the SZ.
			Given the inhomogeneous nature of the alluvium, flow could preferentially occur through high-permeability regions and matrix diffusion could potentially occur into the low permeability regions of the alluvium. Data is available only from single-hole tracer tests conducted at the Alluvial Testing Complex (ATC) (BSC 2003 [162415], Section 6.5.4, Figures 6.5-18 through 6.5-20). Based on this available data, as a conservative approach no credit is taken for diffusion into low-permeability regions within the alluvium.
2.2.08.09.0A	Sorption in the SZ	Sections 6.3 (Items 4 and 7), 6.5.2.4, 6.5.2.5; Attachments I (I.8, I.9)	Sorption of radionuclides onto rock surfaces can occur both in the volcanic rocks and the alluvium. This process is modeled through a suite of partitioning coefficients K_d (BSC 2003 [164870], Section 6.5.2.8) for the radionuclides Am, Cs, Np, Pa, Pu, Ra, Th, and U (Attachment I). In the volcanic rocks, sorption in the matrix is explicitly included in the retardation coefficient R' in Equations 56b and 57 (Section 6.5.2.4.1). Sorption within individual fractures is not included in the conceptual model as an extreme case; however, sorption can occur within flowing zones due to the rubblized matrix, and this effect is included in the retardation coefficient R in Equation 56a. Sorption in the alluvium is described in Equation 77.
			Radionuclides modeled as entrained "irreversible" colloids in *Waste Form and In-Drift Colloids-Associated Radionuclide Concentrations: Abstraction and Summary* (BSC 2003 [161620], Section 6) are sorbed as well.

Table 6.2-1b (continued). FEPs Included in the TSPA-LA for Which
This Model Report Provides the Technical Basis

FEP Number	FEP Name	Where Disposition Described	Summary of Disposition in TSPA-LA
2.2.08.09.0A (continued)			Each developed radionuclide K_d distribution brackets the regional variability in K_d values due to variations in pH, Eh, water composition (representative of J-13 and UE-25 p#1 waters), mineralogy, and the number of rock sorption sites. Additionally, K_d distributions encompass the potential nonlinear behavior of the sorption processes. The distributions are biased towards lower values to account for localized areas where flow rates may be fast enough for reaction rates to be a factor for radionuclides such as Pu that have slower kinetics, thus accounting for sorption kinetics (Table 6.4-1, Attachment I, and Attachment IV).
			The volcanic units are primarily composed of zeolitic and devitrified tuffaceous materials. The alluvium is largely composed of disaggregated tuffaceous material, mixed with clays and other secondary minerals. Because radionuclides have a greater sorption affinity onto clays and secondary minerals than tuffaceous materials, alluvium K_d values can be slightly higher than those for the volcanic units. Available measurements in alluvium samples for Np and Pu were used to develop K_d distributions (Attachment I.8). For Am, Cs, Pu, Pa, Ra, Sr, and Th, data were not available on alluvium samples; hence the K_d distributions developed for devitrified Tuff were used (Attachment I.8). Table I-4 summarizes SZ sorption model parameters.
			Sorption Between Aqueous and Solid Phase: In the volcanic units, Np, Ra, Sr, and U sorption between the aqueous phase and the solid phase (host rock) is modeled in the FEHM flow and transport code using the sampled parameters KDNPVO, KDRAVO, KDSRVO, KDUVO, respectively (BSC 2003 [164870], Section 6.5.2.8); sorption for the same radionuclides in the alluvium is modeled through the parameters KDNPAL, KDRAAL, KDSRAL, and KDUAL.
			Sorption Between Colloidal, Aqueous, and Solid Phase— Reversible Colloids: Equilibrium sorption between aqueous and solid phases and a colloidal phase is modeled for the radionuclides Am, Cs, Pa, Pu, and Th (Attachment I]. The sampled parameters Kd_Pu_Col and Kd_Cs_Col model Pu and Cs partitioning between the aqueous and colloidal phases, respectively. Partitioning between the aqueous and colloidal phase for the radionuclides Am, Th, and Pa is modeled through the sampled parameter Kd_Am_Col. Partitioning between the colloidal and aqueous phase is the same in both the volcanics and the alluvium. Partitioning between the aqueous and solid phase (host rock) for each species differs between the volcanic and alluvial units. In the volcanic units, Pu and Cs aqueous- and solid-phase partitioning is modeled through the sampled parameters Kd_Pu_Vo and Kd_Cs_Vo, respectively. For Am, Th, and Pa, the same partitioning is modeled through the single sampled parameter Kd_Am_Vo. In the alluvium, Pu and Cs partitioning between aqueous and solid phases is modeled with the sampled parameters Kd_Pu_Al, Kd_Cs_Al; for Am, Pa, and Th, it is modeled through the parameter Kd_Am_Al (BSC 2003 [164870], Section 6.5.2.12.
			Sorption of Irreversible Colloids: In the volcanic units, the dispersed "advectively" transported Pu and Am colloids (BSC 2003 [162729], Section 6.4 and BSC 2003 [161620], Section 6.3.3.2) sorb onto fracture surfaces through a colloid retardation factor CORVO (BSC 2003 [164870], Section 6.5.2.11). In the alluvium, these same colloids are effectively sorbed via a sampled retardation factor CORAL (BSC 2003 [164870], Section 6.5.2.11).

Table 6.2-1c: Definition of Parameters Appearing In Table 6.2-1b

Parameter Name	Parameter Definition
KDNPVO	Neptunium sorption coefficient in volcanic units
KDNPAL	Neptunium sorption coefficient in alluvium
KDSRVO	Strontium sorption coefficient in volcanic units
KDSRAL	Strontium sorption coefficient in alluvium
KDUVO	Uranium sorption coefficient in volcanic units
KDUAL	Uranium sorption coefficient in alluvium
KDRAVO	Radium sorption coefficient in volcanic units
KDRAAL	Radium sorption coefficient in alluvium
KD_Pu_Vo	Plutonium sorption coefficient in volcanic units
KD_Pu_Al	Plutonium sorption coefficient in alluvium
KD_Am_Vo	Americium sorption coefficient in volcanic units
KD_Am_Al	Americium sorption coefficient in alluvium
KD_Cs_Vo	Cesium sorption coefficient in volcanic units
KD_Cs_Al	Cesium sorption coefficient in alluvium
FISVO	Flowing interval spacing in the volcanic units
CORAL	Colloid retardation factor in the alluvium
CORVO	Colloid retardation factor in the volcanic units
HAVO	Ratio of horizontal anisotropy in permeability
LDISP	Longitudinal dispersivity
Kd_Pu_Col	Plutonium sorption coefficient onto colloids
Kd_Am_Col	Americium sorption coefficient onto colloids
Kd_Cs_Col	Cesium sorption coefficient onto colloids
Conc_Col	Groundwater concentration of colloids
DCVO	Effective diffusion coefficient in volcanic units
GWSPD	Groundwater specific discharge multiplier
FPVO	Flowing interval porosity

Source: BSC 2003 [164870], Table 6-8

The included FEPs that are not specifically addressed in this report but are supported by its results are given in Table 6.2-2 along with the analysis or model report that addresses them.

Table 6.2-2. Saturated Zone Included FEPs Supported by the Results of This Report

FEP Number	FEP Name	Supporting Sections of This Report	Model Report That Addresses FEP
1.2.02.01.0A	Fractures	6.3, 6.5.1.2.4	*SZ Flow and Transport Model Abstraction*, BSC (2003 [164870], Section 6.2)
1.2.02.02.0A	Faults	6.3, 6.5.1.2.1, 6.5.1.2.4	*SZ Flow and Transport Model Abstraction*, BSC (2003 [164870], Section 6.2)
2.2.03.02.0A	Rock Properties of Host Rock and Other Units	6.5.1.2.1, 6.5.1.2.4, 6.5.1.2.6	*SZ Flow and Transport Model Abstraction*, BSC (2003 [164870], Section 6.2)
2.2.07.13.0A	Water-Conducting Features in the SZ	6.3	*SZ Flow and Transport Model Abstraction*, BSC (2003 [164870], Section 6.2)
2.2.07.16.0A	Dilution of Radionuclides in Groundwater	6.5.1.2.4	*SZ Flow and Transport Model Abstraction*, BSC (2003 [164870], Section 6.2)
2.2.08.10.0A	Colloidal Transport in the SZ	6.5.1.2.6, Attachment II	*SZ Flow and Transport Model Abstraction*, BSC (2003 [164870], Section 6.2)

6.3 BASE-CASE CONCEPTUAL MODEL

The transport of chemical species in the groundwater involves a variety of processes such as advection, dispersion, diffusion, sorption and colloid-facilitated transport. These processes, in general, lead to retardation of the migration of transported species with respect to the bulk movement of the groundwater. Hence, the radionuclide transport times can be several orders of magnitude longer than the transport times computed taking the fluid velocity to be the effective radionuclide migration velocity. Given the complex geohydrologic setting and the computational constraints imposed by the TSPA methodology, the approach taken here is to construct a plausible conceptual transport model that incorporates the main SZ transport processes and is amenable to efficient computation. Alternate conceptual models and the implications of these models for transport predictions are evaluated relative to this base-case model.

The base-case conceptual model of SZ transport begins in the neighborhood of the repository footprint at the water table and ends at the compliance boundary downstream from this footprint. The flow path from the potential repository to the proposed compliance boundary begins in the volcanic tuffs but ends in the alluvium, and different transport processes operate in the volcanic tuffs and the alluvium. The components of the conceptual model are: (1) radionuclides enter the SZ via fluids percolating through the UZ below the proposed repository site. Within the SZ, they are transported with the groundwater that flows subhorizontally in a southerly or southeasterly direction; (2) the radionuclides advect and disperse with the groundwater through the fractured portions of the tuffs near the water table; (3) fluid flow occurs preferentially within the flowing intervals, whereas stagnant fluid resides in the rock matrix. Solutes diffuse in and out of fluid within the rock matrix that is essentially stagnant; (4) sorption reactions occur in volcanics between the rock matrix and some of the radionuclides, tending to retard the transport of these radionuclides; (5) radionuclides can undergo colloid-facilitated transport in the volcanics; (6) the radionuclides advect and disperse with the groundwater through the alluvium; (7) sorption reactions occur in alluvium between the rock and some of the radionuclides, tending to retard the

transport of these radionuclides; and (8) radionuclides can undergo colloid-facilitated transport in alluvium. These are schematically illustrated in Figure 6.3-1.
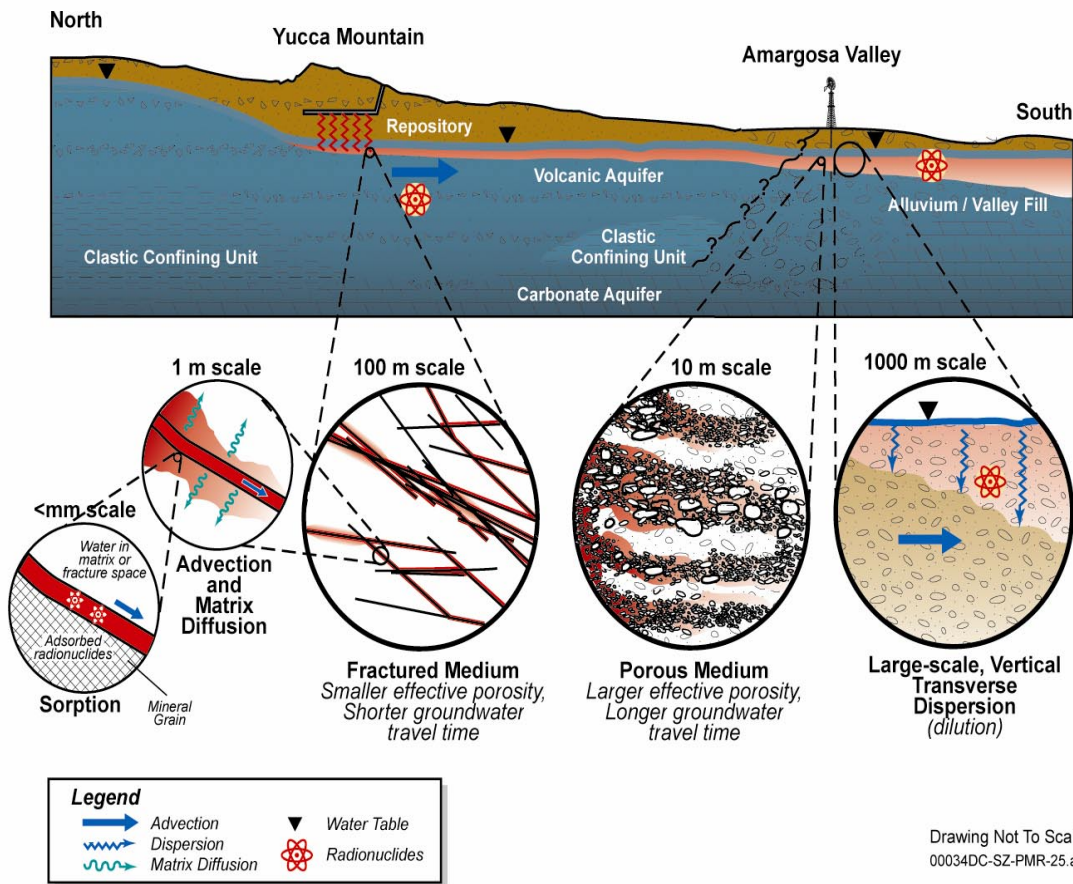
For illustration purposes only.

NOTE: For the sake of clarity, the following processes are not explicitly indicated in this figure: dispersion and colloid-facilitated transport in the volcanics; and advection, longitudinal dispersion, sorption and colloid facilitated transport in the alluvium.

Figure 6.3-1. A Schematic Illustration of the Conceptual Model of Transport Processes in the Volcanic Tuffs and the Alluvium, YM Site

Each of these model components is discussed below:

1. *Radionuclides enter the SZ via fluids percolating through the UZ below the proposed repository site. Within the SZ, they are transported with the groundwater that flows subhorizontally in a southerly or southeasterly direction.* The exact nature of transport through the UZ is not expected to exert a great effect on the conceptual model of site-scale SZ transport, and thus, the SZ transport component of the site-scale SZ model can be developed independently from a transport model for the UZ. As shown in

Section 6.6.2.2 of BSC (2003 [162649]), the general flow direction starting at the repository footprint is to the south and southeast. The flow lines remain shallow and subhorizontal within the SZ. Thus, fluid flow occurs within the fractured volcanics immediately downstream of the repository, entering the alluvium further downstream, and continuing through the alluvium to the compliance boundary.

2. *The radionuclides advect and disperse with the groundwater through the fractured portions of the tuffs near the water table.* Flow occurs within the fractured portions of the tuffs near the water table. Flow intervals identified in well tests correlate with fracture locations (Erickson and Waddell 1985 [105279], p. 18), the extent of fracturing correlates reasonably well with the degree of welding (Waddell et al. 1984 [101064], p. 26), and the degree of welding is one of the criteria used to define the submembers within a lithologic unit. In the SZ flow model, such lithologic members are represented as single zones, each with its equivalent porosity and permeability (i.e., Bullfrog, Tram, and Prow Pass units in Table 6.6-2 of BSC 2003 [162649]). This representation is also used in the transport model; however, the influence of heterogeneities within a member is incorporated into the model via dispersion and matrix diffusion as discussed below. A distinction must be made between fracture zones and individual fractures. Fracture zones are typically spaced tens of meters apart, with thicknesses on the order of meters, and contain broken-up matrix blocks and many intersecting fractures that are conduits to flow and to diffusion and retardation. Individual fractures, on the other hand, tend to be spaced as close as a meter or less, have thicknesses on the order of fractions of millimeters, and may or may not contribute to the flow of groundwater. The conceptual model is that high-permeability regions are offset by low-permeability regions due to the extensive faulting and fracturing observed in the volcanics (Luckey et al. 1996 [100465], pp. 8 to 12) in the model domain. These low-permeability regions effectively will act as large-scale heterogeneities that give rise to large-scale macroscopic dispersion due to the tortuous nature of flow over the scale of hundreds of meters to kilometers. Field studies of transport and dispersion at a variety of length scales (from meters to kilometers) (BSC 2003 [162415], Figures 6.3-79 and 6.3-80; Neuman 1990 [101464], Figure 1) show a trend toward larger apparent dispersion coefficients for transport over longer distances. The estimates of dispersivities from the C-wells tracer tests (BSC 2003 [162415], Section 6.3) fall within the range of values from other sites, suggesting that transport in the fractured tuffs exhibits similar dispersive characteristics. In an equivalent-continuum dispersion model, hydrogeologic features likely to be present at scales smaller than the size of a typical grid cell are simulated as averages. The equivalent-continuum model averages the concentration variations within a grid block into a single value for the block. Concentration differences at scales smaller than the grid cell, if present, are not resolved. Whether this distinction is important depends on specific performance criteria and scenarios for exposure to humans or plants. Because the site-scale SZ flow and transport model is used to predict concentrations for a well-withdrawal scenario (DOE 2002 [155943], Section 4.2.10.31.1; 10 CFR 63.312 [156605]), the above approach is considered adequate.

3. *Fluid flow occurs preferentially within the flowing intervals, whereas stagnant fluid resides in the rock matrix. Solutes diffuse in and out of fluid within the rock matrix that*

is essentially stagnant. Current hydrologic evidence supports the model of fluid flow within fracture zones in the moderately to densely welded tuffs of the SZ (e.g., Waddell et al. 1984 [101064], Table 2, pp. 17 to 22). Hydraulic conductivities measured for core samples in the laboratory are orders of magnitude higher when the sample is fractured (Peters et al. 1984 [121957], p. 60). Also, there generally is a positive correlation between fractures, identified using acoustic televiewer or borehole television tools, and zones of high transmissivity (Erickson and Waddell 1985 [105279], Figure 3; Karasaki et al. 1990 [148309], p. 811). The fluid travels preferentially within regions of large apertures with large sections of the fracture surface containing stagnant fluid or no fluid where the faces are in contact. Matrix materials conduct no fluid under natural groundwater flow conditions but are physically connected to the fracture fluid through the pore network. When a dissolved species travels with the fluid within a fracture, it may migrate by molecular diffusion into the stagnant fluid in the rock matrix. Within the matrix, the fluid velocity is effectively zero; hence the advection of the solute along the fracture is effectively zero. The Brownian motion of the solute molecules becomes dominant, and the effect of advection resumes when the solute re-enters the fracture. The result is a delay of the delivery of the solute to a downgradient location from what would be predicted if the solute had remained in the fracture. Several theoretical, laboratory, and field studies have demonstrated the validity of the matrix-diffusion model. Sudicky and Frind (1981 [148342], pp. 161-163) developed a model of flow in an aquifer with diffusion into a surrounding aquitard to show that the movement of ^{14}C can be much slower than predicted if only movement with the flowing water is considered. Maloszewski and Zuber (1985 [148312], pp. 353-354) reached a similar conclusion with a model for ^{14}C transport that consists of uniform flow through a network of equally spaced fractures with diffusion into the surrounding rock matrix between the joints. Maloszewski and Zuber present analyses of several interwell tracer experiments that show that their matrix diffusion model can be used to provide simulations of these tests that are consistent with the values of matrix porosity obtained in the laboratory and aperture values estimated from hydraulic tests. In all cases, the results are superior to previous analyses that did not include matrix diffusion effects. Finally, a data set of great relevance to the SZ beneath Yucca Mountain is the C-wells reactive tracer test (BSC 2003 [162415], Section 6.3.5), which demonstrated that models incorporating matrix diffusion provide more reasonable fits to the tracer experiment data than those that use a single continuum. The calculated transport times of SZ fluids determined from ^{14}C data (BSC 2003 [162657], Table 19) are on the order of hundreds to thousands of years. As demonstrated in Figures 6.7-2a, 6.7-2b, 6.7-3a, and 6.7-3b of this report, model transit times without matrix diffusion are only on the order of several hundred years but become comparable with transit times estimated from the geochemical data when retardation due to matrix diffusion is included in the model. Thus, the old ^{14}C ages are consistent with the conceptual model of interchange of solutes between fractures and matrix found in the matrix diffusion model. Matrix diffusion is characterized using an abstracted model of uniform flow and transport in equally spaced, parallel fractures. This treatment represents a considerable simplification of the complex fracture network observed in volcanic rocks. It is acceptable because the particle-tracking model is intended to be used in large-scale simulations. The size of a typical computational grid block in the SZ flow and transport model is 500 m by 500 m. Average flowing intervals are subvertical with

an average spacing of 20 m, orders of magnitude smaller than the grid block size. In such circumstances, the use of an abstracted dual-porosity model with equally spaced, parallel fractures to capture the transport behavior is reasonable. In numerical modeling studies, such uncertainties are commonly addressed through the use of simpler conceptual models, such as this one, combined with sensitivity analyses to assess the importance of the uncertain parameters to the final model result. Therefore, a broad range of flowing interval spacings is used (Table 4-2), and the influence on the final results is quantified (Section 8).

4. *Sorption reactions occur in volcanics between the rock matrix and some of the radionuclides, tending to retard the transport of these radionuclides.* Radionuclide-rock interactions potentially can occur on the surfaces of fractures and within the rock matrix. Sorption reactions are chemical reactions that involve the distribution of chemical constituents between water and solid surfaces. Measurements show that the waters in the SZ at the Yucca Mountain (Table I-2) are in oxidizing conditions or in transition between oxidizing-reducing conditions. Further, oxidizing conditions generally lead to lower values of sorption coefficients (Attachment I). Hence this conceptual model takes the geochemical conditions along the entire flow path to be oxidizing. Although the radionuclide-rock reactions can be complex in detail, they are represented in the transport model by a constant called the sorption coefficient K_d (Freeze and Cherry 1979 [101173], p. 403, Equation 9.13). The use of the K_d model requires that the reactions must be in equilibrium, instantaneous (kinetics), and reversible. The validity of these requirements at Yucca Mountain and their implications for the transport model are discussed in Section 6.4 on alternate conceptual models. The surface-area to fluid-volume ratio and the mineral distributions probably are different in the fractures as compared to the matrix. As a conservative approach, sorption on individual fracture surfaces is not included in the transport model. Maloszewski and Zuber (1985 [148312], pp. 353-354) show that, at several sites, better agreements with the field data are obtained by including the effect of chemical exchange reactions in the matrix. Of particular relevance to Yucca Mountain, the lithium tracer in the C-wells reactive tracer experiment (BSC 2003 [162415], Section 6.3.5; Robinson 1994 [101154], pp. 86-93, Figures 5 and 8) was modeled using a matrix diffusion model with the sorption coefficient as an additional adjustable parameter. The fact that the early lithium response had the same timing as that of the nonsorbing tracers, but with a lower normalized peak concentration, is consistent with matrix diffusion coupled with sorption in the matrix (Robinson 1994 [101154], Figure 7).

5. *Radionuclides can undergo colloid-facilitated transport in the volcanics.* Colloids are microscopic particles that are much larger than solute molecules. Solute molecules can absorb onto the colloid particles and be transported along with them. Because the colloidal particles are much larger in size and mass than the radionuclides that sorb onto them, the radionuclides do not affect the transport of the colloid particles.   The irreversibly sorbed radionuclides are taken to transport identically to the colloids to which they are sorbed. A discussion of colloid-facilitated transport is found in Attachment II of this report and BSC 2003 ([162729] Section 6.4). The colloids in the SZ can be of several types including natural colloids (typically clay or silica), waste-form colloids resulting from degradation of spent fuel or glass, and iron-oxyhydroxide colloids resulting from degradation of the waste container. The transport of colloids themselves in groundwater,

as well as the mechanisms of sorption of radionuclides onto these colloid particles, needs to be included in the transport model for the SZ. Mechanisms for transport of colloid particles in groundwater are distinct from those appropriate for the solute molecules and are being considered in detail in BSC (2003 [162729], Section 6.4). In the transport, movement of colloids is taken to occur within fractures only. Due to the relatively large size of the colloids, matrix diffusion of these particles is taken to be negligible. Colloid attachment and detachment to fracture surfaces is modeled by first-order rate expressions, which is approximated as a retardation factor for equilibrium conditions at large length scales. The radionuclides that are reversibly absorbed onto colloids are modeled using the K_c model, which represents the equilibrium partitioning of radionuclides between the aqueous phase and the colloidal phase with the distribution coefficient K_c (CRWMS M&O 1997 [100328], Equation 8-10, pp. 8-35). Based on the estimated rate constants and the range of transport times being considered for transport through saturated fractured tuffs, it was shown (BSC 2003 [162729], Section 6.7) that the equilibrium partitioning is valid for all but the shortest transport times and overestimates transport mobility of radionuclides for the shortest transport times. The distribution coefficient K_c is modeled as a function of radionuclide sorption properties, colloid substrate properties, aqueous chemistry, and colloid concentration but not with any of the properties of the immobile media through which transport occurs. The radionuclides that are irreversibly absorbed onto the colloids are modeled to transport in a manner identical to the colloids onto which they are sorbed (Attachment II). The transport of the colloids is simulated using the advection-dispersion equation. As a conservative approach, diffusion of colloid particles into the matrix is not included in this conceptual model. Several field observations have suggested that a small percentage of colloids transport with essentially no retardation in groundwater (Kersting et al. 1999 [103282], p. 56, 58; Penrose et al. 1990 [100811], p. 228), whereas the majority undergo either reversible or irreversible filtration, which can be described by a retardation factor. In this analysis, filtration is defined as the net effect of chemical sorption of the colloid onto the rock surface and the physical removal of colloids from the advective flow due to sieving and settling. The retardation factor is dependent on several factors such as colloid size, colloid type, and geochemical conditions (e.g., pH, Eh, and ionic strength). Details are presented in BSC (2003 [162729], Section 6). Colloid-facilitated transport is set to zero in the base case SZ transport model because it represents the extreme case of non-sorbing radionuclides.

6. *The radionuclides advect and disperse with the groundwater through the alluvium.* Alluvium is valley-fill material consisting of heterogeneous deposits of sand and gravel interbedded with mud and clay-sized materials (Waddell et al. 1984 [101064], p. 27). This material is not well consolidated and tends to exhibit a more porous, less-fractured nature. Due to the heterogeneous nature of the medium, flow occurs through the more permeable regions within the alluvium, and the lower-permeability regions act as flow barriers. This characteristic tends to reduce the amount of porosity actually available to flow and transport as compared to the total large-scale porosity of the alluvium. To account for this, the effective flow porosity of the alluvium is considered to be a stochastic variable with a range of input values (BSC 2003 [164870], Section 6.5.2.3). Dispersion is caused by heterogeneities at all scales, from the scale of individual pore spaces to the scale of the thickness of individual strata and the length of structural

features such as faults. The spreading and dilution of radionuclides that result from these heterogeneities could be important to the performance of the proposed repository. The largest heterogeneities are represented explicitly in the site-scale SZ flow and transport model (BSC 2003 [162649], Figures 16 and 19, Table 6.5-4). For dispersion at smaller scales, the convective-dispersion model is used with dispersion characterized using a dispersion coefficient tensor.

7. *Sorption reactions occur in alluvium between the solid surfaces and some of the radionuclides, tending to retard the transport of these radionuclides.* In contrast to the fractured tuffs, there are no cross-hole, field-scale tracer transport tests in the alluvium south of Yucca Mountain to confirm the in situ sorption characteristics. However, the transport of sorbing solutes in porous media that is not controlled by fractures has been well studied (e.g., Freeze and Cherry 1979 [101173], Chapter 9, pp. 385 to 457). Sorption coefficients onto alluvium from the Nye County wells have been measured for a few key radionuclides. For the remaining radionuclides, sorption coefficients have been estimated based on the corresponding values measured for crushed tuff (Attachment I). Radionuclides could also precipitate in the saturated zone, forming solid phases on the rock surfaces. The most credible mechanism for this effect to occur is through a different redox condition in the saturated zone. If the conditions were significantly more reducing, the valence states of actinides, such as Np, U, and Pu, and fission products, such as Tc and I, could be lowered. Typically, in these groundwaters, this situation results in much lower solubilities of the radionuclides and hence, precipitation. This effect is an extreme form of retardation that renders the bulk of the radionuclide plume virtually immobile. The base-case model takes the conditions to be oxidizing, which results in higher solubilities and lower sorption coefficients than would be the case if reducing conditions were selected. Therefore, the base-case model produces more rapid transport of some radionuclides in that the use of lower valence states for these radionuclides would yield a less mobile species.

8. *Radionuclides can undergo colloid-facilitated transport in alluvium.* The conceptual model for colloid-facilitated transport in the alluvium is essentially the same as in fractured tuffs in that colloids are modeled as transported only by advective water (no diffusion into stagnant water or into grains), and colloid attachment and detachment onto alluvial surfaces are described by first-order rate expressions. Because the colloidal particles are much larger in size and mass than the radionuclides that sorb onto them, the radionuclides do not affect the transport of the colloid particles. The irreversibly sorbed radionuclides are taken to transport identically to the colloids to which they are sorbed. A discussion of colloid-facilitated transport is found in Attachment II of this report and in BSC 2003 ([162729], Section 6.5). Laboratory site-specific data for colloid transport in the alluvium along with literature data are used to obtain distributions and bounds for attachment and detachment rate constants (BSC 2003 [162729], Table 8). Based on the estimated rate constants and the range of transport times being considered for transport through saturated fractured tuffs, it was shown (BSC 2003 [162729], Section 6.7) that the equilibrium partitioning is valid for all but the shortest transport times and overestimates transport mobility of radionuclides for the shortest transport times.

6.4 ALTERNATIVE CONCEPTUAL MODELS

Credible alternatives to the conceptual model of SZ transport presented above (Section 6.3 of this report) were evaluated in regards to their impact on the radionuclide transit times from the potential repository footprint to the compliance boundary. The key components of each ACM, the screening assessment of each ACM and the basis for the screening assessment are presented in Table 6.4-1.

Table 6.4-1. Alternative Conceptual Models Considered

Alternative Conceptual Model	Key components	Screening Assessment	Basis
Fluid flow in matrix blocks	The matrix material in the intervening space between the flowing intervals in the volcanics has significant permeability and transmits significant amounts of fluid by advection for the flow conditions likely to occur in the SZ.	This alternative conceptual model leads to transit times greater than those calculated by the SZ transport model.	There are three situations possible: (1) flow occurs from the fractures into the matrix, (2) flow occurs from the matrix into the fractures, and (3) flow occurs independently within matrix blocks. In the first case, flow out of the fractures into the matrix would enhance the effects of the matrix diffusion, leading to transit times greater than those calculated by this model. In the second case, considering the steady-state nature of the flow system (BSC 2003 [162649], Sections 5 and 6), if some flow is occurring out of the matrix into the fractures, then equivalent flow must also occur from fractures into the matrix blocks. Thus, the matrix diffusion effects will be negated in some areas and enhanced in others, and the overall effect on the effective diffusion coefficient can be expected to be small. In the third case, an effective porosity would have to be used that is larger than that being used for the fractured flowing intervals, thus leading to transit times greater than those calculated by this model.
Irreversible sorption	Rate of desorption of radionuclides from the rock surfaces is slower than the rate of absorption.	This alternative conceptual model leads to transit times greater than those calculated by the SZ transport model.	Sorption reactions that are not fully reversible result in rates of transport that are slower than would be the case for fully reversible reactions. Therefore, for radionuclides that sorb irreversibly, using a sorption coefficient would result in diminished total radionuclide mass breakthrough from the saturated zone. A potential scenario for which this simplification could lead to longer transit times is when deposition of radionuclides takes place under the ambient geochemical conditions, and later, because of geochemical changes, the deposited radionuclides re-enter the aqueous phase and are transported downstream as a pulse. On the basis of available geochemical and mineralogical data, this situation is not considered to be likely. It is being addressed as a FEP in the revision (Rev. 02) of CRWMS M&O 2001 [153931].

Table 6.4-1 (continued). Alternative Conceptual Models Considered

Alternative Conceptual Model	Key components	Screening Assessment	Basis
Sorption reactions are not instantaneous	Reaction rates for sorption kinetics are slow compared to the rates of solute transport.	This alternative conceptual model is implicitly included in the SZ transport model through the range of uncertainty in the sorption-coefficient values.	Among the radionuclides of concern, Pu has the slowest reaction kinetics (Attachment I). Calculations of the Damköhler number (*Da*) (Attachment IV]) for reaction rates of Pu indicate that, for typical travel times through the SZ, the local equilibrium approach is valid (Attachment IV of this report; DTN: LA0302HV831361.001 [163783]). However, in localized areas, flow rates may be fast enough for kinetic limitations to be a factor for Pu (Attachment I). The possibility of the sorption reaction rate being slow relative to the flow rate is handled by biasing the sorption-coefficient distributions downward for the radionuclides of interest that appear to have slow sorption kinetics (Attachment I).
Radionuclide precipitation	Radionuclides could precipitate in the saturated zone, forming solid phases on the rock surfaces.	This alternative conceptual model leads to transit times greater than those calculated by the SZ transport model.	Thermodynamically, chemical species in supersaturation, with respect to solid phases, possess a driving force that favors the formation of these solid phases. The result for a radionuclide would be an extreme form of retardation that renders the bulk of the radionuclide plume virtually immobile. Given that most radionuclides reaching the SZ would need to transport there in aqueous solution, thermodynamic conditions along the flow path would have to change (relative to the UZ) for species to precipitate. The most credible mechanism for this to occur would be through a different redox condition in the SZ. If the conditions were significantly more reducing, the valence state of actinides, such as Np, U, and Pu, and fission products, such as Tc and I, could be lowered. Typically, in these groundwaters, this condition would result in much lower solubilities of the radionuclides and hence, precipitation. There are insufficient measurements and data concerning the redox behavior of these radionuclides to warrant including redox behavior in model calculations. In all cases, the radionuclides in question have been assigned to their highest valence state, which results in higher solubilities and lower sorption coefficients than would be the case if the lower valence state were selected.

A potential scenario for which this simplification could be less straightforward is when deposition of radionuclides takes place under the ambient geochemical conditions, and later, because of geochemical changes, the deposited radionuclides re-enter the aqueous phase and are transported downstream as a pulse. On the basis of available geochemical and mineralogical data, this situation is not considered to be likely. It is being addressed as a FEP in the revision (Rev. 02) of CRWMS M&O 2001 [153931]. |

Table 6.4-1 (continued). Alternative Conceptual Models Considered

Alternative Conceptual Model	Key Components	Screening Assessment	Basis
Water table rise	Future water table rise could elevate the water table, leading to radionuclide transport through geological horizons currently considered outside of the SZ.	This alternative conceptual model leads to transit times greater than those calculated by the SZ transport model.	Wetter, glacial climatic conditions could occur in the future at the Yucca Mountain site within the 10,000-year period of regulatory concern (CRWMS M&O 2000 [153246], Section 1.8.4.3). These changes in the climate relative to present conditions would affect groundwater flow in the SZ by significantly increasing the amount of recharge to the regional groundwater flow system. These regional and local increases in recharge will tend to increase the groundwater flux through the SZ system and lead to a rise in the water table beneath Yucca Mountain. In previous analyses, the effect of this on the SZ breakthrough curves was modeled using a scaling factor representing the alternative climate state (BSC 2001 [157132], Section 6.4.2). The scaling factor used in this approach is the ratio of average SZ groundwater flux under the future climatic conditions to the flux under present conditions. However, this approach uses the same flow path for radionuclide transport through the SZ under wetter climatic conditions of the future. Alternatively, the rise in the water table due to climatic changes could be included in the model with potentially different flow paths through different hydrogeologic units in the SZ.
			BSC 2003 [162649], Section 6.4.5 presents a modeling exercise that adapts the SZ site-scale flow model to include the effects of estimated water table rise. The results of particle-tracking simulations using this adapted model to the simple flux-scaling approach are presented in Attachment V. The results presented in Figure V-1 and V-2 indicate that the model with the higher water table results in longer simulated transport times for both the nonsorbing species and for neptunium. The simplified approach of scaling the breakthrough curves from the SZ site-scale flow model with the present water-table elevations is, thus, an acceptable representation of transport in the SZ under wetter, glacial climatic conditions relative to the adapted model that incorporates water-table rise associated with future conditions. The reason for the longer travel times using the water-table-rise model relates to the hydrogeologic units encountered by a radionuclide plume arriving at the water table. Transport must occur through lower-permeability confining units, and the flow-path distance through the alluvium is predicted to be longer for the water-table-rise model.
Nonlinear sorption	Sorption reactions have to be modeled using nonlinear isotherms.	This alternative conceptual model is implicitly included in the SZ transport model through the range of uncertainty in the sorption-coefficient values.	The K_d model is based on treating the concentration of the radionuclides absorbed onto the rock surface as a linear function of the concentration of that species in the aqueous solution. This treatment is valid at low concentrations, but at higher concentrations, as absorption sites start getting saturated, the absorbed concentration starts falling below the value predicted by this linear relationship. This effect results in a lower apparent value of K_d at higher concentrations, which is accounted for in the model by biasing the K_d distributions at low values (Attachment I). The use of low K_d values could lead to underestimating the long-term tail of the breakthrough curve; however, since the long-term tailing generally does not occur during the 10,000-year regulatory period, such biasing is acceptable.

Table 6.4-1 (continued). Alternative Conceptual Models Considered

Alternative Conceptual Model	Key Components	Screening Assessment	Basis
Locally varying sorption parameters	Sorption parameters are strong functions of local water chemistry, rock mineralogy, and solute concentrations. The properties have to be calculated locally at each node along the travel path.	This alternative conceptual model is implicitly included in the SZ transport model through the range of uncertainty in the coefficient values for sorption onto the rocks and colloids and for colloid retardation factors.	The approach taken in this model report is to use linear transport equations with transport parameters appearing in the equations being treated as "effective" stochastic variables appropriate for the model scale. This approach is consistent with the current level of available data. Transport parameters such as the K_d coefficients depend on type and concentration of the species, rock mineralogy, and groundwater pH and Eh. In the present model, broad distributions have been developed for effective K_ds (Attachments I, II, and III). No credit is being taken for sorption onto zeolites, and the K_d distributions presented in Attachment I are based on silica surfaces. Given the current level of data available, water pH data are being treated as spatially random along the transport path, and oxidizing conditions are taken as a conservative approach, as justified in Section 6.3 of this report. To evaluate the effect of scale on the K_d distributions, calculations were performed to capture the effect of spatial variability of rock types and variability in water chemistries on effective K_d (Attachment II). The effect of variability in water chemistry was captured in the input K_d distributions that were used for effective K_d calculations. It was observed that the effective K_d distributions calculated for a single 500-m x 500-m grid block were narrower than the input K_d distributions. During performance assessment (PA) modeling studies, calculations will be made through multiple runs, each with a distinct K_d value sampled from the above-mentioned effective K_d distribution. This approach will be more approximate than assigning K_d values on a node basis, as the latter approach will lead to breakthrough behavior that can be described by an even narrower distribution than the effective K_d distribution.
Channeling in alluvium	In alluvium, high permeability channels exist that can provide preferential pathways for flow and transport.	This alternative conceptual model is implicitly included in the SZ transport model through the range of uncertainty in the effective porosity values.	The conceptual model presented in this model report uses the effective-continuum approach, using effective values averaged over the grid block sizes on the order of 500 m x 500 m x 50 m for the parameters of interest, such as porosity. The effective porosity being used in the TSPA-LA calculations (BSC 2003 [164870], Section 6.5.2.3) is represented by a normal distribution with the expected value of 0.18 and a value of 0.027 at 3 standard deviations below the mean. Thus, the PA calculations allow for the eventuality that all the flow is concentrated within a small fraction of the alluvium, corresponding to the low effective porosity of 0.027. The conceptual model presented in this model report is appropriate for these ranges of values.
Diffusion into low-permeability zones	Within alluvium, solutes can diffuse into low-permeability zones, later diffusing out into the flow, which leads to a long tail for the radionuclide breakthrough curve.	This alternative conceptual model leads to transit times greater than those calculated by the SZ transport model.	This phenomenon was not observed to occur in the single-hole tracer tests conducted at the Alluvial Testing Complex (ATC) (BSC 2003 [162415], Section 6.5.4, Figures 6.5-18 through 6.5-20). On a larger scale, this scenario will lead to lower concentrations at breakthrough and longer times for reaching 50% breakthrough concentrations. Thus, the conceptual model presented in this model report is acceptable.

6.5 MODEL FORMULATION OF BASE-CASE CONCEPTUAL MODEL

6.5.1 Overview of Model Formulation

The mathematical model formulation of the conceptual model presented in Section 6.3 is described below. The advection-dispersion equation is stated in Section 6.5.2.1, and the development of a general form of the dispersion tensor for axisymmetric media is given in Section 6.5.2.2. A random-walk particle-tracking method for implementing advection-dispersion in a numerical code is presented in Section 6.5.2.3. A mathematical formulation to treat matrix diffusion in volcanics is presented next in Section 6.5.2.4, followed by a mathematical description of sorptive transport in alluvium in Section 6.5.2.5 and colloid-facilitated transport in Section 6.5.2.6. The computer implementation of the mathematical models in the code FEHM (V 2.20 STN: 10086-2.0-00) [161725] is verified with a suite of example problems using published examples, analytical and semi-analytical solutions and examples run with different codes. These are documented in the verification report for FEHM (V 2.20 STN: 10086-2.0-00) [161725].

6.5.2 Mathematical Model Description

6.5.2.1 Advective Dispersive Transport

The fundamental mass transport equation for transport of a nonreactive, dilute species in a saturated porous medium (with no sources or sinks) has the form (e.g., Bear 1972 [156269], p. 617, Equation 10.5.2):

$$\frac{\partial C}{\partial t} + \nabla \cdot (\vec{v} C) - \nabla \cdot (D' \nabla C) = 0 \qquad \text{(Eq. 1)}$$

where

C denotes the solute concentration in units of moles per liter
t is time
$\vec{v}$ designates the solute average pore-water velocity vector
D' denotes the dispersion tensor.

This equation serves as the starting point for all subsequent development below. The dispersion tensor D' appearing in Equation 1 is the sum of the mechanical dispersion tensor (D) for the flow system and the coefficient of molecular diffusion (D_0) in porous media. The effects of molecular diffusion are significant only at low flow velocities (Bear 1972 [156269], p. 581). The following discussion deals with D for the sake of simplicity. The effects of molecular diffusion can be accounted for by adding in the term D_0 to the diagonal components of the displacement matrix as in Equation 55.

Generally the pore-water velocity and the dispersion tensor vary spatially and temporally. Experimental studies of transport in groundwater have determined the nature of the dispersion tensor and the appropriate values of the dispersivity parameter. Gelhar (1997 [145122], p. 164, Figure 8) showed that distinct values of the longitudinal dispersivity, the transverse dispersivity

in the horizontal direction, and the transverse dispersivity in the vertical direction can be identified based on available field transport studies. The general conceptual model underlying the use of these three terms is one of horizontal flow with tortuous fine-scale flow through heterogeneous media. The details of transport through the heterogeneous media give rise to the spreading of solute in the direction of flow and, to a lesser extent, transverse to the direction of flow. Of course, groundwater flow, though generally horizontal, exhibits vertical velocities locally in regions of upward or downward gradients, such as in areas of recharge or discharge or when the flow is subject to variability in hydraulic conductivity that diverts water vertically.

In practice, it is difficult, from available data, to propose more complex forms of the dispersion process and to determine the alternate dispersivity values from field observations. Nevertheless, it is quite possible that more complex forms are more representative, given the complexity and variety of different heterogeneities present in nature. An important conclusion from the available field data is that longitudinal dispersion is a strong function of scale, that is, the travel length of a solute plume in the medium (e.g., Neuman 1990 [101464], Figure 1). In a typical groundwater flow model at the scale of a flow basin, characteristic flow distances of tens to hundreds of meters vertically may be present, compared to hundreds to thousands of meters horizontally. Given the difference in scale, it is not clear that the longitudinal dispersivity in the vertical direction should be set equal to that in the horizontal direction. In addition, in stratified porous media containing heterogeneities such as irregularly-shaped beds or clay lenses, the characteristic scale of the heterogeneity encountered by a solute will be different in the horizontal and vertical directions, yielding potentially different values for longitudinal dispersion. Therefore, one motivation for the development of the theory in this section is to propose a dispersion tensor that can be used to handle these more general scenarios.

6.5.2.2 General Form of the Dispersion Tensor for Axisymmetric Media

An axisymmetric medium is one that displays rotational symmetry about an axis. For example, a medium composed of horizontal layers of different geological materials, each of which is uniform within the layer, is an axisymmetric medium with the axis of symmetry being vertical. Consider a porous medium that, at the macroscale, exhibits an axis of symmetry $\overline{\lambda}$; that is, physical processes are invariant under rotations about $\overline{\lambda}$. To be considered a tensor, the collection of coefficients making up the dispersion tensor must satisfy certain transformation rules upon changing from one coordinate system to another. It can be shown that the most general, symmetric, second-order tensor that can be constructed from these the vectors $\overline{\lambda}$ and the average macroscale pore velocity $\overline{v}$ is given by the dyadic (Poreh 1965 [163847], p. 3911, Equation 8):

$$\overline{\overline{D}} = \alpha_1 v \overline{\overline{I}} + \alpha_2 \frac{\overline{vv}}{v} + \alpha_3 v \overline{\lambda}\overline{\lambda} + \frac{1}{2}\alpha_4(\overline{\lambda}\overline{v} + \overline{v}\overline{\lambda}) \qquad \text{(Eq. 2)}$$

where

$\overline{\overline{I}}$ represents the unit tensor

v denotes the magnitude of the solute velocity ($v^2 = \sum v_i^2$)

the coefficients α_i are scalar quantities with the dimension of length.

Symmetry is imposed on the dispersion tensor. While traditionally this is taken to be the case for the dispersion tensor (Bear 1972 [156269], p. 611), it is not a fundamental requirement. In this expression for the dispersion tensor, and in what follows, the contribution of molecular diffusion is not explicitly indicated for simplicity. It may be easily added to the diagonal elements.

The four coefficients α_i that appear in Equation 2 are, in general, functions of the scalar quantities v and $\overline{\lambda} \cdot \overline{v}$, which may be functions of time and space for a variable velocity field, such as encountered in heterogeneous media, for example. $\overline{v}$ is an eigenvector of $\overline{D}$ provided that the coefficients α_3 and α_4 are related to each other through the relation:

$$\alpha_4 = -2\cos\theta \alpha_3 = -2\frac{\overline{\lambda} \cdot \overline{v}}{v}\alpha_3 \qquad \text{(Eq. 3-a)}$$

where θ is the angle between the symmetry axis and the velocity vector.

Using Equation 3-a, Equation 2 becomes

$$\overline{D} = \alpha_1 v\overline{I} + \alpha_2 \frac{\overline{vv}}{v} + \alpha_3 v(\overline{\lambda}\overline{\lambda} - \frac{\cos\theta}{v}(\overline{\lambda}\overline{v} + \overline{v}\overline{\lambda})) \qquad \text{(Eq. 3-b)}$$

When Equation 3 holds, the coefficients α_i may be related to their more conventional designations in terms of longitudinal and transverse dispersivity corresponding to eigenvalues of $\overline{D}$ associated with principal axes parallel and perpendicular to the direction of flow, respectively. In this case, two distinct longitudinal and transverse dispersivities can be defined. These correspond to flow parallel and perpendicular to the axis of symmetry and may be assigned as α_L^H, α_L^V and α_T^H, α_T^V, respectively. The superscripts V and H, designating "vertical" and "horizontal," are defined in relation to the axis of symmetry with V parallel and H perpendicular to the symmetry axis $\overline{\lambda}$.

For a general axisymmetric medium, it is possible that the principal axes are not aligned with the direction of flow. Let Φ denote the angle between the major principal axis of the dispersion tensor and the flow velocity. When $\Phi \neq 0$, the terms longitudinal and transverse are not meaningful. There is some precedent for $\Phi \neq 0$ in heterogeneous porous media (de Marsily 1986 [100439], p. 250). Both Gelhar and Axness (1983 [107296], pp. 166-170) and Neuman et al. (1987 [147577], pp. 460-462) have demonstrated theoretically that, in general, $\Phi \neq 0$ is based on a stochastic analysis of transport in heterogeneous media. However, there is disagreement among the authors as to the sign of the angle Φ. At present, there does not exist experimental or field confirmation of the situation when $\Phi \neq 0$, which appears difficult at best to establish.

If Equation 2 holds so that one of the principal axes is aligned with the direction of flow, then (Lichtner et al. 2002 [163821], Equation 19a and 19b):

$$\alpha_L = \alpha_1 + \alpha_2 + \cos^2\theta \alpha_3 \qquad \text{(Eq. 4a)}$$

and

$$\alpha_T = \alpha_1 + (1 - \cos^2 \theta)\alpha_3 \qquad \text{(Eq. 4b)}$$

where, α_L is the longitudinal dispersivity and α_T is the transverse dispersivity, respectively.

Thus, when $\theta = \pi/2$,

$$\alpha_L = \alpha_L^H = \alpha_1 + \alpha_2 \qquad \text{(Eq. 4c)}$$

and

$$\alpha_T = \alpha_T^V = \alpha_1 + \alpha_3 \qquad \text{(Eq. 4d)}$$

When $\theta = 0$,

$$\alpha_L = \alpha_L^V = \alpha_1 + \alpha_2 + \alpha_3 \qquad \text{(Eq. 4e)}$$

and

$$\alpha_T = \alpha_T^H = \alpha_1 \qquad \text{(Eq. 4f)}$$

Solving 4a, 4c, and 4f for the α_i yields the inverse relations:

$$\alpha_1 = \alpha_T^H, \qquad \text{(Eq. 5a)}$$

$$\alpha_2 = \alpha_L - \alpha_T^H - \frac{\cos^2 \theta}{1 - \cos^2 \theta}\left(\alpha_T - \alpha_T^H\right) \qquad \text{(Eq. 5b)}$$

$$\alpha_3 = \frac{\alpha_T - \alpha_T^H}{1 - \cos^2 \theta} \qquad \text{(Eq. 5c)}$$

With these results the dispersion tensor can be written in dyadic form as

$$\overline{D} = \alpha_T^H v \overline{I} + \left[\alpha_L - \alpha_T^H - \frac{\cos^2 \theta}{1 - \cos^2 \theta}\left(\alpha_T - \alpha_T^H\right)\right]\frac{\overline{vv}}{v}$$

$$+ \frac{\alpha_T - \alpha_T^H}{1 - \cos^2 \theta} v\left[\overline{\lambda}\overline{\lambda} - \frac{\cos \theta}{v}\left(\overline{\lambda}\overline{v} + \overline{v}\overline{\lambda}\right)\right] \qquad \text{(Eq. 6)}$$

The longitudinal and transverse dispersivities, α_L and α_T, can be arbitrary functions of the scalar quantities v and θ. Whether or not this four-parameter representation of the dispersion tensor provides an adequate description of flow at an angle to the symmetry axis, it needs to be verified by direct comparison with field observations.

6.5.2.2.1   Special Cases of the Dispersion Tensor

In this section, special cases corresponding to an isotropic medium and an axisymmetric medium with flow parallel and perpendicular to the symmetry axis are considered in more detail. Although not all of these special cases are used explicitly in the SZ transport model, they arise from the general form for extreme values of the parameters λ and θ. It is useful to consider them for comparative purposes.

Isotropic Media

For the special case of an isotropic medium, $\overline{\lambda} = 0$ since there is no preferred axis of symmetry, and it follows that the general form of the dispersion tensor reduces to the well-known form (Poreh 1965 [163847], Equation 15):

$$\overline{D} = \alpha_1 v \overline{I} + \alpha_2 \frac{\overline{v}\,\overline{v}}{v} \qquad\qquad \text{(Eq. 7)}$$

To relate the coefficients α_L and α_T to the usual longitudinal and transverse dispersivity coefficients α_L and α_T, note that $\overline{v}$ is an eigenvector of $\overline{D}$ with eigenvalue $\alpha_1 + \alpha_2$, and

$$\overline{D} \cdot \overline{v} = (\alpha_1 + \alpha_2) v \overline{v} \qquad\qquad \text{(Eq. 8)}$$

Thus, it follows that $\alpha_L = \alpha_1 + \alpha_2$. The remaining two eigenvectors represented by $\overline{\zeta}_i$, orthogonal to $\overline{v}$, belong to the degenerate eigenvalue $\alpha_1 v$. Hence, it follows that

$$\overline{D} \cdot \overline{\zeta}_i = \alpha_1 v \overline{\zeta}_i \qquad\qquad \text{(Eq. 9)}$$

Thus, $\alpha_T = \alpha_1$, and $\alpha_2 = \alpha_L - \alpha_T$.

The resulting dispersion tensor for an isotropic porous medium has the form (Bear 1972 [156269], p. 613, Equation 10.4.16):

$$\overline{D} = \alpha_T v I + (\alpha_L - \alpha_T) \frac{\overline{v}\,\overline{v}}{v}$$

$$= \begin{pmatrix} \alpha_T v + (\alpha_L - \alpha_T)\dfrac{v_1^2}{v} & (\alpha_L - \alpha_T)\dfrac{v_1 v_2}{v} & (\alpha_L - \alpha_T)\dfrac{v_1 v_3}{v} \\[2mm] (\alpha_L - \alpha_T)\dfrac{v_2 v_1}{v} & \alpha_T v + (\alpha_L - \alpha_T)\dfrac{v_2^2}{v} & (\alpha_L - \alpha_T)\dfrac{v_2 v_3}{v} \\[2mm] (\alpha_L - \alpha_T)\dfrac{v_3 v_1}{v} & (\alpha_L - \alpha_T)\dfrac{v_3 v_2}{v} & \alpha_T v + (\alpha_L - \alpha_T)\dfrac{v_3^2}{v} \end{pmatrix} \qquad \text{(Eq. 10)}$$

Axisymmetric Medium: Flow Parallel to Symmetry Axis

For an axisymmetric medium with flow along the axis of symmetry, it follows that

$$\bar{v} = v\bar{\lambda} \qquad \text{(Eq. 11)}$$

and $\overline{D}$ becomes

$$\overline{D} = \alpha_1 v\overline{I} + (\alpha_2 + \alpha_3 + \alpha_4)v\bar{\lambda}\bar{\lambda} \qquad \text{(Eq. 12)}$$

It is apparent that $\bar{v}$ (and $\bar{\lambda}$) is an eigenvector belonging to the eigenvalue $(\alpha_1 + \alpha_2 + \alpha_3 + \alpha_4)v$, and the eigenvalue α_1 is degenerate with eigenvectors in the plane normal to $\bar{\lambda}$.

Introducing the notation α_L^V for longitudinal dispersivity along the axis of symmetry and α_T^H for horizontal transverse dispersivity, the dispersion tensor can be written as

$$\overline{D} = \alpha_T^H v\overline{I} + \left(\alpha_L^V - \alpha_T^H\right)\frac{\overline{v}\overline{v}}{v} \qquad \text{(Eq. 13)}$$

with $\alpha_1 = \alpha_T^H$ and $\alpha_2 + \alpha_3 + \alpha_4 = \alpha_L^V - \alpha_T^H$. This form of the dispersion tensor has the same form as that for an isotropic medium. Thus, $\bar{v}$ is a principal direction of the dispersion tensor satisfying

$$\overline{D} \cdot \bar{v} = \alpha_L^V v\bar{v} \qquad \text{(Eq. 14)}$$

with

$$\alpha_L^V = \alpha_1 + \alpha_2 + \alpha_3 + \alpha_4 \qquad \text{(Eq. 15)}$$

The remaining two eigenvectors are orthogonal to $\bar{v}$ but otherwise arbitrary, belonging to the degenerate eigenvalue $\alpha_T^H v$.

Axisymmetric Medium: Flow Perpendicular to Symmetry Axis

For the special case when $\bar{v}$ and $\bar{\lambda}$ are orthogonal and $\cos\theta = 0$, it follows that

$$\overline{D} \cdot \bar{v} = (\alpha_1 + \alpha_2)v\bar{v} + \frac{1}{2}\alpha_4 v^2 \bar{\lambda} \qquad \text{(Eq. 16a)}$$

and

$$\overline{D} \cdot \bar{\lambda} = \frac{1}{2}\alpha_4 \bar{v} + (\alpha_1 + \alpha_3)v\bar{\lambda} \qquad \text{(Eq. 16b)}$$

From these relations it is apparent that, in general, neither $\bar{v}$ nor $\bar{\lambda}$ are eigenvectors of $\overline{D}$ unless $\alpha_4 = 0$, in which case both vectors $\bar{v}$ and $\bar{\lambda}$ are eigenvectors satisfying the eigenvalue equations

$$\overline{D} \cdot \bar{v} = (\alpha_1 + \alpha_2)v\bar{v} \qquad \text{(Eq. 17a)}$$

$$= \alpha_L^H v\bar{v}$$

and

$$\overline{D} \cdot \overline{\lambda} = (\alpha_1 + \alpha_3) v \overline{\lambda} \qquad \text{(Eq. 17b)}$$

$$= \alpha_T^V v \overline{\lambda}$$

In this case there are two transverse dispersivities, horizontal and vertical, denoted by α_T^H and α_T^V. Longitudinal dispersivity is denoted by α_L^H because, in general, it may be different from α_L^T for flow in the direction parallel to $\overline{\lambda}$.

Noting that $\overline{v} \times \overline{\lambda}$ is an eigenvector belonging to the eigenvalue α_1, which may be identified with α_T^H, it follows that

$$\alpha_1 = \alpha_T^H \qquad \text{(Eq. 18a)}$$

$$\alpha_2 = \alpha_L^H - \alpha_T^H \qquad \text{(Eq. 18b)}$$

and

$$\alpha_3 = \alpha_T^V - \alpha_T^H \qquad \text{(Eq. 18c)}$$

Generally, $\alpha_2 \gg \alpha_3$ since α_2 involves the difference between longitudinal and transverse dispersivities, whereas α_3 is proportional to the difference in transverse dispersivities.

6.5.2.2.2 New Form of the Dispersion Tensor for Axisymmetric Media

To construct a form of the dispersion tensor that could apply to flow at any arbitrary angle to the axis of symmetry and still honor tensorial transformation properties, the appropriate functional form of the coefficients α_L and α_T on the direction of flow must be determined. Two limiting cases must be met for flow parallel and perpendicular to the axis of symmetry. For flow parallel to the symmetry axis, longitudinal dispersion should reduce to the vertical longitudinal dispersivity α_L^V, and transverse dispersion should be isotropic with dispersivity described by α_T^V. For flow perpendicular to the axis of symmetry, longitudinal dispersion should reduce to the horizontal longitudinal dispersivity α_L^H, with transverse dispersion described by the two coefficients, α_T^V and α_T^H. Clearly, it is not possible to deduce a priori the form of the dispersion tensor for flow at an angle to the symmetry axis without additional information. It would be expected that the dispersion tensor would depend on the specific properties of the porous medium and even head differences. Without additional information, it is taken that the longitudinal and transverse dispersivities have the forms

$$\alpha_L = G_L \left(\cos\theta; \alpha_L^V, \alpha_L^H \right) \qquad \text{(Eq. 19a)}$$

and

$$\alpha_T = G_T \left(\cos\theta; \alpha_T^V, \alpha_T^H \right) \qquad \text{(Eq. 19b)}$$

where the only dependence is on the scalar $\cos\theta$ in addition to the dispersivity parameters. The functions $G_{L,T}$ satisfy the end member conditions

$$G_L\left(0;\alpha_L^V,\alpha_L^H\right)=\alpha_L^V \quad \text{(horizontal flow)} \tag{Eq. 20a}$$

$$G_T\left(0;\alpha_T^V,\alpha_T^H\right)=\alpha_T^H \quad \text{(horizontal flow)} \tag{Eq. 20b}$$

$$G_L\left(1;\alpha_L^V,\alpha_L^H\right)=\alpha_L^H \quad \text{(vertical flow)} \tag{Eq. 20c}$$

$$G_T\left(1;\alpha_T^V,\alpha_T^H\right)=\alpha_T^V \quad \text{(vertical flow)} \tag{Eq. 20d}$$

but are otherwise arbitrary. To determine the functional form of $G_{L,T}$, it would be necessary to compare predictions based on a specific form of the dispersion tensor with actual field observations or to carry out numerical experiments involving heterogeneous media.

For the new form of the dispersion tensor proposed here, the following dependency on $\cos\theta$ is chosen

$$G_L=\alpha_L^H+\cos^2\theta\left(\alpha_L^V-\alpha_L^H\right) \tag{Eq. 21a}$$

and

$$G_T=\alpha_T^V+\cos^2\theta\left(\alpha_T^H-\alpha_T^V\right) \tag{Eq. 21b}$$

With this choice of $G_{L,T}$, the desired behavior is obtained that is at least correct for the end member cases of flow parallel and perpendicular to the axis of symmetry. However, clearly an infinite number of functional forms are possible that satisfy the conditions of Equations 20a–d. In what follows, it is taken that the transverse horizontal dispersivity α_T^H has the same value for flow parallel and perpendicular to the axis of symmetry. However, it is not apparent that this necessarily must be the case, which would complicate the formulation.

To obtain expressions for the coefficients α_i in terms of the set $\alpha_L^V,\alpha_L^H,\alpha_T^V$, and α_T^H, the expressions for longitudinal and transverse dispersion given by Equations 4a and 4b are equated to the desired forms given by

$$\alpha_L=\alpha_1+\alpha_2+\cos^2\theta\alpha_3$$

$$=\alpha_L^H+\cos^2\theta\left(\alpha_L^V-\alpha_L^H\right) \tag{Eq. 22a}$$

and

$$\alpha_T=\alpha_1+\left(1-\cos^2\theta\right)\alpha_3$$

$$= \alpha_T^V + \cos^2 \theta \left(\alpha_T^H - \alpha_T^V \right) \tag{Eq. 22b}$$

As can be seen from these relations, the eigenvalue for longitudinal dispersion varies between the horizontal and vertical longitudinal dispersivities as the flow direction varies from perpendicular to parallel to the symmetry axis of the medium. Similarly, the eigenvalue for transverse dispersivity varies between the vertical and horizontal transverse dispersivities.

The coefficient α_1 is taken to be given by

$$\alpha_1 = \alpha_T^H \tag{Eq. 23}$$

independent of the direction of the flow velocity relative to the symmetry axis. To see that this is reasonable, define the vector $\overline{\omega}$ as

$$\overline{\omega} = \overline{\lambda} - \frac{\overline{\lambda} \cdot \overline{v}}{v^2} \cdot \overline{v} \tag{Eq. 24}$$

Then it is seen that the vector $\overline{\xi}_3 = \overline{v} \times \overline{\omega}$ is an eigenvector of the dispersion tensor $\overline{D}$, and $\overline{\omega}$ is always perpendicular to the symmetry axis $\overline{\lambda}$ and the flow velocity $\overline{v}$ with eigenvalue $\alpha_1 v$, and, hence, it should reflect only horizontal transverse dispersion. Equations 22a and 22b provide two equations for the two coefficients α_2 and α_3. It follows that

$$\alpha_2 = \alpha_L^H - \alpha_T^H + \cos^2 \theta \left(\alpha_L^V - \alpha_L^H + \alpha_T^V - \alpha_T^H \right) \tag{Eq. 25 a}$$

$$= \alpha_L - \alpha_T + \alpha_T^V - \alpha_T^H$$

and

$$\alpha_3 = \alpha_T^V - \alpha_T^H \tag{Eq. 25 b}$$

with α_4 given by Equation 3.

In these relations, α_1 is seen to be independent of the angle θ. This behavior is intuitively correct because the vector $\overline{\zeta}_3$ always remains perpendicular to the symmetry axis and the direction of flow, and, hence, the eigenvalue should always be equal to the horizontal transverse dispersivity. In addition, as expected, the eigenvalue corresponding to the eigenvector $\overline{\omega}$ varies from transverse vertical to transverse horizontal as the vectors $\overline{v}$ and $\overline{\omega}$ range from perpendicular to parallel.

In terms of individual matrix elements with $\lambda = (0,0,1)$, the dispersion tensor becomes (Lichtner et al. 2002 [163821], Equations 47a-47f)

$$D_{11} = \alpha_L \frac{v_1^2}{v} + \alpha_T^H \frac{v_2^2}{v} \left(1 + \frac{v_3^2}{v_1^2 + v_2^2} \right) + \alpha_T \frac{v_3^2}{v} \frac{v_1^2}{v_1^2 + v_2^2} \tag{Eq. 26a}$$

$$D_{22} = \alpha_T^H \frac{v_1^2}{v}\left(1 + \frac{v_3^2}{v_1^2 + v_2^2}\right) + \alpha_L \frac{v_2^2}{v} + \alpha_T \frac{v_3^2}{v}\frac{v_2^2}{v_1^2 + v_2^2} \qquad \text{(Eq. 26b)}$$

$$D_{33} = \alpha_T \frac{\left(v_1^2 + v_2^2\right)}{v} + \alpha_L \frac{v_3^2}{v} \qquad \text{(Eq. 26c)}$$

$$D_{12} = \left[\alpha_L - \alpha_T^H\left(1 + \frac{v_3^2}{v_1^2 + v_2^2}\right) + \alpha_T \frac{v_3^2}{v_1^2 + v_2^2}\right]\frac{v_1 v_2}{v} \qquad \text{(Eq. 26d)}$$

$$D_{13} = \left(\alpha_L - \alpha_T\right)\frac{v_1 v_3}{v} \qquad \text{(Eq. 26e)}$$

$$D_{23} = \left(\alpha_L - \alpha_T\right)\frac{v_2 v_3}{v} \qquad \text{(Eq. 26f)}$$

In these relations α_T and α_L are functions of $\cos\theta$ as given by Equations 22a and 22b.

According to this formulation, the dispersion tensor can be expressed in terms of the four dispersivity coefficients $\alpha_L^{V,H}$ and $\alpha_T^{V,H}$. By appropriately choosing α_4, one of the principal axes can always be lined up with the direction of flow. Only through comparison with field data will it be possible to determine the correct form of the coefficients α_i in terms of the invariants θ and v.

In principle, at the laboratory scale the coefficients $\alpha_L^H, \alpha_L^V, \alpha_T^H$, and α_T^V could be estimated by conducting experiments on suitably oriented cores. One approach would be to estimate α_L^H and α_L^V by measuring tracer breakthrough curves on a core sample oriented normal and parallel, respectively, to the axis of symmetry. Transverse dispersivities α_T^H, α_T^V could then be estimated by performing two-dimensional flow experiments on rock slabs, for example. Such results would be of significant theoretical interest. However, it is well known that dispersivity values are a strong function of scale; hence, it is necessary to estimate the dispersivity coefficients at a larger scale using field experiments. In the most general flow situation, the coefficients α_1, α_2, α_3, and α_4 could be estimated from field data using a numerical model in conjunction with nonlinear parameter estimation by fitting an observed 3-D plume. If a tracer test can be conducted in a portion of the aquifer where the fluid velocity is unidirectional and horizontal coinciding with the principal axis of the dispersion tensor (as often is the case), the parameter estimation procedure can be simplified considerably. In this case, the dispersion tensor simplifies to

$$D_{11} = \alpha_L^H v, \quad D_{22} = \alpha_T^H v, \quad D_{33} = \alpha_T^V v \qquad \text{(Eq. 27)}$$

with zero off-diagonal terms.

With appropriately spaced observation wells, the coefficients α_L^H, α_T^H and, if enough 3-D information is available, α_T^V as well, can be estimated. Note that in this particular case, no

information is available about α_L^V. To obtain this coefficient, another test would have to be conducted in a portion of the field where the fluid velocity has a significant vertical component. If the spread of a plume can be measured in such a case, then Equations 26a–f can be used to estimate the value of the coefficient α_L^V and, perhaps, α_T^V. Once the dispersivities are estimated for horizontal and vertical flow, the θ dependence of the dispersivity coefficients for flow at an angle to the symmetry axis could be tested.

6.5.2.2.3   Dispersion Tensor Proposed by Burnett and Frind

Burnett and Frind (1987 [130526, Equations 6a-6f) proposed a dispersion tensor for axisymmetric media, hereafter designated as D_{BF} and referred to as the BF-dispersion tensor. The BF-dispersion tensor involves only three independent parameters.   These refer to longitudinal dispersion α_L, and transverse horizontal α_T^H and vertical α_T^V dispersion. Burnett and Frind (1987 [130526], Equations 6a-6f) derived the form of the dispersion tensor from the form for isotropic media to account for different transverse dispersivities in the horizontal and vertical directions as observed in natural stratified media with flow along the bedding plane (Anderson 1979 [104397]). For example, Zheng and Bennett (1995 [154702], pp. 45 to 46) have used the Burnett-Frind tensor to model dispersion in axisymmetric media.

Burnett and Frind (1987 [130526], Equations 6a-6f) write the dispersion tensor as a matrix of coefficients in the form:

$$
D_{BF} = \begin{pmatrix}
\alpha_L \dfrac{v_1^2}{v} + \alpha_T^H \dfrac{v_2^2}{v} + \alpha_T^V \dfrac{v_3^2}{v} & \left(\alpha_L - \alpha_T^H\right)\dfrac{v_1 v_2}{v} & \left(\alpha_L - \alpha_T^V\right)\dfrac{v_1 v_3}{v} \\[3ex]
\left(\alpha_L - \alpha_T^H\right)\dfrac{v_2 v_1}{v} & \alpha_T^H \dfrac{v_1^2}{v} + \alpha_L \dfrac{v_2^2}{v} + \alpha_T^V \dfrac{v_3^2}{v} & \left(\alpha_L - \alpha_T^V\right)\dfrac{v_2 v_3}{v} \\[3ex]
\left(\alpha_L - \alpha_T^V\right)v\dfrac{v_3 v_1}{v} & \left(\alpha_L - \alpha_T^V\right)\dfrac{v_3 v_2}{v} & \alpha_T^V \dfrac{v_1^2 + v_2^2}{v} + \alpha_L \dfrac{v_3^2}{v}
\end{pmatrix}
\tag{Eq. 28}
$$

The diagonal elements may be written in a form similar to the isotropic case given in Equation 10 as

$$
\left(D_{BF}\right)_{11} = \alpha_T^H v + \left(\alpha_L - \alpha_T^H\right)\frac{v_1^2}{v} + \left(\alpha_T^V - \alpha_T^H\right)\frac{v_3^2}{v}
\tag{Eq. 29a}
$$

$$
\left(D_{BF}\right)_{22} = \alpha_T^H v + \left(\alpha_L - \alpha_T^H\right)\frac{v_2^2}{v} + \left(\alpha_T^V - \alpha_T^H\right)\frac{v_3^2}{v}
\tag{Eq. 29b}
$$

$$
\left(D_{BF}\right)_{33} = \alpha_T^V v + \left(\alpha_L - \alpha_T^V\right)\frac{v_3^2}{v}
\tag{Eq. 29c}
$$

To determine the tensorial properties of the BF-dispersion tensor, it is first noted that $\overline{D}_{BF}$ be interpreted as referring to a particular coordinate system in which the symmetry axis of the medium lies along the z-axis: $\overline{\lambda} = (0,0,1)$. Then v_3 can be written as the scalar product $v_3 = v\cos\theta = \overline{\lambda}\cdot\overline{v}$. With this in mind, the matrix $\overline{D}_{BF}$ can be expressed as

$$\overline{D}_{BF} = \left[\alpha_T^H + \cos^2\theta\left(\alpha_T^V - \alpha_T^H\right)\right]v\overline{I} + \left(\alpha_L - \alpha_T^H\right)\frac{\overline{v}\overline{v}}{v} + \left(\alpha_T^V - \alpha_T^H\right)v \left[\overline{\lambda}\overline{\lambda} - \frac{\cos\theta}{v}\left(\overline{\lambda}\overline{v} + \overline{v}\overline{\lambda}\right)\right] \quad \text{(Eq. 30)}$$

valid for any orientation of the coordinate system relative to the symmetry axis. Accordingly, $\overline{D}_{BF}$ is a tensor by construction. Comparing Equation 30 with Equation 5a,b,c and Equation 3 leads to the following identification of the coefficients α_i:

$$\alpha_1 = \alpha_T^H + \cos^2\theta\left(\alpha_T^V - \alpha_T^H\right) \quad \text{(Eq. 31a)}$$

$$\alpha_2 = \alpha_L - \alpha_T^H \quad \text{(Eq. 31b)}$$

$$\alpha_3 = \alpha_T^V - \alpha_T^H \quad \text{(Eq. 31c)}$$

and

$$\alpha_4 = -2\cos\theta\left(\alpha_T^V - \alpha_T^H\right) = -2\cos\theta\,\alpha_3 \quad \text{(Eq. 31d)}$$

It follows that Equation 3 is satisfied for the BF-dispersion tensor and, thus, both v and ω are eigenvectors belonging to eigenvalues $\alpha_L v$ and $\alpha_T^V v$, respectively, according to Equations 17a and 17b:

$$D_{BF}\cdot\overline{v} = \alpha_L v\overline{V} \quad \text{(Eq. 32a)}$$

and

$$D_{BF}\cdot\overline{\omega} = \alpha_T^V v\overline{\omega} \quad \text{(Eq. 32b)}$$

The eigenvector $\overline{\zeta}_3$, orthogonal to $\overline{V}$ and $\overline{\omega}$, belongs to the eigenvalue α_1

$$D_{BF}\cdot\overline{\zeta}_3 = \left[\alpha_T^H + \cos\theta\left(\alpha_T^V - \alpha_T^H\right)\right]\,v\overline{\zeta}_3 \quad \text{(Eq. 32c)}$$

There are certain limitations with the form of the BF-dispersion tensor. The relation for the generalized dispersion tensor given in Equation 23, in which α_1 is independent of the angle θ, differs from that of $\overline{D}_{BF}$ given in Equation 31a, in which α_1 is a function of $\cos\theta$. Similarly, the generalized relation for α_2 in Equation 25a is different from that obtained for the BF-dispersion tensor given in Equation 31b. In addition, for the BF-dispersion tensor, there is only one coefficient for longitudinal dispersion, which is, therefore, the same for flow in both the vertical

and horizontal directions, i.e., parallel and perpendicular to the axis of symmetry, contrary to what one would expect for nonisotropic porous media.

However, for flow perpendicular to the axis of symmetry, the BF-tensor agrees with the more general form. And for small values of vertical velocity v_3, the generalized form of the dispersion tensor reduces to the form given by Burnett and Frind (1987 [130526], Equations 6a-6f). Hence, in situations where the axis of symmetry is vertical and the flow fields are horizontal to subhorizontal, as is the case at Yucca Mountain (BSC 2003 [162649], Section 6.6), this form of the dispersion tensor is adequate. This is the form that is used in the calculations presented in this report.

6.5.2.3 Random-Walk Particle-Tracking Method

Given a steady-state velocity field generated, for example, for an arbitrary permeability field, a random walk is superimposed on the flow field to describe dispersion and molecular diffusion. The general approach used in particle tracking is to replace the partial differential equation for the solute concentration C, generally expressed by Equation 1, with random-walk displacements defined in differential form by the Langevin equation (Gardiner 1997 [145116], p. 80):

$$dx = A(x,t)dt + B(x,t)dW(t) \qquad \text{(Eq. 33)}$$

for position vector $x(t)$. The matrix A represents the deterministic background displacement determined by $\vec{v}$ and, in addition, contains contributions from the dispersion tensor. The displacement matrix B refers to a stochastic random-walk process that incorporates molecular diffusion and dispersion. The differential $dW(t)$ represents a Wiener process describing Brownian motion with the properties:

$$< dW >= 0 \qquad \text{(Eq. 34)}$$

and

$$< dW(t)dW(t) >= Idt \qquad \text{(Eq. 35)}$$

where the angular brackets represent the ensemble mean.

The equivalent Fokker-Plank equation corresponding to the Langevin equation (Equation 33) for the conditional probability $P(x,t|x_0,t_0)$ is given by (Gardiner 1997 [145116], p. 97):

$$\frac{\partial P}{\partial t} = -\nabla \cdot [A(x,t)P] + \nabla : \nabla \left[\frac{1}{2} B\tilde{B}P \right] \qquad \text{(Eq. 36)}$$

where $\tilde{B}$ represents the transpose matrix. The Fokker-Plank equation may be written in the form of the transport equation by rearranging Equation 36 to obtain:

$$\frac{\partial P}{\partial t} = -\nabla \cdot \left[\left(A(x,t) - \frac{1}{2}\nabla \cdot B\tilde{B} \right) P \right] + \nabla \cdot \left[\frac{1}{2} B\tilde{B}\nabla P \right] \qquad \text{(Eq. 37)}$$

Comparing this modified Fokker-Plank equation with the continuum-based transport equation given in Equation 1 yields the identifications:

$$P(x,t \mid x_0,t_0) = \frac{N_A}{N} C(x,t),$$ (Eq. 38)

where N represents the number of particles and N_A denotes Avogadro's number,

$$A(x,t) = \vec{v} + \nabla \cdot D$$ (Eq. 39)

and

$$\frac{1}{2} B\tilde{B} = D$$ (Eq. 40)

Therefore, it is necessary to obtain the displacement matrix B based on the dispersion tensor D. To do this, the approach used by Tompson et al. (1987 [145195], Appendix A) is followed in which a transformation that diagonalizes the dispersion tensor is carried out. By construction, the eigenvectors of the dispersion tensor depend only on the components of the flow velocity but not on the dispersivity values themselves. One eigenvector always points in the direction of the flow velocity. The other two eigenvectors are perpendicular to the direction of flow. The eigenvalue problem for D reads:

$$De_\lambda = \lambda\bar{e}_\lambda$$ (Eq. 41)

with eigenvalue λ and eigenvector $\bar{e}_\lambda$. Because the dispersion tensor is symmetric (Bear 1972 [156269], p. 611), there exists an orthogonal transformation U that diagonalizes D (Tompson et al. 1987 [145195], p. 106, Equation A-3):

$$\tilde{U}DU\tilde{U}e_\lambda = \lambda\tilde{U}e_\lambda$$ (Eq. 42)

where $\tilde{U}$ is the transpose of U, with

$$\tilde{U}\hat{D}U = D$$ (Eq. 43)

where D is a diagonal matrix, and U satisfies the relations:

$$U\tilde{U} = \tilde{U}U = I$$ (Eq. 44)

Expressing D in the form

$$\hat{D} = Q\tilde{Q}$$ (Eq. 45)

with Q diagonal, then gives

$$2D = 2U\hat{D}\tilde{U} = 2UQ\hat{\tilde{Q}}\tilde{U} = 2UQ\tilde{U}\tilde{Q} = B\tilde{B} \qquad \text{(Eq. 46)}$$

From this relation it follows that the displacement matrix B is given by (Tompson et al. 1987 [145195], p. 107, Equation A-10):

$$B = \sqrt{2}UQ \qquad \text{(Eq. 47)}$$

The implementation of the particle-tracking model requires a finite difference form of Equation 5 at time step n, which in this model is given by:

$$X_i^n = X_i^{n-1} + A_i\Delta t + \sqrt{\Delta t}\sum_j B_{ij}Z_j \qquad \text{(Eq. 48)}$$

with

$$dW_j = Z_j\sqrt{\Delta t} \qquad \text{(Eq. 49)}$$

for a time step Δt, where Z_j represents a random number. In matrix notation,

$$X^n = X^{n-1} + A\Delta t + \sqrt{\Delta t}BZ \qquad \text{(Eq. 50)}$$

Sampling Z from a uniform distribution (Tompson et al. 1987 [145195], p. 40) leads to the expression:

$$Z = 2\sqrt{3}Z' \qquad \text{(Eq. 51)}$$

with Z' occurring with unit probability over the interval $-\frac{1}{2}$ to $\frac{1}{2}$. Then,

$$<ZZ>=12<Z'Z'>=1 \qquad \text{(Eq. 52)}$$

since

$$<Z'Z'>= \int_{-1/2}^{1/2} Z'^2 dZ' = \frac{1}{12} \qquad \text{(Eq. 53)}$$

The final step in the derivation is to determine the form of the displacement matrix B. Tompson et al. (1987 [145195]) derived the expression for an isotropic system, but the equivalent derivation for an anisotropic dispersion model was not available and, hence, is given below for an axisymmetric medium (Lichtner et al. 2002 [163821], Equation 62). The eigenvalues are distinct, and there exist three unique normalized eigenvectors. The matrix U has the form:

$$U = \begin{pmatrix} \dfrac{v_1}{v} & -\dfrac{v_1 v_3}{v\sqrt{v_1^2+v_2^2}} & -\dfrac{v_2}{\sqrt{v_1^2+v_2^2}} \\[3mm] \dfrac{v_2}{v} & -\dfrac{v_2 v_3}{\sqrt{v_1^2+v_2^2}} & -\dfrac{v_1}{\sqrt{v_1^2+v_2^2}} \\[3mm] \dfrac{v_3}{v} & \dfrac{1}{v}\sqrt{v_1^2+v_2^2} & O \end{pmatrix} \qquad \text{(Eq. 54)}$$

In this case the displacement matrix B is given by

$$B = \begin{pmatrix} \dfrac{v_1}{v}\sqrt{2(\alpha_L v + D_0)} & -\dfrac{v_1 v_3 \sqrt{2(\alpha_T v + D_0)}}{v\sqrt{v_1^2+v_2^2}} & -\dfrac{v_2\sqrt{2(\alpha_T^H v + D_0)}}{\sqrt{v_1^2+v_2^2}} \\[3mm] \dfrac{v_2}{v}\sqrt{2(\alpha_L v + D_0)} & -\dfrac{v_2 v_3 \sqrt{2(\alpha_T v + D_0)}}{v\sqrt{v_1^2+v_2^2}} & \dfrac{v_1\sqrt{2(\alpha_T^H v + D_0)}}{\sqrt{v_1^2+v_2^2}} \\[3mm] \dfrac{v_3}{v}\sqrt{2(\alpha_L v + D_0)} & \sqrt{2\dfrac{v_1^2+v_2^2}{v^2}(\alpha_T v + D_0)} & 0 \end{pmatrix} \qquad \text{(Eq. 55)}$$

In summary, the particle trajectory is computed by a finite difference technique expressed in Equation 33. The first displacement term of this equation ($A_i \Delta t$) is deterministic, with A defined in Equation 39. This expression captures the movement of particles in the streamlines defined by the flow field. The term $\nabla \cdot D \Delta t$ is required to reproduce the transport equation correctly for cases in which there are gradients in velocity or dispersion coefficient. It reduces to zero for uniform flow fields and constant dispersivity. What is retained in this case is transport along the flow streamline governed by the flow field. The second term in Equation 33 is a stochastic random-walk term to simulate dispersion, with the form of the matrix B derived for an anisotropic dispersion coefficient tensor in Equation 55.

Determination of the advection portion of the deterministic term $A_i \Delta t$ requires that the velocity at the particle location be determined. In this version of the code FEHM (V 2.20 STN: 10086-2.0-00) [161725], the method is restricted to orthogonal finite-element grids. This simplification means that the control volume associated with each grid point is a brick-shaped element. Velocity interpolation within a cell is then determined quickly and easily using the velocity interpolation scheme first derived by Pollock (1988 [101466], Eq. 4a-5c). Using that scheme, the code determines, for a given particle at a given location within the cell, the time required to exit the cell and the location where it leaves. If this time is greater than the time step Δt, the particle location within the cell is computed. If the time is less than the time step Δt, the particle is forced to stop at this location and then proceed in another step within the adjoining cell. This process is repeated until the ending time Δt is reached. At the end of this time step, the term $\nabla \cdot D \Delta t$ is used to move the particle deterministically to correct for gradients in the dispersion coefficient. A differencing scheme on the finite-element grid using a trilinear interpolation analogous to the method described by LaBolle et al. (1996 [105039], pp. 587 to 588) is used to compute these terms, with the modification that the interpolated quantity is the local Darcy flux rather than the fluid velocity. This modification yields smoother results in situations such as those encountered at volcanic rock-alluvium interfaces, where local porosity can change by several orders of magnitude from a node to its neighbor. Finally, the random-walk term is applied (the final term in Equation 33) using the B matrix derived above (Equation 55).

For this method to work properly, the time step must be selected such that, on average, a particle takes several time steps within each cell. In a system with large variations in pore-water velocity due to permeability and porosity differences from cell to cell, the appropriate time step can vary greatly throughout the domain. In FEHM, this factor is accounted for by dynamically determining the characteristic time step in an approach similar to that developed by Wen and Gomez-Hernandez (1996 [130510], p. 137). In a given cell, the magnitude of the velocity in the cell is used to scale the time step. The time required to traverse the cell completely in each of the three coordinate directions is computed, and the minimum is determined. Then a user-defined parameter called the Courant factor is multiplied by this minimum time to obtain the time step for the particle within the cell. This approach ensures that several steps are taken by a particle within a cell but minimizes computational time by tailoring each time step to the characteristic velocities within the cells.

Applying the random-walk method on grids and flow fields, such as the saturated-zone flow model, it was found that the theoretically simple inclusion of the $\nabla \cdot D$ term to correct for velocity gradients may not be sufficient to account for regions with highly variable velocity fields. In short, computation of $\nabla \cdot D$ on the scale of the finite-element grid may not be sufficient to capture the magnitude of this term adequately. For example, in high-permeability zones immediately adjacent to confining units of low permeability, the gradient is not captured sufficiently accurately to prevent the artificial meandering of a small number of particles into the low-permeability region. As a result, some particles are held up for an unrealistically long time in these zones, resulting in a nonconservative tailing of the solute breakthrough curve at a downstream location. To correct this problem, a user-defined velocity-scaling parameter can be defined to prohibit particles from entering the low-velocity domain by random-walk processes. If the ratio of the velocity before and after the random-walk jump is less than this parameter, the code prohibits the jump, and the particle is returned to the original position where another jump is taken with a different set of random numbers. This simple correction serves the same purpose as the $\nabla \cdot D$ term but is more foolproof in maintaining a physically meaningful set of random-walk jumps.

To report the results of a particle-tracking simulation, two options are available. The first requires the definition of a zone consisting of a set of finite-element grid points representing a portion of the model domain where transport results are desired. For example, a "compliance boundary," which is a given distance from the repository, can be defined by listing all of the nodes in the boundary. Then the code determines the first arrival time of each particle at any node in this fence and reports the cumulative arrival time distribution for all particles. This arrival-time distribution can then be converted to a pumping-well concentration, and the resulting curve can be used as the input to the the PA analysis. Alternatively, the concentration of particles at any cell in the finite-element domain can be reported as the number of particles residing in the cell divided by the fluid mass in the cell. Concentrations computed in this way represent the in situ concentration in response to the injection of a pulse of solute at time zero. To obtain the cumulative breakthrough curve, we may perform a time integration of these results, yielding the in situ concentration breakthrough curve at the node in response to a step change in concentration. Both pulse and step response curves can be obtained in the FEHM particle-tracking code.

6.5.2.4 Matrix Diffusion in Fractured Geological Media

To incorporate the influence of sorption and matrix diffusion, the residence time transfer function (RTTF) particle-tracking method outlined in the FEHM models and methods document (Zyvoloski et al. 1997 [110491], pp. 41 to 42) has been adapted to the particle-tracking algorithm. In this method, adjustments to the travel time of a particle are made to account for the influence of physicochemical processes such as sorption and matrix diffusion. During its path along a streamline, the particle travel time is governed by a transfer function describing the probability of the particle spending a given length of time on that portion of its path. For a cumulative probability distribution function of particle residence times, the travel time of a particle along this portion of its path is computed by generating a random number between 0 and 1 and determining the corresponding residence time. On average, if a large number of particles travel through this portion of the model domain, the cumulative residence time distribution of particles will reproduce the shape of the transfer function. The form of the transfer function is

derived from an analytical or numerical solution to capture the appropriate processes being considered. A suite of type curves were generated for numerically implementing the transfer function.

6.5.2.4.1 Mathematical Description of Matrix Diffusion and Sorption

In this particle-tracking algorithm, the schematic model depicted in Figure 6.5-1 is used to provide a transfer function for the case of fracture flow and diffusion between equally spaced fractures. In this model:

z is the spatial coordinate along the fracture
t is the time
$2b$ is the fracture aperture
2 is the mean fracture spacing
v is the linear groundwater velocity in the fracture
θ is the porosity of the matrix
q is the diffusive flux from fracture to matrix
k_d is the distribution coefficient in the fracture
k_d' is the distribution coefficient in the matrix
R' is the retardation factor in the matrix
R is the retardation factor in the fracture
ρ_b is the bulk density of the matrix
ρ_w is the density of water
D' is the matrix effective diffusion coefficient
D is the dispersion coefficient in the fracture
c is the concentration at z along the fracture
c_0 is the source concentration at $z = z_0$.
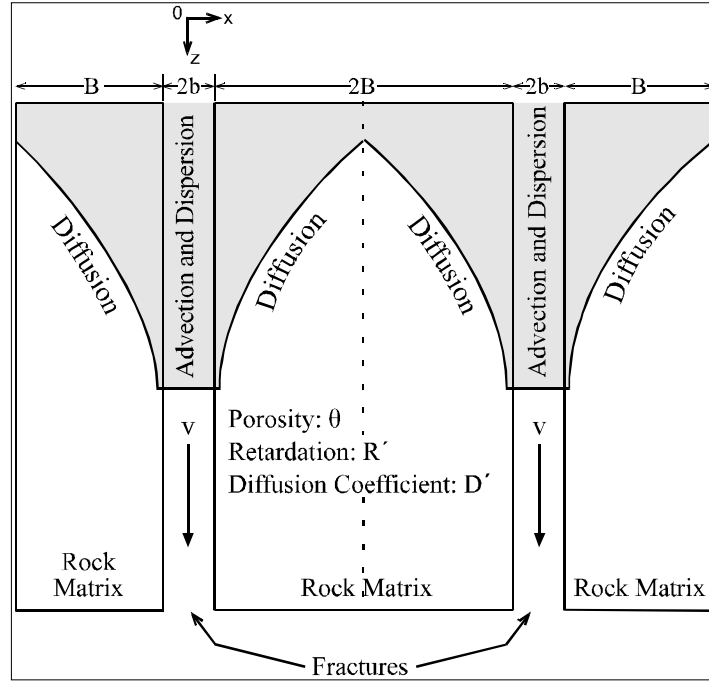
Figure 6.5-1. Schematic of the Matrix Diffusion Submodel

The equations describing the radionuclide transport in the fractures are (Robinson 1994 [101154], p. 81, Equations 1 and 2):

$$\frac{\partial c}{\partial t} + \frac{v}{R}\frac{\partial c}{\partial z} - \frac{D}{R}\frac{\partial^2 c}{\partial z^2} + \frac{q}{bR} = 0 \qquad \text{(Eq. 56a)}$$

and in the matrix:

$$\frac{\partial c}{\partial t} - \frac{D'}{R'}\frac{\partial^2 c}{\partial x^2} = 0 \qquad \text{(Eq. 56b)}$$

The distribution coefficient and the retardation factor are related by (Freeze and Cherry 1979 [101173], p. 404, Equation 9.14):

$$R = 1 + \frac{\rho_b}{\theta \cdot \rho_w} k_d \qquad \text{(Eq. 57)}$$

The transient solution for contaminant transport with $D = 0$ in parallel fractures, for $c = c_0$ at the inlet end with $z = 0$, and $\partial c / \partial x = 0$ at the center line between the fractures at $x = B$ (Figure 6.5-1) is given by (Sudicky and Frind 1982 [105043], p. 1637, Eq.28):

$$\frac{c}{c_0} = 0, T^0 \leq 0 \qquad \text{(Eq. 58)}$$

$$\frac{c}{c_0} = \frac{1}{\pi} \exp\left(\frac{R\lambda z}{v}\right) \int_0^\infty \frac{\varepsilon}{\lambda^2 + \varepsilon^4/4} \exp(\varepsilon_R^{\,0}) \left[\exp(-\lambda T^0) \left\{ \frac{\varepsilon^2}{2} \sin(\varepsilon_I^{\,0}) - \lambda \cos(\varepsilon_I^{\,0}) \right\} \right.$$

$$\left. + \frac{\varepsilon^2}{2} \sin(\Omega_I^{\,0}) + \lambda \cos(\Omega_I^{\,0}) \right] d\varepsilon, \quad T^0 > 0 \tag{Eq. 59}$$

where λ is a first-order decay constant, ε is an integration variable, and

$$T^0 = t - \frac{Rz}{v} \tag{Eq. 60}$$

$$\varepsilon_R^{\,0} = -\frac{\omega\varepsilon}{2}\left(\frac{\sinh(\sigma\varepsilon) - \sin(\sigma\varepsilon)}{\cosh(\sigma\varepsilon) + \cos(\sigma\varepsilon)}\right) \tag{Eq. 61}$$

$$\varepsilon_I^{\,0} = \frac{\varepsilon^2 T^0}{2} - \frac{\omega\varepsilon}{2}\left(\frac{\sinh(\sigma\varepsilon) + \sin(\sigma\varepsilon)}{\cosh(\sigma\varepsilon) + \cos(\sigma\varepsilon)}\right) \tag{Eq. 62}$$

$$\Omega_I^{\,0} = \frac{\omega\varepsilon}{2}\left(\frac{\sinh(\sigma\varepsilon) + \sin(\sigma\varepsilon)}{\cosh(\sigma\varepsilon) + \cos(\sigma\varepsilon)}\right) \tag{Eq. 63}$$

with

$$\omega = \frac{\theta(R'D')^{1/2}z}{bv} \tag{Eq. 64}$$

$$\sigma = (R'/D')^{1/2}(B - b) \tag{Eq. 65}$$

Using the transformation variables:

$$\tau_0 = \frac{z}{v} \tag{Eq. 66}$$

$$\varepsilon_1 = \varepsilon\tau_0^{1/2} \tag{Eq. 67}$$

Equations 58 through 67 can be rewritten as:

$$\frac{c}{c_0} = 0,\ T_1^{\,0} \le 0 \tag{Eq. 68}$$

$$\frac{c}{c_0} = \frac{1}{\pi} \exp(R\lambda\tau_0) \int_0^\infty \frac{\varepsilon_1}{\lambda^2\tau_0^2 + \varepsilon_1^4/4} \exp(\varepsilon_R^{\,0}) \left[\exp(-\lambda\tau_0 T_1^{\,0}) \left\{ \frac{\varepsilon_1^2}{2} \sin(\varepsilon_I^{\,0}) - \lambda\tau_0 \cos(\varepsilon_I^{\,0}) \right\} \right.$$

$$\left. + \frac{\varepsilon_1^2}{2} \sin(\Omega_I^{\,0}) + \lambda\tau_0 \cos(\Omega_I^{\,0}) \right] d\varepsilon_1, \quad T_1^{\,0} > 0 \tag{Eq. 69}$$

where

$$T_1^0 = \frac{t}{\tau_0} - R \qquad \text{(Eq. 70)}$$

$$\varepsilon_R{}^0 = -\frac{\omega_1 \varepsilon_1}{2}\left(\frac{\sinh(\sigma_1 \varepsilon_1) - \sin(\sigma_1 \varepsilon_1)}{\cosh(\sigma_1 \varepsilon_1) + \cos(\sigma_1 \varepsilon_1)}\right) \qquad \text{(Eq. 71)}$$

$$\varepsilon_I{}^0 = \frac{\varepsilon_1^2 T_1^0}{2} - \frac{\omega_1 \varepsilon_1}{2}\left(\frac{\sinh(\sigma_1 \varepsilon_1) + \sin(\sigma_1 \varepsilon_1)}{\cosh(\sigma_1 \varepsilon_1) + \cos(\sigma_1 \varepsilon_1)}\right) \qquad \text{(Eq. 72)}$$

$$\Omega_I{}^0 = \frac{\omega_1 \varepsilon_1}{2}\left(\frac{\sinh(\sigma_1 \varepsilon_1) + \sin(\sigma_1 \varepsilon_1)}{\cosh(\sigma_1 \varepsilon_1) + \cos(\sigma_1 \varepsilon_1)}\right) \qquad \text{(Eq. 73)}$$

with

$$\omega_1 = \frac{\theta(R' D' \tau_0)^{1/2}}{b} \qquad \text{(Eq. 74)}$$

$$\sigma_1 = \left(\frac{R'}{D' \tau_0}\right)^{1/2}(B - b) \qquad \text{(Eq. 75)}$$

For the case of no radioactive decay ($\lambda = 0$):

$$\frac{c}{c_0} = \frac{1}{\pi}\int_0^\infty \frac{2}{\varepsilon_1}\exp(\varepsilon_R{}^0)\left[\sin(\varepsilon_I{}^0) + \sin(\Omega_I{}^0)\right]d\varepsilon_1 \qquad \text{(Eq. 76)}$$

Therefore, to implement this model, the algorithm requires the input of transport parameters defined in Equations 74 and 75. With the transport parameters and the unretarded travel time τ_0 within a given portion of the path known from the advection part of the particle, values of ω_1 and σ_1 are computed, thereby fully defining the transfer function for this portion of the particle's travel path. Given these parameters, the model returns a value of the delayed travel time of the particle from Equation 70 that is consistent with the matrix diffusion model. To implement this model in FEHM, a series of type curves were generated (Output DTN: LA0302RP831228.001) at specified values of ω_1 and σ_1 using a code FRACT_p V1.0 (STN: 11009-1.0-00; LANL 2003 [164509]). For given values of the parameters, the code performs a linear interpolation between the nearest type curves to obtain the result. This approach of tabulating the results of the analytical solution is much more computationally efficient than computing the values through integration at run time. Under limiting conditions of low diffusion and/or large fracture spacing, the infinite spacing solution of Tang et al. (1981 [101160], p. 559, Eq.35) implemented in the cell-based particle-tracking algorithm of FEHM can be used instead of the finite spacing model. A provision in the code allows the Tang solution to be invoked in this particle-tracking model as well, but it should be used only when the characteristic diffusion time to the centerline between the fractures (of order B^2/D') is much greater than the time of the simulation.

The final step of the model development is to integrate the matrix diffusion model with the random-walk transport model developed in Section 6.5.2.3. Specifically, the time intervals over which the time delays are applied must be set in a manner that allows for computationally efficient and accurate solutions to be obtained. In this model, the time delay is applied to a particle at the time at which it exits a cell, after having determined the cumulative time the particle spent in advective transport through the cell. Within a cell, the transport properties of diffusion and sorption are, by definition, uniform, so that a unique set of transport dimensionless parameters can be defined. Alternatively, the time delay could be applied at each segment of the particle path, resulting in potentially many time delays for a particle within each cell as it is transported by advection and random-walk dispersion. However, in initial prototype testing using this approach, it was determined that the technique, although theoretically equivalent to the application of time delay once per cell, showed that practical limitations of reduced accuracy and reduced computational efficiency resulted. Therefore, the code was developed with the time delay applied only at the time the particle exits the cell, which can occur either by advection or by random-walk dispersion.

To apply the time delay, the particle is held at that location until the time of the simulation run catches up to the time of that particle, after which the particle is allowed to resume its transport. Finally, it is noted that for sorption without matrix diffusion, the time delay is computed deterministically by computing a retardation factor based on the sorption coefficient K_d, but otherwise, the method is identical to the matrix-diffusion method. Alternatively, this particular case could have been handled through a simple adjustment of the transport velocity, but the implementation using the time-delay method was simpler because it is consistent with the matrix-diffusion method just described.

6.5.2.5   Mathematical Description of Sorptive Transport in Alluvium

Equation 1 for advective-dispersive transport can be generalized to include sorption onto the rock surfaces as follows (Freeze and Cherry 1979 [101173], Equations 9.9 and A10.14):

$$\frac{\partial C}{\partial t} + \nabla \cdot (\vec{v}C) - \nabla \cdot (D\nabla C) = \frac{\rho_b}{\rho_w \theta} \frac{\partial S}{\partial t} \qquad \text{(Eq. 77)}$$

where S is the mass of the transported species adsorbed on the solid per unit bulk dry mass of the porous medium. For linear, reversible, equilibrium sorption, the K_d model can be used, and S and C are related as follows (Freeze and Cherry 1979 [101173], Equation 9.12):

$$S = K_d C \qquad \text{(Eq. 78)}$$

6.5.2.6   Colloid-Facilitated Transport

Radionuclides can attach to the colloids either reversibly or irreversibly. The radionuclides that are attached to the colloids reversibly are partitioned between the colloids and the aqueous phase. On the other hand, the radionuclides that are irreversibly attached to the colloids stay attached to the particles for the entire duration of the transit through the SZ to the compliance boundary. The

colloid-facilitated transport of the radionuclides follows different mechanisms for the two different types of attachments, which are summarized in Table 6.5-1 and described below.

Table 6.5-1. Colloid-Facilitated Transport of Radionuclides

Radionuclides Attached Reversibly to Colloids	Radionuclides Attached Irreversibly to Colloids (transport in a manner identical to colloids)	
Radionuclides spend part of the time attached to the colloids and part of the time in the aqueous phase.	Radionuclides are embedded in the colloids, mostly those derived from the waste form degradation. This is discussed in BSC (2003 [162729], Section 6.6). The radionuclides travel in a manner identical to the colloids themselves.	
	Normal	**Fast**
Radionuclides are treated in the SZ transport model using equations similar to those for aqueous phase transport (Attachment II) but with modified parameters. The diffusion coefficient in volcanics is reduced with respect to that for aqueous transport. This is given by Eq. 80a in Section 6.5.2.6. The equation is derived in BSC (2003 [164870], Section 6.5.1.1). The sorption coefficient is modified and given in Eq. 81, Section 6.5.2.6 and derived in BSC (2003 [164870] Section 6.5.1.1). K_c needed in Eq. 80a and 81 is given in Eq. 80b. The groundwater concentration of colloids and the sorption coefficient onto colloids are summarized in Table 4-2 and taken from BSC (2003 [161620], Table 5). Section 7.1.2.5.2 gives confidence-building arguments for this process based on laboratory data and theoretical considerations from literature. The transport of these radionuclides is simulated in the SZ transport model using the same approach as the aqueous species but with modified diffusion coefficient and K_d as described above.	The colloids undergo "reversible filtration." This is discussed in BSC (2003 [162729], Section 6.4) where field and laboratory data are analyzed to get "attachment rate constants" and "detachment rate constants." These lead to a retardation factor for the colloids (Eq. 79). The same retardation factor applies to the fraction of radionuclides absorbed irreversibly onto colloids. The range of values for this fraction is given in BSC (2003 [161620], Table 10). Section 7.1.2.5.1 gives confidence-building arguments for "colloid filtration" based on C-wells data. The transport of these radionuclides is simulated in the SZ transport model using the same approach as the aqueous species but with zero diffusion coefficient and colloid retardation factor as explained above.	A small fraction of colloids travels with the groundwater without any retardation. The radionuclides sorbed onto this fraction also travel without any retardation. The travel times for this fraction are the same as those for non-sorbing radionuclides. The range of values of this fraction is given in Table 4-2 and discussed in BSC (2003 [161620], Table 10). Section 7.1.1.1.3 gives confidence-building arguments for the occurrence of this process based on Nevada Test Site (NTS) data. The breakthrough curves for these radionuclides are identical to those without sorption.

6.5.2.6.1 Radionuclides Attached Irreversibly to the Colloids

These radionuclides are embedded in the colloids and travel in a manner identical to the colloids themselves. The majority of the colloid particles undergo filtration during transport through the SZ, however a small fraction travels along with the movement of the bulk water without any retardation. The transport of colloid particles is included in the SZ transport model using the process of reversible filtration (BSC 2003 [162729] Sections 6.4.1 and 6.5.2). The transport of the colloids is simulated using the advection-dispersion equation, and colloids are taken not to diffuse. Filtration of the colloids can be described by a retardation factor, R_{col}. In this analysis filtration is defined as the net effect of chemical sorption of the colloid onto the rock surface and the physical removal of colloids from the advective flow due to sieving and settling. The value of R_{col} is dependent on several factors such as colloid size, colloid type, and geochemical conditions (e.g., pH, Eh, and ionic strength) (BSC 2003 [162729], Section 6.3). These factors are folded into the distribution of R_{col} that has been developed from field and experimental data collected under varying geochemical conditions with different colloid types and sizes (BSC 2003 [162729], Tables 7 and 8). Attachment rate constants, k_{att}, and detachment rate constants, k_{det}, of colloids to the rock matrix have been measured, and R_{col} distributions have been developed for the fractured volcanics and for the alluvium. The relationship between R_{col}, k_{att}, and k_{det} is given by:

$$R_{col} = 1 + \frac{k_{att}}{k_{det}}$$

(Eq. 79)

The attachment rate constant is also used to determine the fraction of the colloids that transport with no retardation. Specifically, colloids for which one over the attachment rate constant is smaller than the travel time through the system will transport with no retardation. The fraction of colloids that transport unretarded is documented in BSC (2003 [162729], Table 9).

6.5.2.6.2   Radionuclides Attached Reversibly to the Colloids

Radionuclides cannot diffuse into the matrix while attached to colloids because the colloid particles themselves cannot diffuse into the matrix (Section 6.3). Hence, the fraction of radionuclides that are attached irreversibly onto colloids does not experience any matrix diffusion and is transported at the same rate as the colloid particles. The fraction of radionuclides that are reversibly attached onto the colloids experiences a reduction in the diffusion process because this fraction can diffuse into the matrix only while unattached to the colloids. In the volcanics, this is implemented through a reduction in the effective diffusion coefficient for the radionuclide, given by the following equation (BSC 2003 [164870], Section 6.5.1.1):

$$D_e^{adjusted} = \frac{D_e}{\left(1 + k_c\right)^2}$$

(Eq. 80a)

where

$D_e^{adjusted}$ is the effective diffusion coefficient of the radionuclide adjusted for the effect of reversible attachment to colloids,

D_e is the effective diffusion coefficient of the radionuclide in the matrix, and

k_c is the distribution parameter expressing the relative amount of radionuclide residing on the colloids with respect to that in the aqueous phase, given by (Attachment II of this report):

$$k_c = C_c * k_{d-c} \qquad \text{(Eq. 80b)}$$

where

C_c is the colloid concentration in the groundwater, and

k_{d-c} is the sorption coefficient for the radionuclide onto the colloids.

In the alluvium, diffusion is not an issue; however, the sorption coefficient for the radionuclide onto the rock surface is modified due to the competition with the colloids as follows (BSC 2003 [164870], Section 6.5.1.1):

$$k_d^{new} = \frac{k_d^{original}}{\left(1 + k_c\right)} \qquad \text{(Eq. 81)}$$

where

$k_d^{original}$ is the sorption coefficient for the radionuclide in the alluvium in the absence of colloids, and

k_d^{new} is the sorption coefficient for the radionuclide in the alluvium in the presence of reversible attachment to colloids.

6.5.3   Base-Case Model Inputs

The base-case flow model (BSC 2003 [162649], Section 6.6; DTN: LA0304TM831231.002 [163788]) was used directly as an input to the base-case transport model. The flow model provides the numerical grid with geometric coefficients and the groundwater flow velocity field, which are used by the transport model. Modifications were made to the input file to include base-case transport parameter values. These modifications do not impact the results of the flow calculations. The parameters modified are rock bulk density, rock bulk porosity, effective porosity in alluvium, flowing-interval porosity, matrix porosity in volcanics, effective diffusion coefficient in the volcanic matrix, and flowing-interval spacing in volcanics and alluvium. Table 6.5-2 provides a list of input parameters for the base-case transport model. This table gives the parameter name, its description and intended use, base-case value, type of uncertainty and the source DTN. Additional parameters that are not included in the base-case model but are needed for the abstractions analysis and subsequent feed to TSPA (BSC 2003 [164870]) are listed in Table 6.5-3. The values of all of these parameters involve uncertainties. For each parameter, the rationale for the selection of the range of value, probability distribution, and expected value is summarized in Section 4.1.2 and details are given in Attachment I and in BSC (2003 [164870] Section 6.5.2). The transport base case reported in this section focuses on providing, as output, a single case of the transport model calculations. The ranges of input uncertainties are listed in Table 4-2. For most parameters, the base-case value was chosen to be the median of the

uncertainty distribution, except for the sorption coefficient, which was assigned a value of 0 for the base case, which leads to faster transit times for the base case than the stochastic simulations. The propagation of the uncertainties to the output breakthrough curves (Output DTN: LA0309SK831231.001) is documented in Section 8.

Table 6.5-2. Base-Case Model Inputs

Input Name (name of the variable in the FEHM V 2.20 code)	Input Description and Intended Use	Base-Case Value	Units	Type of Uncertainty	Source/DTN
DENRD in the control statement "rock"	Bulk density in alluvium needed for retardation calculations in Equations 76 and 77.	1910	kg/m^3	Epistemic [a]	BSC (2003 [164870]) SN0306T0502103.007 [163946]
K_d in the control statement "sptr"	Sorption coefficient in alluvium needed for retardation calculations in Equations 77 and 78.	0.0	mL/g	Epistemic	Attachment I. Output DTN: LA0310AM831341.002
PSD in the control statement "rock," fraction	Effective porosity in the alluvium needed for converting Darcy flux to fluid velocity and retardation calculations in Equations 77 and 78.	0.18	-	Epistemic	BSC (2003 [164870]) SN0306T0502103.007 [163946]
Enters indirectly via the Flowing Interval Aperture through the relation, fraction [b] Porosity = (Aperture/Spacing)	Flowing interval porosity needed for converting Darcy flux to fluid velocity and retardation calculations in Equations 56a and 56b.	0.01	-	Epistemic	BSC (2003 [164870])
Enters indirectly via the Flowing Interval Aperture through the relation [b] Porosity = (Aperture/Spacing)	Flowing interval spacing needed for converting Darcy flux to fluid velocity and retardation calculations in Equations 56a and 56b.	20	m	Epistemic	SN0306T0502103.007 [163946]
APERTURE in the control statement "sptr" [b]	Flowing interval aperture needed for converting Darcy flux to fluid velocity and retardation calculations in Equations 56a and 56b.	0.2	m	Epistemic	Obtained as the product of flowing interval porosity and flowing interval spacing given this table.
POR_MATRIX in the control statement "sptr," fraction	Matrix porosity in volcanics, needed for diffusion and retardation calculations in Equations 56b and 57.	0.15 – 0.25	-	Epistemic	BSC (2003 [164870]) SN0306T0502103.007 [163946]
DIFM in the control statement "sptr"	Effective diffusion coefficient in volcanics, needed for diffusion calculations in Equation 57b.	5.0x10^{-11}	m^2/s	Epistemic	BSC (2003 [164870]) SN0306T0502103.007 [163946]

Table 6.5-2 (continued). Base-Case Model Inputs

Input Name (name of the variable in the FEHM V 2.20 code)	Input Description and Intended Use	Base-Case Value	Units	Type of Uncertainty	Source/DTN
K_d in the control statement "sptr"	Matrix sorption coefficient in volcanics, needed for retardation calculations in Equation 56a and 57.	0.0	mL/g	Epistemic	Output DTN: LA0310AM831341.002
AL in the control statement "sptr"	Dispersivity, longitudinal, needed for dispersion calculations in Equation 1 and 56a.	10.0	m	Epistemic	Section 4.1.2.16
ATH in the control statement "sptr"	Dispersivity, transverse, horizontal, needed for dispersion calculations in Equation 1.	0.05	m	Epistemic	Section 4.1.2.17
ATV in the control statement "sptr"	Dispersivity, transverse, vertical, needed for dispersion calculations in Equation 1.	0.0005	m	Epistemic	Section 4.1.2.18

Source: Output DTN: LA0306SK831231.001

[a] Epistemic uncertainty is defined as uncertainty in the parameter space of a conceptual model for which some knowledge is obtainable (BSC 2002 [158794], Section 4.1.1).

[b] Input listed in Table 4-2 for flowing-interval porosity was multiplied by flowing interval spacing to obtain flowing interval aperture.

Table 6.5-3. Additional Parameters Needed for Abstraction Analysis

Input Name (variable name and the control statement where it appears in the FEHM V 2.20 code)	Input Description	Base Case Value(s)	Units	Type of Uncertainty	Source/DTN
Multiplying factor[a] for SKD in control statement "flow"	Specific discharge multiplication factor	1	-	Stochastic	BSC (2003 [164870]) SN0306T0502103.007 [163946]
SCALEX, SCALEY in control statement "fper," ratio	Permeability horizontal anisotropy	4.2	-	Stochastic	SN0306T0502103.007 [163946]
RD_FRAC in the control statement "sptr," ratio	Colloid retardation factor in volcanics for irreversible colloids	0	-	Epistemic	Table 4-2
Needed in Equations 79 and 80 for calculating the relative concentration of radionuclide on colloids, needed for colloid facilitated reversible transport	Groundwater concentration of colloids	0	g/mL	Epistemic	Table 4-2
Needed in Equations 79 and 80 for calculating the relative concentration of radionuclide on colloids, needed for colloid facilitated reversible transport	Sorption coefficient onto colloids	0	mL/g	Epistemic	Table 4-2
In TSPA calculations, used for post processing the breakthrough curves generated by the transport model, fraction	Fraction of colloids transported unretarded	0.0005[b]	-	Epistemic	BSC 2003 ([162729], Section 6.6)
Used for calculating colloid sorption coefficient using Equation 57, which is in turn input as the variable K_d in the control statement "sptr," ratio	Colloid retardation factor in alluvium for irreversible colloids	0	-	Epistemic	Table 4-2

[a] Base-case permeabilities and recharge and boundary fluxes are multiplied by this factor to vary specific discharge without affecting the flow calibration.

[b] This value is different from the base case value given in Table 4-2. This parameter does not enter the base case transport model directly. It is used in TSPA calculations for post-processing the breakthrough curves output from this report.

6.6   BASE-CASE MODEL RESULTS

The base case model results (Output DTN: LA0306SK831231.001) are discussed in this section. The conceptual and mathematical model described in Sections 6.3 and 6.5 of this report was implemented in the numerical code FEHM V 2.20 (STN: 10086-2.20-00) [161725]. The FEHM V 2.20 application is based on a finite-volume/finite-element heat- and mass-transfer code that simulates non-isothermal, multiphase, multi-component flow and solute transport in porous media. The details of this code, its usage and verification example are given in the *Validation Test Plan (VTP) for the FEHM Application Version 2.20* (LANL 2003 [164150]). The calibrated base-case SZ site-scale flow model (DTN: LA0304TM831231.002 [163788]), which is described in detail in the SZ flow model report (BSC 2003 [162649]), was used as the starting input.

The purpose of this model report is to provide a base-case model to be used as the starting point for the SZ abstractions model (BSC 2003 [164870], Section 6.3) for use in the TSPA calculations to assess various exposure scenarios. For this purpose, a single base-case transport model is presented here along with its outputs. The propagations of uncertainties in the input parameters to the output breakthrough curves are presented in Section 8 by documenting the breakthrough curves at the 18-km compliance boundary (10 CFR 63.302 [156605]) for minimum and maximum values of the various parameters. The barrier capabilities of the SZ transport are presented in Section 6.7 of this report, where the influence of key parameters on the radionuclide breakthrough is discussed.

The input transport parameter values and the sources for these values for the base-case model are given in Table 6.5-2. Particle source locations were chosen to cover the anticipated repository footprint at the water table. Calculations were performed for an instantaneous release of particles at the source location. The breakthrough curve at the 18-km compliance boundary was calculated by starting 1000 particles distributed over the repository footprint and by outputting the cumulative number of particles crossing an east-west vertical plane across the entire width and depth of the model. Output of this model is shown in Figure 6.6-1 where normalized cumulative mass is plotted on the *y*-axis and the time in years on the log scale on the *x*-axis.
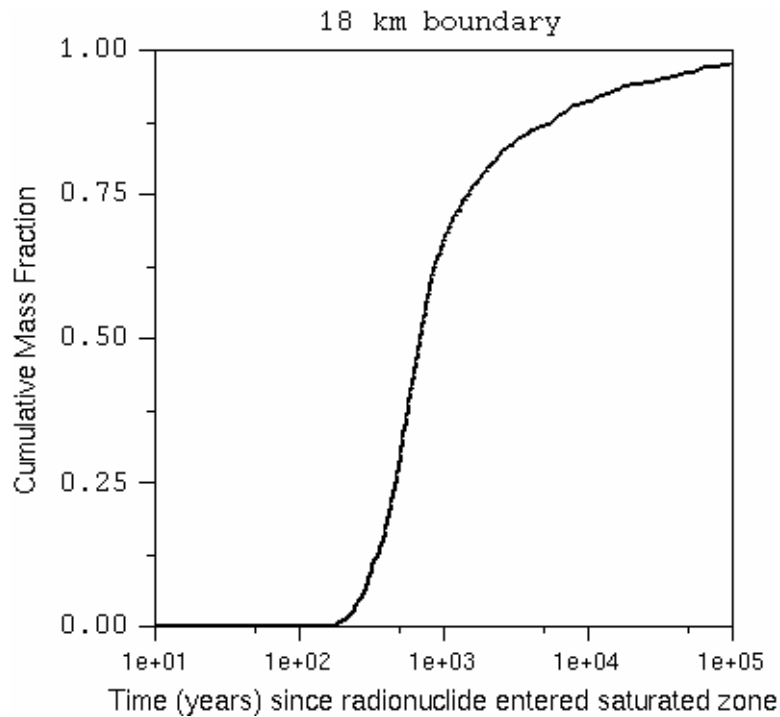
18 km boundary

Output DTN: LA0306SK831231.001

Figure 6.6-1. Breakthrough Curve at the 18-km Boundary for the Transport Base Case

The breakthrough curve plotted in Figure 6.6-1 corresponds to a breakthrough time at 50% concentration of 705 years. A similar model calculation was performed where the number of input tracer particles was changed (from 1000 in the base case) to nine particles spread over the repository footprint, and the output option was changed to produce detailed particle tracks as they moved from the source location to the 18-km compliance boundary. These are plotted against a shaded relief map of the SZ site scale model area in Figure 6.6-2. Note that there is very minimal transverse spreading of the flow paths due to the small value of transverse dispersivities (Table 6.5-2). The flow paths in Figure 6.6-2 appear to converge towards the southern portion of the model due to the large-scale heterogeneities that are explicitly included in the hydrologic framework model (BSC 2003 [162649], Table 6.5-4).
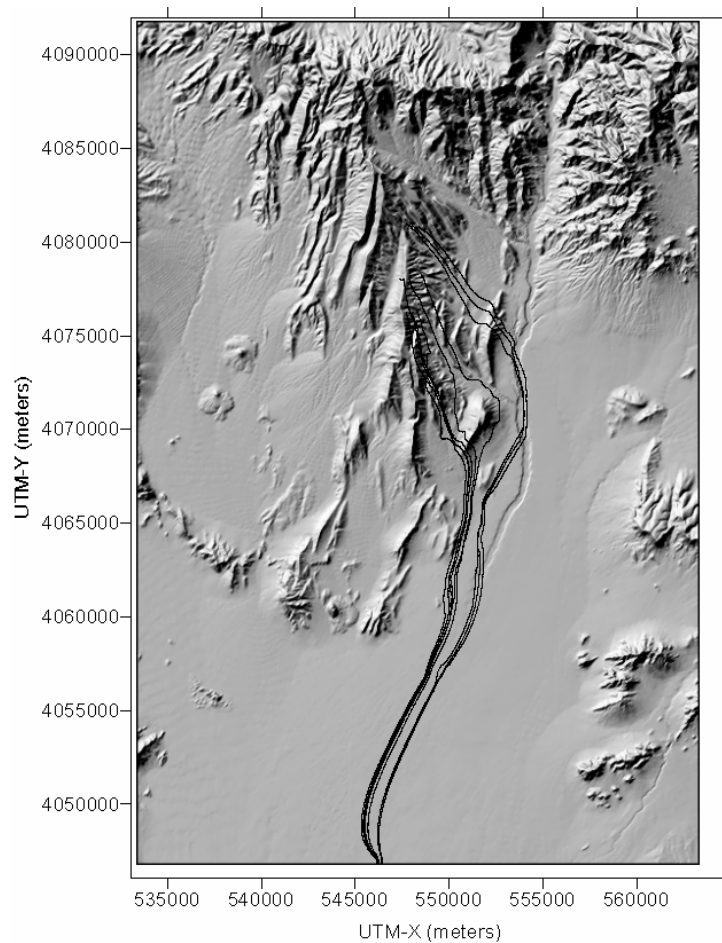
Figure 6.6-2. Particle Tracks Resulting from the Base-Case Transport Model

6.7 BARRIER CAPABILITY

6.7.1 Introduction

This section presents transport model calculations designed to illustrate the function of the saturated zone barrier. These simulations explore in greater detail some of the key aspects of the system, important uncertain model parameters, physical properties, and boundaries to illustrate the functioning of the saturated zone as a barrier to radionuclide migration. Combined with the validation section (Section 7) and the analysis of model uncertainties (Section 8.3), this section describes the technical basis for the saturated-zone barrier in the context of the Yucca Mountain waste disposal system.

In its simplest form, the saturated zone performs two functions in its role as a barrier to radionuclide migration: (1) it delays the transport of radionuclides from beneath the proposed repository to the compliance boundary, and (2) it attenuates the concentration of radionuclides in the mobile water. By examining the processes of matrix diffusion, advection, and dispersion for

various ranges of parameters, the role of various processes on the delay and dilution of radionuclides is presented. Also presented are intermediate breakthrough curves at the contact between the fractured volcanic tuffs and the alluvium to assess the relative importance of the two key hydrostratigraphic rock types. Because all parameters are estimated rather than known with certainty, a few key parameters in this section are varied to complement the results from Section 8.3. Finally, transport simulations for the fraction of radionuclides bound to colloids are also examined because of the importance of this process to radionuclide transport predictions in the saturated zone.

The base-case simulation is presented in Section 6.6 of this report. This case serves as a reference point for exploring the role of processes and features of the system in subsequent simulations. The solid black curve in Figure 6.7-1a shows the breakthrough curve at the 18 km boundary, which can also be thought of as an arrival time distribution for transport through the saturated zone. The base-case simulation (solid black curve) is the breakthrough curve for a conservative, nonsorbing radionuclide in the absence of radioactive decay. Breakthrough times on the order of hundreds of years are predicted for the bulk of the mass arriving at the water table, with travel times extending into the thousands of years for the slowest moving 20% of the mass (Figure 6.7-1b is discussed below).
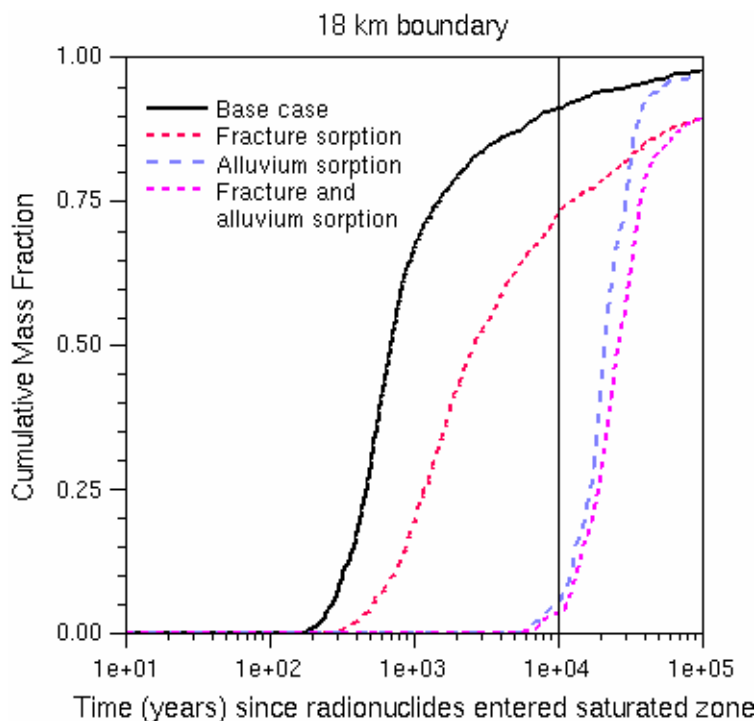
Output DTN: LA0307ZD831231.001

Figure 6.7-1a. Breakthrough Curves for the Base Case, Conservative Radionuclides and Sorbing Radionuclides: 18-km Boundary
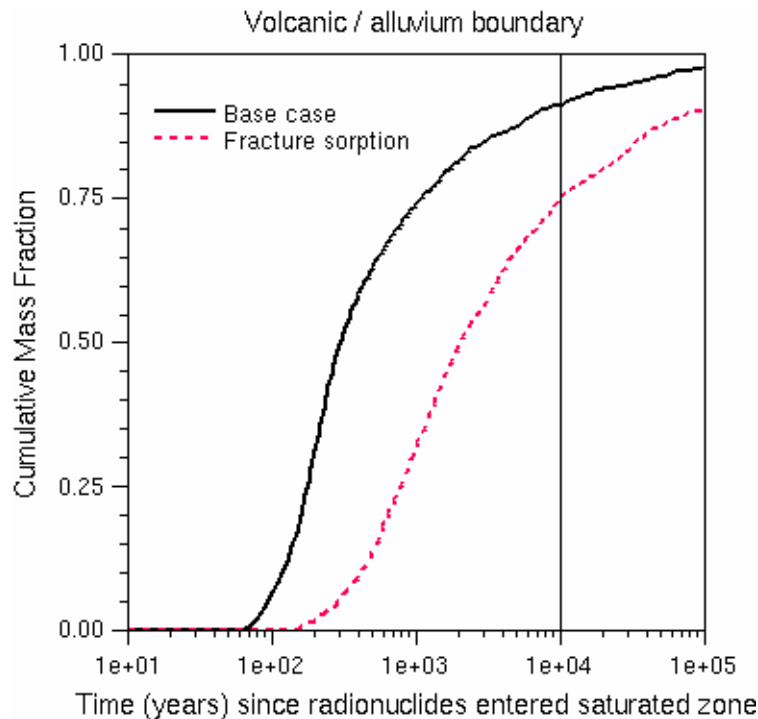
Volcanic / alluvium boundary

Figure 6.7-1b. Breakthrough Curves for the Base Case, Conservative Radionuclides and Sorbing Radionuclides: Volcanic/Alluvium Boundary

6.7.2   Saturated Zone Subsystem Performance: Saturation in Volcanics and Alluvium

Most radionuclides are expected to sorb to the rock, which should delay their arrival at the compliance boundary. Figure 6.7-1a also shows several simulations of sorbing radionuclides. The curve labeled "Fracture sorption" allows sorption in the fracture continuum of the volcanic tuffs and reflects a small matrix sorption coefficient of 1.3 mL/g. Including only this process yields a breakthrough curve similar to the base case breakthrough curve but with significantly delayed travel times. A fracture retardation factor of 1.5 is used, which is a relatively small value meant to represent a weakly sorbing radionuclide. The final two curves in the figure show the influence of sorption in the alluvium (either with or without sorption in the fractured volcanics). Travel times largely in excess of 10,000 years are predicted in the saturated zone alone for a sorption coefficient of 6.3 mL/g, meant to fall in the range of K_d values for weakly sorbing radionuclides such as neptunium. It is seen from these curves that sorption in the alluvium can increase the transport time by orders of magnitude of even the weakly sorbing radionuclides such as neptunium. Thus for the base case SZ transport model with the inclusion of sorption in the alluvium, these results demonstrate that the saturated-zone barrier provides a travel time delay on the order of the regulatory time scale of interest for the repository for all but the conservative or very weakly sorbing radionuclides.

6.7.3 Saturated-Zone Subsystem Performance: Fractured Volcanic Tuffs and Alluvium

To illustrate in more detail the function of the saturated zone, breakthrough curves were computed at an intermediate location in the model at a boundary defined by the transition from fractured volcanic tuffs to alluvium. Figure 6.7-1b shows breakthrough curves for the base case and fracture sorption scenarios at the volcanic/alluvium boundary, which is approximately 10 km south of the southern boundary of the repository footprint. Comparing these simulations to the equivalent curves in Figure 6.7-1a, it is observed that the early parts of the breakthrough curves differ from each other, but the latter parts are very close to each other. This shows that alluvium plays a significant role for short transport times. By contrast, the tails of the breakthrough curves are due primarily to transport through fractures and matrix diffusion. Therefore, while the fractured volcanic tuffs are expected to provide significant delay for a fraction of the mass, the fastest moving portion of a radionuclide is controlled by transport through the alluvium. The reason for this result is that alluvium transport is expected to be characterized by continuum flow and transport through the bulk medium, in contrast to the fracture transport expected in the volcanics. Finally, based on the fracture sorption breakthrough curve in Figure 6.7-1b, sorption in the fractured tuffs is expected to provide significant travel-time delays, even without considering the subsequent transport through the alluvium.

6.7.4 Saturated-Zone Sensitivity Analyses: Advection, Diffusion, and Dispersion

The processes of advection, dispersion, and diffusion into the rock matrix all play key roles in the prediction of saturated-zone barrier performance. In this section, the importance of these processes is illustrated by examining breakthrough curves for a variety of scenarios in which one or more parameters are changed to isolate a particular process. These results are presented in the context of saturated-zone transport barrier performance, focusing on results relevant to the arrival times and dispersion of radionuclides. Figures 6.7-2a (18-km boundary) and 6.7-2b (volcanic/alluvium contact) show the breakthrough curves for a conservative radionuclide for the base case, a case with matrix diffusion but no hydrodynamic dispersion (referred to hereafter simply as diffusion and dispersion, respectively), and a case with dispersion but no diffusion. Both diffusion and dispersion result in the spreading of breakthrough curves at the 18-km boundary (or the volcanic/alluvium contact). The implication for radionuclide dilution is that any sharp pulse of high concentration reaching the saturated zone would be attenuated due to diffusion and dispersion by the time that mass reached the compliance boundary. Additional discussion of this point is provided in Section 6.7.6.
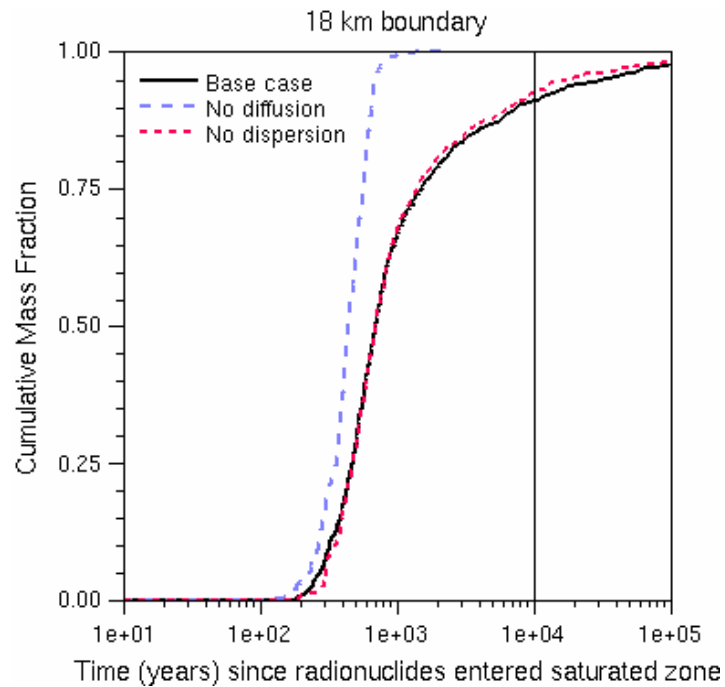
Output DTN: LA0307ZD831231.001

Figure 6.7-2a. Breakthrough Curves Comparing the Base Case, Nondispersive, and Nondiffusive Cases: 18-km Boundary
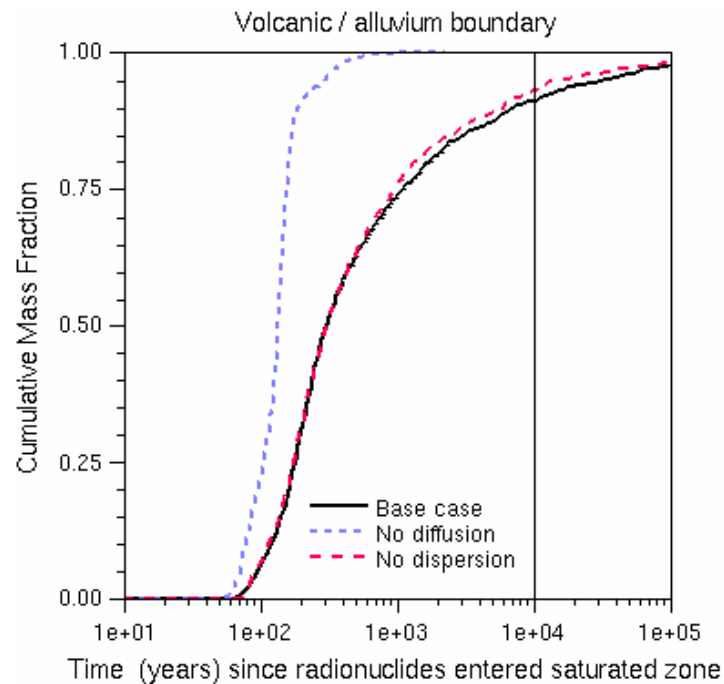
Output DTN: LA0307ZD831231.001

Figure 6.7-2b. Breakthrough Curves Comparing the Base Case, Nondispersive, and Nondiffusive Cases: Volcanic/Alluvium Boundary

Regarding the relative importance of diffusion and dispersion in spreading the arrival time distribution, Figures 6.7-2a and 6.7-2b suggest that as long as diffusion in volcanics matrix occurs, the additional spreading afforded by a dispersion mechanism is very small (note the close similarity of the base case and "no dispersion" curves). By contrast, the no-diffusion breakthrough curve deviates significantly from the base case, showing the role of diffusion both for dispersing the mass and delaying the arrival times. One important factor to consider is that the dispersion being examined in this sensitivity analysis is only the hydrodynamic dispersion that occurs at scales smaller than the model grid block, as parameterized with the random-walk dispersion model. Larger-scale heterogeneities (e.g., hydrostratigraphic units of contrasting permeabilities, faults) are explicitly incorporated in the model. Therefore, because these large-scale dispersion mechanisms are "built into" the model, they are not turned off in the no-dispersion simulations presented here. Nevertheless, the breakthrough curve comparisons show the importance of diffusion as a mechanism for both delaying the travel times and spreading the distribution of the arrival times. Small-scale dispersion is relatively unimportant.

Another factor requiring examination is the spatial distribution of the contaminant source term. These breakthrough curves have been generated for a distributed release of contaminants, simulated by distributing a patch of particles throughout the repository footprint. There is a possibility that some of the spreading of arrival times is caused by the different starting locations of the particles, especially if there is a wide range of permeabilities and fluid fluxes directly beneath the repository. In contrast, if the radionuclide source term occurs due to the failure of only one or a few waste packages, the source term at the saturated zone would more closely resemble a point source. Figures 6.7-3a and 6.7-3b examine the role of the contaminant source in controlling the breakthrough curve by comparing the distributed source with one in which all particles are introduced at a single location near the center of the repository footprint. The breakthrough curve at the 18-km boundary (Figure 6.7-3a) for the case without diffusion is sharper than the one for the base case, and the difference between the curves is more pronounced at later times. This suggests that the spreading at early arrival times for nondiffusive transport is caused by the distributed source. However, diffusion into the rock matrix tends to mask this effect at later times. For example, in Figure 6.7-3b, a comparison of the base-case curves (solid black—distributed source; dashed green—point source) shows that apart from a slight difference in the first arrival times, the breakthrough curves track each other closely, suggesting that the details of the release location(s) at the repository footprint should have a relatively minor effect on the predicted breakthrough curve.

Regarding advection, it is expected that specific discharge is one of the most important uncertain parameters in the SZ transport model, owing to its first-order influence on solute velocity and the fact that available data and models provide relatively wide bounds on its estimated value. Figures 6.7-4a (18-km boundary) and 6.7-4b (volcanic/alluvium contact) show the predicted breakthrough curve for a conservative radionuclide over a broad range of values of specific discharge. This wide range of fluxes (Table 4-2 of this report) covers both the uncertainty in the specific discharge and the anticipated increases in groundwater flux caused by the change to a future, wetter climate. As expected, the groundwater flux controls the travel-time distribution, suggesting that future characterization and modeling efforts focusing on reducing uncertainties in specific discharge are most likely to reduce overall uncertainties in the behavior of the saturated-zone barrier.
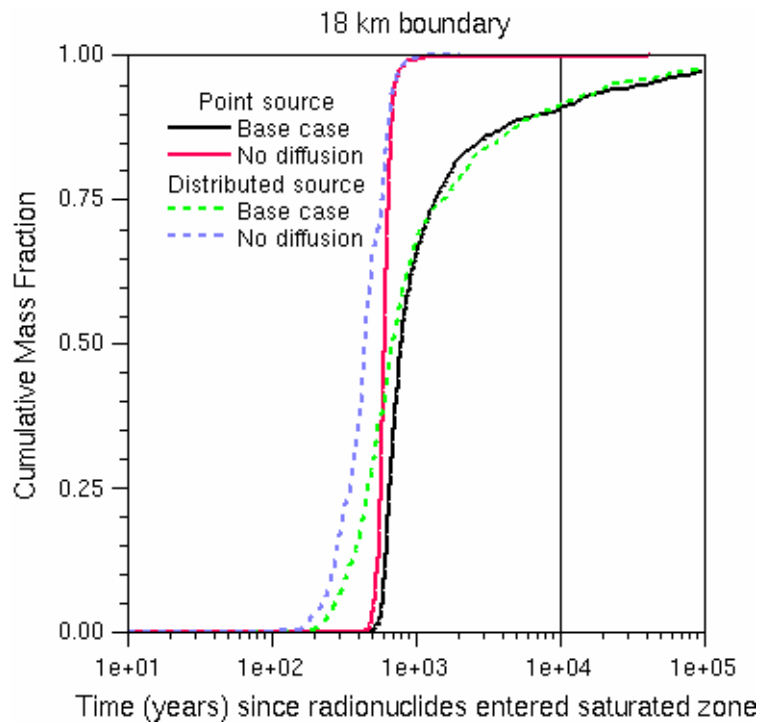
Output DTN: LA0307ZD831231.001

Figure 6.7-3a. Breakthrough Curves for the Base-Case Parameters with Point Source and Distributed Source for Input to the Saturated Zone: 18-km Boundary
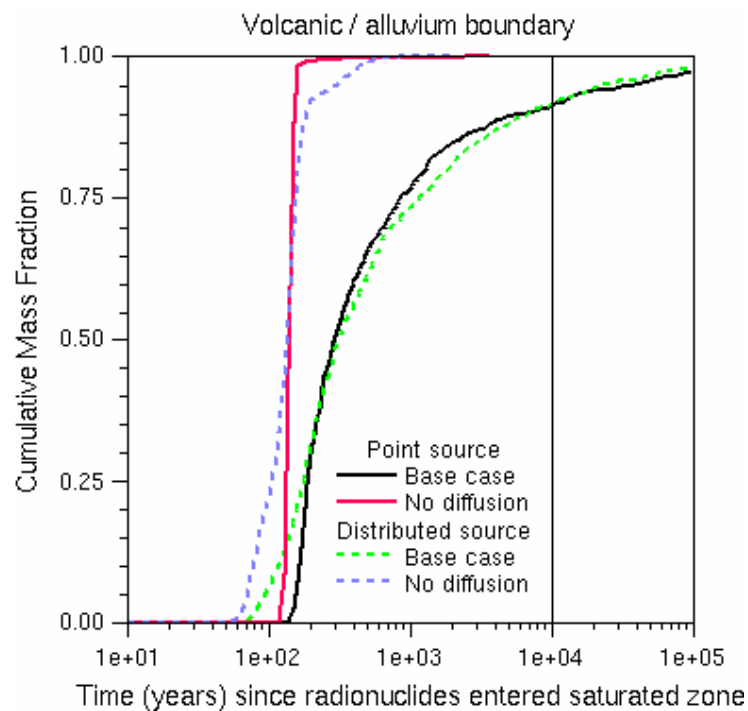
Output DTN: LA0307ZD831231.001

Figure 6.7-3b. Comparison of Breakthrough Curves for the Point Source and Distributed Source, Base Case, and Nondiffusive Case: Volcanic/Alluvium Boundary
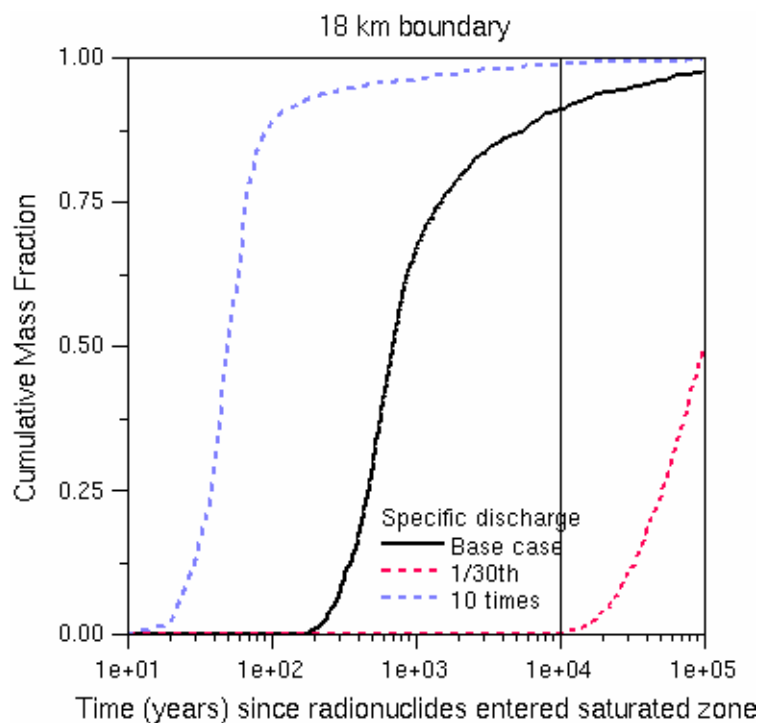
Output DTN: LA0307SK831231.002

Figure 6.7-4a. Breakthrough Curves for the Base Case and Cases with
Lower and Higher Specific Discharge: 18-km Boundary
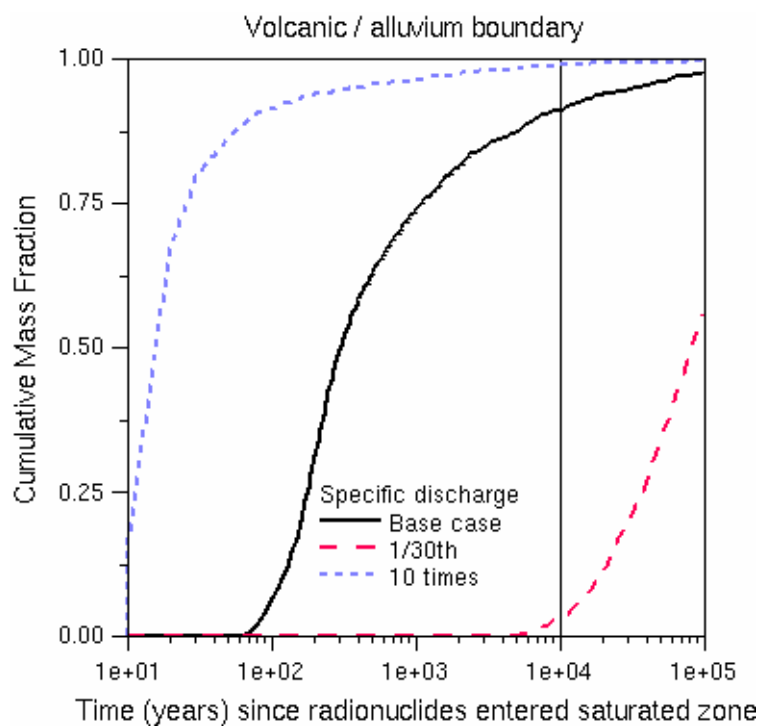
Output DTN: LA0307SK831231.002

Figure 6.7-4b. Breakthrough Curves for the Base Case and Cases with Lower and
Higher Specific Discharge: Volcanic/Alluvium Boundary

6.7.5 Colloid-Facilitated Transport in the Saturated Zone

In the final set of simulations of this section, calculations are presented that illustrate the performance of the saturated-zone barrier to retard the migration of radionuclides bound to colloids. Given that the most deleterious colloid-related effect on saturated-zone performance is likely to be the mobility of otherwise immobile radionuclides via colloids, the focus of this section is on that process. Furthermore, attention is restricted here to radionuclides irreversibly attached to colloids (termed "irreversible colloids" in the figures). These radionuclides do not diffuse into the volcanic matrix due to the large size of the colloids. Thus the matrix diffusion coefficient is set to 0 in this simulation. Retardation occurs due to the reversible filtration of the colloids themselves in the alluvium and in the fractures within the volcanic units. The colloid retardation factor distributions for the volcanics and the alluvium were constructed from numerous laboratory and field experiments. The construction of these distributions is described in detail in BSC (2003 [162729], Sections 6.4 and 6.5). Median values given in BSC (2003 [164870], Section 6.5.2; DTN: SN0306T0502103.007 [163946]) for the colloid retardation factor in alluvium of 33.9 and in the volcanics of 26 are used in the simulation. Figure 6.7-5a shows the expected behavior of colloidal-species transport compared to the base-case aqueous species transport. First arrivals are predicted to be slightly less than 10,000 years, with most of the inventory arriving at the compliance boundary with arrival times greater than 10,000 years. However, note that if larger specific discharge values are used, as would be the case for a future, wetter climate, the entire breakthrough curve would shift to travel times of less than 10,000 years. The difference between the aqueous and colloid breakthrough curves is attributable to reversible filtration of the colloids, which are modeled using a retardation factor that will be treated as a stochastic parameter in TSPA calculations. Thus, the modeling suggests that for the fraction of the radionuclide inventory that reaches the saturated zone within the compliance time period, the saturated zone is expected to impart a significant travel-time delay, but perhaps not sufficient to prevent some of these radionuclides from reaching the biosphere. Finally, comparison of the colloid breakthrough curves of Figures 6.7-5a and 6.7-5b shows that transport of colloid-bound radionuclides in the volcanics accounts for about one fourth of the total travel time through the system.
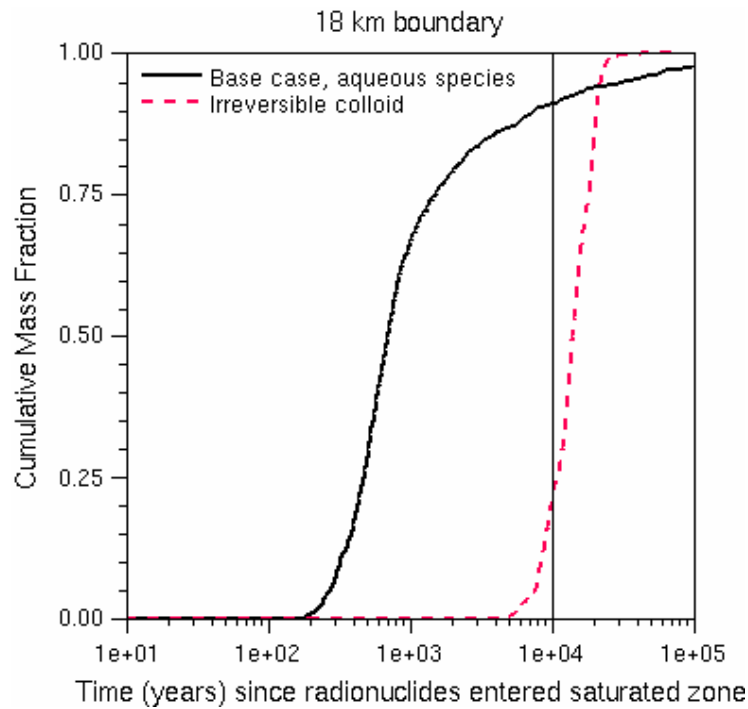
Output DTN: LA0307ZD831231.001

Figure 6.7-5a. Comparison of Breakthrough Curves for the Base Case and Radionuclides Irreversibly Attached to Colloids: 18-km Boundary
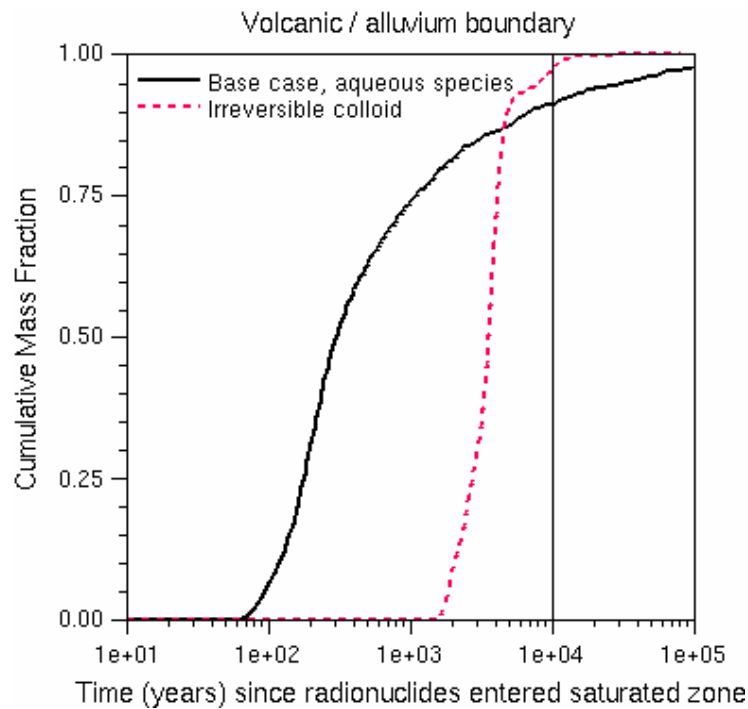
Output DTN: LA0307ZD831231.001

Figure 6.7-5b. Comparison of Breakthrough Curves for the Base Case and Radionuclides Irreversibly Attached to Colloids: Volcanic/Alluvium Boundary

6.7.6 Discussion of Saturated-Zone Barrier Performance

The two functions of the saturated-zone barrier, which are the ability to delay the arrival and attenuate the radionuclides via the mechanisms of dispersion and diffusion, have been demonstrated in this section through a series of model simulations. It is seen that sorption in the alluvium can increase the transport time by orders of magnitude of even the weakly sorbing radionuclides such as neptunium. Thus for the base case SZ transport model with the inclusion of sorption in the alluvium, travel times in excess of 10,000 years are expected within the saturated zone for all but the most weakly or nonsorbing radionuclides. For nonsorbing species, travel times on the order of 1000 years are expected. Radionuclides irreversibly bound to colloids may be delayed by several thousand years, but the actual value is quite uncertain due to the multiplicative impact of uncertainties in the specific discharge and the effective filtration retardation factor of colloids. Travel times for radionuclides irreversibly bound to the fast fraction of colloids are expected to be on the order of 1000 years, the same as those for the nonsorbing case. In essence, the saturated-zone barrier provides a travel-time delay on the order of or greater than the regulatory time period of interest for many radionuclide, but not those expected to travel without significant retardation due to sorption or colloid filtration.

To understand the role played by the saturated-zone barrier in attenuating radionuclides, the spread of arrival times at the compliance boundary in the form of cumulative arrival-time distributions was examined rather than simulating the in situ concentrations. The justification for this approach relates to the regulatory framework in which the modeling is being performed. Radionuclide mass flux is calculated by assuming that the entire annual radionuclide mass reaching the accessible environment is captured (10 CFR 63.332 (b)(2) [156605]). The concentration is then calculated by assuming that this mass is uniformly distributed in the representative volume of groundwater that would be withdrawn annually (3,000 acre-feet per year as defined by 10 CFR 63.332(a)(3) [156605]). Therefore, in situ concentrations are not relevant to barrier performance. The mass flux of radionuclides divided by the representative volume is the concentration of interest. Radionuclide mass flux at a compliance boundary is a common metric used in studies of contaminant transport in groundwater (e.g., Dagan et al. 1992 [163800], pp. 1369-1370). The approach taken here is patterned after the well-known solute mass flux approach. Hence, it is acceptable to use the particle-tracking model, although it has limitations requiring the use of a large number of input particles in applications where in situ concentrations are needed.

Nevertheless, attenuation of radionuclides during their transit from beneath the repository to the compliance boundary can be treated qualitatively by recognizing that the spread of the arrival-time distribution is related to the ability of the saturated zone to dilute radionuclide concentrations. The approximate duration over which relative concentration in the breakthrough curves rise from 0 to 1 can be compared to the duration of a transient pulse of high concentration. If the latter is smaller than the former, then the saturated-zone barrier will dilute the input pulse of high concentration to a lower value through the process of hydrodynamic dispersion and matrix diffusion. Thus, based on the breakthrough curves provided in this section, a high concentration, short-duration pulse of radionuclides of duration of about 100 years or less would become spread out in time within the saturated zone alone, to a high

degree of certainty. This characteristic of the saturated-zone barrier has implications on how the system is modeled for TSPA. Specifically, it implies that short-time-scale, high-concentration pulses need not be simulated explicitly as long as the correct overall radionuclide mass is input into the model.

For reasons related to the discussion above, transverse dispersion, though included in the SZ site-scale transport model, was not examined in sensitivity studies of barrier performance because it is not likely to be important to the function of the barrier. Small transverse dispersivity values estimated for the saturated zone will spread radionuclides a short distance orthogonal to the principal transport direction. This would have a significant influence on the in situ concentration but not on the overall flow path through which the plume travels. Therefore, the mass flux reaching the compliance boundary will not be affected significantly.

Finally as seen from Figures 6.7-4a and 6.7-4b, and BSC (2003 [164870], Section 6.7.1) the transit time through the SZ is a strong function of specific discharge. Therefore, studies that would reduce the bounds on specific discharge (under present-day conditions and due to the influence of climate change) would be the most important for reducing overall uncertainty in saturated-zone barrier performance. Colloid-transport data would also be useful, especially in the alluvium, where both colloid transport and aqueous-species transport data from multi-well tests are not available.

7. VALIDATION

The SZ site-scale transport model is designed to provide an analysis tool that facilitates understanding of solute transport in the aquifer beneath and downgradient from the repository. It is also a computational tool for performing radionuclide migration predictions in the saturated zone. For these predictions to be creditable, it must be demonstrated that the SZ transport model has been validated for its intended use. This statement means that there is established "confidence that a mathematical model and its underlying conceptual model adequately represents with sufficient accuracy the phenomenon, process, or system in question" (AP-SIII.10Q, Rev. 2, ICN 0, *Models*, Section 3.13).

The validation activities for the SZ transport model are carried out according to the *Technical Work Plan for: Saturated Zone Flow and Transport Modeling and Testing* (BSC 2003 [163965], Section 2.3). For validation of the SZ transport model, the technical work plan (TWP) states that the Level II validation "will be achieved by satisfying the criteria listed in items a) through f) of Appendix B of the *Scientific Processes Guidelines Manual* (SPGM; BSC 2002 [160313]), together with post-model development validation methods based on corroborative field and laboratory data" (BSC 2003 [163965], Section 2.3). The TWP specifies that post-development validation of the transport model will include the following comparisons:

1. Quantitative comparison of predicted transit times from the repository footprint to the compliance boundary with those derived from analyses of field hydrochemical and isotopic data. Validation will be considered acceptable if the range of model results is consistent with the range derived from the data. The distributions of transit times will be compared with groundwater ages to ensure that calculated breakthrough behavior is consistently faster than natural aging of the waters.

2. Qualitative comparison of predicted flow paths with flow paths from analysis of field hydrochemistry and isotopic data. Validation will be considered acceptable if the predicted flow paths starting at the repository footprint lie within the appropriate flow region inferred from the data.

As a result of the time and spatial scales involved and the fact that radionuclides cannot be used as tracers in field experiments, validation and confidence building for the SZ transport model has to rely on indirect data and inferences derived from technically related laboratory and field tests and natural analogs. Recognizing that the model is being used to perform probabilistic calculations in which parameter uncertainties are propagated through the model, the intent of the validation and confidence-building activities is to confirm that radionuclide parameters and processes operative at the Yucca Mountain site are adequately represented with sufficient accuracy in the SZ site-scale transport model. This confirmation is accomplished by a series of different approaches that include: (1) comparisons to analog sites, (2) model-data comparisons, and (3) comparison with data published in refereed journals.

Confidence building during model development was based on the available laboratory and analog data as well as comparison with an independent site-scale groundwater flow model for the Yucca Mountain saturated zone (Winterle et al. 2003 [163823], pp. 152-153), as described in

detail in Section 7.1. These data were not used for post-development model validation, and only the comparison with the field hydrochemical and isotopic data were used as a post-development method for satisfying the validation criteria as detailed in Section 7.2.

The validation exercises performed here demonstrate that the parameters and processes selected have an experimental or observational basis and that the model-derived flow paths and transit times are consistent with field data. The model is validated for use in a stochastic analysis that establishes ranges of potential behavior of the SZ transport system. The SZ site-scale transport model is valid for simulating radionuclide transport in the saturated zone resulting in generation of radionuclide breakthrough curves several kilometers downstream from the source region. This model is intended for use with stochastic simulations using large uncertainty ranges for certain parameters such as specific discharge, fracture spacing and aperture, diffusion coefficient, and sorption coefficients. Care should be exercised in interpreting individual simulations for a single set of parameter values. Also, care should be exercised if the parameters used fall outside the range of parameter values given in this report.

7.1 CONFIDENCE BUILDING IN THE CONCEPTUAL MODEL

Confidence building in the radionuclide parameters (Section 7.1.1) and submodel components (Section 7.1.2) during the SZ transport model development was achieved by examining data from natural and man-made analogs and field and laboratory studies. These data were not used for post-development model validation activities.

7.1.1 Analog Studies to Support Transport Parameters

The study of radionuclide transport parameters based on observations at analog sites leads to increased confidence in the parameters that are used in the transport model presented in this report. The transport parameter values and processes for radionuclides of concern are sensitive to the site-specific geological and geochemical conditions. However, the SZ site-scale transport model is intended for use in making TSPA predictions using a wide range of parameter input values that reflect uncertainty in the input. The analog studies provide a qualitative comparison of the information with the parameters used in this model report. The analog studies considered here are the Nevada Test Site and uranium analog sites—Uranium Mill Tailings Remedial Action (UMTRA) sites in the United States (U.S.); El Borrocal in Spain; Palmottu, Finland; the Alligator Rivers site in Australia; Pocos de Caldas in Brazil; the Cigar Lake site in Canada; and Los Alamos in the U.S.

7.1.1.1 Nevada Test Site

Discussed in this section are relevant information and insights gained from radionuclide migration studies performed at the NTS, which is the U.S. continental nuclear weapons testing site. These results are relevant because the geology and geochemistry are similar to those at the Yucca Mountain due to the proximity between the two. Between 1951 and 1992, 828 underground tests were conducted at the NTS at locations indicated in Figure 7-1 (Wolfsberg et al. 2002 [162688]). In general, though not exclusively, tests were conducted below the water table, making radionuclide migration information potentially important to consider for the SZ

transport model. Tests in Yucca Flat and Frenchman Flat were principally situated in Quaternary-aged alluvium, analogous to the alluvium downgradient from Yucca Mountain. In contrast, tests beneath Pahute Mesa were generally conducted in volcanic-rock aquifers, which is a useful analog for the fractured volcanic tuffs beneath Yucca Mountain. Therefore, observations of radionuclide migration from these tests are useful corroborative information relevant to the main rock types in the flow path from beneath Yucca Mountain to the compliance boundary.
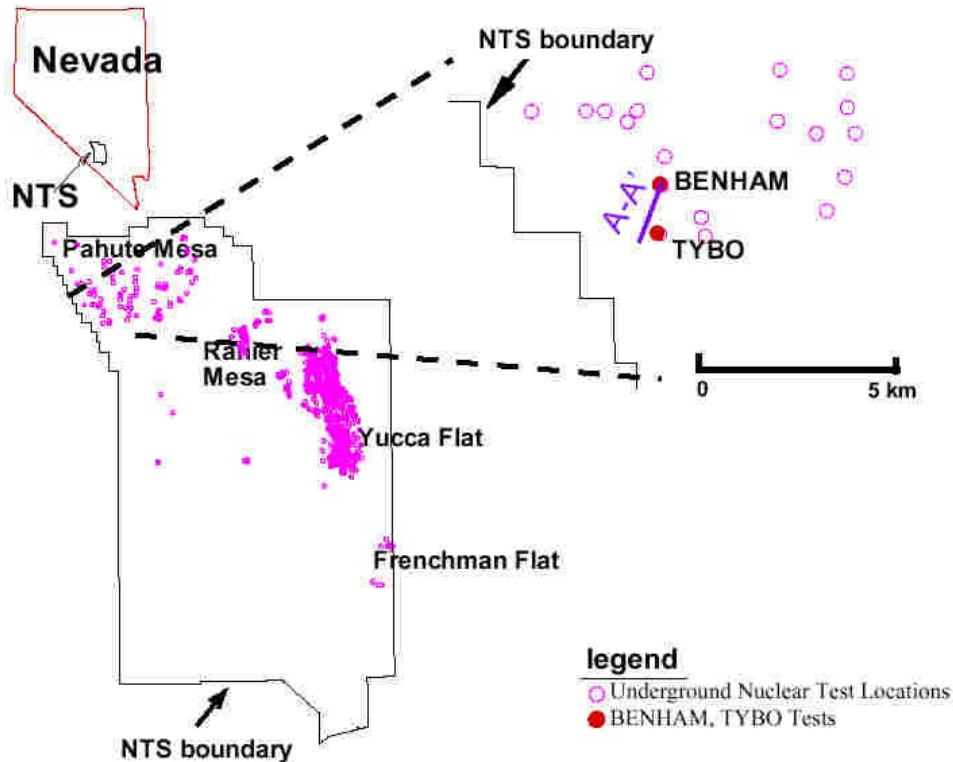
Source: Wolfsberg et al. 2002 [162688], Figure 1-1.

Figure 7-1. Locations of Underground Nuclear Tests and the Specific Locations of the TYBO and BENHAM Tests at the Nevada Test Site

For several decades, radiological data have been gathered to examine the potential migration of radionuclides in groundwater away from underground nuclear tests. Smith (2002 [162687]) summarizes the radiochemical investigations performed by the U.S. Department of Energy (DOE) Defense and Environmental Management Programs to characterize the current and potential future migration rates of radionuclides from these tests. In addition to general conclusions about the relative mobility of radionuclides at the NTS, there are more site-specific results in both alluvium and volcanic-rock aquifers that provide points of reference for large-scale mobility under hydrogeologic conditions similar to the Yucca Mountain saturated zone. The next section summarizes the general conclusions, followed by detailed discussions on observations and testing at the CAMBRIC site and the ER-20-5 wells adjacent to the

TYBO-BENHAM site. For the latter discussions, the NTS results are compared to the SZ transport conceptual model to demonstrate consistency with NTS data and analyses.

7.1.1.1.1 General Conclusions from NTS Investigations

To understand the similarities and differences between potential transport in the saturated zone beneath Yucca Mountain and migration away from an underground nuclear test, a brief conceptual description derived from Smith (2002 [162687], pp. 20-23) is provided. Transport from a nuclear test occurs in two steps: (1) a so-called "prompt transport" occurring over time scales of the nuclear detonation, and (2) groundwater transport occurring over a scale of years to centuries, depending on the flow regime. Prompt processes are generally thought to be as a plasma or gas through localized zones of failure in the rock. After this initial period, the system typically reverts over a period of years to a more ambient condition. However, the near-field system is permanently changed as a result of the nuclear detonation. Generally, a cavity is created containing a large inventory of radionuclides in the form of a solidified glass. The interaction of this glass with groundwater results in a long-term source for radionuclides in the groundwater. Above the cavity, a so-called chimney of hydrologically affected rock exists as a result of the underground explosion. If this chimney is of higher permeability than the surrounding rock, residual heat from the detonation can create a thermally buoyant water flow and radionuclide transport pathway up the chimney to zones of permeable rock in the aquifer. Then, groundwater flow under natural conditions transports radionuclides in the prevailing direction and at a velocity governed by the aquifer flow conditions.

Only the far-field flow and transport from underground tests are directly relevant to Yucca Mountain SZ transport. Therefore, data from downgradient wells provide the most useful information for the present study. However, the far-field observations contain inherent uncertainties due to the other transport processes (e.g., prompt transport, buoyant transport in the chimney). Additional indirect evidence on radionuclide mobility is also available by comparing the radionuclide concentrations in the cavity, chimney, and far-field fluids collected and summarized in Smith (2002 [162687]). Caution must be exercised with cavity and chimney data because they can have unique thermal and geochemical conditions that could influence the speciation and sorption characteristics of the radionuclides. As a result, including radionuclide concentrations from cavities and chimneys could potentially introduce data that were collected under conditions that are not representative of the saturated zone beneath and downgradient of Yucca Mountain. Despite these limitations, the following summarizes conclusions of Smith (2002 [162687], p. 31) on the relative mobilities of radionuclides derived from cavity, chimney, and far-field radionuclide measurements.

- The most mobile radionuclides at the NTS, traveling essentially unretarded compared to tritiated water (^{3}H), are: ^{14}C, ^{36}Cl, ^{85}Kr, ^{99}Tc, and ^{129}I.

- By contrast, the following radionuclides are relatively immobile, appearing in the cavity and chimney waters but generally not in the far-field: ^{90}Sr, ^{137}Cs, ^{152}Eu, ^{154}Eu, and ^{239}Pu.

- Despite this conclusion, several radionuclides generally considered to be immobile, such as plutonium, sorb to natural colloids and appear to migrate over significant distances. For example, Kersting et al. (1999 [103282], p. 59) showed that the concentration of

plutonium observed in wells significantly downstream from the source was very small ($\sim 10^{-14}$ M) and, therefore, concluded that only a very limited fraction of the plutonium associated with the test was mobile (additional details provided in Section 7.1.1.1.3 of this report).

- Wolfsberg et al. (2002 [162688], Section 7.7.3) report that Cs, Sr, and Eu isotopes were also found in these wells in the presence of colloids.

- Finnegan and Thompson (2002 [162695], pp. 13-14) detected ^{237}Np in the same wells where the more reactive radionuclides listed above were found.

These results are qualitatively consistent with the SZ transport model conceptualization and parameter distributions. Sorption coefficients are set to zero for radionuclides found to be mobile at the NTS, most notably ^{14}C, ^{36}Cl, ^{99}Tc, and ^{129}I. The SZ base case transport model represents the case of these radionuclides. For less-mobile radionuclides, such as ^{90}Sr and ^{137}Cs, as discussed in Attachment I, relatively large sorption coefficients are recommended, and hence, significant retardation. In general, the relative mobilities of the different radionuclides included in the SZ transport model are consistent with the data available from the NTS radiological measurements.

7.1.1.1.2   Radionuclide Transport in Alluvium (CAMBRIC Test)

Transport from the CAMBRIC test, conducted in 1965 in the alluvium in Frenchman Flat, has been extensively studied in subsequent years to understand the rates of radionuclide migration in groundwater. Wells were drilled to obtain radionuclide concentrations in both the near-field and far-field, and a 16-year aquifer pump test was conducted to determine the migration rates through the alluvium from the test cavity to the pumping well under forced-gradient conditions. The pumping well, RNM-2S, was drilled 91 m south of the CAMBRIC test and screened from 16 m to 41 m below the bottom of the CAMBRIC cavity (Smith 2002 [162687], p. 7). After about two years of pumping, essentially simultaneous breakthrough of ^{3}H, ^{85}Kr, ^{36}Cl, ^{129}I, ^{106}Ru, and ^{99}Tc were observed. A tritium breakthrough curve published in Tompson et al. (1999 [162686], Figure 35) shows a peak concentration about 5.5 years after pumping started and a slow decline in concentrations thereafter, until the end of the test. By contrast, cations ^{90}Sr, ^{137}Cs, ^{152}Eu, ^{154}Eu, and ^{239}Pu, though present in the cavity fluids, were not observed in the well during the 16 years of pumping (Smith 2002 [162687], p. 7).

The lack of arrival of less mobile radionuclides at the pumping well, allows a lower bound to be placed on the retardation factor. As an order-of-magnitude estimate, lack of arrival after 16 years when the first arrival of tritium was about two years, lead to retardation factors of at least 8. Using the range of porosities reported in the same study of 0.1 to 0.38 (Tompson et al. 1999 [162686], Table 20), this value of the retardation factor leads to K_d values between 5 and 10 mL/g, which are consistent with the ranges given in Attachment I for these radionuclides. Complications include a time-varying flow rate and analytical detection limit issues for plutonium (Tompson et al. 1999 [162686], p. 152). Nevertheless, this minimum value of 8 can be compared to the retardation factors exceeding 1000 based on models and laboratory data for ^{90}Sr and ^{137}Cs (Tompson et al. 1999 [162686], Table 25). In short, breakthrough was not expected based on laboratory data and sorption models, and it did not occur in the field, which

lends credence to the concept of retardation by sorption in the alluvium. However, a tight bound on the actual retardation factor is not possible from this field test.

7.1.1.1.3 Radionuclide Transport in the Volcanics (TYBO-BENHAM Study)

The interpretations presented in this section were obtained from a report by Wolfsberg et al. (2002 [162688], Chapter 1), who performed a comprehensive analysis of transport at the NTS. Underground tests called BENHAM (in 1968) and TYBO (in 1975) were conducted at Pahute Mesa in volcanic rocks beneath the water table (Figure 7-1). Subsequently, to investigate the potential migration of radionuclides, observation wells ER-20-5 #1 and ER-20-5 #3, approximately 300 m southwest of TYBO, were drilled and completed in the Topopah Spring welded tuff, which is the same unit in which the TYBO test was carried out (Pawloski 1999 [162685], p. 20). Sampling of these observation wells between 1996 and 1998 indicates elevated concentrations of isotopes of H, C, Cl, Sr, Tc, I, Cs, Co, Eu, Am, and Pu (Wolfsberg et al. 2002 [162688], Tables 1-1 and 1-2). Kersting et al. (1999 [103282], p. 56) studied the low levels of plutonium found in the two observation wells in greater detail. Plutonium was detected in ER-20-5 #3 at approximately the elevation of the BENHAM working (detonation) point and in ER-20-5 #1, approximately 500 m above the lava (Figure 7-2). The plutonium in both wells was found associated with colloidal material, and isotopic fingerprinting by Kersting et al. (1999 [103282], p. 58) showed that the plutonium originated at BENHAM rather than TYBO, despite the closer proximity of the ER-20-5 wells to TYBO.
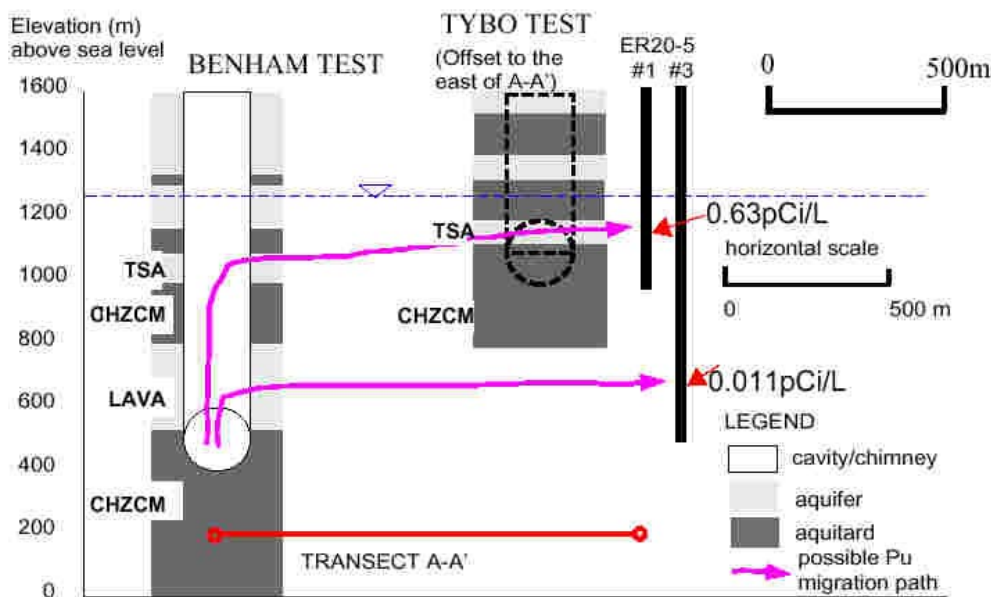
Figure 7-2. Schematic of Possible Pathways from the BENHAM Test to the ER-20-5 Observation Wells

This observation suggests that plutonium, typically considered to be relatively immobile, in fact migrated 500 m vertically and 1300 m horizontally. Kersting et al. (1999 [103282], p. 58) point

out that it is unlikely that plutonium from BENHAM was transported via prompt injection (at the time of detonation) over the distances necessary for observation at the two separate ER-20-5 wells. Further, because the plutonium detected in the ER-20-5 wells was entirely associated with colloids, plutonium migration via colloid-facilitated transport in groundwater is the most likely explanation. Wolfsberg et al. (2002 [162688], Chapter 1) constructed an integrated model of the system based on the conceptual model depicted in Figure 7-2. That study concluded that for expected values for parameters, migration of small amounts of plutonium from BENHAM to the observation points is plausible in less than 30 years (Wolfsberg et al. 2002 [162688], p. 8-3). Their colloid-facilitated transport model employed a kinetic model for the sorption of plutonium onto colloids. It was found that slow desorption of plutonium from the colloids is required to allow a small fraction of the mass to travel via colloids. In the SZ site-scale transport model, two mechanisms of colloid-facilitated transport are incorporated: one is a reversible sorption model, and the other is an irreversible sorption model for radionuclide attachment onto colloids. The only retardation mechanism for the latter is retardation of the colloids by filtration, which is modeled using a retardation-factor-type parameter. This latter approach is consistent with the field observation from the TYBO-BENHAM and ER-20-5 wells that a fraction of the inventory of otherwise immobile radionuclides is transported via colloids.

There is no way to fingerprint the source of the other radionuclides detected at these observation wells using isotope ratios. Nevertheless, the plutonium observations pointing to a BENHAM source can be used to hypothesize that the other radionuclides cited above also migrated the 1300 m horizontally from BENHAM, given that a groundwater transport pathway is implied by the plutonium data. For some of these other radionuclides, such as americium, colloid-facilitated transport is a likely mechanism: this explanation is adopted in the SZ transport model by treating americium using a colloid-facilitated transport model. Others, such as ^{90}Sr and ^{137}Cs, are normally considered to be aqueous, sorbing radionuclides. Based on the available information, it is not possible to choose among the following explanations: (1) colloids are also responsible for migration, (2) sorption is not effective due to limited contact with the rock during fracture flow, or (3) the source of these radionuclides is not BENHAM, but TYBO, and transport distances are much shorter. The SZ transport model allows the possibility of relatively rapid transport of these radionuclides through fractures, making the model, though uncertain, consistent with the ER-20-5 observations for these radionuclides.

7.1.1.2 Transport of Uranium at Natural Analog Sites

This section briefly summarizes information on transport of uranium from different analogue sites to determine their relevance to conditions present at Yucca Mountain. Based on monitoring programs at UMTRA sites across the U.S., under oxidizing conditions representative of the transport path in the saturated zone, uranium transports as a nonsorbing to weakly sorbing contaminant (BSC 2002 [160405], Section 12.3). This finding is consistent with the conceptual and mathematical model presented in Section 6 and the ranges of K_d values developed for uranium in Attachment I.

A study of natural uranium ore bodies at El Berrocal in Spain (BSC 2002 [160405], Section 12.4.2.1) and a study of radionuclide migration in fractured gneisses and migmatites at Palmottu, Finland (BSC 2002 [160405], Section 12.4.2.2) led to the conclusion that effects of

matrix diffusion are seen in up to several tens of millimeters of rock matrix adjacent to fracture surfaces. These studies also showed that reactive processes between the radionuclides and the rock matrix effectively immobilized the radionuclides.

In studies at Cigar Lake, Canada; Alligator Rivers, Australia; and Pocos de Caldas, Brazil (BSC 2002 [160405], Section 12.4.3), it was found that uranium, thorium and rare-earth elements transported in association with colloids. Similar conclusions were reached in studies at the Nevada Test Site and Los Alamos in the U.S. (BSC 2002 [160405], Section 12.4.3).

7.1.2 Submodel Components

Confidence building in submodel components of the SZ transport model was conducted through comparison of the conceptual model of SZ transport with the results of field tests conducted at the C-wells complex, the ATC, and the CAMBRIC site on the NTS. At the C-wells complex, which is located approximately 2 km southeast of the high-level radioactive waste repository footprint at Yucca Mountain, a series of conservative and reactive tracer tests were conducted in the various hydrogeologic units, principally fractured volcanic tuffs. Tracer tests were conducted separately in Bullfrog Tuff and Prow Pass Tuff units to study contaminant transport in different fractured volcanic media (BSC 2003 [162415], Section 6.4). The tracer test conducted at the C-wells is used to identify the important transport processes for the fractured volcanics. Conceptualization of transport processes for the alluvium were also based on field tests conducted at the NC-EWDP-19D1 wells and the at the CAMBRIC site on the NTS. At the NC-EWDP-19D1 wells, three single-well, injection-withdrawal tests were conducted in the saturated alluvium. In each of the three tracer tests, two nonsorbing solute tracers with different diffusion coefficients were simultaneously injected. Detailed information on the identification of the various transport processes is provided in BSC (2003 [162415], Section 6.5). Summary-level discussions of the conceptual model elements follow in Sections 7.1.2.1 to 7.1.2.9 of this report. More lengthy discussions in Section 6 give added detail to the inclusion of the following in the SZ transport model:

- Advection in the volcanics (see Section 6.3, item number 2)
- Dispersion in the volcanics (see Section 6.3, item number 2)
- Matrix diffusion in the volcanics (see Section 6.3, item number 3)
- Sorption in the volcanics (see Section 6.3, item number 4)
- Colloid facilitated transport in the volcanics (see Section 6.3, item number 5)
- Advection in the alluvium (see Section 6.3, item number 6)
- Diffusion and dispersion in the alluvium (see Section 6.3, item number 6)
- Sorption in the alluvium (see Section 6.3, item number 7)
- Colloid facilitated transport in the alluvium (see Section 6.3, item number 8)

7.1.2.1 Advection Through Fractures in the Volcanics

Figure 7-3 shows the results of a cross-hole tracer test in the Bullfrog Tuff member of the Crater Flat Group for the three soluble tracers: PFBA, bromide, and lithium (a weakly sorbing tracer).

The injection and production wells were separated by approximately 30 m at the test depth (BSC 2003 [162415], Table 6.1-1). The fractional recovery for PFBA and bromide was 0.69 and that for lithium was 0.39 (BSC 2003 [162415] Section 6.3.5). This is consistent with the interpretation of lithium as a sorbing tracer. Tracer breakthrough curves are plotted as normalized concentration versus time (normalization is performed by dividing by the tracer mass injected) at the production well so that they can be compared directly to one another. The most prevalent feature in these breakthrough curves is the presence of multiple peaks. This result was due to the presence of two advective pathways between the wells and the particular means for injecting the tracer mixture, which gave rise to two distinct flow paths of overlapping travel times. This feature is a site-specific detail due to the local hydrologic conditions. The general behavior of the system implied by the breakthrough curves in Figure 7-3 is that advection occurs primarily in the fractures. Rapid travel velocities between the wells (solute breakthrough within the first 10 hours of the test) are consistent with the conceptual model element of fracture flow through the volcanics. This test was conducted under forced gradient conditions (BSC 2003 [162415], Sections 6.3.5.3 and 6.3.5.4) and the solute velocities are expected to be much higher than the natural gradient conditions. By contrast, advection in the matrix would have resulted in much longer transport times. Therefore, these observations lend strong support to the use of a fracture-flow model for advection in the volcanics.
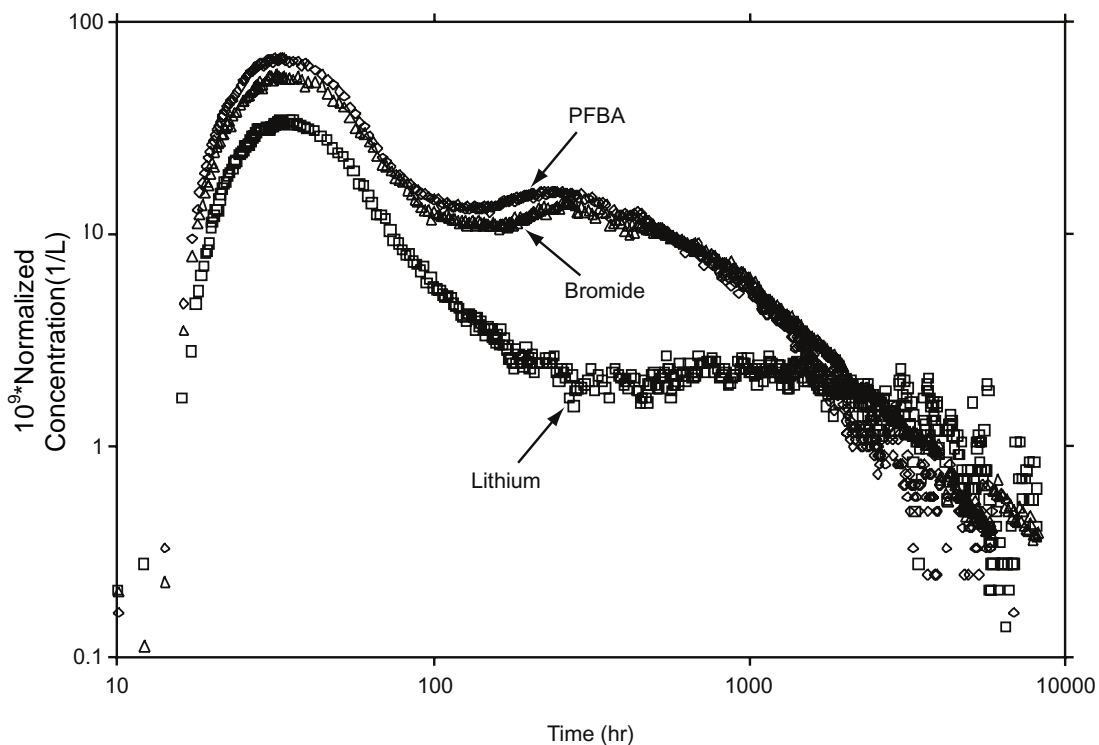
Source: BSC 2003 [162415], Figure 6.3-21.

NOTE: Log-log scales are used for the axes so that the bimodal nature of the tracer responses can be seen more clearly.

Figure 7-3. Normalized Tracer Concentrations Versus Time in the Bullfrog Tuff
Tracer Test Conducted from October 1996 to September 1997

7.1.2.2   Dispersion in the Volcanics

A computer modeling analysis of the C-wells test has been used to derive field-scale transport parameters for longitudinal dispersivity. A plot of the longitudinal dispersivity values as a function of test scale for several NTS fractured-rock, tracer-test programs is shown in Figure 7-4. The plot indicates that the longitudinal dispersivity increases with test scale, the range of the test scale going from less than one meter to over 100 meters (Leap and Belmonte 1992 [156838], pp. 87–95). Figure 7-5 shows the range of longitudinal dispersivities as a function of scale derived from the C-wells multiple-tracer tests (darkened area) superimposed on a plot of dispersivity versus scale prepared by Neuman (1990 [101464], Figure 3). Note that the lower end of the range of length scales associated with the darkened area corresponds to the interwell separation in the tracer tests and the upper end corresponds to the test interval thickness (used as an upper bound for the transport distance). The range of longitudinal dispersivities derived from the C-wells tests and the scale dependence of longitudinal dispersivity in the tests plotted in Figure 7-4 are consistent with the understanding developed in the literature. This result lends strong support to the use of a longitudinal dispersivity model.
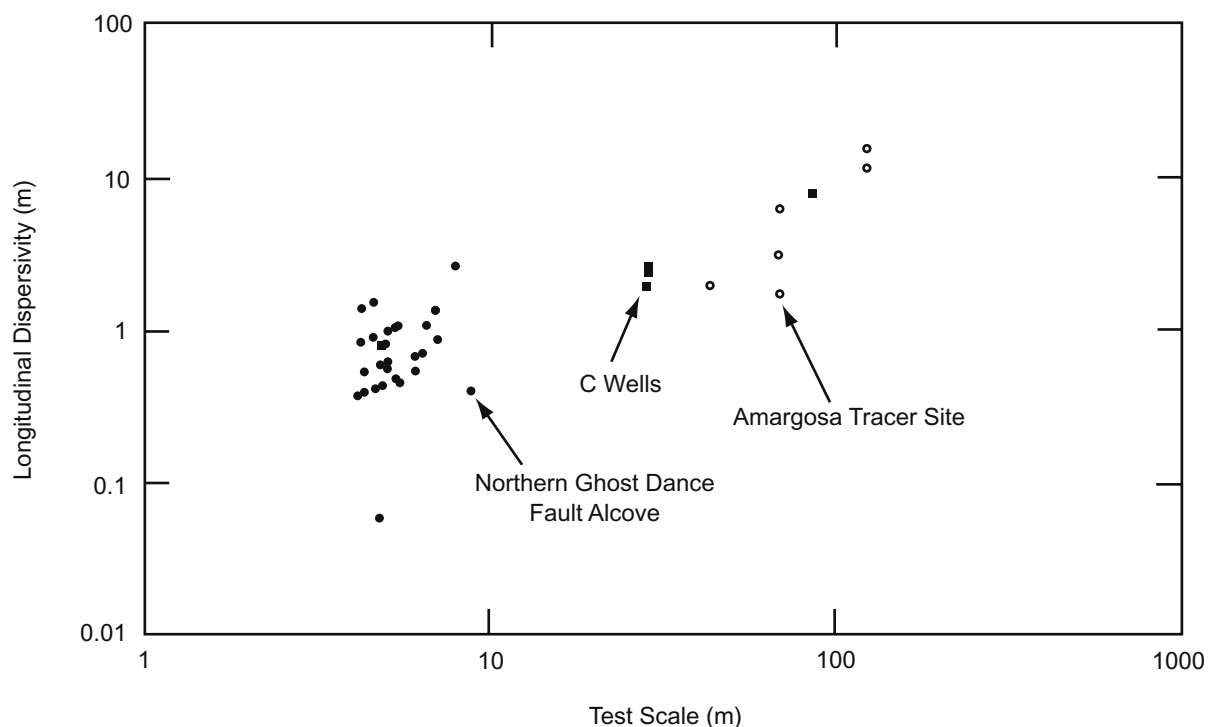
Source: BSC 2003 [162415], Figure 6.3-79.

Figure 7-4. Longitudinal Dispersivity as a Function of Test Scale in Several Tracer Tests
Conducted in the Vicinity of Yucca Mountain

There is no site-specific information available to select the transverse dispersivity in the fractured volcanics. Values were chosen based on the *Saturated Zone Flow and Transport Expert Elicitation Project* (CRWMS M&O 1998 [100353], pp. 3-11 and LG-11 to LG-14).
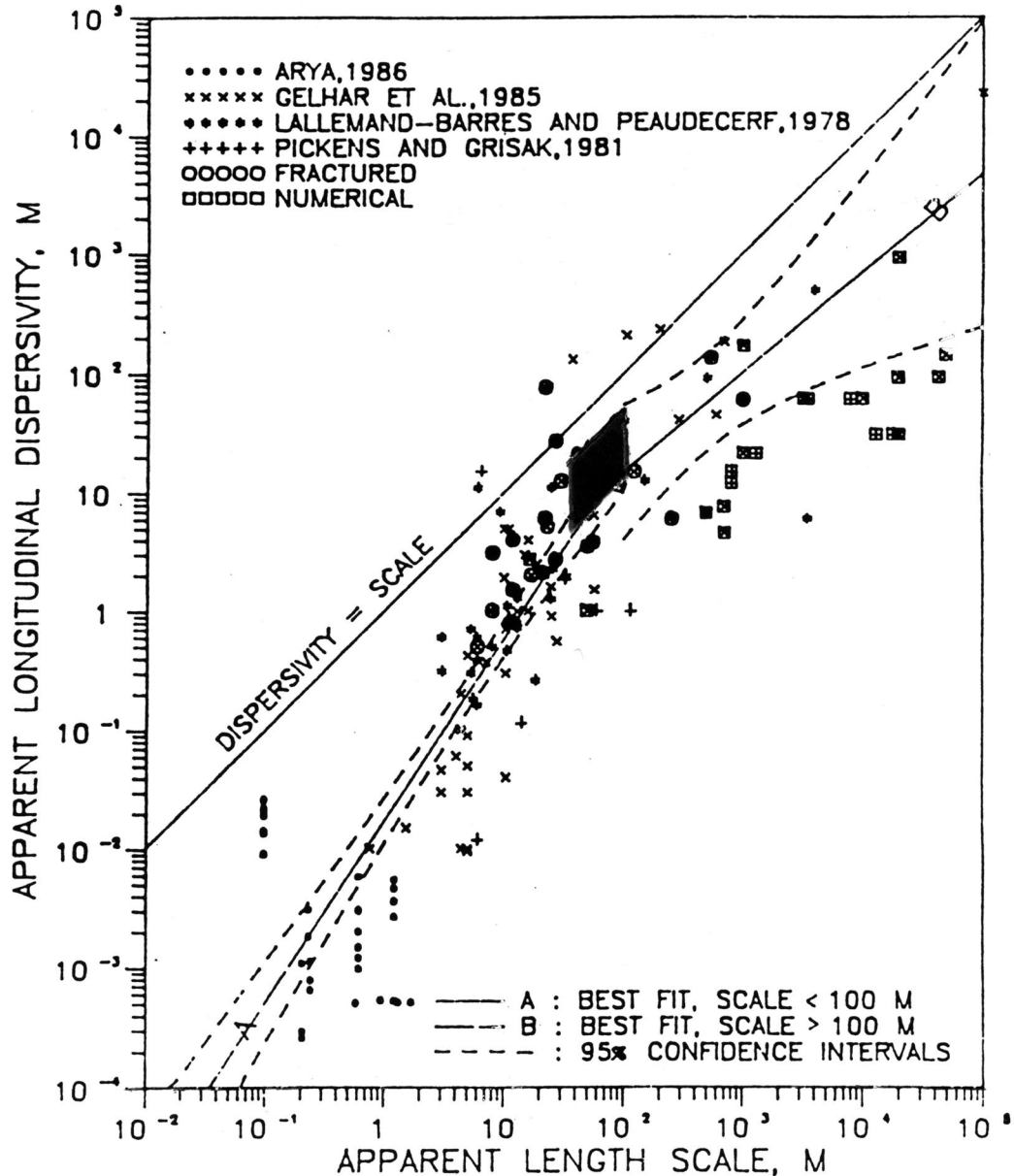
Source: BSC 2003 [162415], Figure 6.3-80.

NOTE: The darkened box shows the range of values derived from the multiple-tracer tests. The right edge of the box corresponds to the interwell separation distance, and the left edge of the box corresponds to the test interval thickness (taken to be the upper limit of transport distance).

Figure 7-5. Plot of Longitudinal Dispersivity Versus Length Scale Showing the Range of C-Wells Values Derived from Interpretations of the Prow Pass and Bullfrog Multiple-Tracer Tests

7.1.2.3 Matrix Diffusion in the Volcanics

For the purposes of validating the matrix-diffusion model for the fractured volcanics, the critical result from the C-wells tests is the relative heights of the peaks for the various tracers shown in Figure 7-3. For the conservative tracers, the fact that the tracer with the lower molecular diffusion coefficient (PFBA) exhibited a higher peak concentration is consistent with the dual-porosity model in which tracer travels in the fractures but also diffuses into the rock matrix.

When using a dual-porosity medium, as was done in this study, nonuniqueness of tracer test interpretations is an issue. For instance, long tails in tracer responses can be interpreted as being the result of either large longitudinal dispersion or significant matrix diffusion. In addition, at short time and distance scales, there may be a significant influence of diffusion into stagnant free water within fractures in addition to "true" matrix diffusion. Thus, matrix-diffusion parameters obtained from laboratory tracer experiments should be used cautiously when predicting contaminant migration at larger scales in fractured media. Nevertheless, in the multiple-tracer tests, nonuniqueness of interpretations was minimized by simultaneously fitting the tracer responses using known ratios of diffusion coefficients as constraints on the relative matrix diffusion of different tracers. The method of interpreting the field test data are given in detail in (BSC 2003 [162415], Section 6.3.5) and the parameter values obtained from the data fit are reported in (BSC 2003 [162415], Tables 6.3-6, 6.3-7 and 6.3-10). The mass transfer coefficients and fracture aperture values given in the above reference along with the base case matrix porosity given in Table 4-2 of this report (0.15 to 0.25) lead to matrix diffusion coefficient values in the range of 1.6×10^{-8} m^2/s to 8×10^{-13} m^2/s, which overlaps with the range given in Table 4-2 of this report. Rational for the selection of the range of diffusion coefficient values given in Table 4-2 of this report are given in Section 4.1.2.10 of this report and in (BSC 2003 [164870], Section 6.5.2.6).

The intent of the present discussion is to build confidence in the conceptual model of diffusive mass transfer in the volcanics. All the C-wells test results discussed in (BSC 2003 [162415], Section 6.3.5) are consistent with diffusive mass transfer having a strong influence on the migration of solutes in fractured volcanic tuffs. Therefore, the field evidence strongly supports the use of a matrix-diffusion model as opposed to a single-continuum model for transport in the fractured volcanics.

7.1.2.4 Sorption in the Volcanics

As with matrix diffusion, sorption can also be observed in the C-wells tests by examining the reactive tracer shown in Figure 7-3. Lithium, the sorbing tracer, exhibits further attenuation but a similar arrival time as the two conservative tracers. Note that a matrix-diffusion model explains this observation more completely than a single-continuum model, which would predict delayed arrival times for a sorbing tracer in addition to attenuation. Using the dual porosity equivalent continuum model, sorption within fractures leads to a delayed peak time along with attenuation, whereas sorption in matrix but not within fractures leads to the same peak arrival time but with attenuated response (Robinson 1994 [101154] Figure 7). Thus the field observed response of lithium is indicative of sorption within the volcanic matrix and not within the fractures on the scale of the C-wells test (tens of meters). Sorption coefficients were measured in the laboratory and compared to field-estimated values of K_d. The lithium K_d values estimated

from the field tracer tests are in the same range but consistently higher than the corresponding K_d values measured at the lowest lithium concentrations in the laboratory. These results suggest that the use of laboratory-derived K_d values to predict sorbing species transport in the saturated fractured tuffs near the C-wells location would tend to underpredict the amount of sorption experienced by the species in the field. The fact that the field K_d values tended to be greater than the laboratory K_d values suggests that lithium may have come into contact with alteration minerals in the field that were not present or were depleted in the lab rock samples. Any loosely adhering alteration minerals (e.g., clays) that may have been present in the core samples would very likely have been lost during crushing and sieving of the material when it was prepared for the batch-sorption experiments (BSC 2003 [162415], Section 6.3.5.8.4). Nevertheless, given the consistency of the breakthrough curves with sorption and the field estimates of K_d yielding similar values to those in the laboratory (which are considered conservative for PA because the values from the field tests are generally higher), the available data strongly support the use of a K_d-based matrix sorption model for the fractured volcanics. Broad ranges of values for K_d are being used in the TSPA analysis (Attachment III, Table III-14) to account for the uncertainties in determining this parameter.

7.1.2.5 Colloid-Facilitated Transport in the Volcanics

The approach used in the SZ transport model for colloid-facilitated transport is presented in Section 6.5.2.6 and Table 6.5-1.

7.1.2.5.1 Radionuclides Attached Irreversibly to the Colloids

The radionuclides attached irreversibly to colloids transport in a manner identical to the colloids. Tests were conducted at the C-wells to study the transport of colloids. In addition to the conservative and reactive tracers, 360-nm-diameter carboxylate-modified polystyrene microspheres were injected in the Bullfrog tracer test to examine how finite-sized particles transport through the fractured tuffs. These microspheres are meant to provide insight into the potential behavior of colloids transporting in the groundwater. Figure 7-6 shows a comparison of the microsphere breakthrough curve with the PFBA tracer. Microspheres do indeed transport through the medium at the scale of this test, but the concentrations are attenuated compared to a conservative solute. The fractional recovery of the microspheres is 0.145 compared to 0.69 for the PFBA (BSC 2003 [162415] Section 6.3.5.5). This result is probably due to filtration effects in the medium, although the possibility of settling cannot be ruled out. The SZ transport model applies a reversible-filtration model to simulate colloid-facilitated transport. The retardation factors estimated from the colloid attachment and resuspension rates given in Table 6.3-8 of BSC 2003 [162415] are in the range of about 6 to 794, which is the range given in the Table 4-2 of this report. The data in Figure 7-6 strongly support the concept of a filtration component of the conceptual model.

7.1.2.5.2 Radionuclides Attached Reversibly to the Colloids

Published work from literature is described in this subsection to build confidence in the conceptual model for the transport of the radionuclides attached reversibly to the colloids. Early models considered equilibrium partitioning of contaminants between the solute phase, colloid surfaces, and media surfaces (Hwang et al. 1989 [165931], p. 600; Smith and Degueldre 1993

[144658], pp. 145-150; and Grindrod 1993 [165928], pp. 171-175). These efforts focused on describing transport through fractured media. Corapcioglu and Jiang (1993 [105761], pp. 2217-2221) introduced a numerical model with first order reversible rate expressions describing colloid attachment and detachment to media surfaces. Their model (with some adjustments) was later used to describe Cs^{137} transport facilitated by silica colloids through glass bead columns (Noell et al. 1998 [106920], pp. 48-52). Ibaraki and Sudicky (1995a [109297], pp. 2948-2951; and 1995b [165930], pp. 2961-2964) were the first to implement kinetic expressions in a model to explicitly describe colloid-facilitated contaminant transport in discrete fractures and fracture networks, although their approach was essentially mathematically identical to that of Corapcioglu and Jiang (1993 [105761], pp. 2217-2221). Oswald and Ibaraki (2001 [165961], p.217-218) later extended the model to account for matrix diffusion of colloids, a phenomenon that was observed in laboratory experiments conducted in a fractured saprolite of high matrix porosity (the exclusion of this phenomenon from the SZ transport model, as discussed in Section 6.3, leads to potentially shorter transit time predictions).
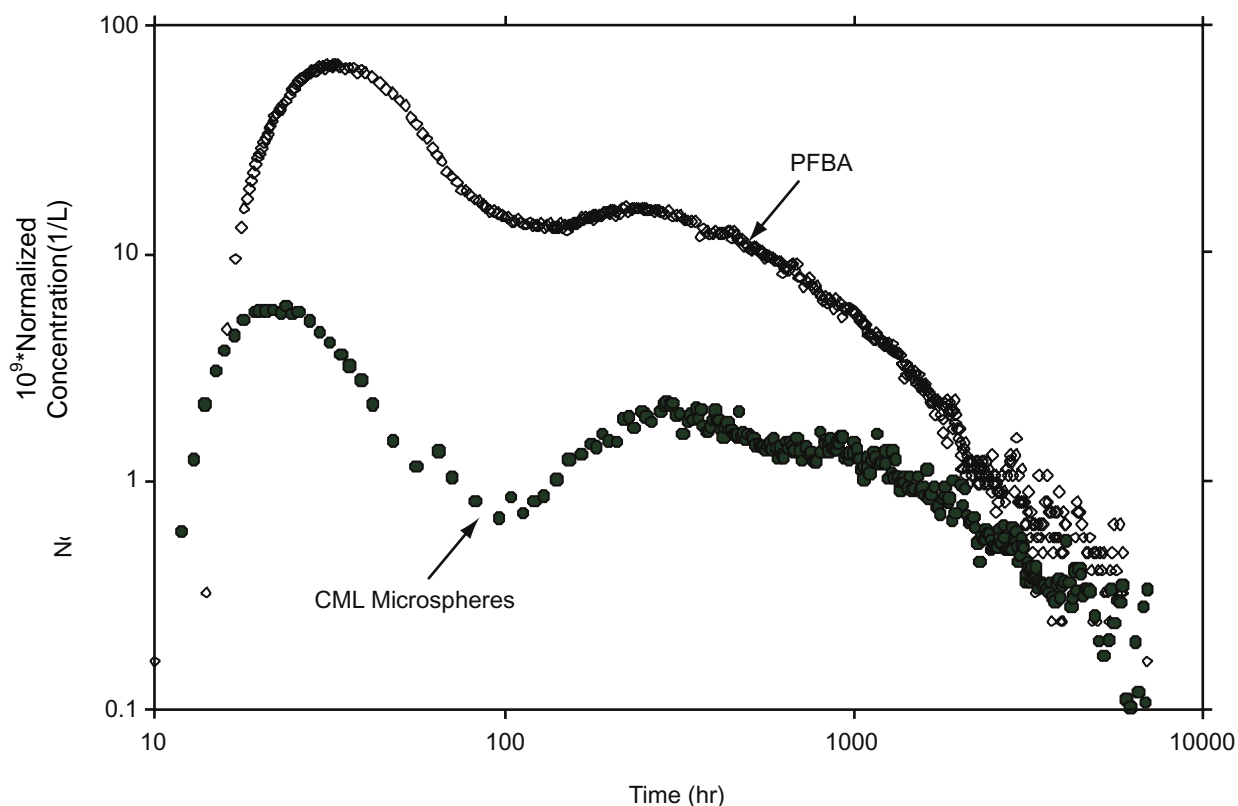
Source: BSC 2003 [162415], 6.3-22.

NOTE: Log-log scales are used for the axes so that the bimodal nature of the tracer responses can be seen more clearly.

Figure 7-6. Normalized Concentrations of PFBA and 360-nm-Diameter Carboxylate-Modified Polystyrene Latex Microspheres in the Bullfrog Tuff Tracer Test

7.1.2.6 Advection in the Alluvium

7.1.2.6.1 Alluvial Tests at NC-EWDP-19D1

Three single-well injection-withdrawal tracer tests were conducted in the saturated alluvium at NC-EWDP-19D1 between December 2000 and April 2001. In each of the three tracer tests, two nonsorbing solute tracers with different diffusion coefficients were simultaneously injected (a halide and an FBA dissolved in the same solution). The three tests were conducted in essentially the same manner except for the time that was allowed to elapse between the cessation of tracer and chase-water injection and the initiation of pumping—that is, the so-called "rest" or "shut-in" period. The rest period was systematically varied from ~0.5 hr to ~2 days and to ~30 days in the tests to vary the time allowed for tracers to diffuse into stagnant water in the flow system and for the tracers to migrate with the natural groundwater flow. Test interpretations were based on comparing the responses of the different tracers in the same test as well as the responses of similar tracers in the different tests. Differences in the responses of the two tracers injected in the same test provided information on diffusion into stagnant water in the system, whereas differences in the responses of tracers injected in different tests (after correcting for the effects of diffusion) provided information on tracer drift during the rest periods of the tests. Because the three tracer tests used different drift durations, a comparison of the results, combined with an idealized model of the groundwater flow behavior near the well, could be used to estimate the specific discharge. Values ranging from 1.2 to 9.4 m/y, depending on conceptual model and parameter uncertainties, were obtained (BSC 2003 [162415], Table 6.5-7). This range is in agreement with the values calculated in the calibrated site-scale SZ flow model (BSC 2003 [162649], Section 6.6.2.3) and the range of input values used in this model report (Table 4-2). The SZ site-scale transport model is intended for use in making TSPA predictions using a wide range of parameter input values that reflect uncertainty in the input. Hence, a comparison of the range of values is considered sufficient. This result lends strong support to the process of advection in the alluvium.

7.1.2.6.2 CAMBRIC (NTS)

Velocities of movement under forced-gradient conditions used in the CAMBRIC experiment are not directly relevant to natural-gradient flow and transport at Yucca Mountain. However, modeling analyses performed by Tompson et al. (1999 [162686], Chapter 10) for the NTS Environmental Restoration (ER) Project provide information on relevant hydrologic and transport parameter estimates for alluvium at the site. Using a heterogeneous distribution of permeability and constant porosities ranging from 0.1 to 0.38 (Tompson et al. 1999 [162686], Table 20), Tompson showed that a continuum model, after calibration, was able to match the tritium breakthrough curve well (Tompson et al. 1999 [162686], Figure 40). Note that this range of porosities compares favorably with the uncertainty range of 0.02 to 0.3 for the effective alluvium porosity in Table 4-2 of this report. In a simulation of tracer migration in which the fluid extraction rate is specified, the key parameters controlling the breakthrough curve are the effective porosity, which controls the mean arrival time, and the correlation length of the heterogeneity, which controls the macrodispersive spreading of the breakthrough curve. In the SZ transport model, porosity and permeability are taken to be uniform within hydrogeologic units, and the dispersion is governed by a macrodispersion model. The NTS and YMP models are both continuum models, so the mean arrival time is controlled by the effective porosity. The

models handle dispersion differently, which does not affect the mean arrival time. The fact that both are continuum models means that effective porosity values derived by Tompson et al. (1999 [162686], Table 20) should be relevant to the SZ transport model. The CAMBRIC test and modeling of Tompson et al. (1999 [162686], Chapter 10), therefore, confirms that a continuum model with porosity values of the same order of magnitude as the small-scale, measured porosity of the alluvial material is valid.

7.1.2.7   Diffusion and Dispersion in the Alluvium

Figure 7-7 shows a representative result from one of the single-well injection-withdrawal tracer experiments. The normalized tracer responses for two solutes and microspheres are shown. The two solute tracers had essentially identical responses (within experimental error) in this test (and other similar tests carried out in this interval). Flow interruptions during the tailing portions of the two longer tests (not shown) provided additional evidence for minimal diffusive mass transfer in the aquifer. The results here suggest that, in contrast to the fractured tuffs, the alluvium exhibits more of a continuum model behavior with less diffusion into stagnant fluid, such as the pore water of low-permeability material. This result may be scale-dependent such that, over longer transport times, diffusion becomes a more important factor. Nevertheless, these results support the conservative conceptual model of single-continuum transport with little or no diffusion into stagnant regions.
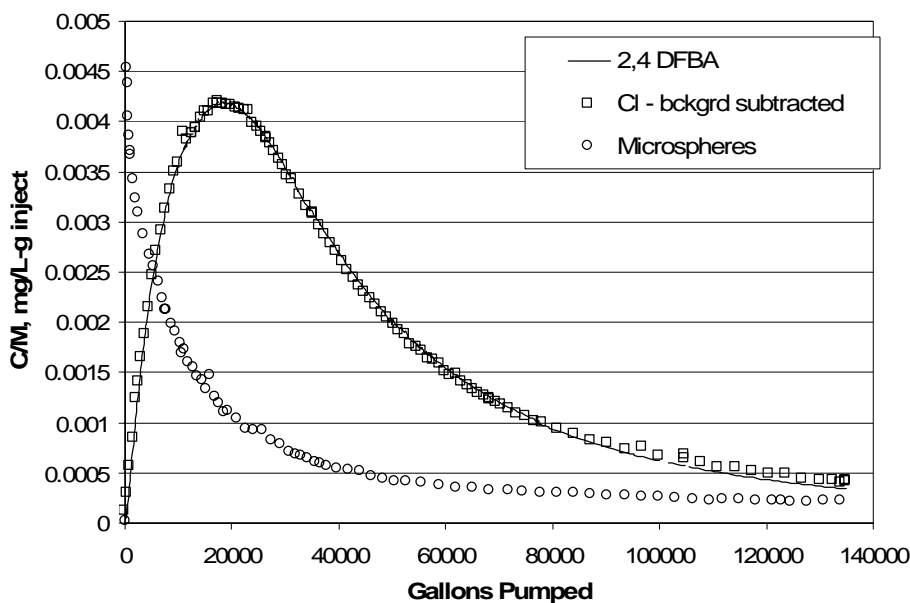
Source: BSC 2003 [162415], Figure 6.5-18.

NOTE: Microspheres were 640-nm diameter carboxylate-modified polystyrene latex spheres tagged with a UV-excited fluorescent dye for detection.

Figure 7-7. Normalized Concentrations of Tracers in Production Water from NC-EWDP-19D1 as a Function of Gallons Pumped After a Rest Period of ~0.5 Hours

Using a semianalytical method, data from the NC-EWDP-19D1 test were used to provide an estimate of 5 m for the longitudinal dispersivity (BSC 2003 [162415], Section 6.5.4.2.4) along with a porosity of 10% and a transverse dispersivity of 2 m, the scale of the test being estimated around 8 m. Also, the literature is full of information on dispersivity values in alluvial aquifers. (Neuman 1990 [101464], Figures 1 to 3) compiles a comprehensive list of dispersivity values in porous media including alluvium at different scales (Figure 7-5). Using scientific judgment, one can infer that values for dispersivity from the literature are applicable to the alluvial system at Yucca Mountain. All these considerations lend strong support to the conceptual model of dispersion in the alluvium. Broad ranges of values for dispersivities are being used in the TSPA analysis (BSC 2003 [164870], Table 3) to account for the uncertainties in determining this parameter.

7.1.2.8 Sorption in the Alluvium

No site-specific field data are available to confirm that sorption occurs in the alluvium downgradient from Yucca Mountain. Laboratory-scale experimental results are available, however. Figure 7-8 presents the results of several column transport experiments using groundwater and alluvium obtained from the site of the ATC Well NC-EWDP-19D1. These experiments involved injecting lithium bromide as pulses at three different concentrations spanning the range of Li concentrations expected in the field.

Examination of the results (Figure 7-8) indicates that the data are consistent with a model that includes sorption. This result suggests that sorption is occurring in the columns. The issue of lack of site-specific field evidence is mitigated by two considerations. First, transport field tests using sorbing tracers in similar hydrogeologic settings have shown that sorption does occur in such systems (LeBlanc et al. 1991 [163781], p. 905; Hess et al. 2002 [163780], pp. 36-6 and 36-14; Thorbjarnarson and Mackay 1994 [163782], pp. 413-414). Second, as demonstrated earlier, the fractured volcanic tuffs were shown to sorb tracers in the C-wells tracer experiments. These rocks have a similar mineralogic content as the alluvium and a similar fluid geochemistry. Therefore, demonstrated sorption in the fractured tuffs provides a line of site-specific field evidence in favor of sorption in the alluvium. All of these considerations lend strong support to the validity of the conceptual model of sorption in the alluvium. Broad ranges of values for sorption coefficients in alluvium are being used in TSPA analysis (BSC 2003 [164870], Table 3) to account for the uncertainties in determining this parameter.
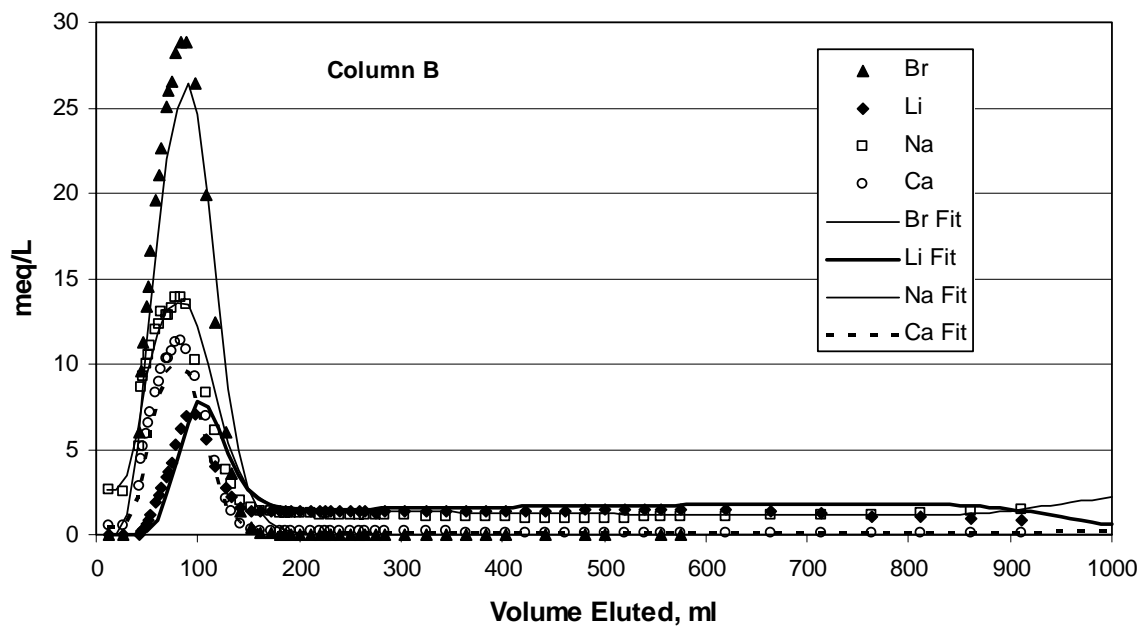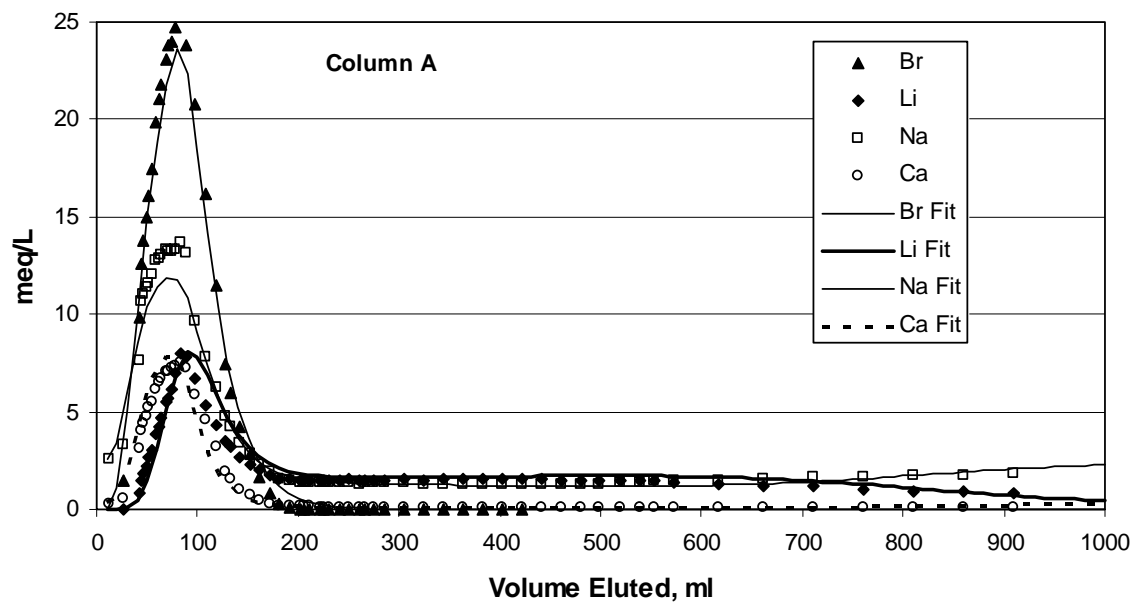
Source: BSC 2003 [162415], Figure 6.5-32 (model)

Figure 7-8. Column Data (Concentration in the units of milli-equivalent/liter) and MULTRAN Fits for Experiments with a LiBr Injection Concentration of 0.0275 M

7.1.2.9 Colloid-Facilitated Transport in the Alluvium

The approach used in the SZ transport model for colloid-facilitated transport is presented in Section 6.5.2.6 and Table 6.5-1.

7.1.2.9.1 Radionuclides Attached Irreversibly to the Colloids

The radionuclides attached irreversibly to colloids transport in a manner identical to the colloids. Tests were conducted at the C-wells to study the transport of colloids. The microsphere results shown in Figure 7-7 provide information on colloid filtration and detachment rates in the alluvial flow system. Qualitatively, compared to the conservative aqueous tracers, a much earlier breakthrough of microspheres in the withdrawal portion of the test was observed, followed by a very long tail. These observations are consistent with a model in which colloidal-sized particles undergo filtration in the alluvium. Filtration holds some microspheres up very close to the borehole. Upon pumping the aquifer, those microspheres close to the borehole are produced, essentially, instantly. Borehole effects could influence the early return of the microspheres as well. The fraction of microspheres that traveled farther into the medium undergo filtration during their return, resulting in the long tail. The tail could be influenced by plume drift and aquifer heterogeneities. This qualitative evidence lends support to the conceptual model of filtration of colloids in the alluvium.

7.1.2.9.2 Radionuclides Attached Reversibly to the Colloids

The discussion in Section 7.1.2.5.2 also applies to the alluvium.

7.1.3 Comparison of Flow Paths and Transit Times Against Those Computed by an Independent Site-Scale Model

An independent site-scale groundwater flow model of the Yucca Mountain saturated zone was developed by the NRC (Winterle et al. 2003 [163823]). Two different flow models of the flow system were considered. They differed in the material geometries, the number of material zones, and the permeability values assigned to each material type. Each model was calibrated to the measured heads by a trial and error process. Particle flow paths and travel times to the 18-km compliance boundary (10 CFR 63.302 [156605]) were calculated from the model using advection only, excluding dispersion, diffusion, and retardation. The first model predicted flow paths starting to the east but shortly turning southward and traveling more or less directly southwards (Winterle et al. 2003 [163823], Figure 4). The particle travel times predicted by this model ranged from 1800 to 110,000 years (Winterle et al. 2003 [163823], Figure 5). The second model showed flow paths moving farther east before swinging south (Winterle et al. 2003 [163823], Figure 8). This model predicted flow times in the range of 7100 years to 205,000 years (Winterle et al. 2003 [163823], p. 153).

The general trend of flow paths reported in the Winterle et al. (2003 [163823], Figures 4 and 8) study, starting eastwards and then moving southwards to the compliance boundary, compares favorably with the flow paths in Figure 7-9b of this report, although the latter show a more westward component in the southern part of the model compared to the Winterle et al. (2003 [163823], Figure 8) study. Although the model described in this report does not predict the

upper end of the travel times reported by Winterle et al. (2003 [163823], p.153), the range of transit times reported here overlaps with those reported by them. This result corroborates the SZ site-scale transport model.

7.2   POST-DEVELOPMENT VALIDATION

Numerical results from the SZ transport model have been compared both to data and to independent models to provide confidence that, when piecing together the submodels with appropriate geologic-, hydrologic-, and boundary-condition information, the overall model is consistent with available observational data. Specifically, the flow pathways from the model are compared to hydrochemistry data, and the transit times computed from the SZ site-scale transport model are compared to ^{14}C data at the field scale.

7.2.1   Comparison of Flow Paths Against Those Deduced from Hydrochemistry Data

Flow paths of tracer particles were calculated for the base-case transport model. The particles were started in the vicinity of the repository footprint and allowed to transport downstream to the compliance boundary. The transport parameter values used in this model calculation are given in Table 6.5-2 of this report. The results are shown in Figure 7-9b. Also shown in Figure 7-9 (a and b) are flow paths deduced from the hydrochemistry data (BSC 2003 [162657], Section 6.7.11). Chemical and isotopic compositions were measured for groundwater samples taken from a number of wells in the area of the SZ site-scale flow model. As explained in detail in (BSC 2003 [162657], Section 6.7.11), graphical analysis was done of the variations in the concentrations of the chloride (Cl$^-$), sulphate (SO$_4^{2-}$), and SiO$_2$ ions and in the oxygen isotopic ratio (δ^{18}O) and the hydrogen isotopic ratio (δD) to estimate plausible flow lines. Of particular interest are the flow paths labeled # 2 and #7 in Figure 7-9a and b from this analysis. Flow Path #7, which is derived from hydrochemistry data, originates in the vicinity of the repository footprint and generally overlaps the model-calculated flow paths as seen in Figure 7-9b. FlowPath #2 is also of interest here, although it originates northeast of the repository, because it closely bounds Flow Path #7 to the east. Note that the flow path #9 (shown by broad dashed line in Figure 7-9a going from east to west), which appears to cut across the flow paths #2 and #7 in the two dimensional figure, actually represents regional underflow in the deep carbonate aquifer that underlies the volcanics and the alluvium in the SZ model area, and thus does not interfere with the flow paths #2 and 7.

Flow Path #2 traces the movement of groundwater from the Fortymile Canyon area southward along the axis of Fortymile Wash into the Amargosa Desert. This pathway is drawn on the basis of similar anion and cation concentrations along the flow path and dissimilarities to regions to the east and west. Further details are presented in (BSC 2003 [162657], Section 6.7.11).

Flow Path #7 traces the movement of groundwater from northern Yucca Mountain southeastward toward wells in the Dune Wash area and then southwestward along the western edge of the Fortymile Wash (BSC 2003 [162657], Section 6.7.11). High ^{234}U/^{238}U activity ratios and low Cl$^-$, SO$_4^{2-}$, δD and δ^{18}O values characterize this flow path. A detailed discussion is presented in (BSC 2003 [162657], Section 6.7.11).

NOTE: (1) Colored symbols in the figure represent details of geochemical data, not directly relevant to the present discussion. Hence, for the sake of clarity, the detailed legend is not included here, and the interested readers are referred to the source of the figure.
(2) Flow path Number 9 shown by broad dotted blue arrows pointing easterly is flow through deep regional aquifer and does not interfere with the flow paths 1 through 8 in the shallow volcanics and alluvium.

Source: BSC 2003 [162657], Figure 62.

Figure 7-9a. Transport Pathways Deduced from Hydrochemistry

Figure 7-9b. Transport Pathways Deduced from Hydrochemistry Data (in red, enlarged from Figure 7-9a) Overlaying Flow Paths Calculated from the SZ Transport Model (in black) for Tracer Particles Starting at the Repository Footprint

The flow paths deduced from the geochemistry data are qualitative in nature and denote broad areas of flow continuity inferred from available data, rather than specific streamlines. They are meant to represent broad flow directions and not the detailed variations that can be seen in a streamline computed from the model. It is seen in Figure 7-9b that the model streamlines originating at the repository footprint follow the general orientation and remain within the flow regions defined by the Flow Paths #7 and #2 deduced from the geochemistry data. Hence, this validation is considered acceptable as defined in the TWP (BSC 2003 [163965], Section 2.3, second validation criteria).

7.2.2   Comparison of Transit Times Against Those Deduced from ^{14}C Data

The radioactive isotope of carbon, ^{14}C, is produced in the atmosphere primarily by the interaction of cosmic rays with the atmospheric ^{14}N. ^{14}C decays with a half-life of 5730 years. ^{14}C is rapidly incorporated into the atmospheric CO_2 and becomes available for terrestrial processes including that of dissolution into atmospheric precipitation (BSC 2003 [162657], Section 6.7.1.2.2). ^{14}C enters the SZ groundwater through recharge and is transported principally as bicarbonate

(BSC 2003 [162657], Section 6.7.1.2.2) as a nonsorbing species. Estimates of groundwater age are obtained from the measured ^{14}C activity, corrected for possible water/rock interactions (BSC 2003 [162657], Section 6.7.1.2.2). In interpreting these age estimates, it must be noted that the possibility of a fraction of younger water mixing with older water leading to the apparent age as determined from the ^{14}C activity cannot be ruled out with complete certainty. Radiometric dates in geochemically open systems are mixed dates that can be used for estimating upper and lower bounds of the ground water ages. Hence the values obtained from ^{14}C activity data should be interpreted as representing the likely range of groundwater ages, without excluding some probability of groundwater ages having values outside the indicated range.

Data from water samples taken from 7 wells in the vicinity of the Yucca Mountain were analyzed for ^{14}C activity (BSC 2003 [162657], Section 6.7.6.6.2) and the resulting ages are reported to lie in the range of 11,430 years to 16,390 years (BSC 2003 [162657], Table 16). These ages reflect the time from atmospheric precipitation to the present and thus include travel time through the UZ as well as the SZ, along with the residence time within SZ. Thus they are not direct indicators of transit times in the SZ, but they do provide a plausible upper bound on the SZ transit time.

Groundwater transit times can also be inferred from measured ^{14}C activity from water samples taken from wells that are inferred to lie along a flow path (BSC 2003 [162657], Section 6.7.11). Data from two wells were used: UE-25 WT#3 and NC-EWDP-19D, both of which are downstream of the repository footprint, and lie on the interpreted Flow Path #7 that starts at the Yucca Mountain and moves downstream in a overall southwardly direction (Figure 7-9a). The approximate distance between the two wells is 15 km (BSC 2003 [162657], Section 6.7.9.1). The ^{14}C travel times lie in the range of 0 years to 3027 years over the sampled depths (BSC 2003 [162657], Section 6.7.9, Table 19), with the data being clustered around two ranges: one in the interval of 70 to 359 years and the other in the interval of 2048 to 3027 years. Using the interwell distance of 15 km as stated above, these ranges translate into groundwater velocity ranges of 214 to 42 m/yr and 7.3 to 5 m/yr. Using a nominal distance of 18 km from the repository footprint to the compliance boundary and taking constant velocities along the flow path, these velocities lead to transit time ranges of 84 to 429 years and 2466 to 3600 years. As discussed in the previous paragraph, in interpreting these transit time estimates, it must be noted that the possibility of a fraction of younger water mixing with older water leading to the apparent age as determined from the ^{14}C activity cannot be ruled out with complete certainty. Hence the values obtained from ^{14}C activity data should be interpreted as representing the likely range of groundwater travel times, without excluding a small probability of groundwater ages having values outside the indicated range.

There are two simplifications built into the above estimates (in addition to the ^{14}C data interpretation as discussed in (BSC 2003 [162657], Sections 6.7.8 and 6.7.9): one is that in calculating velocities from the travel time estimates, a nominal travel distance is used equal to the well separation, and the second is that a constant velocity is used along the entire flow path. Regarding the first simplification, using a nominal distance instead of the distance along the actual flow path, details of the tortuousness of the flow path are neglected. In actuality, the distance along the flow path will be somewhat greater than the interwell spacing, and thus the calculated velocity will be somewhat less than the actual velocity. However, the influence of

this simplification on the estimated travel time to the 18-km boundary is somewhat offset by the fact that the actual travel distance along the flow path (including the segment beyond the well UE-25 WT#3) is also replaced by the somewhat lower value of 18 km, thus a ratio is taken of two numbers which are both somewhat lower than the actual values in the field. Secondly, in using a constant velocity along the flow path from the well UE-25 WT#3 to the compliance boundary, an average of velocities in the volcanics and the alluvium is applied to the additional distance of 3 km that is traveled within the alluvium from the well NC-EWDP-19D to the compliance boundary. Considering that the porosity in alluvium is many orders of magnitude greater than the volcanic rocks, the effect of this simplification could be quite large. This would result in the estimated upper limit of 3600 years being an underestimation of the actual travel time.

Transport model simulations were conducted to evaluate the propagation of uncertainty in the input parameter values to the output breakthrough curves, as documented in Section 8 of this report. Starting with the base-case parameter values (Section 6), scenarios were constructed by considering one parameter at a time, using the upper and lower limit of each parameter value (Table 8.3-1). The parameters considered include specific discharge, horizontal anisotropy ratio in permeability, effective porosity in the alluvium, flowing interval aperture in the volcanics, effective diffusion coefficient in volcanics, and the longitudinal dispersivity. Reactive transport parameters were also considered in the analysis described in Section 8 but are not considered here, as they are not relevant to ^{14}C transport. The time at which 50% of the injected particles broke through the compliance boundary 18 km downstream from the repository footprint is given in Table 8.3-1.

It can be seen from Table 8.3-1 that most of the nonsorbing cases (Case numbers 1, 2, 3, 5, 8, 9, and 13) considered predict travel times within the range estimated on the basis of the ^{14}C hydrochemistry data discussed on the previous page of 84 to 3600 years. The base-case transport model leads to a transit time of 705 years, well within the range predicted by hydrochemistry data. This validation is considered acceptable, as defined in the TWP (BSC 2003 [163965], Section 2.3, first bullet of validation criteria). There are three outlier cases—using the limits of data interpretation discussed in the first paragraph of this section, and as discussed below, they are considered to be within the requirements of the model validation criteria:

- The case of maximum specific discharge leads to a travel time of 50 years, which is lower than the lower limit of 84 years calculated above. This case is within the criteria specified in TWP (BSC 2003 [163965], Section 2.3, first bullet of validation criteria).

- The case of minimum specific discharge leads to a travel time greater than 10,000 years, which is greater than the upper limit of 3600 years calculated from the ^{14}C data. As noted in the first paragraph of this section, the value of 3600 years is an estimate of the upper bound in the range of inferred transit times, and longer travel times cannot be completely excluded from consideration, based on the available data.

  A transit time of 3600 years would result from a specific discharge of approximately 0.15 m/yr. The rationale for choosing a lower value of 0.02 m/yr as the bounding value of the uncertainty distribution is based on expert elicitation (CRWMS M&O 1998 [100353], Figures 3-2a through 3-2e) and field data at the ATC (BSC 2003 [162415],

Section 6.5), and is discussed in (BSC 2003 [164870], Section 6.5.2.1). As seen in Figure 6-7 of (BSC 2003 [164870]), the uncertainty distribution at the low values of the specific discharge multiplier tapers off to 0 at a value of 1/30, and the cumulative probability of finding a value of specific discharge multiplier less than 1/4 (corresponding to the approximate travel time of 3600 years) is low (about 0.08), and only a few stochastically sampled values are expected to fall below the factor of 1/4.

- The case of a minimum value of flowing-interval aperture, which corresponds to the product of the minimum value of flowing-interval porosity and the minimum value of flowing-interval spacing, leads to a transit time greater than 10,000 years, which is greater than the upper limit of 3600 years calculated from the ^{14}C data. As noted in the first paragraph of this section, the value of 3600 years is an estimate of the upper bound in the range of inferred transit times, and longer travel times cannot be completely excluded from consideration, based on the available data.

A transit time of 3600 years would result from a flowing-interval aperture of approximately 2×10^{-4} m. The flowing interval aperture is calculated as the product of the flowing interval spacing and the flowing interval porosity. The rationale for choosing a lower value of 1.2×10^{-5} m as the limiting value of the uncertainty distribution, which corresponds to the lower limit 1.2 m for spacing and 10^{-5} for porosity, is discussed in detail in (BSC 2003 [164870], Sections 6.5.2.4 and 6.5.2.5). As seen in Figure 6-13 of (BSC 2003 [164870]), the uncertainty distribution at the low values of the porosity tapers off to zero at about 10^{-5}, and that of the interval spacing tapers off to zero at about 1.2 m (BSC 2003 [164870], Figure 6-12). Hence, the probability of finding a value of aperture less than 2×10^{-4} m (corresponding to the approximate travel time of 3600 years) is low, less than approximately 5%. Thus, only a few stochastically sampled values are expected to fall below the validated lower limit of about 2×10^{-4} m.

INTENTIONALLY LEFT BLANK

8. CONCLUSIONS

The SZ site-scale transport model is the culmination of efforts incorporating geologic, hydrologic, and geochemistry data from laboratory and field testing with theoretical models of radionuclide transport into a coherent representation of transport through the saturated zone near Yucca Mountain. This model uses as its basis the calibrated SZ site-scale flow model, which, in turn, is based on a 3-D finite element mesh with 500×500 m^2 horizontal elements.

The SZ site-scale transport model matches field data both quantitatively and qualitatively. These data include transit times derived from ^{14}C and flow paths inferred from Cl$^-$ and SO$_4^-$ hydrochemical data. The base case transport model leads to the breakthrough curve (Figure 6.6-1) at the 18 km compliance boundary (10 CFR 63.302 [156605]) corresponding to a breakthrough time at 50% concentration of 705 years.

The analysis of K_d data (Attachment I) and the modeling to upscale these data to a 500-m grid (Attachment III), combined with expert judgment (Attachment III) lead to the K_d distributions presented in Table III-14.

When using the SZ site-scale transport model for TSPA calculations, there are limitations that must be noted with regard to the following:

- *Input parameter values/ranges*. The transport model is intended for use with stochastic simulations using large uncertainty ranges for particular parameters such as specific discharge, fracture spacing and aperture, diffusion coefficient, and sorption coefficients. Care should be exercised in interpreting individual simulations for single sets of parameter values. Also, care should be exercised if the parameters used fall outside the range of parameter values (Table 4-2) or outside the range established by model validation (Section 7.2).

- *Useable path-line distances*. The flow field underlying the SZ transport model is based on the dual-porosity, effective-continuum approach requiring large grid blocks that effectively average fracture, rock matrix, and alluvium properties. Also, the parallel fracture model used to model advection/diffusion in the volcanics is valid only for grid-block sizes much larger than the expected flowing-interval spacing of 21 m. It is recommended in the SZ flow model report (BSC 2003 [162649], Section 8) that to produce meaningful results, the flow path should be long compared to the grid-block size. Because the grid-block size is 500 m, a minimum distance of 2 kilometers is recommended for path lines used in PA calculations.

- *Sufficient number of input particles for particle tracking*. Radionuclide transport is implemented in the SZ transport model using particle tracking with a random walk method (Sections 6.5.2.3 and 6.5.2.4). In order to obtain reproducible results, a sufficient number of particles must be input to the model. The base case transport model utilizes 1000 input particles (Output DTN: LA0306SK831231.001), visually judged to be sufficient for the purpose of obtaining a smooth breakthrough curve at the 18-km compliance boundary (Figure 6.6-1). However, a larger number of input particles may be required depending on the purpose of the model use.

8.1 SUMMARY OF MODELING ACTIVITIES

Available hydrogeology, hydrochemistry, field, and laboratory data on transport processes were reviewed to form a conceptual model of the transport processes of importance to the SZ site-scale region. Available data on sorption of radionuclides were synthesized to develop distributions for sorption parameters. A mathematical formulation of the conceptual model was developed and incorporated in a numerical code (FEHM V 2.20 [STN: 10086-2.20-00]). A calibrated numerical model of groundwater flow (the SZ site-scale flow model) was taken as the basis for transport calculations. A series of validation and confidence-building activities was completed. Finally, results of this model were provided (Output DTN: LA0306SK831231.001), and the associated uncertainties were discussed (Section 8.3).

8.1.1 Hydrogeologic Setting and Conceptual Flow Model

Yucca Mountain is located about 150 km northwest of Las Vegas, Nevada, in the Great Basin section of the Basin and Range province. This province is characterized by generally linear, north-trending mountain ranges separated by intervening basins. Yucca Mountain consists of a group of north-trending block-faulted ridges composed of volcanic rocks bounded by basins composed of volcanic rocks, alluvium, and, to the west, some small basaltic lava flows. The geology in the vicinity of Yucca Mountain consists of blocks of ash-flow and ash-fall tuffs, which pinch out to the south beneath valley-fill alluvium, underlain by a thick carbonate aquifer.

The groundwater in the area has been the subject of several investigations at the regional scale and the scale of interest for radionuclides that might enter the groundwater beneath the proposed repository. Yucca Mountain is part of the Alkali Flat-Furnace Creek sub-basin of the Death Valley groundwater basin. Water inputs to the sub-basin include groundwater influx along the northern boundary, recharge from precipitation in high elevation areas, and recharge from surface runoff in the Fortymile Canyon. Discharge within the sub-basin occurs at the Alkali Flat (Franklin Lake Playa) and possibly at the Furnace Creek in Death Valley.

The water table in the vicinity of the repository footprint is deep, as much as 750 m below the surface. The saturated zone occurs in thick ash-flow and ash-fall tuffs, underlain by the regional carbonate aquifer. The saturated volcanic units have been grouped into two confining layers and two aquifers. In general, the confining units are zeolitic, nonwelded tuffs, and the aquifers are welded, fractured tuffs.

The general conceptual model of SZ flow in the model area is that groundwater flows southwards from recharge areas in the north and at higher elevations, through the Tertiary volcanic rocks, towards the Amargosa Desert. Water inputs to the site-scale model include inflow along the northern boundary, recharge from precipitation at higher elevations, and recharge from surface runoff in the Fortymile Wash area. In the northern portion of the model, the flow occurs through the fractured volcanic rocks underlain by the carbonate aquifer. Towards the southern portion of the model area, the flow enters the valley-fill alluvium. Discharge from the model occurs via the alluvium, across the model boundary to the south and southeast, and through pumping of wells in the Amargosa Valley.

The overall groundwater flow is modeled as a 3-D steady-state system. A confined aquifer solution is used for the flow model. The dual-porosity, effective-continuum approach is used to model flow and transport, which averages fracture and surrounding rock properties in a given grid block, with the modification that several of the important fault zones are included as explicit features. The permeability to flow of the various tuff units and sub-units underlying the proposed repository site is mainly controlled by the degree of fracturing and faulting. A vertical-to-horizontal permeability anisotropy ratio of 0.1 is taken for most hydrologic units.

8.1.2 Conceptual Model of Transport

The flow paths from the repository site to the compliance boundary begin in the volcanic tuffs below the repository footprint and end in the alluvium of the Amargosa Valley. Radionuclides will likely enter the SZ via downward percolation of water from the UZ. Once the solutes enter the groundwater in the SZ, they remain there until they encounter a region of natural or artificial groundwater discharge. Within the SZ, radionuclides are transported in the upper-few-hundred meters below the water table with pore water that flows sub-horizontally in a southwardly direction through the highly fractured portions of the tuff, leading to the alluvium in the south.

Flow within the tuffs occurs through the highly fractured regions, with stagnant fluid residing in the rock matrix. The matrix materials conduct no fluid under natural groundwater flow conditions, but radionuclides diffuse between the fractured regions and the surrounding rock matrix, leading to retardation of the radionuclide migration.

The highly fractured tuff regions are most probably offset by low permeability regions, which effectively act as large-scale heterogeneities giving rise to large-scale macroscopic dispersion over the scale of kilometers. Field studies show that the dispersivity estimates from C-wells tracer experiments fall within the range of values from other sites, suggesting that transport in the fractured tuffs exhibits similar dispersive characteristics.

Sorption of radionuclides on rock surfaces is a mechanism that will enhance retardation of the solute movement. Radionuclide/rock interactions potentially can occur on the surfaces of fractures and within the rock matrix. This distinction is important because the surface-area-to-fluid-volume ratio and the mineral distributions probably are different in the fractures as compared to the matrix. Sorption within the rock matrix is supported by the C-wells tracer experiments. Sorption on fracture surfaces is not included in TSPA simulations of radionuclide transport.

Sorption reactions are represented in the transport model by a constant called the sorption coefficient or K_d. Ranges of K_d values and probability distributions are developed for various radionuclides to encompass the uncertainties in the theoretical model as well as the uncertainties from in situ hydrochemical conditions that affect the K_d values.

Due to the more porous, less fractured nature of the alluvial material, fluid flow in the alluvium is well represented using a porous continuum conceptual model. Flow and transport occurs through the relatively more permeable regions with the low-permeability regions acting as flow barriers contributing to dispersion. The fact that flow occurs only through the relatively permeable portion of the alluvium is accounted for by assigning a wide distribution to the effective porosity of the alluvium. Because the site-scale SZ flow and transport model is used to

predict concentrations under a well-withdrawal scenario, the potentially complex distribution of radionuclides within a grid block will be averaged in the process of extracting water from the aquifer.

Transport of radionuclides via colloids is an important mechanism. Radionuclides can adsorb onto colloids either reversibly or irreversibly. The reversibly-attached radionuclides are modeled using the K_c coefficient that accounts for colloid transport as well as the partitioning of the solutes between the colloids, the groundwater, and the rock surface. The influence of matrix diffusion is diminished for this fraction of the radionuclides, and this is accounted for by calculating a modified diffusion coefficient. The irreversibly attached radionuclides transport in the same way as the colloids themselves: a small fraction of these travels with the groundwater unretarded while the majority undergo filtration, which is accounted for using an effective K_d for the colloids.

8.1.3 Mathematical Model and Numerical Approach

The mathematical basis (and the associated numerical approaches) of the site-scale SZ transport model is designed to incorporate the important transport processes in an efficient numerical code to compute radionuclide breakthrough curves and transit times for use in TSPA simulations. A particle-tracking approach is used to compute solute trajectories and travel times, combined with a random-walk model to incorporate dispersion. A semi-analytical method is used for including retardation due to diffusion and sorption, as well as colloid-facilitated transport in the random-walk model.

8.1.4 Model Validation and Confidence Building

Recognizing that the site-scale SZ transport model is being used to perform probabilistic calculations in which parameter uncertainties are propagated through the model, the intent of validation was to confirm the radionuclide parameters and processes included in the model. Confidence in the results of the model was built by a series of different approaches that included: (1) comparisons to analog sites, (2) model-data comparisons, (3) comparison with data published in refereed journals, and (4) comparison to an independent site-scale groundwater flow model for the Yucca Mountain SZ. The data used in the confidence building for the relevant transport parameters (e.g., sorption coefficient), submodel processes (e.g., advection, sorption), and site scale model processes (e.g., flow pathways, transit times) were based on laboratory testing, field tests, natural analog sites, and expert elicitations. The model was validated by post-development comparison of model transit times with those inferred from ^{14}C data and qualitative comparison of flow paths predicted by the model and those inferred from the hydrochemistry data.

8.2 OUTPUTS

8.2.1 Technical Output

The technical output of this report is comprised of (a) the SZ site-scale transport model and associated input and output files (base-case transport files); and (b) SZ Distribution Coefficients (K_ds) data for U, Np, Pu, Cs, Am, Pa, Sr, Th, Ra, C, Tc, and I (Table III-14). The output breakthrough curves and travel times will be integrated into the SZ flow and transport abstractions model for use in the TSPA calculations.

8.2.2 Developed Output Listed by Data Tracking Number

The outputs associated with the site scale SZ transport model are listed in Table 8.2-1.

Table 8.2-1. Output Data

Transport Model		
Data Description	**Source**	**Data Tracking Number**
Saturated zone distribution coefficient (K_d) data for U, Np, Pu, Cs, Am, Pa, Sr, Th, and Ra	Attachments I and III	LA0310AM831341.002
Type curve data for FEHM macro 'sptr' based on Sudicky and Frind solution	Section 6	LA0302RP831228.001
Modeling calculations of radionuclide sorption via surface-complexation reactions and solubilities of U, Sr, Ba in water	Attachment I	LA0306AM831343.001 Files contained in the directory "output"
Files for FEHM V 2.20 for SZ site-scale transport model, FEHM files for base case	Section 6.5.3 and Section 6.6	LA0306SK831231.001
Files for FEHM V 2.20 for evaluating barrier capabilities	Section 6.7	LA0307ZD831231.001
Files for FEHM V 2.20 for comparison of flow paths against those from hydrochemistry data	Section 7.2.1	LA0307SK831231.001
Files for FEHM V 2.20 for specific discharge	Section 6.5.3 and Section 6.6	LA0307SK831231.002
Files for FEHM V 2.20 for evaluating propagation of uncertainty in the input parameter values	Section 8.3.2	LA0309SK831231.001
Files for GSLIB for generating stochastic realizations of rock types from mineralogic data	Attachment III	LA0309RP831321.001
Files FEHM V 2.20 for calculation of effective K_d distribution for U	Attachment III	LA0309RP831341.004
Files FEHM V 2.20 for calculation of effective K_d distribution for Cs	Attachment III	LA0309RP831341.001
Files FEHM V 2.20 for calculation of effective K_d distribution for Np	Attachment III	LA0309RP831341.002
Files FEHM V 2.20 for calculation of effective K_d distribution for Pu	Attachment III	LA0309RP831341.003

8.3 OUTPUT UNCERTAINTY

8.3.1 Types of Uncertainty

Model-form uncertainty (BSC 2002 [158794], Section 4.1.1) in regards to the transport model is unavoidable given the sparseness of observed data and the limited amount of information available to corroborate or refute alternative models. This form of uncertainty is explicitly addressed by discussing alternative conceptual models (ACMs) in Section 6.4 of this report. The discussion and screening of the ACMs is based on available understanding and data. As discussed in Section 6.4, several of the ACMs are implicitly included in the model through the use of uncertainty distributions for parameter values. Although the model is meant to represent the saturated zone transport accurately, for the case of those ACMs that could not be included in the model, the transport model was selected such that it resulted in transit times faster than those expected for the ACM.

There is epistemic uncertainty (BSC 2002 [158794], Section 4.1.1) in the parameter space of the base-case conceptual model. This form of uncertainty is explicitly described by using probability distributions for appropriate model parameters. Expected uncertainty ranges for the various transport parameters are discussed in Section 4.1.2 and summarized in Table 4-2, of this report. The development and discussion of the K_d parameters needed for modeling reactive transport and the K_c parameters needed for modeling colloid-facilitated transport are presented in Attachments I, II and III of this report. The probability distributions for all other model parameters are presented and discussed in the model report *SZ Flow and Transport Model Abstraction* (BSC 2003 [164870], Section 6.5.2). These uncertainties are propagated through the model to the output breakthrough curves, presented in Section 8.3.2 of this report. Radionuclide transit times are most sensitive to groundwater-specific discharge. This is because increasing the specific discharge not only increases the advective velocity but also reduces the time available for matrix diffusion to be effective. In assessing the sensitivity of breakthrough times to the specific discharge through the model, permeabilities of the various units are scaled along with the specific discharge to preserve the model calibration. Other parameters of importance to the breakthrough times are matrix diffusion, the sorption coefficient in the volcanics as well as the alluvium, the effective fracture porosity in the volcanics (as reflected in the flowing interval aperture and spacing), the effective porosity in the alluvium, the sorption coefficients for reversible colloids and retardation factor for irreversible colloids in the volcanics and alluvium. The volcanic retardation factors are important since the distribution contains large values that results in significant retardation even though transport times in the volcanics are shorter than the transport times in the alluvium. The alluvium retardation factors are lower than the volcanics but the contaminants spend the majority of the time in the alluvium. Therefore, any retardation in the alluvium results in large effects in the overall travel time. It should be also noted that although the time for 50% breakthrough shows only a moderate sensitivity to the value of longitudinal dispersivity (Figure 8.3-13), the leading and tailing edge of the breakthrough curve are significantly affected for dispersivity values near the upper limit. Thus dispersivity could be an important parameter to consider in situations where the first and last arrival times for radionuclides play an important role. Quantification of the sensitivity of the model output breakthrough curves for various radionuclides of concern to parameter uncertainties are further evaluated in the model report *SZ Flow and Transport Model Abstraction* (BSC 2003 [164870], Section 6.7, 6.9, and 8).

There are uncertainties associated with scaling parameter values from the scale of measurements to the scale of interest. Much of the data used for deriving parameter values in this report is from laboratory or field experiments conducted on spatial and temporal scales much smaller than those expected to occur in site-scale SZ model. Most of the measurements are done on sample sizes less than a meter, with the exception of the C-wells and ATC field tests, which were conducted on the scale of tens of meters. This scale is still several orders of magnitude smaller than the site scale. Necessarily, these parameter values reflect the rock properties on the scale of measurement. Because the objective here is to calculate cumulative breakthrough curves at a compliance boundary, large grid spacing (500 m x 500 m) is used in the numerical model. This leads to significant averaging of properties in the model calculations, thereby reducing the sensitivity of the output results to the stochastic variations in the parameter values. This is well demonstrated by the analysis presented in Attachment III for upscaling the distribution of the K_d values from a 4-m to a 500-m scale in the absence of spatial correlations. These calculations demonstrate that the resulting 500-m-scale K_d distribution is actually narrower, with a standard deviation of 0.7 cc/g (and a mean of 6.99 cc/g) than the two starting 4-m-scale K_d distributions with standard deviations of 2 cc/g and 3.6 cc/g. However, geological formations are inherently inhomogeneous, and they embed fractures, faults, and other heterogeneities on a variety of scales. Spatial correlations over some length scales often exist. Thus, it is difficult to extrapolate the measurements on a small scale to the SZ site scale. For this reason, wide distributions of input parameter values (Table 4-2) are used in the TSPA analysis (BSC (2003 [164870], Section 6.5.2).

8.3.2   Propagation of Uncertainty in the Input Parameter Values to the Output

Starting with the SZ site scale base-case transport model, sensitivity of the output breakthrough curves to each of the uncertain input parameters was investigated by considering the upper and lower levels of each parameter individually (Table 8.3-1).

Table 8.3-1. Effect of Parameter Ranges on 50% Breakthrough Times

	Parameter	Base Case Value(s)	Uncertainty Range (Units)	Output Range, Time (Years) for 50% Breakthrough
1	Specific discharge multiplication factor [a]	1	1/30 – 10	50 to >10,000
2	Permeability horizontal anisotropy	4.2	0.05 – 20 (ratio)	352 to 922
3	Bulk density in alluvium	1910	1669 – 2151 kg/m^3	705
4	Sorption coefficient in alluvium	0.0	0 – 10000 (mL/g)	705 to >10,000
5	Effective porosity in the alluvium	0.18	0. 02 – 0.3 (fraction)	349 to 913
6	Colloid retardation factor in alluvium for irreversible colloids	0	0 [e] – 5188 (ratio)	705 to >10,000
7	Effective sorption coefficient for radionuclides with reversible sorption onto colloids in alluvium [b]	0	0 – 10,000 (mL/g)	705 to >10,000
8	Flowing interval aperture [c]	0.2	1.2×10^{-5} – 41.7 [d] (m)	443 to >10,000
9	Effective diffusion coefficient in volcanics	5.0×10^{-11}	5.0×10^{-12} – 5.0×10^{-10} (m^2/s)	520 to 2100
10	Matrix sorption coefficient in volcanics	0.0	0 – 10,000 (mL/g)	705 to >10,000
11	Colloid retardation factor in volcanics for irreversible colloids	0	0 [e] – 794 (ratio)	705 to >10,000
12	Effective sorption coefficient for radionuclides with reversible sorption onto colloids in volcanics [b]	0	0 – 10000 (mL/g)	705 to >10,000
13	Dispersivity, longitudinal	10.0	0.10 – 2000 (m)	664 to 1486

NOTE: [a] Base-case permeabilities and the recharge and boundary fluxes are multiplied by this factor to vary specific discharge without affecting the flow calibration.

[b] See Equations 79 to 81 in Section 6.5.2.6.

[c] Flowing interval aperture is the product of the flowing interval porosity and flowing interval spacing.

[d] This value is made to address the case when flowing interval spacing is very large.

[e] This value is lower than the lower limit of 6 given in Table 4-2, thus bracketing the range from Table 4-2. The lower value is chosen for this analysis in order to include the base case.

8.3.2.1 Specific Discharge Multiplier

The results from simulations that evaluate the effect of changes in the specific discharge are shown in Figure 8.3-1. In these simulations, the base-case flow model was modified to scale the input recharge fluxes by the same factor as the rock permeabilities to preserve the model calibration. The results show that output is very sensitive to the level of uncertainty in this parameter. For the case of upper limit of specific discharge multiplier where the base case fluxes are multiplied by a factor of 10, time to 50% breakthrough is 50 years (with extremely fast fluid flow such as would be expected for the very unlikely case of a high permeability channel going continuously over the distance of 18 km in a highly faulted region). The lower limit of specific discharge multiplier, a factor of 1/30, leads to breakthrough times at greater than 10,000 years. This indicates that information that helps reduce the uncertainty of this parameter will greatly improve the ability of the model to predict the results.
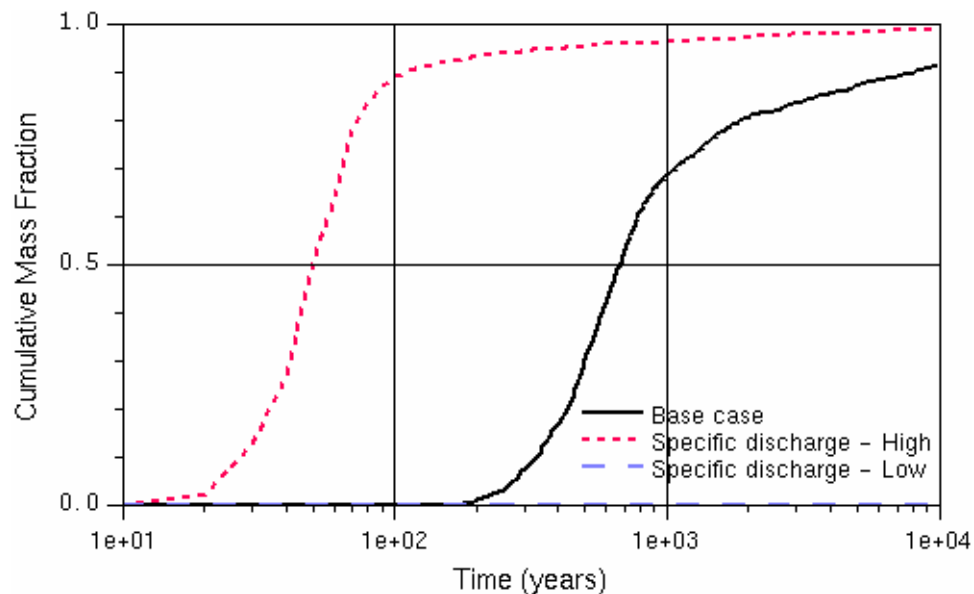
Output DTN: LA0309SK831231.001

Figure 8.3-1. Propagation of Input Uncertainty in the Specific Discharge to the Output Breakthrough Curves at the 18-km Boundary

8.3.2.2 Horizontal Permeability Anisotropy

The results from simulations that evaluate the effect of changes in the ratio of horizontal permeability anisotropy are shown in Figure 8.3-2. The base-case flow model was modified to include the permeability ratios; however, note that the flow model was not recalibrated for the different values of permeability. The output shows a moderate level of variation resulting from the uncertainty limits of this parameter (0.05 to 20, Table 8.3-1) with the time for 50% breakthrough varying between 352 to 922 years. This variation results mainly from the variation in the flow paths due to the changed velocity fields corresponding to the different ratios of the east-west versus the north-south permeabilities.
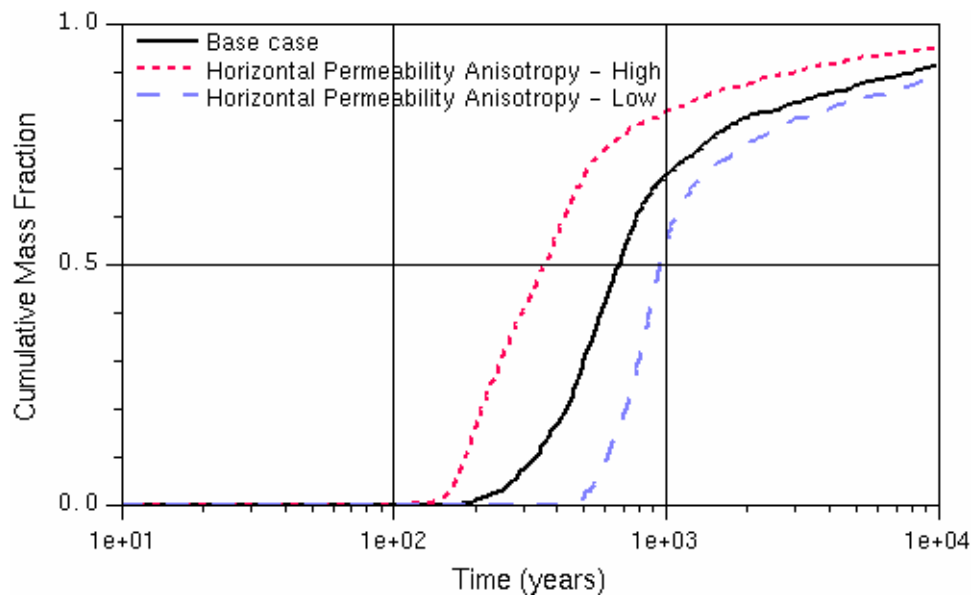
Output DTN: LA0309SK831231.001

Figure 8.3-2. Propagation of Input Uncertainty in the Horizontal Permeability Anisotropy Ratio to the Output Breakthrough Curves at the 18-km Boundary

8.3.2.3 Bulk Density in Alluvium

The results from simulations that evaluate the effect of changes in the bulk density in the alluvium are shown in Figure 8.3-3. Note that these simulations are for the base case without sorption. There is no significant difference between the breakthrough curves because the bulk density enters the transport calculations only through the retardation factor as given in Equation 57 (Section 6.5.2.4.1) of this report.
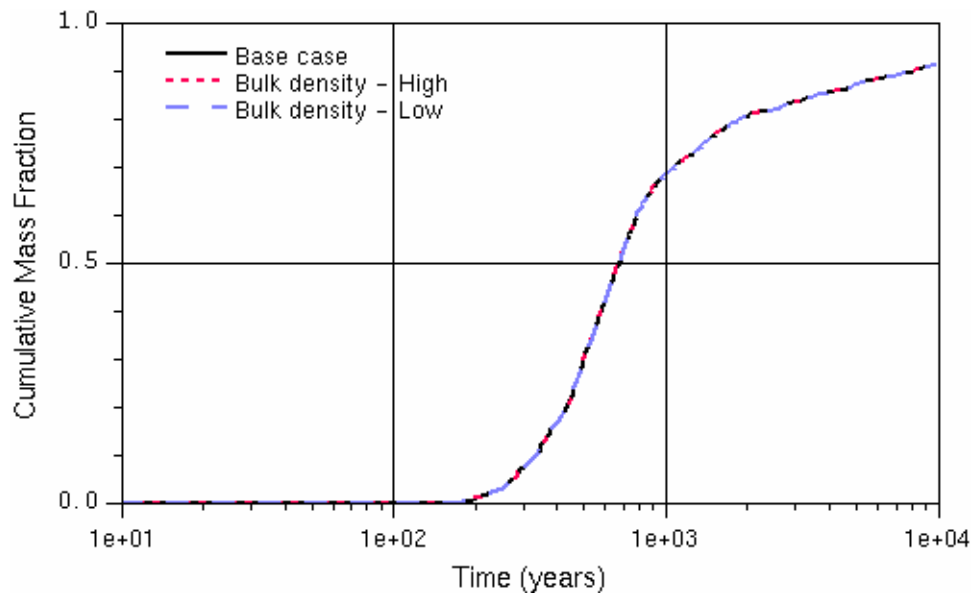
Output DTN: LA0309SK831231.001

Figure 8.3-3. Propagation of Input Uncertainty in the Bulk Density of Alluvium to the Output Breakthrough Curves at the 18-km Boundary

8.3.2.4   Sorption Coefficient in Alluvium

The results from simulations that evaluate the effect of changes in sorption coefficient in alluvium on the output breakthrough curves are shown in Figure 8.3-4. The results indicate that when the sorption coefficient is high, no breakthrough of the tracers is observed in 10,000 years. Thus, the alluvium could form a very effective barrier for sorbing radionuclides. The base-case simulation is the same as for the low-sorption case because the base case value of the sorption coefficient is 0, meant to capture the behavior of a nonsorbing radionuclide.
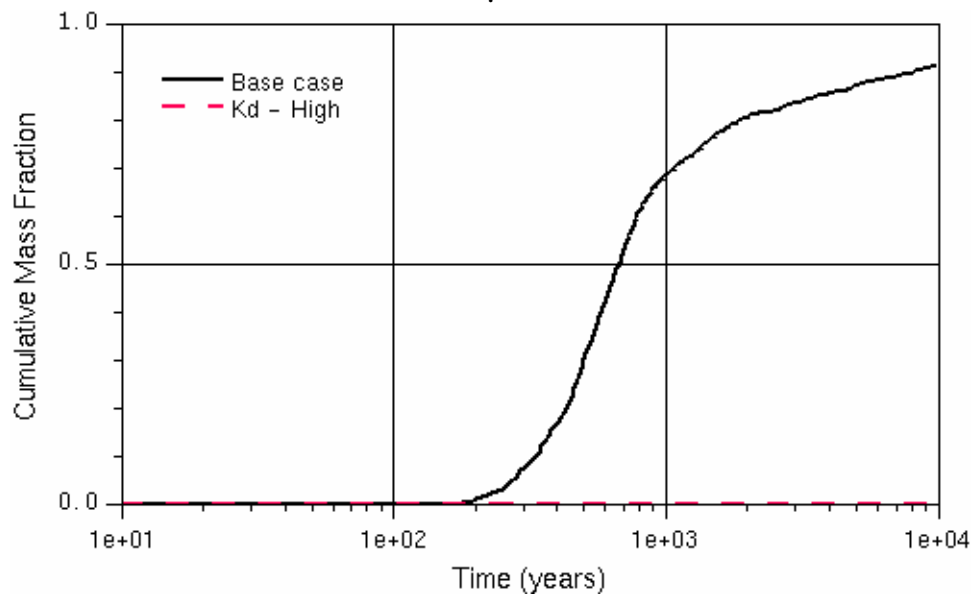
Output DTN: LA0309SK831231.001

Figure 8.3-4. Propagation of Input Uncertainty in the Sorption Coefficient in Alluvium to the Output Breakthrough Curves at the 18-km Boundary

8.3.2.5 Effective Porosity in Alluvium

The results from simulations that evaluate the effect of changes in the effective porosity in the alluvium are shown in Figure 8.3-5. Note that in these simulations, the influence of the alluvium porosity on the retardation factor (Equation 57 of this report) does not show up because the base case does not include sorption. Thus, the effect seen in Figure 8.3-5 is that resulting from the effect of porosity on the fluid velocity through the relation:

$$\bar{v} = \frac{\bar{u}}{\theta} \qquad \text{(Eq. 82)}$$

where

$\bar{u}$ is the Darcy velocity obtained from the base-case flow model

$\bar{v}$ is the fluid velocity

θ is the porosity.

A moderate sensitivity is seen in Table 8.3-1 with the 50% breakthrough time spanning 349 to 913 years for the input range of values from 0.02 to 0.3.
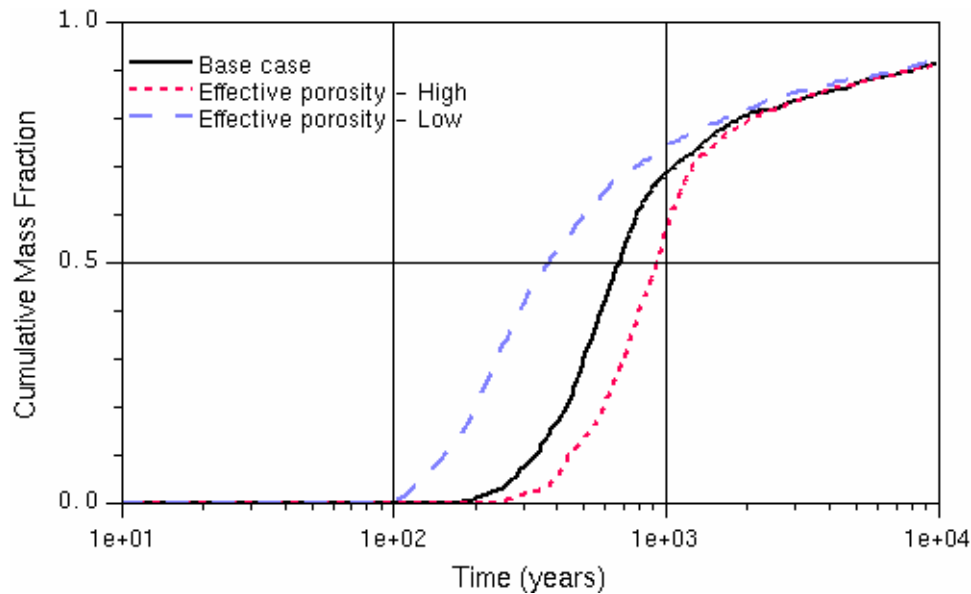
Output DTN: LA0309SK831231.001

Figure 8.3-5. Propagation of Input Uncertainty in the Effective Porosity of Alluvium to the Breakthrough Curves at the 18-km Boundary

8.3.2.6 Retardation Factor in Alluvium for Radionuclides Attached Irreversibly to Colloids

The results from simulations that evaluate the effect of changes in the colloid retardation factor in the alluvium are shown in Figure 8.3-6. As discussed in Section 6.5.2.6, these results include the retardation of the colloid particles due to reversible filtration in the porous media. The effect of colloids transported unretarded is applied in the TSPA calculations after the breakthrough curves are calculated from the SZ transport model, and hence it is not considered here. For comparison the base case, which considers nonsorbing radionuclides without any retardation, is also shown. Note that the retardation arises from the reversible filtration of the colloids in the alluvium. The range of uncertainty in the retardation factor of 0 to 794 translates into an output uncertainty range of 705 to >10,000 years for the breakthrough time for 50% of the colloids years.
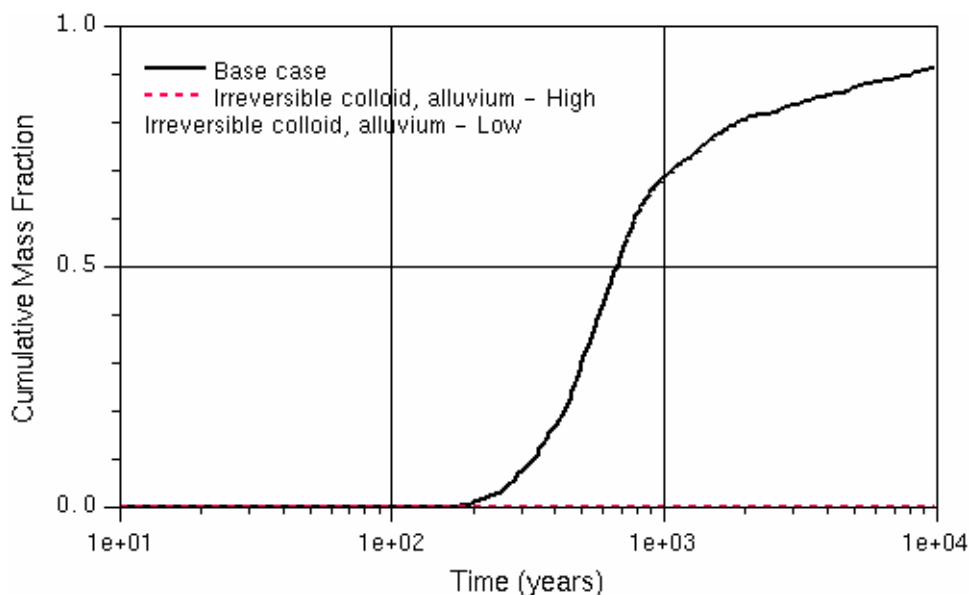
Output DTN: LA0309SK831231.001

Note: Effect of colloids transported unretarded is applied in the TSPA calculations after the breakthrough curves are calculated from the SZ transport model, and hence it is not considered here.

Figure 8.3-6. Propagation of Input Uncertainty in the Colloid Retardation Factor in Alluvium for Irreversible Colloids to the Breakthrough Curves at the 18-km Boundary

8.3.2.7   Reversible Sorption onto Colloids in the Alluvium

The results from simulations that evaluate the effect of changes in distribution parameters for reversible sorption onto colloids in alluvium are shown in Figure 8.3-7. Note that by using Equations 78 to 80 of this report, the modified sorption coefficient for this case has the same range of values as the original sorption coefficient in alluvium; that is, 0 to 10000 mL/g (Table 8.3-1 of this report). Thus, the results for the lower limiting case are identical to the base case, and those for the upper limiting case show no breakthrough at all within 10,000 years.

Output DTN: LA0309SK831231.001

Figure 8.3-7. Propagation of Input Uncertainty in the Colloid Retardation Factor in Alluvium for Reversible Colloids to the Output Breakthrough Curves at the 18-km Boundary

8.3.2.8 Flowing Interval Aperture in Volcanics

The results from simulations that evaluate the effect of changes in flowing interval aperture in volcanics on the breakthrough curves are shown in Figure 8.3-8. When the flow aperture is at the lower end of the parameter distribution, 1.2×10^{-5} m (see Table 8.3-1), the retardation due to matrix diffusion is amplified so much that it overtakes the effects of increased velocities in the flowing interval. This results in no breakthrough observed during the 10,000 years considered. The reverse is true for the upper limit of the aperture, 41.7 m, where there is very little diffusion, and breakthrough occurs somewhat earlier than in the base case (in 443 years rather than the base-case value of 705 years).

Output DTN: LA0309SK831231.001

Figure 8.3-8. Propagation of Input Uncertainty in the Flowing Interval Aperture in Volcanics to the Breakthrough Curves at the 18-km Boundary

8.3.2.9 Effective Diffusion Coefficient in Volcanics

The results from simulations that evaluate the effect of changes in effective diffusion coefficient in volcanics on the breakthrough curves are shown in Figure 8.3-9. The range of 5.0×10^{-12} to 5.0×10^{-10} (m^2/s) in the input value results in the range of 520 to 2100 years for output (50% breakthrough time). Considering that this parameter affects only the transport through the volcanics and not through that in the alluvium, it has a significant impact on the output.

Output DTN: LA0309SK831231.001

Figure 8.3-9. Propagation of Input Uncertainty in the Effective Diffusion Coefficient in Volcanics to the Output Breakthrough Curves at the 18-km Boundary

8.3.2.10 Matrix Sorption Coefficient in Volcanics

The results from simulations that evaluate the effect of changes in matrix sorption coefficient in volcanics on the output breakthrough curves are shown in Figure 8.3-10. The results indicate that when the sorption coefficient is high (10,000 mL/g), no breakthrough of the tracers is observed in 10,000 years. Thus, the volcanics could form a very effective barrier for those radionuclides that diffuse and adsorb in the matrix. The base-case simulation is the same as for the low-sorption case because the base case value of the matrix sorption coefficient is 0, which is the same as the lower limit value.
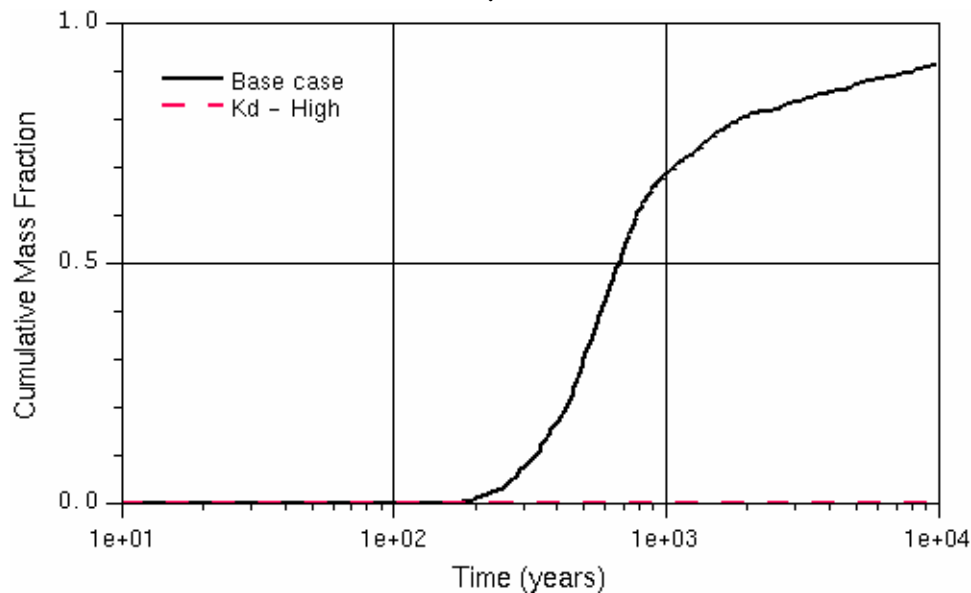
Output DTN: LA0309SK831231.001

Figure 8.3-10. Propagation of Input Uncertainty in the Matrix Sorption Coefficient in Volcanics to the Output Breakthrough Curves at the 18-km Boundary

8.3.2.11 Retardation Factor in Volcanics for Radionuclides Attached Irreversibly to Colloids

The results from simulations that evaluate the effect of changes in the colloid retardation factor on the transport of irreversibly sorbed radionuclides in volcanics on the output breakthrough curves are shown in Figure 8.3-11. As discussed in Section 6.5.2.6, these results include the retardation of the colloid particles due to reversible filtration in the porous media. The effect of colloids transported unretarded is applied in the TSPA calculations after the breakthrough curves are calculated from the SZ transport model, and hence it is not considered here. For comparison the base case, which considers nonsorbing radionuclides without any retardation, is also shown. Note that the colloids are modeled as having no diffusion into the volcanic matrix, and the retardation arises from the reversible filtration of the colloids within the fractures. The range of uncertainty in the retardation factor of 0 to 794 translates into an output uncertainty range of 705 to >10,000 years for the breakthrough time for 50% of the colloids years.
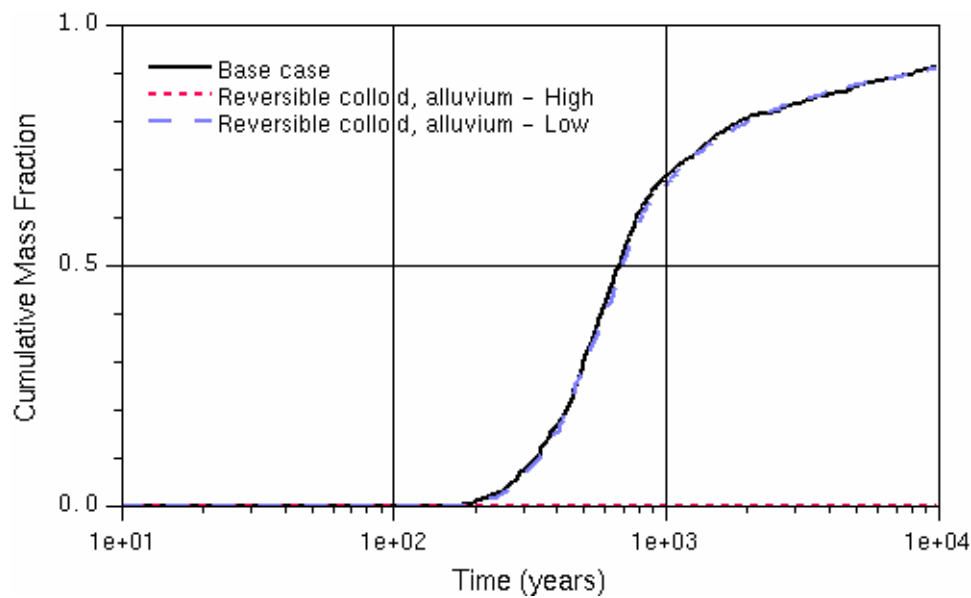

Output DTN: LA0309SK831231.001
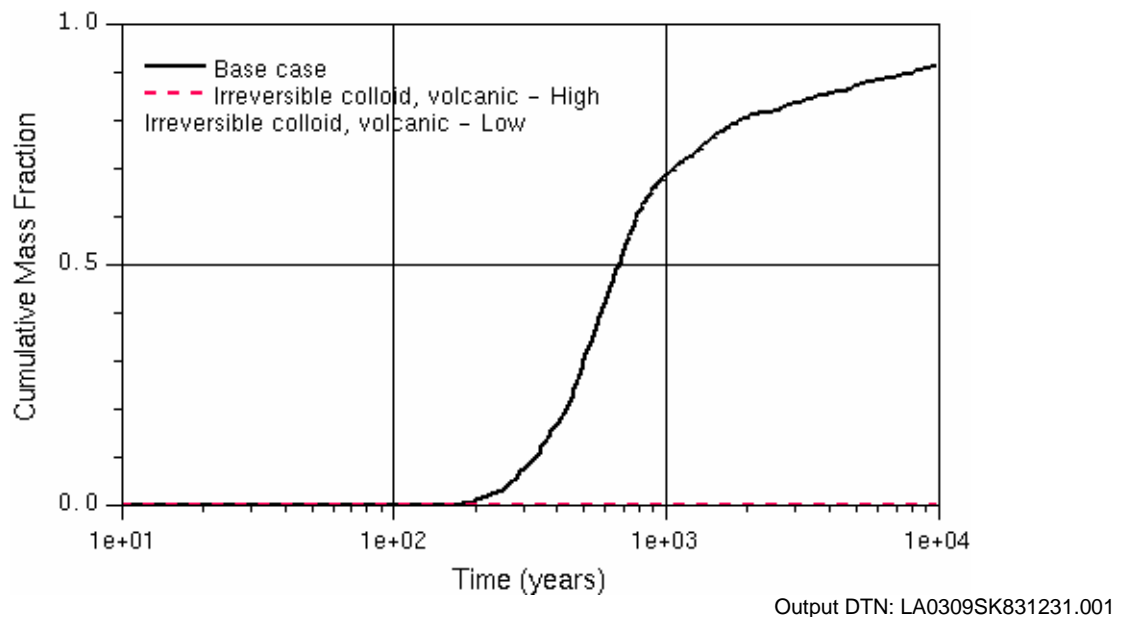
Note: Effect of colloids transported unretarded is applied in the TSPA calculations after the breakthrough curves are calculated from the SZ transport model, and hence it is not considered here.

Figure 8.3-11. Propagation of Input Uncertainty in the Colloid Retardation Factor in Volcanics for Irreversible Colloids to the Output Breakthrough Curves at the 18-km Boundary

8.3.2.12   Reversible Sorption onto Colloids in the Volcanics

As described in Section 6.5.2.6.2, transport of radionuclides attached reversibly to colloids is described by the distribution parameter K_c, which in turn is a product of the concentration of colloids in the groundwater and the sorption coefficient for the radionuclide onto the colloids. The results from simulations that evaluate the effect of changes in the distribution parameter K_c for reversible sorption onto colloids in the volcanics are shown in Figure 8.3-12. Note that using Equations 80a, 80b and 81of this report, the modified sorption coefficient for this case has the same range of values as the original sorption coefficient in volcanics; that is, 0 to 10,000 mL/g (Table 8.3-1 of this report). Thus, the results for the lower limiting case are identical to the base case, and those for the upper limiting case show no breakthrough at all within 10,000 years.
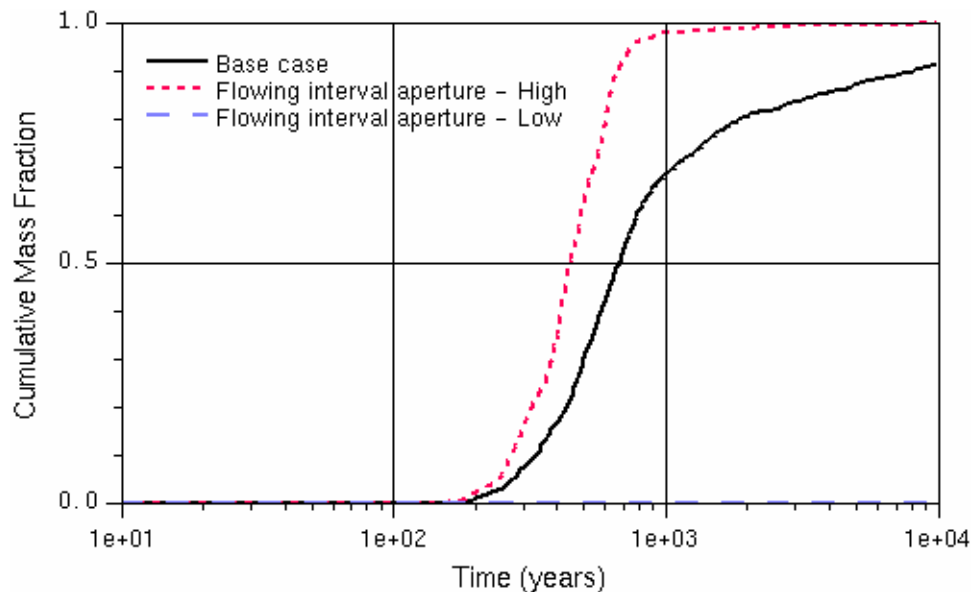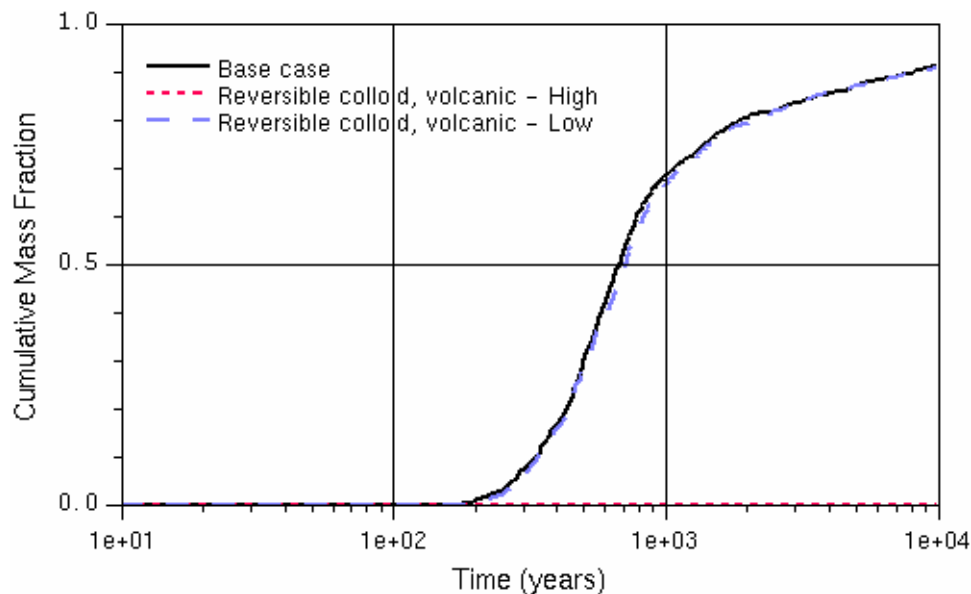

Output DTN: LA0309SK831231.001

Figure 8.3-12. Propagation of Input Uncertainty in the Distribution Parameter K_c in Volcanics for Reversible Colloids to the Output Breakthrough Curves at the 18-km Boundary

8.3.2.13   Longitudinal Dispersivity

The results from simulations that evaluate the effect of changes in longitudinal dispersivity on the output breakthrough curves are shown in Figure 8.3-13. In these simulations the same longitudinal dispersivity values were applied to both the volcanics and the alluvium together. At the minimum value of dispersivity (0.1 m), the results with a breakthrough time of 664 years, are only slightly different from the base case (which has a dispersivity value of 10 m). This is because at low values of dispersivity, both the effects of spreading in the source term and diffusion tend to mask the effects of dispersion. At maximum values of dispersivity (2000 m), an earlier low-concentration breakthrough is observed, which continues at a lower concentration relative to the base case for the duration of the simulation. The 50% breakthrough is delayed to 1,486 years. The high dispersivity case has an overall longer release time (start to end of release) than the other cases.
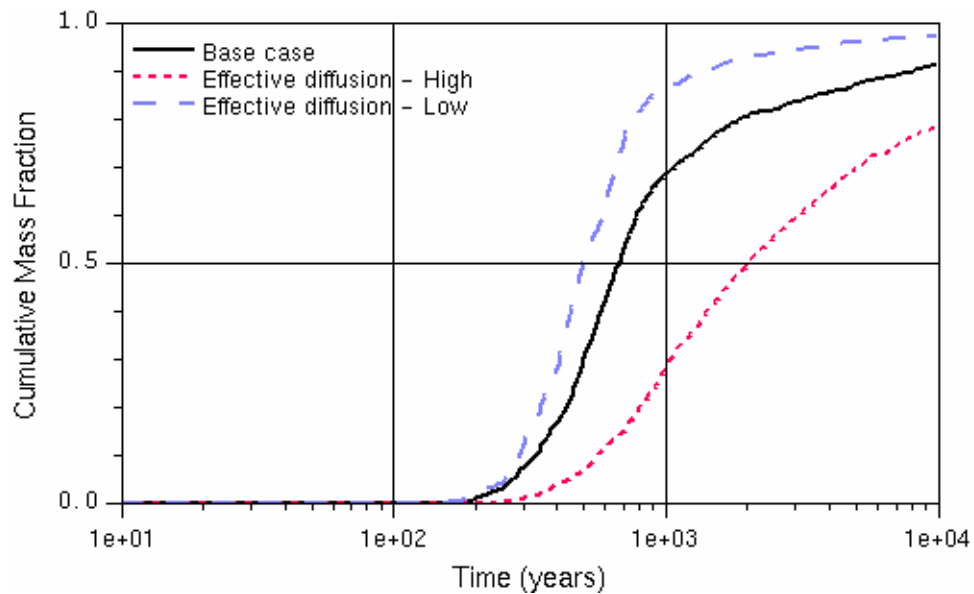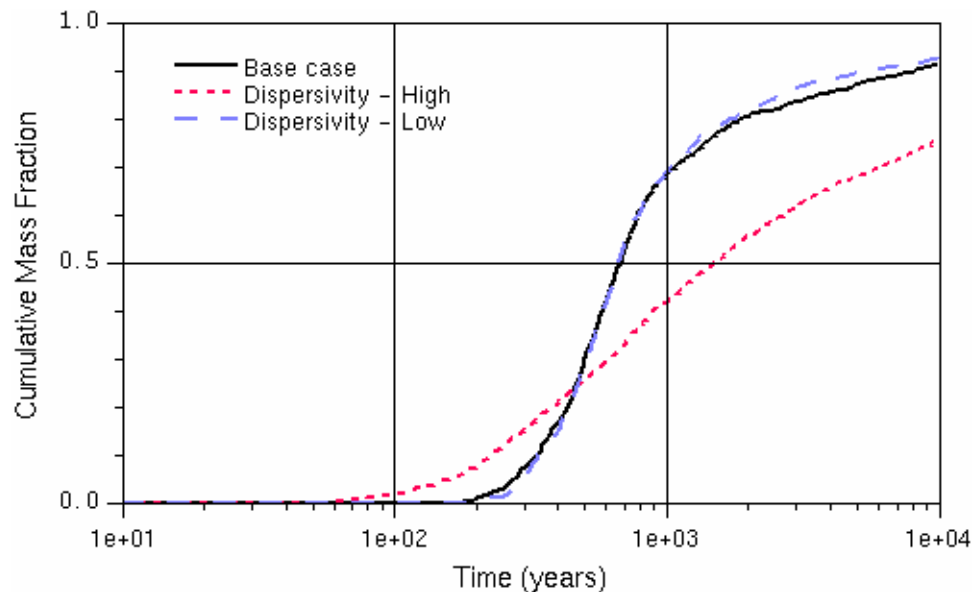

Output DTN: LA0309SK831231.001

Figure 8.3-13. Propagation of Input Uncertainty in the Longitudinal Dispersivity to the Output Breakthrough Curves at the 18-km Boundary

INTENTIONALLY LEFT BLANK

9. INPUTS AND REFERENCES

9.1   DOCUMENTS CITED

104512   Allard, B 1982. *Sorption of Actinides in Granitic Rock*. SKB TR-82-21. Stockholm, Sweden: Svensk Kärnbränsleförsörjning A.B. TIC: 205892.

147235   Allard, B. and Beall, G.W. 1979. "Sorption of Americium on Geologic Media." *Journal of Environmental Health, A14,* (6), 507-518. New York, New York: Marcel Dekker. TIC: 224102.

104410   Allard, B.; Beall, G.W.; and Krajewski, T. 1980. "The Sorption of Actinides in Igneous Rocks." *Nuclear Technology*, *49*, (3), 474–480. La Grange Park, Illinois: American Nuclear Society. TIC: 245772.

162982   Allard, B.; Olofsson, U.; Torstenfelt, B.; and Kipatsi, H. 1983. *Sorption Behaviour of Well-Defined Oxidation States*. SKB TR-83-61. Stockholm, Sweden: Svensk Kärnbränsleförsörjning A.B. TIC: 206122.

104397   Anderson, M.P. 1979. "Using Models to Simulate the Movement of Contaminants Through Groundwater Flow Systems." *CRC Critical Reviews in Environmental Control.* Pages 97-156. Boca Raton, Florida: CRC Press. TIC: 224010.

144539   Bahr, J.M. and Rubin, J. 1987. "Direct Comparison of Kinetic and Local Equilibrium Formulations for Solute Transport Affected by Surface Reactions." *Water Resources Research*, *23*, (3), 438–452. Washington, D.C.: American Geophysical Union. TIC: 246894.

162983   Beall, G.W.; Lee, W.W.-L.; and Van Luik, A.E. 1986. "Americium Speciation and Distribution Coefficients in a Granitic Ground Water." *Scientific Basis for Nuclear Waste Management IX, Symposium held September 9–11, 1985, Stockholm, Sweden*. Werme, L.O., ed. *50*, 501–508. Pittsburgh, Pennsylvania: Materials Research Society. TIC: 203664.

156269   Bear, J. 1972. *Dynamics of Fluids in Porous Media.* Environmental Science Series. Biswas, A.K., ed. New York, New York: Elsevier. TIC: 217356.

129676   Bedinger, M.S.; Sargent, K.A.; Langer, W.H.; Sherman, F.B.; Reed, J.E.; and Brady, B.T. 1989. *Studies of Geology and Hydrology in the Basin and Range Province, Southwestern United States, for Isolation of High-Level Radioactive Waste—Basis of Characterization and Evaluation.* U.S. Geological Survey Professional Paper 1370A. Washington, D.C.: U.S. Government Printing Office. ACC: NNA.19910524.0125.

101036   Benson, L.V. and McKinley, P.W. 1985. *Chemical Composition of Ground Water in the Yucca Mountain Area, Nevada, 1971-84*. Open-File Report 85-484. Denver, Colorado: U.S. Geological Survey. ACC: NNA.19900207.0281.

100727   Benson, L. V.; Robison, J. H.; Blankennagel, R. K.; and Ogard, A. E. 1983. *Chemical Composition of Ground Water and the Locations of Permeable Zones in the*

Yucca Mountain Area, Nevada. Open-File Report 83-854. Denver, Colorado: U.S. Geological Survey. ACC: NNA.19870610.0028.

144728   Berry, J.A.; Hobley, J.; Lane, S.A.; Littleboy, A.K.; Nash, M.J.; Oliver, P.; Smith-Briggs, J.L.; and Williams, S.J. 1989. "Solubility and Sorption of Protactinium in the Near-Field and Far-Field Environments of a Radioactive Waste Repository." *Analyst*, *114*, 339–347. Cambridge, England: Royal Society of Chemistry. TIC: 247004.

162984   Bertetti, F.P.; Pabalan, R.T.; and Almendarez, M.G. 1998. "Studies of Neptunium {superscript V} Sorption on Quartz, Clinoptilolite, Montmorillonite, and α-Alumina." *Adsorption of Metals by Geomedia*. Jenne, E.A., ed. Pages 131–148. New York, New York: Academic Press. TIC: 239501.

100023   Broxton, D.E.; Warren, R.G.; Hagan, R.C.; and Luedemann, G. 1986. *Chemistry of Diagenetically Altered Tuffs at a Potential Nuclear Waste Repository, Yucca Mountain, Nye County, Nevada*. LA-10802-MS. Los Alamos, New Mexico: Los Alamos National Laboratory. ACC: MOL.19980527.0202.

157132   BSC 2001. *Input and Results of the Base Case Saturated Zone Flow and Transport Model for TSPA*. ANL-NBS-HS-000030 REV 00 ICN 01. Las Vegas, Nevada: Bechtel SAIC Company. ACC: MOL.20011112.0068.

156965   BSC 2001. *Probability Distribution for Flowing Interval Spacing.* ANL-NBS-MD-000003 REV 00 ICN 02. Las Vegas, Nevada: Bechtel SAIC Company. ACC: MOL.20010625.0304.

158794   BSC (Bechtel SAIC Company) 2002. *Guidelines for Developing and Documenting Alternative Conceptual Models, Model Abstractions, and Parameter Uncertainty in the Total System Performance Assessment for the License Application*. TDR-WIS-PA-000008 REV 00, ICN 01. Las Vegas, Nevada: Bechtel SAIC Company. ACC: MOL.20020904.0002.

158730   BSC 2002. *Mineralogic Model (MM3.0) Analysis Model Report.* MDL-NBS-GS-000003 REV 00 ICN 02. Las Vegas, Nevada: Bechtel SAIC Company. ACC: MOL.20020423.0151.

160405   BSC (Bechtel SAIC Company) 2002. *Natural Analogue Synthesis Report.* TDR-NBS-GS-000027 REV 00 ICN 02. Las Vegas, Nevada: Bechtel SAIC Company. ACC: MOL.20020520.0288

160059   BSC 2002. *Radionuclide Screening*. ANL-WIS-MD-000006 REV 01. Las Vegas, Nevada: Bechtel SAIC Company. ACC: MOL.20020923.0177.

159530   BSC 2002. *Rock Properties Model Analysis Model Report.* MDL-NBS-GS-000004 REV 00 ICN 03. Las Vegas, Nevada: Bechtel SAIC Company. ACC: MOL.20020429.0086.

160313   BSC 2002. *Scientific Processes Guidelines Manual.* MIS-WIS-MD-000001 REV 01. Las Vegas, Nevada: Bechtel SAIC Company. ACC: MOL.20020923.0176.

158966   BSC 2002. *The Enhanced Plan for Features, Events, and Processes (FEPs) at Yucca Mountain.* TDR-WIS-PA-000005 REV 00. Las Vegas, Nevada: Bechtel SAIC Company. ACC: MOL.20020417.0385.

161773   BSC (Bechtel SAIC Company) 2003. *Analysis of Hydrologic Properties Data.* MDL-NBS-HS-000014 REV 00. Las Vegas, Nevada: Bechtel SAIC Company. ACC: DOC.20030404.0004

163152   BSC 2003. *Dissolved Concentration Limits of Radioactive Elements.* ANL-WIS-MD-000010 REV 02. Las Vegas, Nevada: Bechtel SAIC Company. ACC: DOC.20030624.0003.

163128   BSC 2003. *Features, Events, and Processes in SZ Flow and Transport.* ANL-NBS-MD-000002 REV 02A. Las Vegas, Nevada: Bechtel SAIC Company. ACC: MOL.20030823.0129.

162657   BSC 2003. *Geochemical and Isotopic Constraints on Groundwater Flow Directions and Magnitudes, Mixing, and Recharge at Yucca Mountain.* ANL-NBS-HS-000021 REV 01A. Las Vegas, Nevada: Bechtel SAIC Company. ACC: MOL.20030604.0164.

165179   BSC (Bechtel SAIC Company) 2003. *Q-List.* TDR-MGR-RL-000005 REV 00. Las Vegas, Nevada: Bechtel SAIC Company. ACC: DOC.20030930.0002.

162729   BSC (Bechtel SAIC Company) 2003. *Saturated Zone Colloid Transport.* ANL-NBS-HS-000031 REV 01. Las Vegas, Nevada: Bechtel SAIC Company. ACC: DOC.20030916.0008.

162415   BSC 2003. *Saturated Zone In-Situ Testing*. ANL-NBS-HS-000039 REV 00A. Las Vegas, Nevada: Bechtel SAIC Company. ACC: MOL.20030602.0291.

162649   BSC 2003. *Site-Scale Saturated Zone Flow Model.* MDL-NBS-HS-000011 REV 01. Las Vegas, Nevada: Bechtel SAIC Company. ACC: MOL.20030626.0296.

164870   BSC 2003. *SZ Flow and Transport Model Abstraction.* MDL-NBS-HS-000021 REV 00. Las Vegas, Nevada: Bechtel SAIC Company. ACC: DOC.20030818.0007.

163965   BSC 2003. *Technical Work Plan for: Saturated Zone Flow and Transport Modeling and Testing*. TWP-NBS-MD-000002 REV 01. Las Vegas, Nevada: Bechtel SAIC Company. ACC: DOC.20030618.0021.

161620   BSC 2003. *Waste Form and In-Drift Colloids-Associated Radionuclide Concentrations: Abstraction and Summary*. MDL-EBS-PA-000004 REV 00. Las Vegas, Nevada: Bechtel SAIC Company. ACC: DOC.20030626.0006.

129679   Burbey, T.J. and Wheatcraft, S.W. 1986. *Tritium and Chlorine-36 Migration from a Nuclear Explosion Cavity.* DOE/NV/10384-09. Reno, Nevada: University of Nevada, Desert Research Institute, Water Resources Center. TIC: 201927.

130526   Burnett, R.D. and Frind, E.O. 1987. "Simulation of Contaminant Transport in Three Dimensions: 2. Dimensionality Effects." *Water Resources Research, 23,* (4), 695-705. Washington, D.C.: American Geophysical Union. TIC: 246359.

161770   Canori, G.F. and Leitner, M.M. 2003. *Project Requirements Document.* TER-MGR-MD-000001 REV 01. Las Vegas, Nevada: Bechtel SAIC Company. ACC: DOC.20030404.0003.

101374   Chipera, S.J. and Bish, D.L. 1989. *Quantitative X-Ray Diffraction Analyses of Samples Used for Sorption Studies by the Isotope and Nuclear Chemistry Division, Los Alamos National Laboratory.* LA-11669-MS. Los Alamos, New Mexico: Los Alamos National Laboratory. ACC: NNA.19890414.0062.

111081   Chipera, S.J.; Vaniman, D.T.; Carlos, B.A.; and Bish, D.L. 1995. *Mineralogic Variation in Drill Core UE-25 UZ#16, Yucca Mountain, Nevada.* LA-12810-MS. Los Alamos, New Mexico: Los Alamos National Laboratory. ACC: NNA.19940427.0099.

105761   Corapcioglu, M.Y. and Jiang, S. 1993. "Colloid-Facilitated Groundwater Contaminant Transport." *Water Resources Research, 29,* (7), 2215-2226. Washington, D.C.: American Geophysical Union. TIC: 222362

101584   Cotton, F.A. and Wilkinson, G. 1980. *Advanced Inorganic Chemistry: A Comprehensive Text.* 4th Edition. New York, New York: John Wiley & Sons. TIC: 217739.

100328   CRWMS M&O 1997. *Report of Results of Hydraulic and Tracer Tests at the C-Holes Complex.* Deliverable SP23APM3. Las Vegas, Nevada: CRWMS M&O. ACC: MOL.19971024.0074.

100353   CRWMS M&O 1998. *Saturated Zone Flow and Transport Expert Elicitation Project.* Deliverable SL5X4AM3. Las Vegas, Nevada: CRWMS M&O. ACC: MOL.19980825.0008.

152259   CRWMS M&O 2000. *Modeling Sub Gridblock Scale Dispersion in Three-Dimensional Heterogeneous Fractured Media (S0015).* ANL-NBS-HS-000022 REV 00 ICN 01. Las Vegas, Nevada: CRWMS M&O. ACC: MOL.20001107.0376.

146962   CRWMS M&O 2000. *Saturated Zone Transport Methodology and Transport Component Integration.* MDL-NBS-HS-000010 REV 00. Las Vegas, Nevada: CRWMS M&O. ACC: MOL.20000824.0513.

153246   CRWMS M&O 2000. *Total System Performance Assessment for the Site Recommendation.* TDR-WIS-PA-000001 REV 00 ICN 01. Las Vegas, Nevada: CRWMS M&O. ACC: MOL.20001220.0045.

153931   CRWMS M&O 2001. *Features, Events, and Processes in SZ Flow and Transport.* ANL-NBS-MD-000002 REV 01. Las Vegas, Nevada: CRWMS M&O. ACC: MOL.20010214.0230.

163800   Dagan, G.; Cvetkovic, V.; and Shapiro, A. 1992. "A Solute Flux Approach to Transport in Heterogeneous Formations, 1. The General Framework." *Water Resources Research*, *28*, (5), 1369–1376. Washington, D.C.: American Geophysical Union. TIC: 254598.

105803   Daniels, W.R.; Wolfsberg, K.; Rundberg, R.S.; Ogard, A.E.; Kerrisk, J.F.; Duffy, C.J.; Newton, T.W.; Thompson, J.L.; Bayhurst, B.P.; Bish, D.L.; Blacic, J.D.; Crowe, B.M.; Erdal, B.R.; Griffith, J.F.; Knight, S.D.; Lawrence, F.O.; Rundberg, V.L.; Skyes, M.L.; Thompson, G.M.; Travis, B.J.; Treher, E.N.; Vidale, R.J.; Walter, G.R.; Aguilar, R.D.; Cisneros, M.R.; Maestas, S.; Mitchell, A.J.; Oliver, P.Q.; Raybold, N.A.; and Wanek, P.L. 1982. *Summary Report on the Geochemistry of Yucca Mountain and Environs.* LA-9328-MS. Los Alamos, New Mexico: Los Alamos National Laboratory. ACC: NNA.19870406.0243.

100439   de Marsily, G. 1986. *Quantitative Hydrogeology: Groundwater Hydrology for Engineers.* San Diego, California: Academic Press. TIC: 208450.

162985   Dixit, S. and Van Cappellen, P. 2002. "Surface Chemistry and Reactivity of Biogenic Silica." *Geochimica et Cosmochimica Acta, 66,* (14), 2559-2568. [New York, New York]: Pergamon. TIC: 254531.

103021   DOE (U.S. Department of Energy) 1997. *Regional Groundwater Flow and Tritium Transport Modeling and Risk Assessment of the Underground Test Area, Nevada Test Site, Nevada.* DOE/NV-477. Las Vegas, Nevada: U.S. Department of Energy. ACC: MOL.20010731.0303.

155943   DOE 2002. *Yucca Mountain Science and Engineering Report.* DOE/RW-0539, Rev. 1. Washington, D.C.: U.S. Department of Energy, Office of Civilian Radioactive Waste Management. ACC: MOL.20020404.0042.

105279   Erickson, J.R. and Waddell, R.K. 1985. *Identification and Characterization of Hydrologic Properties of Fractured Tuff Using Hydraulic and Tracer Tests—Test Well USW H-4, Yucca Mountain, Nye County, Nevada.* Water-Resources Investigations Report 85-4066. Denver, Colorado: U.S. Geological Survey. ACC: NNA.19890713.0211.

162695   Finnegan, D.L. and Thompson, J.L. 2002. *Laboratory and Field Studies Related to Radionuclide Migration at the Nevada Test Site in Support of the Underground Test Area and Hydrologic Resource Management Projects.* LA-13919-MS. Los Alamos, New Mexico: Los Alamos National Laboratory. ACC: MOL.20030926.0011.

100033   Flint, L.E. 1998. *Characterization of Hydrogeologic Units Using Matrix Properties, Yucca Mountain, Nevada.* Water-Resources Investigations Report 97-4243. Denver, Colorado: U.S. Geological Survey. ACC: MOL.19980429.0512.

154365   Freeze, G.A.; Brodsky, N.S.; and Swift, P.N. 2001. *The Development of Information Catalogued in REV00 of the YMP FEP Database.* TDR-WIS-MD-000003 REV 00 ICN 01. Las Vegas, Nevada: Bechtel SAIC Company. ACC: MOL.20010301.0237.

101173   Freeze, R.A. and Cherry, J.A. 1979. *Groundwater.* Englewood Cliffs, New Jersey: Prentice-Hall. TIC: 217571.

145116   Gardiner, C.W. 1997. *Handbook of Stochastic Methods for Physics, Chemistry and the Natural Sciences.* 2nd Edition. 442. New York, New York: Springer-Verlag. TIC: 247770.

145122   Gelhar, L.W. 1997. "Perspectives on Field-Scale Application of Stochastic Subsurface Hydrology." *Subsurface Flow and Transport: A Stochastic Approach.* Dagan, G. and Neuman, S.P., eds. Pages 157-176. New York, New York: Cambridge University Press. TIC: 247805.

107296   Gelhar, L.W. and Axness, C.L. 1983. "Three-Dimensional Stochastic Analysis of Macrodispersion in Aquifers." *Water Resources Research, 19,* (1), 161-180. Washington, D.C.: American Geophysical Union. TIC: 222815.

165928   Grindrod, P. 1993. *The Impact of Colloids on the Migration and Dispersal of Radionuclides within Fractured Rock.* Pages 161-181. Austin, Texas: Intera Information Technologies. TIC: 222399.

163780   Hess, K.M.; Davis, J.A.; Kent, D.B.; and Coston, J.A. 2002. "Multispecies Reactive Tracer Test in an Aquifer with Spatially Variable Chemical Condition, Cape Cod, Massachusetts: Dispersive Transport of Bromide and Nickel." *Water Resources Research*, *38*, (8), 36–36.17. Washington, D.C.: American Geophysical Union. TIC: 254599.

161904   Hummel, W.; Berner, U.; Curti, E.; Pearson, F.J.; and Thoenen, T. 2002. *Nagra/PSI Chemical Thermodynamic Data Base 01/01.* Parkland, Florida: Universal Publishers. TIC: 253421.

165931   Hwang, Y.; Chambré, P.L.; Lee, W.W.-L.; and Pigford, T.H. 1989. "Analytic Studies of Colloid Transport in Fractured Porous Media." *Scientific Basis for Nuclear Waste Management XIII, Symposium held November 27-30, 1989, Boston, Massachusetts.* Oversby, V.M. and Brown, P.W., eds.. *176,* 599-605. Pittsburgh, Pennsylvania: Materials Research Society. TIC: 203658.

109297   Ibaraki, M. and Sudicky, E.A. 1995. "Colloid-Facilitated Contaminant Transport in Discretely Fractured Porous Media 1. Numerical Formulation and Sensitivity Analysis." *Water Resources Research, 31,* (12), 2945-2960. Washington, D.C.: American Geophysical Union. TIC: 245719.

165930   Ibaraki, M. and Sudicky, E.A. 1995. "Colloid-Facilitated Contaminant Transport in Discretely Fractured Porous Media 2. Fracture Network Examples." *Water Resources Research, 31,* (12), 2961-2969. Washington, D.C.: American Geophysical Union. TIC: 252318.

148309   Karasaki, K.; Landsfeld, M.; and Grossenbacher, K. 1990. "Building of a Conceptual Model at the UE25-c Hole Complex." *High Level Radioactive Waste Management, Proceedings of the International Topical Meeting, Las Vegas, Nevada, April 8-12,*

1990. 2, 811-817. La Grange Park, Illinois: American Nuclear Society.
TIC: 202058.

106313   Keeney-Kennicutt, W.L. and Morse, J.W. 1985. "The Redox Chemistry of Pu(V)O+2 Interaction with Common Mineral Surfaces in Dilute Solutions and Seawater." *Geochimica et Cosmochimica Acta, 49,* 2577-2588. New York, New York: Pergamon Press. TIC: 237000.

103282   Kersting, A.B.; Efurd, D.W.; Finnegan, D.L.; Rokop, D.J.; Smith, D.K.; and Thompson, J.L. 1999. "Migration of Plutonium in Ground Water at the Nevada Test Site." *Nature, 397,* ([6714]), 56-59. [London, England: Macmillan Journals].
TIC: 243597.

162421   Kersting, A.P. and Reimus, P.W., eds. 2003. *Colloid-Facilitated Transport of Low-Solubility Radionuclides : A Field, Experimental, and Modeling Investigation.* UCRL-ID-149688. [Livermore, California] : Lawrence Livermore National Laboratory. TIC : 254176.

105039   LaBolle, E.M.; Fogg, G.E.; and Tompson, A.F.B. 1996. "Random-Walk Simulation of Transport in Heterogeneous Porous Media: Local Mass-Conservation Problem and Implementation Methods." *Water Resources Research, 32,* (3), 583-593.
Washington, D.C.: American Geophysical Union. TIC: 245563.

147527   Langmuir, D. and Herman, J.S. 1980. "The Mobility of Thorium in Natural Waters at Low Temperatures." *Geochimica et Cosmochimica Acta, 44,* 1753-1766. New York, New York: Pergamon Press. TIC: 237029.

164150   LANL (Los Alamos National Laboratory) 2003. *Validation Test Plan (VTP) for the FEHM Application Version 2.20.* SDN: 10086-VTP-2.20-01. [Los Alamos, New Mexico]: Los Alamos National Laboratory. ACC: MOL.20030314.0010.

156838   Leap, D.I. and Belmonte, P.M. 1992. "Influence of Pore Pressure on Apparent Dispersivity of a Fissured Dolomitic Aquifer." *Ground Water, 30,* (1), 87-95.
[Worthington, Ohio: Water Well Journal Publishing]. TIC: 239275

163781   LeBlanc, D.R.; Garabedian, S.P.; Hess, K.M.; Gelhar, L.W.; Quadri, R.D.; Stollenwerk, K.G.; and Wood, W.W. 1991. "Large-Scale Natural Gradient Tracer Test in Sand and Gravel, Cape Cod, Massachusetts 1. Experimental Design and Observed Tracer Movement." *Water Resources Research, 27,* (5), 895-910.
Washington, D.C.: American Geophysical Union. TIC: 254593.

163821   Lichtner, P.C.; Kelkar, S.; and Robinson, B. 2002. "New Form of Dispersion Tensor for Axisymmetric Porous Media with Implementation in Particle Tracking." *Water Resources Research*, *38,* (8), 21-1 to 21-16. Washington, D.C.: American Geophysical Union. TIC: 254597.

100465   Luckey, R.R.; Tucci, P.; Faunt, C.C.; Ervin, E.M.; Steinkampf, W.C.; D'Agnese, F.A.; and Patterson, G.L. 1996. *Status of Understanding of the Saturated-Zone Ground-Water Flow System at Yucca Mountain, Nevada, as of 1995.* Water-

Resources Investigations Report 96-4077. Denver, Colorado: U.S. Geological Survey. ACC: MOL.19970513.0209.

148312   Maloszewski, P. and Zuber, A. 1985. "On the Theory of Tracer Experiments in Fissured Rocks with a Porous Matrix." *Journal of Hydrology, 79,* 333-358. Amsterdam, The Netherlands: Elsevier. TIC: 222390.

162986   Marmier, N.; Delisée, A.; and Fromage, F. 1999. "Surface Complexation Modeling of Yb(III) and Cs(I) Sorption on Silica." *Journal of Colloid and Interface Science, 212,* (2), 228-233. [New York, New York]: Academic Press. TIC: 254530.

101464   Neuman, S.P. 1990. "Universal Scaling of Hydraulic Conductivities and Dispersivities in Geologic Media." *Water Resources Research, 26,* (8), 1749-1758. Washington, D.C.: American Geophysical Union. TIC: 237977.

147577   Neuman, S.P.; Winter, C.L.; and Newman, C.M. 1987. "Stochastic Theory of Field-Scale Fickian Dispersion in Anisotropic Porous Media." *Water Resources Research, 23,* (3), 453-466. Washington, D.C.: American Geophysical Union. TIC: 225294.

155218   Nitsche, H.; Gatti, R.C.; Standifer, E.M.; Lee, S.C.; Müller, A.; Prussin, T.; Deinhammer, R.S.; Maurer, H.; Becraft, K.; Leung, S.; and Carpenter, S.A. 1993. *Measured Solubilities and Speciations of Neptunium, Plutonium, and Americium in a Typical Groundwater (J-13) from the Yucca Mountain Region.* LA-12562-MS. Los Alamos, New Mexico: Los Alamos National Laboratory. ACC: NNA.19930507.0136.

100163   Nitsche, H.; Roberts, K.; Prussin, T.; Muller, A.; Becraft, K.; Keeney, D.; Carpenter, S.A.; and Gatti, R.C. 1995. *Measured Solubilities and Speciations from Oversaturation Experiments of Neptunium, Plutonium and Americium in UE25p#1 Well Water from the Yucca Mountain Region.* LA-12563-MS. Los Alamos, New Mexico: Los Alamos National Laboratory. ACC: MOL.19951006.0171.

106920   Noell, A.L.; Thompson, J.L.; Corapcioglu, M.Y.; and Triay, I.R. 1998. "The Role of Silica Colloids on Facilitated Cesium Transport Through Glass Bead Columns and Modeling." *Journal of Contaminant Hydrology, 31,* (1-2), 23-56. Amsterdam, The Netherlands: Elsevier. TIC: 245510.

163274   NRC (U.S. Nuclear Regulatory Commission) 2003. *Yucca Mountain Review Plan, Final Report.* NUREG-1804, Rev. 2. Washington, D.C.: U.S. Nuclear Regulatory Commission, Office of Nuclear Material Safety and Safeguards. TIC: 254568.

165961   Oswald, J.G. and Ibaraki, M. 2001. "Migration of colloids in discretely fractured porous media: effect of colloidal matrix diffusion." *Journal Contaminant Hydrology, 52,* 213-244. New York, New York: Elsevier. TIC: 255089.

162987   Pabalan, R.T.; Turner, D.R.; Bertetti, F.P.; and Prikryl, J.D. 1998. "Uranium{superscript VI} Sorption onto Selected Mineral Surfaces, Key Geochemical Parameters." *Adsorption of Metals by Geomedia.* [Jenne, E.A., ed]. Pages 99-130. New York, New York: Academic Press. TIC: 239504.

142177   Parkhurst, D.L. 1995. *User's Guide to PHREEQC—A Computer Program for Speciation, Reaction-Path, Advective-Transport, and Inverse Geochemical Calculations.* Water-Resources Investigations Report 95-4227. Lakewood, Colorado: U.S. Geological Survey. TIC: 248314.

162685   Pawloski, G. 1999. *Development of Phenomenological Models of Underground Nuclear Tests on a Pahute Mesa, Nevada Test Site—BENHAM and TYBO.* UCRL-ID-136003. Livermore, California: Lawrence Livermore National Laboratory. ACC: MOL.20030926.0012.

100811   Penrose, W.R.; Polzer, W.L.; Essington, E.H.; Nelson, D.M.; and Orlandini, K.A. 1990. "Mobility of Plutonium and Americium Through a Shallow Aquifer in a Semiarid Region." *Environmental Science & Technology, 24,* 228-234. Washington, D.C.: American Chemical Society. TIC: 224113.

121957   Peters, R.R.; Klavetter, E.A.; Hall, I.J.; Blair, S.C.; Heller, P.R.; and Gee, G.W. 1984. *Fracture and Matrix Hydrologic Characteristics of Tuffaceous Materials from Yucca Mountain, Nye County, Nevada.* SAND84-1471. Albuquerque, New Mexico: Sandia National Laboratories. ACC: NNA.19900810.0674.

101466   Pollock, D.W. 1988. "Semianalytical Computation of Path Lines for Finite-Difference Models." *Ground Water, 26,* (6), 743-750. Worthington, Ohio: National Water Well Association. TIC: 226464.

163847   Poreh, M. 1965. "The Dispersivity Tensor in Isotropic and Axisymmetric Media." *Journal of Geophysical Research, 70,* (6), 3901-3913. Washington, D.C.: American Geophysical Union. TIC: Copyright Requested

162956   Reimus, P.W.; Haga, M.J.; Humphrey, A.R.; Counce, D.A.; Callahan, T.J.; and Ware, S.D. 2002. *Diffusion Cell and Fracture Transport Experiments to Support Interpretations of the BULLION Forced-Gradient Experiment.* LA-UR-02-6884. [Los Alamos, New Mexico]: Los Alamos National Laboratory. TIC: 253859.

163008   Reimus, P.W.; Ware, S.D.; Benedict, F.C.; Warren, R.G.; Humphrey, A.; Adams, A.; Wilson, B.; and Gonzales, D. 2002. *Diffusive and Advective Transport of {superscript 3}H, {superscript 14}C, and {superscript 99}Tc in Saturated, Fractured Volcanic Rocks from Pahute Mesa, Nevada.* LA-13891-MS. Los Alamos, New Mexico: Los Alamos National Laboratory. TIC: 253905.

101154   Robinson, B.A. 1994. "A Strategy for Validating a Conceptual Model for Radionuclide Migration in the Saturated Zone Beneath Yucca Mountain." *Radioactive Waste Management and Environmental Restoration, 19,* (1-3), 73-96. Yverdon, Switzerland: Harwood Academic Publishers. TIC: 222513.

100416   Robinson, B.A.; Wolfsberg, A.V.; Viswanathan, H.S.; Bussod, G.Y.; Gable, C.W.; and Meijer, A. 1997. *The Site-Scale Unsaturated Zone Transport Model of Yucca Mountain.* Milestone SP25BM3. Los Alamos, New Mexico: Los Alamos National Laboratory. ACC: MOL.19980203.0570.

101355   Rundberg, R.S.; Ogard, A.E.; and Vaniman, D.T., eds. 1985. *Research and Development Related to the Nevada Nuclear Waste Storage Investigations, April 1– June 30, 1984.* LA-10297-PR. Los Alamos, New Mexico: Los Alamos National Laboratory. ACC: NNA.19920922.0018.

106481   Rundberg, R.S.; Partom, I.; Ott, M.A.; Mitchell, A.J.; and Birdsell, K. 1987. *Diffusion of Nonsorbing Tracers in Yucca Mountain Tuff.* Milestone R524. Los Alamos, New Mexico: Los Alamos National Laboratory. ACC: NNA.19930405.0074.

162687   Smith, D.K. 2002. *Evaluation of the Radiochemistry of Near-Field Water Samples at the Nevada Test Site Applied to the Definition of a Hydrologic Source Term.* UCRL-ID-149049. Livermore, California: Lawrence Livermore National Laboratory. ACC: MOL.20030926.0013.

144658   Smith, P.A. and Degueldre, C. 1993. "Colloid-Facilitated Transport of Radionuclides Through Fractured Media." *Journal of Contaminant Hydrology, 13,* 143-166. Amsterdam, The Netherlands: Elsevier. TIC: 224863.

160702   Steinborn, T.L. 2002. *Data Qualification Report: Mineralogy Data for Use on the Yucca Mountain Project.* TDR-NBS-HS-000005 REV 00. Las Vegas, Nevada: Bechtel SAIC Company. ACC: MOL.20020807.0442.

148342   Sudicky, E.A. and Frind, E.O. 1981. "Carbon 14 Dating of Groundwater in Confined Aquifers: Implications of Aquitard Diffusion." *Water Resources Research, 17,* (4), 1060-1064. Washington, D.C.: American Geophysical Union. TIC: 247712.

105043   Sudicky, E.A. and Frind, E.O. 1982. "Contaminant Transport in Fractured Porous Media: Analytical Solutions for a System of Parallel Fractures." *Water Resources Research, 18,* (6), 1634-1642. Washington, D.C.: American Geophysical Union. TIC: 217475.

101160   Tang, D.H.; Frind, E.O.; and Sudicky, E.A. 1981. "Contaminant Transport in Fractured Porous Media: Analytical Solution for a Single Fracture." *Water Resources Research, 17,* (3), 555-564. Washington, D.C.: American Geophysical Union. TIC: 225358.

101361   Thomas, K.W. 1987. *Summary of Sorption Measurements Performed with Yucca Mountain, Nevada, Tuff Samples and Water from Well J-13.* LA-10960-MS. Los Alamos, New Mexico: Los Alamos National Laboratory. ACC: NNA.19900604.0045.R

163782   Thorbjarnarson, K.W. and Mackay, D.M. 1994. "A Forced-Gradient Experiment on Solute Transport in the Borden Aquifer. 3. Nonequilibrium Transport of the Sorbing Organic Compounds." *Water Resources Research, 30,* (2), 401-419. Washington, D.C.: American Geophysical Union. TIC: 252320.

162686   Tompson, A.F.B.; Bruton, C.J.; and Pawloski, G.A. 1999. *Evaluation of the Hydrologic Source Term from Underground Nuclear Tests in Frenchman Flat at the Nevada Test Site: The CAMBRIC Test.* UCRL-ID-132300. Livermore, California: Lawrence Livermore National Laboratory. ACC: MOL.20030926.0014.

145195   Tompson, A.F.B.; Vomvoris, E.G.; and Gelhar, L.W. 1987. *Numerical Simulation of Solute Transport in Randomly Heterogeneous Porous Media: Motivation, Model Development, and Application.* UCID 21281. Livermore, California: Lawrence Livermore National Laboratory. ACC: MOL.19950131.0007.

125967   Treher, E.N. and Raybold, N.A. 1982. *The Elution of Radionuclides Through Columns of Crushed Rock from the Nevada Test Site.* LA-9329-MS. Los Alamos, New Mexico: Los Alamos National Laboratory. ACC: NNA.19920922.0021.

125972   Triay, I.; Robinson, B.; Lopez, R.; Mitchell, A.; and Overly, C. 1993. "Neptunium Retardation with Tuffs and Groundwaters from Yucca Mountain." *High Level Radioactive Waste Management, Proceedings of the Fourth International Conference, Las Vegas, Nevada, April 26-30, 1993*. 2, 1504-1508. La Grange Park, Illinois: American Nuclear Society. TIC 208542.

145123   Triay, I.R.; Birdsell, K.H.; Mitchell, A.J.; and Ott, M.A. 1993. "Diffusion of Sorbing and Non-Sorbing Radionuclides." *High Level Radioactive Waste Management, Proceedings of the Fourth Annual International Conference, Las Vegas, Nevada, April 26-30, 1993. 2,* 1527-1532. La Grange Park, Illinois: American Nuclear Society. TIC: 208542.

101023   Triay, I.R.; Cotter, C.R.; Huddleston, M.H.; Leonard, D.E.; Weaver, S.C.; Chipera, S.J.; Bish, D.L.; Meijer, A.; and Canepa, J.A. 1996. *Batch Sorption Results for Neptunium Transport Through Yucca Mountain Tuffs.* LA-12961-MS. Los Alamos, New Mexico: Los Alamos National Laboratory. ACC: MOL.19980924.0050.

101024   Triay, I.R.; Furlano, A.C.; Weaver, S.C.; Chipera, S.J.; and Bish, D.L. 1996. *Comparison of Neptunium Sorption Results Using Batch and Column Techniques.* LA-12958-MS. Los Alamos, New Mexico: Los Alamos National Laboratory. ACC: MOL.19980924.0049.

104129   Triay, I.R.; Meijer, A.; Cisneros, M.R.; Miller, G.G.; Mitchell, A.J.; Ott, M.A.; Hobart, D.E.; Palmer, P.D.; Perrin, R.E.; and Aguilar, R.D. 1991. "Sorption of Americium in Tuff and Pure Minerals Using Synthetic and Natural Groundwaters." *Radiochimica Acta, 52/53,* 141-145. München, Germany: R. Oldenbourg Verlag. TIC: 222704.

100422   Triay, I.R.; Meijer, A.; Conca, J.L.; Kung, K.S.; Rundberg, R.S.; Strietelmeier, B.A.; and Tait, C.D. 1997. *Summary and Synthesis Report on Radionuclide Retardation for the Yucca Mountain Site Characterization Project.* Eckhardt, R.C., ed. LA-13262-MS. Los Alamos, New Mexico: Los Alamos National Laboratory. ACC: MOL.19971210.0177.

144693   Triay, I.; Robinson, B.; Mitchell, A.; Overly, C.; and Lopez, R. 1993. "Transport of Neptunium through Yucca Mountain Tuffs." *Scientific Basis for Nuclear Waste Management XVI, Symposium held November 30-December 4, 1992, Boston, Massachusetts.* Interrante, C.G. and Pabalan, R.T., eds. *294,* 797-802. Pittsburgh, Pennsylvania: Materials Research Society. TIC: 208880.

162989   Turner, D.R.; Pabalan, R.T.; and Bertetti, F.P. 1998. "Neptunium(V) Sorption on Montmorillonite: An Experimental and Surface Complexation Modeling Study." *Clays and Clay Minerals, 46,* (3), 256-269. Boulder, Colorado: Clay Minerals Society. TIC: 254532.

154495   USGS (U.S. Geological Survey) n.d. Bulk Density. [Denver, Colorado: U.S. Geological Survey]. ACC: NNA.19940406.0076.

144579   Valocchi, A.J. 1985. "Validity of the Local Equilibrium Assumption for Modeling Sorbing Solute Transport Through Homogeneous Soils." *Water Resources Research, 21,* (6), 808-820. Washington, D.C.: American Geophysical Union. TIC: 223203.

101064   Waddell, R.K.; Robison, J.H.; and Blankennagel, R.K. 1984. *Hydrology of Yucca Mountain and Vicinity, Nevada-California—Investigative Results Through Mid-1983.* Water-Resources Investigations Report 84-4267. Denver, Colorado: U.S. Geological Survey. ACC: NNA.19870406.0343.

130510   Wen, X-H. and Gomez-Hernandez, J.J. 1996. "The Constant Displacement Scheme for Tracking Particles in Heterogeneous Aquifers." *Ground Water, 34,* (1), 135-142. Worthington, Ohio: Water Well Journal Publishing. TIC: 246656.

100191   Wilson, M.L.; Gauthier, J.H.; Barnard, R.W.; Barr, G.E.; Dockery, H.A.; Dunn, E.; Eaton, R.R.; Guerin, D.C.; Lu, N.; Martinez, M.J.; Nilson, R.; Rautman, C.A.; Robey, T.H.; Ross, B.; Ryder, E.E.; Schenker, A.R.; Shannon, S.A.; Skinner, L.H.; Halsey, W.G.; Gansemer, J.D.; Lewis, L.C.; Lamont, A.D.; Triay, I.R.; Meijer, A.; and Morris, D.E. 1994. *Total-System Performance Assessment for Yucca Mountain—SNL Second Iteration (TSPA-1993).* SAND93-2675. Executive Summary and two volumes. Albuquerque, New Mexico: Sandia National Laboratories. ACC: NNA.19940112.0123.

163823   Winterle, J.R.; Claisse, A.; and Arlt, H.D. 2003. "An Independent Site-Scale Groundwater Flow Model for Yucca Mountain." *Proceedings of the 10th International High-Level Radioactive Waste Management Conference (IHLRWM), March 30-April 2, 2003, Las Vegas, Nevada.* Pages 151-158. La Grange Park, Illinois: American Nuclear Society. TIC: 254559.

162688   Wolfsberg, A.; Glascoe, L.; Lu, G.; Olson, A.; Lichtner, P.; McGraw, M.; Cherry, T.; and Roemer, G. 2002. *TYBO/BENHAM: Model Analysis of Groundwater Flow and Radionuclide Migration from Underground Nuclear Tests in Southwestern Pahute Mesa, Nevada.* LA-13977. Los Alamos, New Mexico: Los Alamos National Laboratory. ACC: MOL.20030926.0009

154702   Zheng, C. and Bennett, G.D. 1995. *Applied Contaminant Transport Modeling, Theory and Practice.* New York, New York: Van Nostrand Reinhold. TIC: 249865.

110491   Zyvoloski, G.A.; Robinson, B.A.; Dash, Z.V.; and Trease, L.L. 1997. *Summary of the Models and Methods for the FEHM Application—A Finite-Element Heat- and Mass-Transfer Code.* LA-13307-MS. [Los Alamos, New Mexico]: Los Alamos National Laboratory. TIC: 235587.

9.2   CODES, STANDARDS, REGULATIONS, AND PROCEDURES

156605   10 CFR 63. Energy: Disposal of High-Level Radioactive Wastes in a Geologic Repository at Yucca Mountain, Nevada. Readily available.

AP-2.22Q, Rev. 1, ICN 0. *Classification Analyses and Maintenance of the Q-List.* Washington, D.C.: U.S. Department of Energy, Office of Civilian Radioactive Waste Management. ACC: DOC.20030930.0002.

AP-SI.1Q, Rev. 5, ICN 2. *Software Management.* Washington, D.C.: U.S. Department of Energy, Office of Civilian Radioactive Waste Management. ACC: DOC.20030902.0003.

AP-SIII.10Q, Rev. 2, ICN 0. *Models.* Washington, D.C.: U.S. Department of Energy, Office of Civilian Radioactive Waste Management. ACC: DOC.20030929.0003.

9.3   SOFTWARE

155323   BSC (Bechtel SAIC Company) 2001. *Software Code: PHREEQC.* V2.3. PC. 10068-2.3-00.

161725   LANL (Los Alamos National Laboratory) 2003. *Software Code: FEHM.* V2.20. SUN, PC. 10086-2.20-00.

164509   LANL 2003. *Software Code: FRACT_p.* V1.0. PC, LINUX 2.4.18. 11009-1.0-00.

153099   LBNL (Lawrence Berkeley National Laboratory) 2000. *Software Code: GSLIB.* V1.0GAMV3V1.201. SUN w/Unix OS. 10398-1.0GAMV3V1.201-00.

149114   SNL (Sandia National Laboratories) 2000. *Software Code: GSLIB V2.0 MSISIM.* V2.0. 10098-2.0MSISIMV2.0-00.

149117   SNL 2000. *Software Routine: calc_cdf.c.* V1.0. ANL-NBS-HS-000022.

163836   SNL 2002. *Software Code: cr8sptr.c.* V 2.0. SUN, Sun O.S. 5.7. 10927-2.0-00.

163837   SNL 2002. *Software Code: gs2fehm.c.* V 1.0. SUN, Sun O.S. 5.7. 10923-1.0-00.

9.4   SOURCE DATA, LISTED BY DATA TRACKING NUMBER

105937   GS920408312321.003. Chemical Composition of Groundwater in the Yucca Mountain Area, Nevada 1971—1984. Submittal date: 04/24/1987

145530   GS930308312323.001. Chemical Composition of Groundwater and the Locations of Permeable Zones in the Yucca Mountain Area. Submittal date: 03/05/1993.

162788   LA000000000010.001. The Elutions of Radionuclides Through Columns of Crushed Rock from the Nevada Test Site. Submittal date: 03/02/1992.

162789   LA000000000035.001. Transport of Neptunium Through Yucca Mountain Tuffs. Submittal date: 01/22/1993.

162790   LA000000000035.002. Neptunium Retardation with Tuffs and Groundwater from Yucca Mountain. Submittal date: 01/22/1993.

162791   LA000000000042.001. Summary of Sorption Measurements Performed with Yucca Mountain, Nevada, Tuff Samples and Water from Well J-13. Submittal date: 04/16/1993.

107144   LA000000000086.002. Mineralogic Variation in Drill Core UE-25 UZ#16 Yucca Mountain, Nevada. Submittal date: 03/28/1995.

147087   LA0002JC831361.001. Column Studies Using G4-268 Devitrified Tuff with J-13 Well Water and Radionuclides (H-3 and Pu-239). Submittal date: 03/16/2000. (Reference Only)

149557   LA0003JC831362.001. Preliminary Matrix Diffusion Coefficients for Yucca Mountain Tuffs. Submittal date: 4/10/2000.

149399   LA0004WS831372.002. Sorption of Np, Pu, and Am on Rock Samples from Busted Butte, NV. Submittal date: 04/19/2000.

162476   LA0010JC831341.001. Radionuclide Retardation Measurements of Sorption Distribution Coefficients for Barium. Submittal date: 10/19/2000.

153321   LA0010JC831341.002. Radionuclide Retardation Measurements of Sorption Distribution Coefficients for Cesium. Submittal date: 10/19/2000.

153322   LA0010JC831341.003. Radionuclide Retardation Measurements of Sorption Distribution Coefficients for Strontium. Submittal date: 10/19/2000.

153323   LA0010JC831341.004. Radionuclide Retardation Measurements of Sorption Distribution Coefficients for Selenium. Submittal date: 10/19/2000.

153320   LA0010JC831341.005. Radionuclide Retardation Measurements of Sorption Distribution Coefficients for Uranium. Submittal date: 10/19/2000.

153318   LA0010JC831341.006. Radionuclide Retardation Measurements of Sorption Distribution Coefficients for Plutonium. Submittal date: 10/19/2000.

153319   LA0010JC831341.007. Radionuclide Retardation Measurements of Sorption Distribution Coefficients for Neptunium. Submittal date: 10/19/2000.

163042   LA0012AM831341.002. NP Sorption onto Clinoptilolite-Rich Tuff in J-13 Water Under Atmospheric Conditions. Submittal date: 12/19/2000.

163043   LA0101AM831341.001. Uranium Sorption Coefficients for Minerals and Tuffs Under Oxidizing Conditions in J-13 Water. Submittal date: 01/23/2001.

161525   LA0108TV12213U.001. Static Batch Sorption Coefficients and Retardation Coefficients. Submittal date: 08/14/2001.

156870   LA0109MD831341.001. Adsorption of NP-237 in Three Types of Alluvium as a Function of Time and Stratigraphic Position. Submittal date: 09/14/2001.

156871   LA0109MD831341.002. Adsorption of TC-99 in Three Types of Alluvium as a Function of Time and Stratigraphic Position. Submittal date: 09/14/200

160051   LA0206AM831234.001. Eh-pH Field Measurements on Nye County EWDP Wells. Submittal date: 06/21/2002.

163852   LA0206AM831234.002. Geochemical Field Measurements on Nye County EWDP Wells. Submittal date: 06/21/2002.

162433   LA0301AA831352.001. Experiments on Pu(V)-Colloid Transport in Columns Packed with Material from Nye County Borehole 19D, Zone 4. Submittal date: 01/23/2003.

162435   LA0301PR831361.003. Breakthrough Curves of Tritium, Plutonium, and Various Colloids in Saturated UE20C Fractured Cores from the Nevada Test Site. Submittal date: 01/22/2003.

162436   LA0301PR831361.004. Breakthrough Curves of Tritium, Plutonium, and Various Colloids in Saturated PM-1 and PM-2 Fractured Cores from the Nevada Test Site. Submittal date: 01/22/2003.

163783   LA0302HV831361.001. A Study of Kinetic Reaction Rates for Plutonium Sorption in Devitrified Tuffs. Submittal date: 02/10/2003. (Reference Only)

163784   LA0302MD831341.003. Neptunium-237 Sorption in Alluvium from NC-EWDP Wells 191MA, 10SA, and 22SA Under Ambient Conditions. Submittal date: 02/11/2003.

163785   LA0302MD831341.004. Uranium Sorption in Alluvium from NC-EWDP Wells 19M1A, 10SA, and 22SA Under Ambient Conditions. Submittal date: 02/11/2003.

163558   LA0303HV831352.002. Colloid Retardation Factors for the Saturated Zone Fractured Volcanics. Submittal date: 03/31/2003.

163559   LA0303HV831352.004. Colloid Retardation Factors for the Saturated Zone Alluvium. Submittal date: 03/31/2003.

163788   LA0304TM831231.002. SZ Site-Scale Flow Model, FEHM Files for Base Case. Submittal date: 04/14/2003.

163789   LA0305AM831341.001. 1977 to 1987 Sorption Measurements of Am, Ba, Cs, Np, Pu, Pa, Sr, Th, and U with Yucca Mountain Tuff Samples. Submittal date: 05/21/2003.

165523   LA0309AM831341.002. Batch Sorption Coefficient Data for Barium on Yucca Mountain Tuffs in Representative Water Compositions. Submittal date: 09/25/2003.

165524   LA0309AM831341.003. Batch Sorption Coefficient Data for Cesium on Yucca Mountain Tuffs in Representative Water Compositions. Submittal date: 09/25/2003.

165525   LA0309AM831341.004. Batch Sorption Coefficient Data for Neptunium on Yucca Mountain Tuffs in Representative Water Compositions. Submittal date: 09/25/2003.

165526   LA0309AM831341.005. Batch Sorption Coefficient Data for Plutonium on Yucca Mountain Tuffs in Representative Water Compositions. Submittal date: 09/25/2003.

165527   LA0309AM831341.006. Batch Sorption Coefficient Data for Strontium on Yucca Mountain Tuffs in Representative Water Compositions. Submittal date: 09/25/2003.

165528   LA0309AM831341.007. Batch Sorption Coefficient Data for Uranium on Yucca Mountain Tuffs in Representative Water Compositions. Submittal date: 09/25/2003.

166195   LA0311SK831341.001. SZ Site-scale Transport Model, Surface Area Data. Submittal date: 11/20/2003.

107142   LADV831321AQ97.001. Mineralogic Variation in Drill Holes. Submittal date: 05/28/1997.

109044   LADV831321AQ99.001. Quantitative XRD Results for the USW SD-6 and USW WT-24 Drill Core Samples. Submittal date: 04/16/1999.

109004   LAJC831321AQ98.005. Quantitative XRD Results For Drill Core USW SD-7, USW SD-9, USW SD-12 and UE-25 UZ#16. Submittal date: 10/27/1998.

109047   LASC831321AQ98.001. Results of Real-Time Analysis For Erionite In Drill Hole USWWT-24, Yucca Mountain, Nevada. Submittal date: 02/10/1998.

151523   MO0007MAJIONPH.010. Major Ion Content of Groundwater from Borehole UE-25 P #1 Extracted from ANL-NBS-HS-000021, Geochemical and Isotopic Constraints on Groundwater Flow Directions, Mixing and Recharge at Yucca Mountain, Nevada. Submittal date: 07/27/2000.

151530   MO0007MAJIONPH.013. Major Ion Content of Groundwater from Selected YMP and Other Boreholes Extracted from ANL-NBS-HS-000021, Geochemical and Isotopic Constraints on Groundwater Flow Directions, Mixing and Recharge at Yucca Mountain, Nevada. Submittal date: 07/27/2000.

155229   MO0010CPORGLOG.002. Calculated Porosity From Geophysical Logs Data From "Old 40" Boreholes. Submittal date: 10/16/2000.

163795   MO0101XRDDRILC.002. XRD Analyses of Drill Core from Boreholes UE-25 A#1 AND USW G-2. Submittal date: 01/26/2001.

163796   MO0101XRDMINAB.001. XRD Analyses of Drill Core From Boreholes UE-25B#1, USW G-1, USW G-3, USW GU-3, and USW G-4. Submittal date: 01/26/2001.

163480   MO0105GPLOG19D.000. Geophysical Log Data from Borehole NC EWDP 19D. Submittal date: 05/31/2001.

163797   MO0106XRDDRILC.003. XRD Analyses of Drill Core from Borehole USW H-6. Submittal date: 06/08/2001.

155989   MO0109HYMXPROP.001. Matrix Hydrologic Properties Data. Submittal date: 09/17/2001.

164527   MO0307SEPFEPS4.000. LA FEP List. Submittal date: 07/31/2003. (Reference only)

165530   MO0309THDPHRLL.000. Input Data File (LLNL.DAT) for Thermodynamic Data Software Code PHREEQC, Version 2.3. Submittal date: 09/22/2003.

165529   MO0309THDPHRQC.000. Input Data File (PHREEQC.DAT) for Thermodynamic Data Software Code PHREEQC, Version 2.3. Submittal date: 09/22/2003.

155045   SN0004T0501399.003. Statistical Summary of Porosity Data. Submittal date: 04/13/2000.

163946   SN0306T0502103.007. Updated Saturated Zone Transport Abstraction Model Uncertain Inputs. Submittal date: 06/12/2003.

9.5   OUTPUT DATA, LISTED BY DATA TRACKING NUMBER

LA0302RP831228.001. Type Curve Data for FEHM Macro "SPTR" Based on Sudicky and Frind Solution. Submittal date: 02/11/2003.

LA0306AM831343.001. Modeling Calculations of Radionuclide Sorption Via Surface-Complexation Reactions. Submittal date: 06/09/2003.

LA0306SK831231.001. SZ Site-Scale Transport Model, FEHM Files for Base Case. Submittal date: 06/25/2003.

LA0307SK831231.001. Files for FEHM V 2.20 for Comparison of Flow Paths Against Those From Hydrochemistry Data. Submittal date: 07/31/2003.

LA0307SK831231.002. Files for FEHM V 2.20 for Specific Discharge. Submittal date: 07/31/2003.

LA0309SK831231.001. Files for FEHM V 2.20 for Evaluating Propagation of Uncertainty in the Input Parameter Values. Submittal date: 07/31/2003.

LA0307ZD831231.001. Files for FEHM V 2.20 for Evaluating Barrier Capabilities. Submittal date: 07/31/2003.

LA0309AM831341.001. Saturated Zone Distribution Coefficients (KDS) for U, NP, PU, CS, AM, PA, SR, TH, RA, C, TC, and I. Submittal date: 09/24/2003.

LA0309RP831321.001. Calculation of the Rock Type Distributions, SZ Transport Model. Submittal date: 09/23/2003.

LA0309RP831341.001. Calculation of Kd Distributions for Cesium. Submittal date: 09/23/2003.

LA0309RP831341.002. Calculation of Kd Distributions for Neptunium. Submittal date: 09/30/2003.

LA0309RP831341.003. Calculation of Kd Distributions for Plutonium. Submittal date: 09/30/2003.

LA0309RP831341.004. Calculation of Kd Distributions for Uranium. Submittal date: 09/29/2003.

LA0310AM831341.002. Saturated Zone Distribution Coefficients (K_ds) for U, Np, Pu, Cs, Am, Pa, Sr, Th, Ra, C, Tc, and I. Submittal date: 10/21/2003.

ATTACHMENT I. TECHNICAL BASIS FOR SORPTION-COEFFICIENT PROBABILITY DISTRIBUTION FUNCTIONS

I.1 INTRODUCTION

This appendix provides the bases for the derivation of sorption-coefficient probability distributions used in the saturated-zone transport model. The sorption-coefficient data on which the distributions are based were obtained in laboratory experiments in which representative rock samples from the Yucca Mountain site were contacted with groundwaters (or simulated groundwaters) representative of the site spiked with one or more of the elements of interest. Sorption experiments were carried out as a function of rock type, time, element concentration, atmospheric composition, grain size, and temperature. In some cases, the solids remaining from sorption experiments were contacted with unspiked groundwater in desorption experiments. The sorption and desorption experiments together provide information on the equilibration rates of the sorption reactions.

For elements that sorb primarily through surface-complexation reactions, the experimental data are augmented with the results of modeling calculations using PHREEQC (V2.3, STN: 10068-2.3-00; BSC 2001 [155323]) with the thermodynamic input data files LLNL.DAT (DTN: MO0309THDPHRLL.000 [165530]) and PHREEQC.DAT (DTN: MO0309THDPHRQC.000 [165529]). The inputs for the modeling calculations include groundwater compositions, rock surface areas, binding constants for the elements of interest, and thermodynamic data for solid and solution species (Table 4-1). These modeling calculations provide a basis for interpolation and extrapolation of the experimentally derived sorption-coefficient data set.

The primary controls on sorption behavior of the elements of interest in the saturated zone at Yucca Mountain include the detailed characteristics of mineral surfaces in the rock units through which water flows in the saturated zone, the detailed chemistry of groundwater in the saturated zone, the sorption behavior of each element, and the concentrations of the various radionuclides in the waters. These parameters will be discussed in the following sections.

As noted in the model report *SZ Flow and Transport Model Abstraction* (BSC 2003 [164870]), the saturated zone transport model uses a stochastic approach to calculate the transport rates of radionuclides of interest. In this approach, each realization (i.e., calculation) selects a single value for the sorption coefficient of each radionuclide from a probability distribution that represents the range of sorption-coefficient values that could be encountered in the saturated volcanic section or in the alluvial section. This attachment provides probability distributions for each element of interest on the two major rock types (devitrified and zeolitic tuff) found in the saturated volcanic section. It also provides probability distributions for sorption coefficients in alluvium. The influence of expected variations in water chemistry, radionuclide concentrations, and variations in rock surface properties within one of the major rock types or alluvium were incorporated into the probability distributions. The distributions types were based in part on actual experimental data and in part on professional judgment regarding the impact of variables not considered in the experimental program on the distributions. For example, there are potential impacts from variations in water compositions outside those addressed in the experimental program (e.g., Eh), variations in surface areas, variations in mineralogical composition, etc. In the case of mineralogical composition, an attempt was made to emphasize those experiments that

used samples closest to the mean composition of the hydrologic units as defined in the transport model. Thus, experimental data points for devitrified tuff samples containing significant quantities of clays were discounted, leading more conservative estimates of K_d.

This analysis of sorption coefficients focuses on room temperature conditions. Available data show little statistical variation in the sorption coefficient values up to 80°C (DTN: LA0010JC831341.002 [153321] and LA0010JC831341.003 [153322]). Temperatures in the SZ are expected to be in the neighborhood of 35°C (BSC 2003 [162649], Table 7.4-1). Hence sorption coefficient values at elevated temperatures are not discussed in this model report.

I.2   AQUIFER MATRIX COMPOSITIONS ALONG MOST PROBABLE TRANSPORT PATHWAYS

Sources of data on aquifer matrix compositions in the saturated zone are provided in Attachment III, Table III-3. These data have been incorporated into a site mineralogic model BSC 2002 [158730]. There are two dominant rock types in the saturated zone along potential flow paths in volcanics to the 18-km boundary: devitrified tuff and zeolitic tuff. Devitrified tuff is composed primarily of silica (quartz and cristobalite) and alkali feldspar. It may also contain minor to trace amounts of mica, hematite, calcite, tridymite, kaolinite, and hornblende and minor amounts ($< 25\%$) of smectite and/or zeolite. For the purposes of this analysis, sorption-coefficient distributions for devitrified tuff are based on data obtained on samples that are composed primarily of silica phases and feldspar with only trace amounts of other minerals. Although devitrified tuff samples that contain significant amounts ($> 5\%$) of clays or zeolites generally have higher sorption coefficients than samples that do not, the distribution of these types of altered rocks along the flow path is not well enough established to reliably incorporate these rock types into the sorption-coefficient probability distributions. Sorption-coefficient distributions for zeolitic tuff use only samples that contain more than 50% zeolite, with the balance made up of silica phases, alkali feldspar, clays, and/or glass.

The total number of samples of each rock type used in the analysis in this attachment included 38 devitrified tuffs and 34 zeolitic tuffs. Not all of these samples were obtained from the saturated zone. Nonetheless, these samples are taken to be representative of devitrified and zeolitic tuffs in the saturated zone at Yucca Mountain.

As explained further below, surface areas for the sorption substrates are an input to PHREEQC (V2.3; BSC 2001 [155323]) calculations. Surface-area analyses for 20 tuff samples presented by Triay et al. (1996 [101023], p. 62) are incorporated with DTN: LA0311SK831341.001 [166195]. These analyses calculated with averages are presented in Table I-1.

I.3   RADIONUCLIDES-OF-INTEREST AND THEIR POTENTIAL CONCENTRATION RANGES IN THE TRANSPORT SYSTEM

The list of radionuclides for which sorption-coefficient data are required was derived in the analysis and modeling report *Radionuclide Screening* (BSC 2002 [160059], Table 11). The list includes isotopes of americium, cesium, neptunium, protactinium, plutonium, radium, strontium, thorium, and uranium. Because different isotopes of a given (heavy) element behave the same in chemical reactions, this discussion will focus on this list of elements.

Sorption coefficients for the radionuclides-of-interest are often a function of the concentrations of the radionuclides present in solution. Thus, experiments have been carried out as a function of radionuclide concentration for most of the elements of interest. In most cases, experiments were carried out over a range of concentration up to a solubility limit. At the solubility limit, a pure solid phase incorporating the element of interest is precipitated out of solution. Therefore, the concentration of an element in solution cannot rise much higher than the solubility limit. Experiments in which the final solution concentrations for a given element of interest exceeded the solubility limit are not useful in this analysis and will be discounted.

Table I-1. Surface Areas (m^2/g) for Yucca Mountain Tuffs

Borehole	Sample Type				
	Not Crushed	Dry Sieved	Wet Sieved With J-13 Water: Trial #1	Wet Sieved With J-13 Water: Trial #2	Wet Sieved With UE-25 p#1 Water
Devitrified Tuff					
USW G1-732	2.1	2.7	2.6	2.5	3.3
USW G1-1936	4.5	4.9	3.6	3.9	3.7
USW G4-270	2	6.4	5.1		5
USW G4-275	2.9	4.5			
USW G4-2570	2.8	3.6	2.9	2.9	2.8
USW GU3-747	2.2	2.9	2.8	2.4	2.8
USW GU3-2325	1.8	2.5	2.2	1.8	2.5
Average	**2.6**	**3.9**	**3.2**	**2.7**	**3.4**
Zeolitic Tuff					
USW G1-1405	32	28	26		31
USW G2-1813			34		
USW G2-1951			66		
USW GU3-1992			32		
USW G4-1506	22	30	27		25
USW G4-1529	37	21	22		31
USW G4-1530	40	41			
USW G4-1625	28	27	28		33
USW G4-1772	23	22	23	23	23
USW G4-2077	19	18			
Average	**28.7**	**26.7**	**32.3**	**23**	**28.6**
Vitric Tuff					
USW G2-767	0.89	1.1	0.62	0.71	0.87
USW GU3-1249	0.52	0.92	0.99		0.87
USW GU3-1407	1.7	3.3	3		3.2
Average	**1.0**	**1.8**	**1.5**	**0.71**	**1.6**

Source: DTN: LA0311SK831341.001 [166195] based on Triay et al. (1996 [101023], p. 62)

Because experiments have been carried out at concentrations up to the solubility limit for most elements of interest, the experimental results reflect this dependency. The only element for which the experimental concentrations did not approach a solubility limit was cesium. The solubility of cesium compounds is very high (Section I-8.2). Thus, the sorption-coefficient probability distributions for cesium must be calibrated to the cesium concentrations expected in the saturated zone.

I.4   WATER COMPOSITIONAL RANGES ALONG TRANSPORT PATHWAYS

The chemistry of water in the saturated zone along potential flow paths to the accessible environment is discussed in *Geochemical and Isotopic Constraints on Groundwater Flow Directions and Magnitudes, Mixing, and Recharge at Yucca Mountain* (BSC 2003 [162657], Table 5). In the saturated zone, there are two rather distinct water types in the ambient system. One is typified by water from well UE-25 J-13 (J-13), located on the east side of Fortymile Wash. The other is from well UE-25 p#1 (p#1), located near the southern entrance to the Exploratory Shaft Facility. Well J-13 is pumped from volcanic units (Topopah Spring Tuff) whereas p#1 water is pumped from the carbonate aquifer.

The J-13 and p#1 waters were used in sorption experiments as end-member compositions intended to bracket the impact of water composition on sorption coefficients. As shown in Table I-2, for most constituents, these two water compositions approximately bracket the compositions of other wells both in volcanics and alluvium along the potential flow paths to the accessible environment. The pH of the waters from alluvium wells ranges outside that given by J-13 and p#1; however, this is accommodated in the experiments, as seen in Section I.8, where water pH ranged up to 8.4. As will become evident in the discussions of the sorption behavior of individual elements given below, variations in water chemistry have a significant impact on the sorption behavior of a limited number of elements, particularly uranium and neptunium. To constrain these potential impacts, modeling studies with PHREEQC (V2.3, STN: 10068-2.3-00; BSC 2001 [155323]) with the thermodynamic input data files LLNL.DAT (DTN: MO0309THDPHRLL.000 [165530]) and PHREEQC.DAT (DTN: MO0309THDPHRQC.000 [165529]) were carried out as discussed further below.

Because water from the p#1 well was not available to the experimental program at all times, a synthetic p#1 water was developed. This water (Table I-2) was primarily intended to have a bicarbonate concentration similar to that found in UE-25 p#1. It was used in experiments with uranium, neptunium and plutonium because the solution and sorption behavior of these elements is sensitive to the bicarbonate and carbonate concentrations in solution (Nitsche et al. 1993 [155218], pp. 54, 60, and 78, and Nitsche et al. 1995 [100163], p. 39).

Table I-2. Compositions of Waters Used in Sorption Experiments

Chemical Constituent	UE-25 J-13 Water [f]	Range of Concentrations [f] in Downgradient Wells in Volcanics (mg/L)	Range of Concentrations [f] in Downgradient Wells in Alluvium (mg/L)	UE-25 p#1 Water (mg/L)	Synthetic p#1 Water (mg/L)
Ca^{2+}	12 [a]	0.8–37	0.8–20.3	100 [b]	
Mg^{2+}	2.1 [a]	< 0.1–10	0.0–7.7	39 [b]	
Na^+	42 [a]	38–120	57.9–180.5	150 [b]	261 [f]
K^+	5 [a]	1.1–8.9	1.8–5.5	12 [b]	
SiO_2	57 [a]	36–57	40.5–61	41 [b]	
Cl^-	7.1 [a]	6.0–13	5.6–18	28 [b]	
F^-	2.4 [d]	1.0–6.7	1.6–4.2	4.7 [c]	
SO_4^{2-}	17 [a]	14–38	18.7–61.7	160 [b]	
HCO_3^-	124 [e]	107–344	110–255.5	694 [b]	691 [f]
CO_3^{2-}	0.0 [d]	0.0	0.0–23.5	0.0 [c]	
pH	7.2 [a]	6.8–8.4	7.5–8.9	6.6 [a]	
Eh	-	-	128 – 197 [g] mv	-	-

(a) MO0007MAJIONPH.013 [151530]
(b) MO0007MAJIONPH.010 [151523]
(c) GS920408312321.003 [105937]
(d) GS930308312323.001 [145530]
(e) Computed from other data in this table
(f) Triay et al. (1996 [101024], p. 4)
(g) LA0206AM831234.001 [160051]

I.5 EXPERIMENTAL TECHNIQUES

The basic technique for the laboratory determination of sorption coefficients involved the contact of a groundwater sample, spiked with the radionuclide of interest, with a crushed sample of tuff or alluvium (Daniels et al. 1982 [105803]). The rock sample was generally obtained as a core sample. The core was crushed in a jaw crusher and subsequently sieved to a selected grain-size fraction. The sieving process was usually carried out under water. Initially, several different grain-size fractions were used in the experiments. With experience, it was concluded that the 75- to 500-μm fraction was the most appropriate for use in these types of experiments. Results for samples that included all sizes below a certain grain size (e.g., < 35 μm) tended to produce higher sorption-coefficient values than the 75- to 500-μm fraction.

Because the tuffs are very fine grained (i.e., crystal sizes on the order of 10–20 μm), crushing would not produce significant increases in mineral surface area. Mineral fractionation is the process by which certain minerals, such as clays, may become enriched in a very fine-grain size fraction due to sieving effects. Mineralogic analysis of different mineral fractions, including fines, indicates some mineral fractionation has occurred (Chipera and Bish 1989 [101374], Appendix I). Thus, this fractionation may be the cause of the enhanced sorption observed in the fractions that include fines.

One gram of crushed rock material (usually the 75 to 500-μm fraction) was added to a test tube with 20 mL groundwater spiked with the radionuclide(s) of interest. The test tube was put on a shaker table for a predetermined period to allow reaction to occur. After the predetermined time had passed, the solution was separated from the solid phase by either centrifugation or filtration. Centrifugation was preferred for those elements thought to have an affinity for the filter medium. The separations were not always perfect due to various experimental constraints. In some cases, the solid fraction was separately counted. A sorption coefficient was usually calculated from the difference between the initial and final solution concentrations. Corrections were generally made for sorption onto the surface of the test tube during the equilibration (shaking) period.

Some potential sources of errors and experimental artifacts that may pertain to the sorption coefficients include weighing errors, counting errors, errors resulting from solutions being oversaturated with the element of interest, errors from imperfect solid/liquid separations, errors from inaccurate correction for sorption onto container walls, recording errors, transcription errors, inadvertent laboratory errors, and calculation errors. These errors cannot be quantitatively assessed. However, their existence will become apparent in the scatter of the data on diagrams presented in Section I.8.

I.6   APPROACH TO THE DERIVATION OF SORPTION-COEFFICIENT RANGES FOR MAJOR ROCK TYPES IN THE YUCCA MOUNTAIN FLOW SYSTEM

The derivation of sorption-coefficient probability distributions for the elements of interest on the major rock types in Yucca Mountain involves both an evaluation of available experimental data and sorption modeling. Experimental data are used to evaluate the impact of variations in (a) rock sorption properties (within each of the two major groupings), (b) radionuclide concentrations, (c) sorption kinetics, and (d) water chemistry, on sorption coefficients for the elements of interest.

The radionuclides of interest are divided into three groups of radioelements. For the first group, including americium, neptunium, plutonium, thorium, and uranium, experimental data are used to evaluate the impact of radionuclide concentrations, sorption kinetics, and variations in water chemistry on sorption coefficients. Surface-complexation modeling is used to further evaluate the impact of variations in water chemistry and surface area on sorption coefficients. The surface-complexation models used in this analysis are based on the code PHREEQC (V2.3, STN: 10068-2.3-00; BSC 2001 [155323]), using the thermodynamic input data files LLNL.DAT (DTN: MO0309THDPHRLL.000 [165530]) and PHREEQC.DAT (DTN: MO0309THDPHRQC.000 [165529]). The binding constants required for surface-complexation modeling are either obtained from the literature or derived from experimental data involving sorption of the radioelement on silica.

In the second group of elements, including cesium, protactinium, radium, and strontium, the ranges of sorption-coefficient values for the major rock types are derived directly from the available experimental data and the ranges for environmental variables expected in the transport system. Although it would be preferable to have a theoretical model to evaluate the impacts of variations in water chemistry and rock chemistry on sorption coefficients for these radionuclides, there are not sufficient data available to properly constrain such a model.

For the third group, including carbon, iodine and technetium, the sorption coefficient is taken to be zero in the volcanic rocks and in the alluvium. This approach is taken due to the lack of available data and leads to model breakthrough times longer than the transit times that would result in the presence of sorption of these radionuclides on to the rock surfaces.

I.7 SURFACE-COMPLEXATION MODELING

The PHREEQC (V2.3; BSC 2001 [155323]) surface-complexation model used in this analysis is a nonelectrostatic model (Parkhurst 1995 [142177], pp. 10–11). Inputs required for modeling include deprotonation constants, binding constants for elements of interest, total site concentrations, water chemistry, and a thermodynamic database for solution species and solids. Because the tuffs contain up to 76 weight percent silica (Broxton et al. 1986 [100023], p. 39), a silica surface was used to represent the mineral surfaces in the tuffs. The surface-complexation models included the effects of competition from common constituents in the rock such as calcium, magnesium, sodium, potassium, and aluminum. Deprotonation constants for silica were obtained from Dixit and Cappellen (2002 [162985], p. 2565). Binding constants were obtained from Dixit and Cappellen (2002 [162985], p. 2565) for aluminum on silica, from Marmier et al. (1999 [162986], p. 228) for sodium on silica, and from Triay et al. (1997 [100422], p. 169) for potassium and calcium on silica. The total site concentrations were obtained from surface areas reported in Triay et al. (1996 [101023], p. 62) (DTN: LA0311SK831341.001 [166195]), and a site density of 2.3 sites/nm^2 is used as recommended by Pabalan et al. (1998 [162987], p. 124). The thermodynamic databases used for the modeling were the LLNL.DAT (DTN: MO0309THDPHRLL.000 [165530]) and PHREEQC.DAT (DTN: MO0309THDPHRQC.000 [165529]).

I.8 DISCUSSION AND ANALYSIS OF EXPERIMENTAL SORPTION-COEFFICIENT DATA AND SURFACE-COMPLEXATION MODELING

The data and modeling results for each element are discussed in separate sections, arranged in alphabetical order.

I.8.1 Americium

According to Nitsche et al. (1993 [155218], p. 78), the solubility of americium in J-13 water is controlled by AmOH(CO)$_3$. At 25°C and a pH of 8.5, the solubility is 2.4 ($\pm$ 1.9) x 10^{-9} M/L. At 25°C and a pH of 7.0, the solubility is 1.2 ($\pm$ 0.3) x 10^{-9} M/L.

I.8.1.1 Devitrified Tuff

Sorption coefficients (K_d) measured on devitrified tuffs are plotted versus calculated final solution concentrations in Figure I-1. The points identified by the term "sorption" refer to experiments in which J-13 water spiked with americium was contacted with devitrified tuff. The points identified by the term "desorption" refer to experiments in which the solid remaining after the "sorption" step was contacted with unspiked J-13 water. The steep negative slopes evident at the higher concentrations for individual samples reflect a mass balance constraint. That is, the final solution concentration is calculated using the starting solution concentration and the measured sorption coefficient. This approach forces a linear dependence of the sorption

coefficient on the final solution concentration. The offset between the points for the various samples primarily reflects different starting concentrations.

The positions of samples along a slope reflect variations in the degree of equilibration among various experiments on the same sample with the same starting concentration. When the sorption experiments are initiated, these trends start on the abscissa at the initial concentration. As the experiment duration is increased, americium is sorbed to the solid phase, the solution concentration decreases correspondingly, and the value of K_d increases. At equilibrium, the solution concentration remains constant with time and the K_d is at a maximum value. For desorption experiments, the trend is reversed. As the duration of a desorption experiment increases, the solution concentrations increase as americium is released from the solid, and the value of K_d decreases. At equilibrium, the K_d value obtained from a desorption experiment should approach the K_d value obtained from the associated sorption experiment unless the isotherm is quite nonlinear, in which case, the trends could be offset. The offset would be due to a different total americium concentration in the sorption and desorption experiments. The K_d value on which the two trends converge is considered the equilibrium value.

As shown in Figure I-1, the calculated final solution concentrations were higher than the solubility of $AmOH(CO)_3$ in numerous experiments with samples JA-32 and YM-54. Thus, the results for these experiments must be discounted. For the remaining experiments, the sorption coefficients range from 1,000 to more than 10,000 mL/g. In one sample (GU3-688), americium concentrations were analyzed by isotope dilution mass spectrometry (Triay et al. 1991 [104129], p. 142-144). This technique has higher sensitivity than the (radioactivity) counting techniques normally used, thereby allowing the use of lower americium concentrations. The result obtained for this sample is in the range of the results obtained for the other samples.

The sorption coefficients derived from desorption experiments are generally larger than those derived from the sorption experiments on a given sample (Figure I-1). This result could be due to slow desorption kinetics or due to a nonlinear isotherm.

Americium on Devit. Tuff in J-13

Legend:
- ■ Sorption G1-1883
- □ Desorption G1-1883
- ◆ Sorption GU3-0433
- ◇ Desorption GU3-0433
- ▲ Sorption JA-32
- △ Desorption JA-32
- ● Sorption YM-22
- ○ Desorption YM-22
- ✕ Sorption YM-54
- + Desorption YM-54
- ■ GU3-688
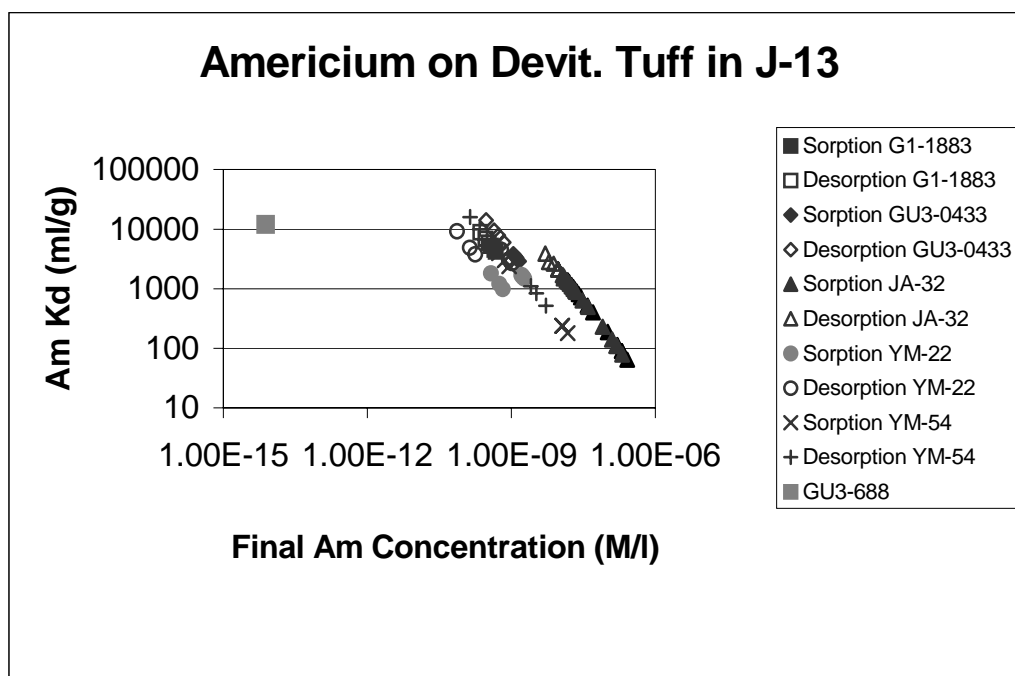
DTN: LA0305AM831341.001 [163789]

Figure I-1. Americium Sorption Coefficients on Devitrified Tuff
Versus Calculated Final Americium Concentration in Solution

Americium sorption coefficients are plotted versus duration of the sorption and desorption experiments in Figure I-2. The trend in the data (ignoring data from samples JA-32 and YM-54) suggests that americium sorption-coefficient values are not very sensitive to the duration of the experiments except in those experiments with very short durations. Thus, the kinetics of the americium sorption reactions appear to be relatively fast.

The effects of variations in water chemistry on americium sorption coefficients have not been tested experimentally except for variations in solution pH. All the americium sorption and desorption experiments carried out with Yucca Mountain samples used J-13 water. Americium sorption and desorption coefficients in J-13 water are plotted versus pH in Figure I-3. It is evident that there is no clear trend among the data points plotted. The variations in sorption coefficients observed in multiple experiments with the same rock sample could reflect (radioactivity) counting statistics, long-term stability of the counting equipment, sorption kinetics, imperfect separation of the solid and liquid phases, and/or the consistency of adsorption of americium to the walls of the experimental containers. Counting statistics are generally a small percentage of the measured sorption coefficient. Sorption kinetics may explain some of the scatter but not all of it. The other factors are likely significant, but they cannot be quantified with the available data.

DTN: LA0305AM831341.001 [163789]
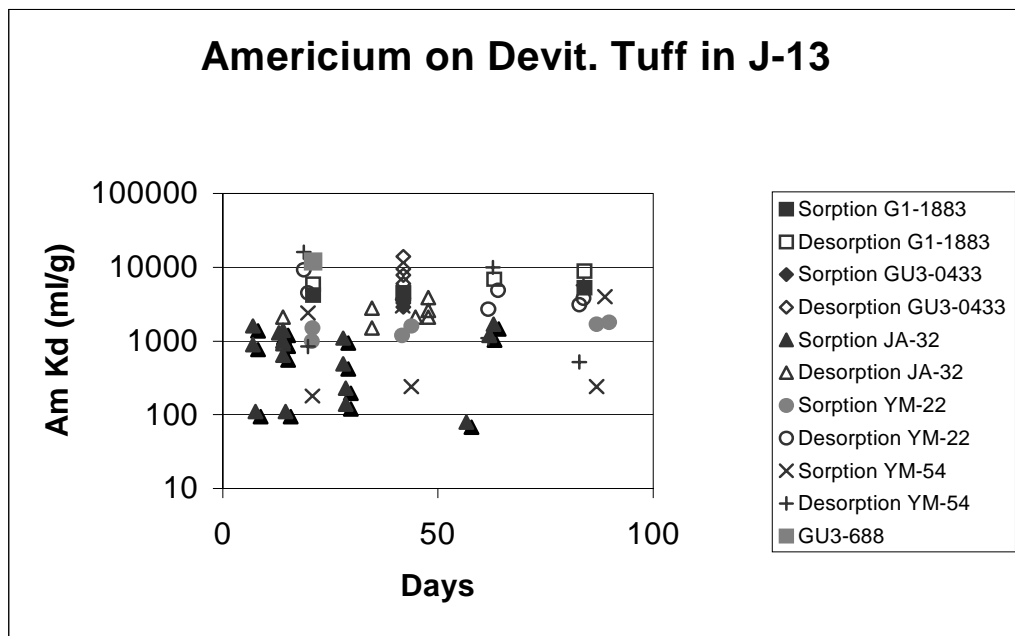
Figure I-2. Americium Sorption Coefficients for Devitrified Tuff as a Function of Experiment Duration
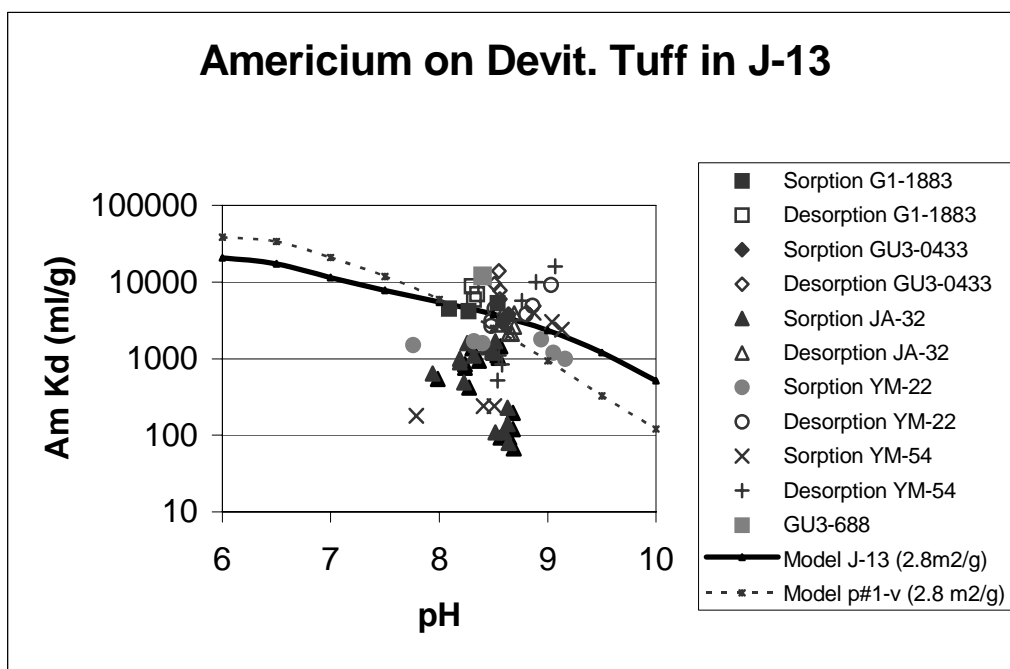
DTN: LA0305AM831341.001 [163789]

NOTE: Model curves derived with PHREEQC surface-complexation modeling are also shown (Output DTN: LA0306AM831343.001 file output/Amsij13.pun).

Figure I-3. Americium Sorption Coefficients on Devitrified Tuff Versus pH of J-13 Water

To gauge the potential impact of variations in water chemistry on americium sorption coefficients, surface complexation modeling was carried out with PHREEQC (V2.3; BSC 2001 [155323]) with the thermodynamic input data files LLNL.DAT (DTN: MO0309THDPHRLL.000 [165530]) and PHREEQC.DAT (DTN: MO0309THDPHRQC.000 [165529]). In the modeling, surface sites on devitrified tuff were taken to be equivalent to surface sites on silica, 2.8 m^2/g (Allard et al. 1980 [104410]). Binding constants for americium species on silica were derived by fitting data presented by Beall et al. (1986 [162983], p. 502) for the sorption of americium onto quartz (2.8 m^2/g; Allard et al. 1980 [104410], p. 478) in Oak Ridge National Laboratory (ORNL) Standard Water (Allard and Beall (1979 [147235] p 511). This water is similar in composition to J-13. As shown in Figure I-4, the sorption coefficients for americium on quartz (Beall et al. 1986 [162983], p. 502) as a function of pH could be fit very well using two surface reactions involving an americium sulfate complex and an americium carbonate complex. These reactions are listed in Table I-3.

Table I-3. Surface Complexation Reactions for Americium

Reaction	Log K
$SiOH + Am^{3+} + SO_4^{2-} \leftrightarrow SiOAmSO_4 + H^+$	5.5
$SiOH + Am^{3+} + CO_3^{2-} \leftrightarrow SiOAmCO_3 + H^+$	6.5

Data: Beall et al. 1986 [162983]

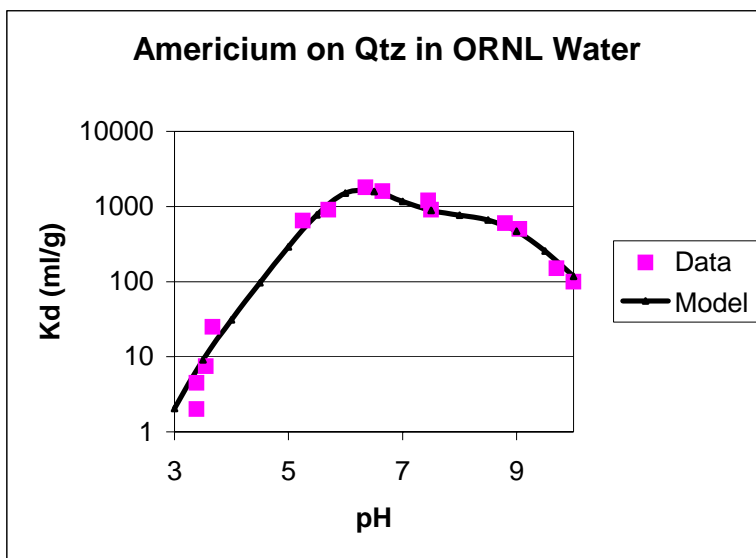Model: Output DTN: LA0306AM831343.001 file output/Amornl5.pun

NOTE: Model curves derived with PHREEQC surface-complexation modeling are also shown (Output DTN: LA0306AM831343.001 file output/Amornl5.pun).

Figure I-4. Americium Sorption Coefficients on Quartz from Beall et al. (1986 [162983]) and Model Fit
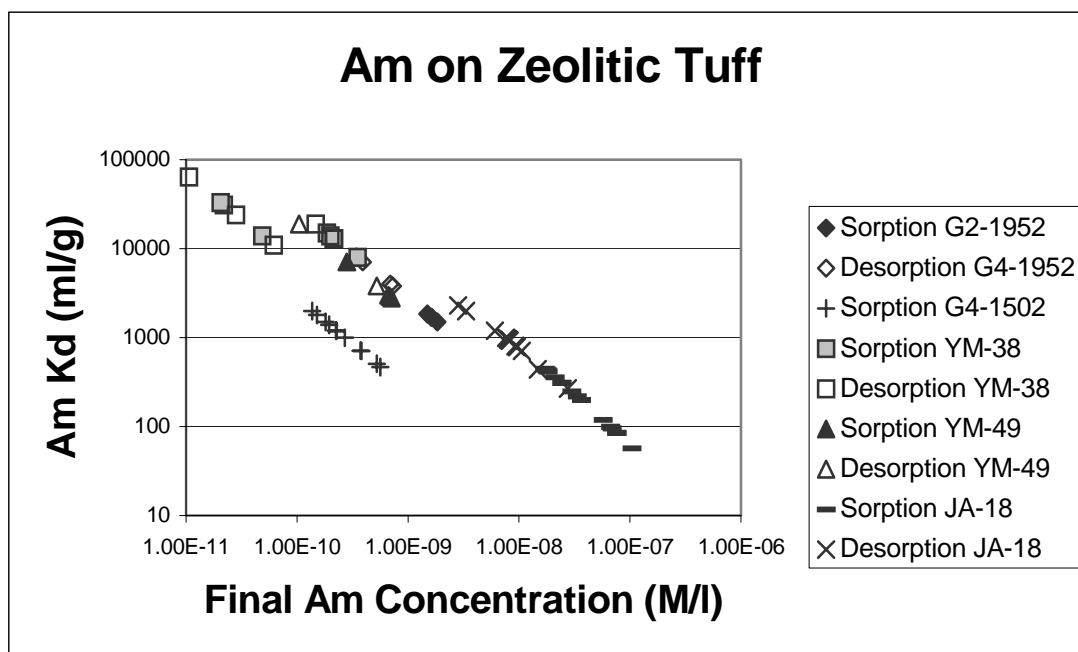
Using a surface area of 2.8 m^2/g, americium sorption coefficients were calculated for "devitrified tuff" in J-13 water as a function of pH. The model curves are shown in Figure I-3. The fact that the model sorption coefficient for J-13 at a pH value of 8.5 lies in the middle of the range of experimental values provides confidence that the model is reasonable. The model curves move up or down linearly with surface area. Thus, at least part of the range of experimental values could reflect variations in devitrified tuff surface areas.

The model curve shown in Figure I-3 indicates that sorption coefficients for americium will increase with decreasing pH in the pH range from 7.0 to 9.0. Thus, in terms of pH, the experimentally derived sorption coefficients are at the low end of the range of coefficients to be expected in the saturated zone. The effect of variation in major ion chemistry of groundwater is shown by the curve calculated for borehole p#1 groundwater. Americium sorption coefficients calculated using p#1 water are similar to those calculated using J-13 water. Thus, variations in water chemistry are not expected to have a major impact on americium sorption coefficients.

On the basis of the experimental data and model curves plotted in Figure I-3, the range of americium sorption coefficients expected for devitrified tuffs in the saturated volcanic section at Yucca Mountain is selected as 1,000 to 10,000 mL/g. The probability distribution type selected is a truncated normal distribution with a mean of 5500 mL/g and standard deviation of 1500 mL/g. The data for JA-32 and YM-54 were discounted in derivation of the distribution because the final solutions in the experiments with these samples were oversaturated with AmOH(CO)$_3$.
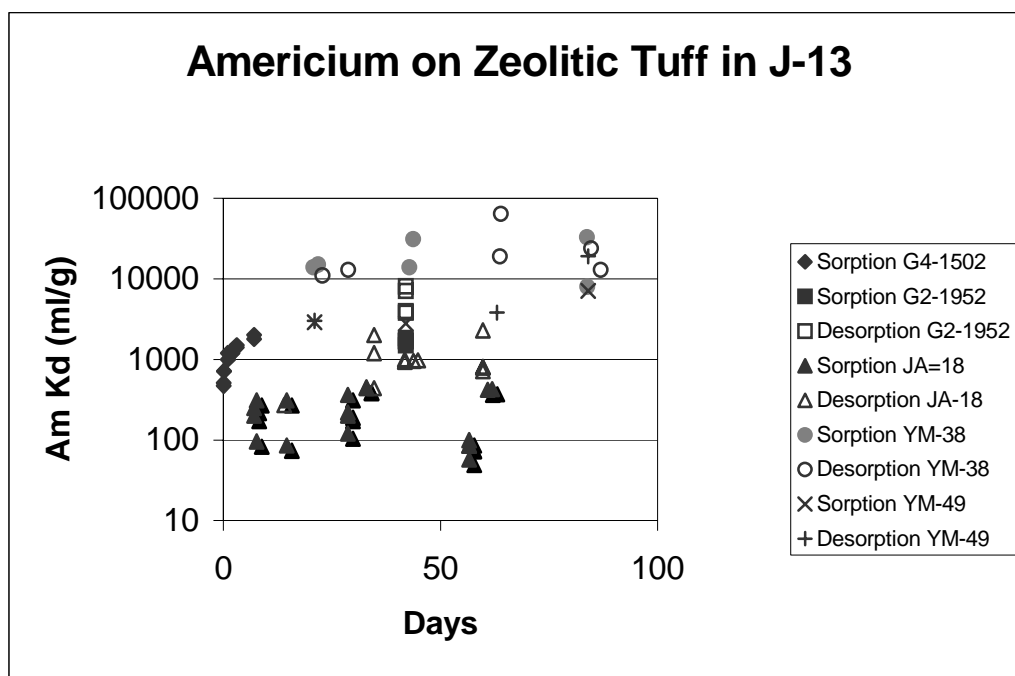
I.8.1.2   Zeolitic Tuff

The measured sorption coefficients for zeolitic tuff are plotted versus calculated final solution concentrations in Figure I-5. The calculated final solution concentrations were higher than the solubility of $AmOH(CO)_3$ in essentially all the experiments with sample JA-18. Therefore, the sorption coefficients obtained for this sample are discounted in the derivation of the sorption-coefficient probability distribution for americium on zeolitic tuff. Sorption experiments with sample G4-1952 were close to saturation with $AmOH(CO)_3$. The sorption coefficients obtained for this sample will be used in the derivation of the distribution.

<figure>

Am on Zeolitic Tuff

Y-axis: Am Kd (ml/g)
X-axis: Final Am Concentration (M/l)

Legend:
◆ Sorption G2-1952
◇ Desorption G4-1952
+ Sorption G4-1502
▣ Sorption YM-38
▢ Desorption YM-38
▲ Sorption YM-49
△ Desorption YM-49
▬ Sorption JA-18
✕ Desorption JA-18

</figure>

DTN: LA0305AM831341.001 [163789]

Figure I-5. Americium Sorption Coefficients on Zeolitic Tuff
Versus Calculated Final Americium Concentration in Solution

Americium sorption coefficients for zeolitic tuff are plotted versus duration of the sorption and desorption experiments in Figure I-6. As with the devitrified tuffs, the trend in the data (excluding sample JA-18) suggests americium sorption-coefficient values obtained in experiments with solutions undersaturated with $AmOH(CO)_3$ are not very sensitive (< 10 times) to the duration of the experiments except in those experiments with short durations (e.g., sample G4-1502). Thus, the kinetics of the americium sorption reactions on zeolitic tuff appear to be relatively fast.
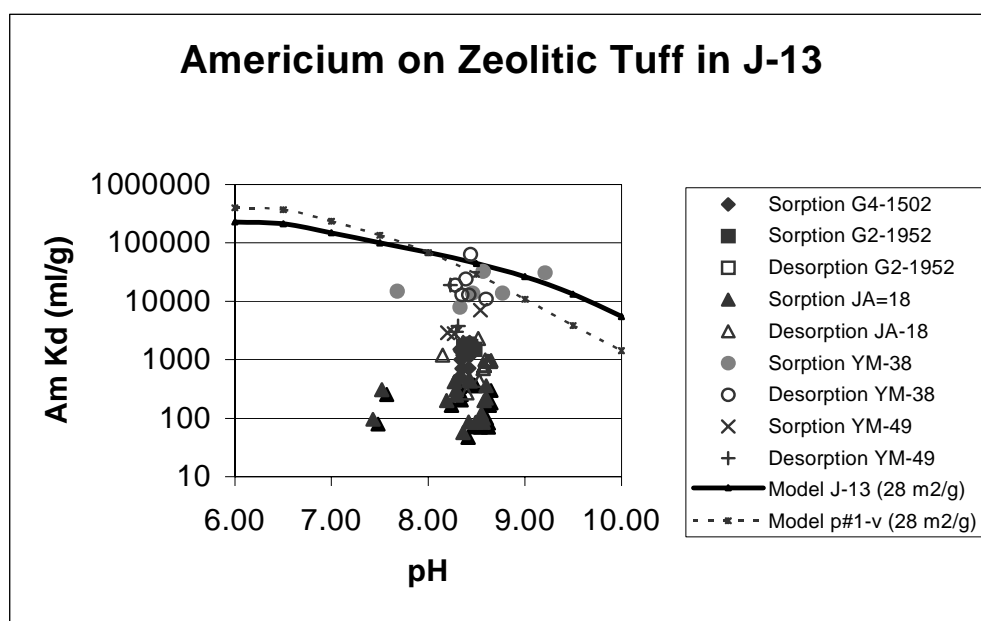
Americium on Zeolitic Tuff in J-13

DTN: LA0305AM831341.001 [163789]

Figure I-6. Americium Sorption Coefficients for Zeolitic Tuff
as a Function of Duration of Sorption and Desorption Experiments

The surface complexation model developed for zeolitic tuff is similar to the model developed for devitrified tuff except that a surface area of 28 m^2/g was used as a representative value (Table I-1 of this report). The model sorption coefficient at a pH of 8.5 lies at the high end of the range of experimental values (Figure I-7). It might be expected that the sorption coefficients for zeolitic tuffs would be on the order of 10 times larger than those for devitrified tuffs to reflect the factor of 10 increase in surface area. The fact that the americium sorption coefficients obtained for zeolitic tuffs are not, on average, a factor of 10 larger than those measured in devitrified tuffs suggests not all the surface area in the zeolitic tuffs may be accessible to americium. Alternatively, the binding sites in the interior of zeolite crystals may not have a high affinity for americium species.

As with devitrified tuff, the model curves for zeolitic tuffs shown in Figure I-7 indicate that sorption coefficients for americium will increase with decreasing pH in the pH range from 7.0 to 9.0. Thus, in terms of pH, the experimentally derived sorption coefficients are at the low end of the range of coefficients to be expected in the unsaturated zone. The effect of variation in major ion chemistry of groundwater is shown by the curve calculated for borehole p#1 groundwater. Americium sorption coefficients calculated using p#1 water are similar to the coefficients calculated using J-13 water.

On the basis of the experimental data and model curves plotted in Figure I-7, the range of americium sorption coefficients selected for zeolitic tuffs in the saturated volcanic section at Yucca Mountain is 1,000 to 10,000 mL/g. The probability distribution type selected is a truncated normal distribution with the mean of 5500 mL/g and the standard deviation of 1500 mL/g . The upper end of this distribution could have been set at 100,000 mL/g instead of 10,000 mL/g based on the available data and modeling results. However, the 10,000 mL/g value is large enough to effectively keep americium from being transported over the regulatory time frame. In addition, by using an upper limit of 10,000 mL/g, the same distribution can be used for devitrified and zeolitic tuffs. The data for sample JA-18 were discounted in the derivation of the distribution because the final solutions in the experiments with this sample were oversaturated with $AmOH(CO)_3$.

Americium on Zeolitic Tuff in J-13

Legend:
- ◆ Sorption G4-1502
- ■ Sorption G2-1952
- □ Desorption G2-1952
- ▲ Sorption JA=18
- △ Desorption JA-18
- ● Sorption YM-38
- ○ Desorption YM-38
- × Sorption YM-49
- + Desorption YM-49
- — Model J-13 (28 m2/g)
- - - - Model p#1-v (28 m2/g)

DTN: LA0305AM831341.001 [163789]

NOTE: Model curves derived with PHREEQC surface-complexation modeling are also shown
        (DTN: LA0306AM831343.001 file output/ Amzeop1.pun)

Figure I-7. Americium Sorption Coefficient Data and Modeling
Results for Zeolitic Tuff as a Function of pH

I.8.1.3   Alluvium

The probability distribution for devitrified tuff will be used as a default for the americium sorption-coefficient probability distribution in alluvium. Alluvium along the flow path is composed largely of disaggregated tuffaceous materials. Because devitrified tuff makes up a major portion of the volcanic units exposed at the surface, it should be a major component in alluvium. In addition, clays and other secondary minerals are enriched in alluvial materials.

These characteristics should result in higher sorption coefficients for alluvial materials compared to intact devitrified tuff.

I.8.2 Cesium

The solubility of cesium in J-13 water at 25°C is very high. In fact, cesium concentrations in Yucca Mountain groundwaters will not have a solubility limitation (BSC 2003 [163152], Section 6.17).

I.8.2.1 Devitrified Tuff

Experimentally derived sorption coefficients for cesium on devitrified tuff are plotted against the calculated final cesium concentrations of the experiments in Figure I-8. The data points are separated into groups on the basis of when the experiments were carried out (pre-1990 = "old" and post-1990 = "new"), water type, and on whether the sorption coefficient was determined from a sorption or a desorption experiment. There are also data for sorption isotherms on samples YM-22 and G1-2840.
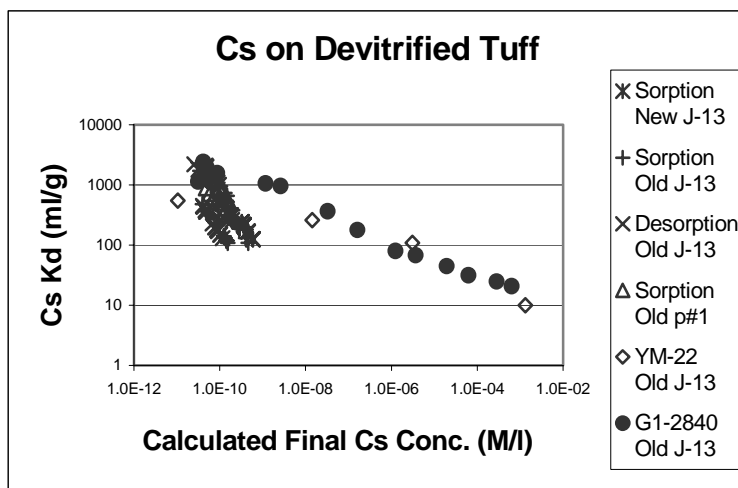
DTN: LA0010JC831341.002 [153321], LA0305AM831341.001 [163789], LA0309AM831341.003 [165524]

Figure I-8. Cesium Sorption Coefficients on Devitrified Tuff
Versus Calculated Final Cesium Concentration in Solution

Sorption coefficients obtained in "new" experiments lie within the range defined by the "old" experiments at similar cesium concentrations. Although most of the sorption experiments resulted in K_d values greater than 100 mL/g, these experiments were carried out at cesium concentrations below 1.0 x 10^{-6} M/L. At higher cesium concentrations, the K_d values obtained were between 10 and 100 mL/g. Nonlinear sorption isotherms were obtained for samples YM-22 and G1-2840 in J-13 water. The data for sample G1-2840 were fit using a Freundlich equation as shown in Figure I-9. Sorption coefficients obtained in experiments with p#1 water

fall in the middle of the cluster of points in Figure I-8 near 1×10^{-10} M/L. Thus, there is little or no impact of variations in water chemistry on cesium sorption coefficients on devitrified tuff.

Cs on Devitrified Tuff G1-2840 in J-13

$y = 0.0024x^{0.7212}$

Cs on Solid (M/g)

Calculated Final Cs Conc (M/l)
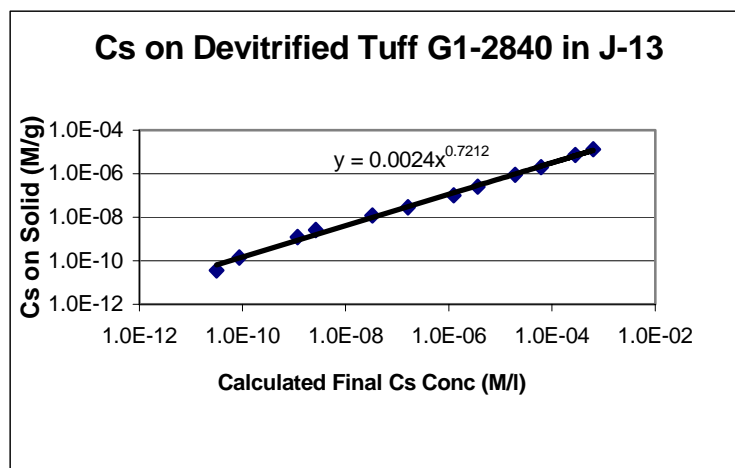
DTN: LA0010JC831341.002 [153321], LA0305AM831341.001 [163789]

Figure I-9. Freundlich Isotherm Fit to Sorption-Coefficient Data for
Cesium on Devitrified Tuff Sample G1-2840 in J-13 Water

The effects of experiment duration on the cesium sorption coefficients for devitrified tuff are shown in Figure I-10. The large range in sorption coefficients obtained at a given duration (e.g., 21 days) mainly reflects variations in cesium solution concentrations, although variations in ion-exchange capacities may also contribute to the range. The range of sorption-coefficient values is fairly constant with duration when the results for samples YM-22 and G1-2840 are excluded. This range extends from just above 100 mL/g to above 1,000 mL/g. The constancy indicates cesium sorption reactions are fast.
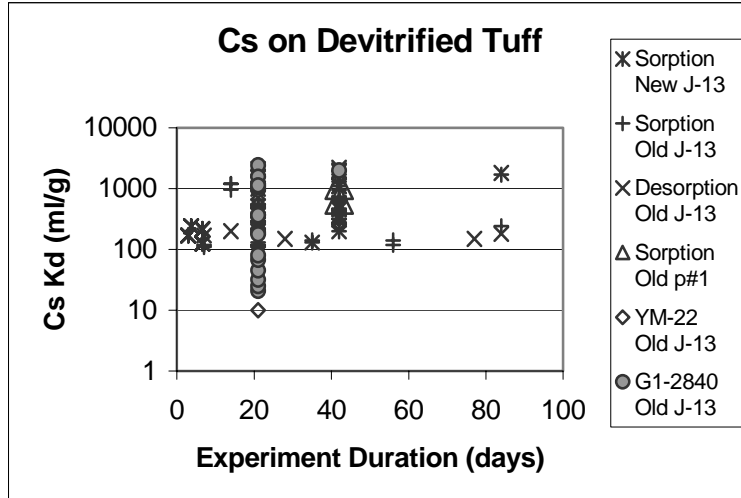
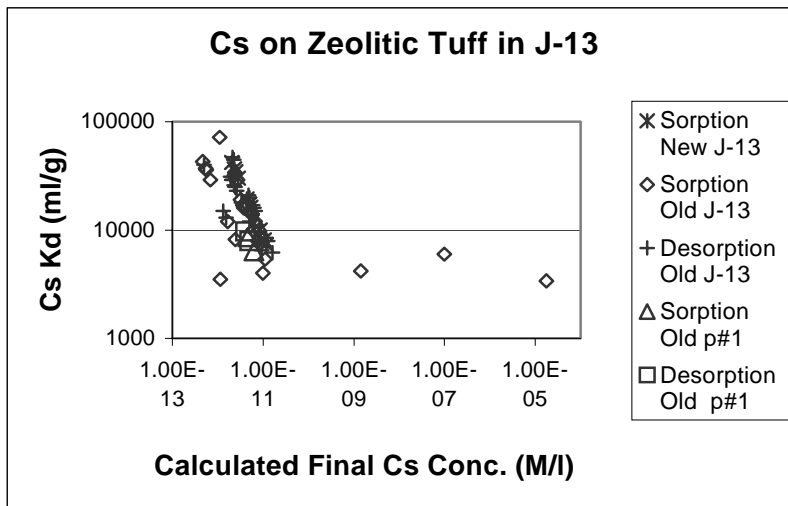Figure I-10. Cesium Sorption Coefficients on Devitrified Tuff Versus Experiment Duration
for Sorption (Forward) and Desorption (Backward) Experiments

The cesium sorption-coefficient probability distribution derived for devitrified tuff in the saturated zone is a normal distribution with a range of 100 to 1,000 mL/g, mean value of 728 mL/g, and a standard deviation of 464 mL/g. The low end of the chosen range was selected based on the minimum value observed in experiments with solution concentrations less than 10^{-7} M/L. The upper end of the distribution was chosen as a minimum upper limit given the potential impacts of low cesium solution concentrations and high ion-exchange capacities.

I.8.2.2   Zeolitic Tuff

Experimentally derived sorption coefficients for cesium on zeolitic tuff are plotted against the calculated final cesium concentrations of the experiments in Figure I-11. The data points are separated into groups on the basis of when the experiments were carried out (pre-1990 = "old" and post-1990 = "new"), water type, and on whether the sorption coefficient was determined from a sorption or a desorption experiment. There are also data for a sorption isotherm on sample YM-38.

Cs on Zeolitic Tuff in J-13

DTN: LA0010JC831341.002 [153321], LA0305AM831341.001 [163789], LA0309AM831341.003 [165524]

Figure I-11. Cesium Sorption Coefficients on Zeolitic Tuff Versus
Calculated Final Cesium Concentration in Solution

The range of measured cesium sorption coefficients for zeolitic tuffs is 3,500 to 72,000 mL/g. A sorption isotherm was obtained for sample YM-38 in J-13 water. As shown in Figure I-12, the isotherm is nearly linear. Sorption coefficients obtained in experiments with borehole p#1 water fall at the lower end of the range of values obtained for experiments with J-13 water (Figure I 11). Thus, there is some impact of variations in water chemistry on cesium sorption coefficients on zeolitic tuff, although this impact is minor.

Cs on Zeolitic Tuff YM-38 in J-13

$y = 1.8197x^{0.9397}$
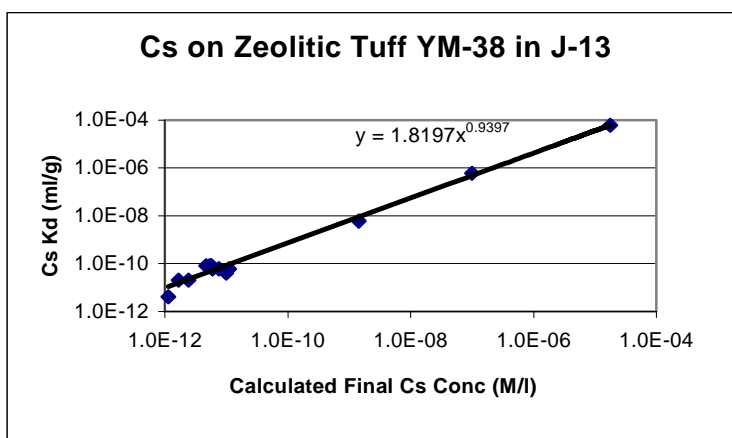
DTN: LA0305AM831341.001 [163789]

Figure I-12. Freundlich Isotherm Fit to Sorption-Coefficient Data for Sample YM-38 in J-13 Water

The effects of experiment duration on the value of K_d for cesium on zeolitic tuff are shown in Figure I-13. The large range in sorption coefficients obtained at a given duration mainly reflects variations in cesium solution concentrations, although there must also be some contribution from variations in ion-exchange capacities of the zeolitic tuff samples used in the experiments. The range of sorption-coefficient values is fairly consistent with duration. For example, the range of sorption-coefficient values for the 3.6-day experiments is similar to the range for the 42-day experiments. This result indicates the sorption reaction kinetics are fast.

DTN: LA0010JC831341.002 [153321], LA0305AM831341.001 [163789], LA0309AM831341.003 [165524]

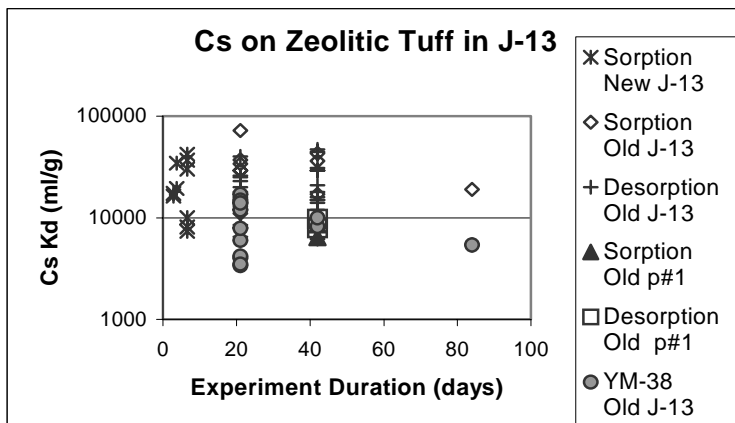Figure I-13. Cesium Sorption Coefficients on Zeolitic Tuff Versus Experiment Duration
for Sorption (Forward) and Desorption (Backward) Experiments

The cesium sorption-coefficient probability distribution selected for zeolitic tuff in the saturated zone is a exponential distribution with a range of 4000 to 42,000 mL/g, a mean of 16,942 mL/g and a standard deviation of 14,930 mL/g. The low end of the chosen range was selected based on the minimum value observed in the available experiments, including those with p#1 water. The upper end of the distribution was chosen as a minimum upper limit given the potential impacts of lower cesium solution concentrations and higher ion-exchange capacities than those encountered in the experimental program.

I.8.2.3   Alluvium

The probability distribution for devitrified tuff will be used as a default for the cesium sorption-coefficient probability distribution in alluvium. Alluvium along the flow path is composed largely of disaggregated tuffaceous materials. Because devitrified tuff makes up a major portion of the volcanic units exposed at the surface, it should be a major component in alluvium. In addition, clays and other secondary minerals are enriched in alluvial materials. These characteristics should result in higher sorption coefficients for alluvial materials compared to intact devitrified tuff.

I.8.3   Neptunium

According to Nitsche et al (1993 [155218] Table VI), the solubility of neptunium in J-13 water at 25°C and a pH of 8.5 is 4.4 x 10^{-5} M/L, and the solubility-controlling solid is Np_2O_5 under oxidizing conditions (Eh > 180 mV) (Eh is the oxidation/reduction potential normalized to the standard hydrogen electrode). At a pH of 6.9, the solubility is higher at 1.3 x 10^{-4} M/L under oxidizing conditions (Eh > 250 mV). The solubility of neptunium in borehole p#1 water at 25°C and a pH of 8.5 is 7.0) x 10^{-6} M/L and 4.7 (± 0.4) x 10^{-5} M/L at 25°C and a pH of 7.0 according to Nitsche et al. (1995 [100163], Table I).

I.8.3.1   Devitrified Tuff

The results of sorption experiments with devitrified tuff are shown in Figure I-14. Some of the experiments with J-13 water had final neptunium concentrations above 7.0 x 10^{-6} M/L. Thus, the results for these experiments should be discounted because the experiments could have been oversaturated with Np_2O_5. All but four of the experiments with synthetic p#1 water had final neptunium solution concentrations less than 2.5 x 10^{-5} M/L. The results for the four experiments with oversaturated final solutions will be discounted. The remaining data points, plotted in Figure I-15, are suggestive of a dependence of the sorption coefficient on the final neptunium solution concentration.
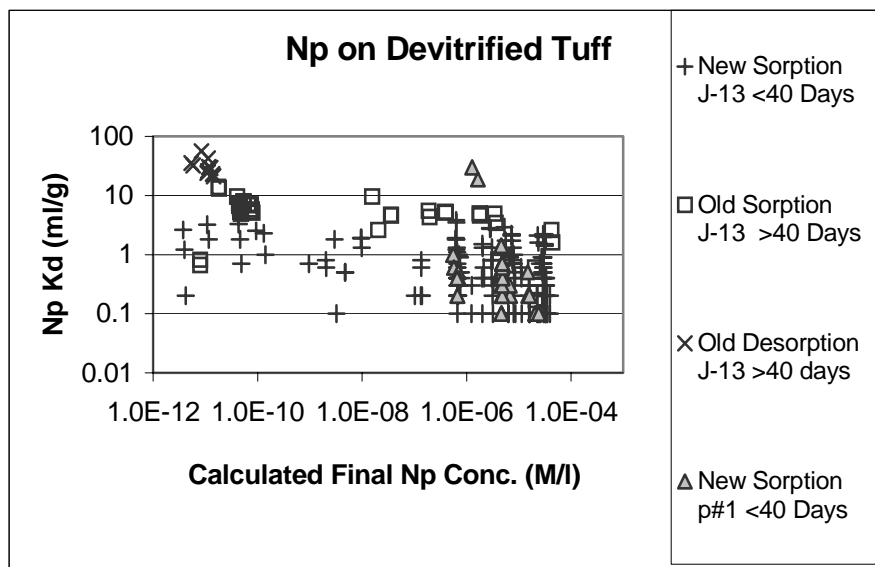
DTN: LA0010JC831341.007 [153319], LA0305AM831341.001 [163789], LA0309AM831341.004 [165525]

Figure I-14. Neptunium Sorption Coefficients on Devitrified Tuff
Versus Calculated Final Neptunium Concentration in Solution
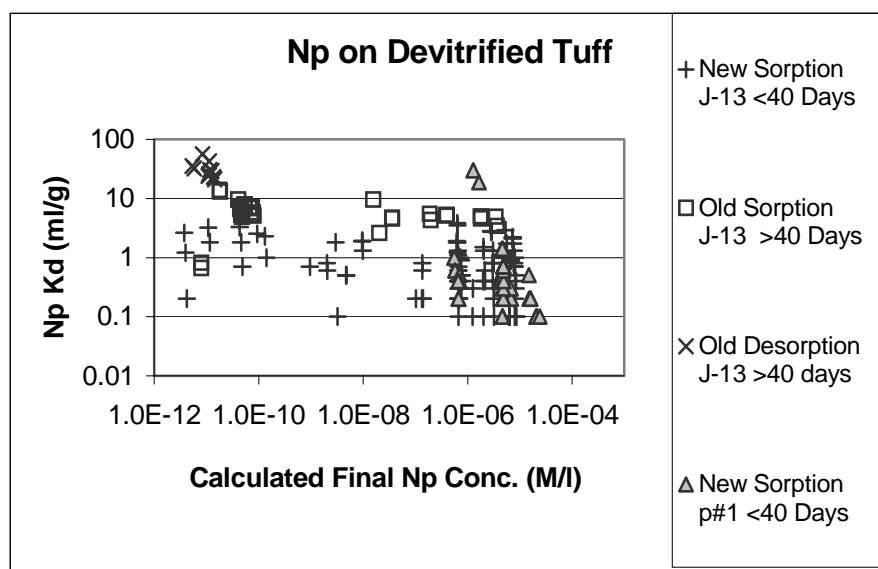
Figure I-15. Neptunium Sorption Coefficients on Devitrified Tuff
Versus Calculated Final Neptunium Concentration in Solution

DTN: LA0010JC831341.007 [153319], LA0305AM831341.001 [163789], LA0309AM831341.004 [165525]

NOTE: Experiments oversaturated with Np_2O_5 have been omitted.

Neptunium sorption experiments carried out as a function of experiment duration are shown in Figure I-16. There is a significant difference between the results for "old" and "new" experiments with the "old" results generally having higher values than the "new" results. The most straightforward explanation is that the difference is due to the fact that the "old" results represent experiments with longer durations than the "new" results. Within the "old" data points, the sorption-coefficient values appear to reach a steady-state level after 42 days.

The impact of variations in pH on neptunium coefficients on devitrified tuffs is shown in Figure I-17. There is a lot of scatter in the "new" data, and there do not appear to be clear positive or negative trends among these data points. Nor does there appear to be much difference between the results for J-13 water and synthetic p#1 water. The "old" data points are more consistent and show very little dependence of the neptunium sorption coefficient on pH except at pH values less than 7.0. Curves calculated from the PHREEQC (V2.3; BSC 2001 [155323]) surface complexation model with the thermodynamic input data files LLNL.DAT (DTN: MO0309THDPHRLL.000 [165530]) and PHREEQC.DAT (DTN: MO0309THDPHRQC.000 [165529]) for "devitrified tuff" in J-13 and p#1 waters are also plotted. The neptunium binding constants on silica were obtained from Turner et al. (1998 [162989], p. 264). The J-13 curve lies between the "old" sorption and desorption points. This result suggests the curve may reflect the equilibrium values of neptunium sorption coefficients on devitrified tuff better than the experimental data. In this interpretation, the sorption data points reflect experiments that have not reached an equilibrium state.
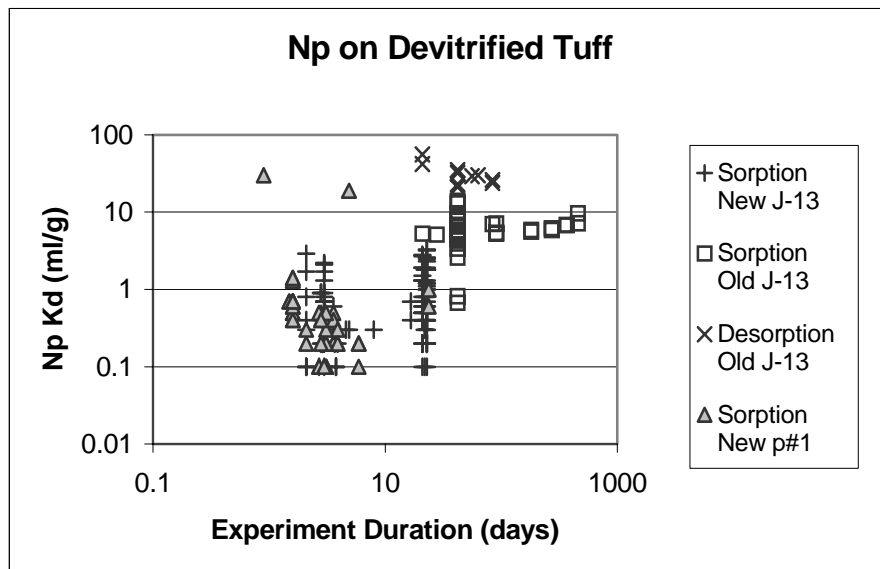
Np on Devitrified Tuff

DTN: LA0010JC831341.007 [153319], LA0305AM831341.001 [163789], LA0309AM831341.004 [165525]

NOTE: Experiments oversaturated with Np_2O_5 have been omitted.

Figure I-16. Neptunium Sorption Coefficients on Devitrified Tuff Versus Experiment
Duration for Sorption (Forward) and Desorption (Backward) Experiments.

Np on Devitrified Tuff
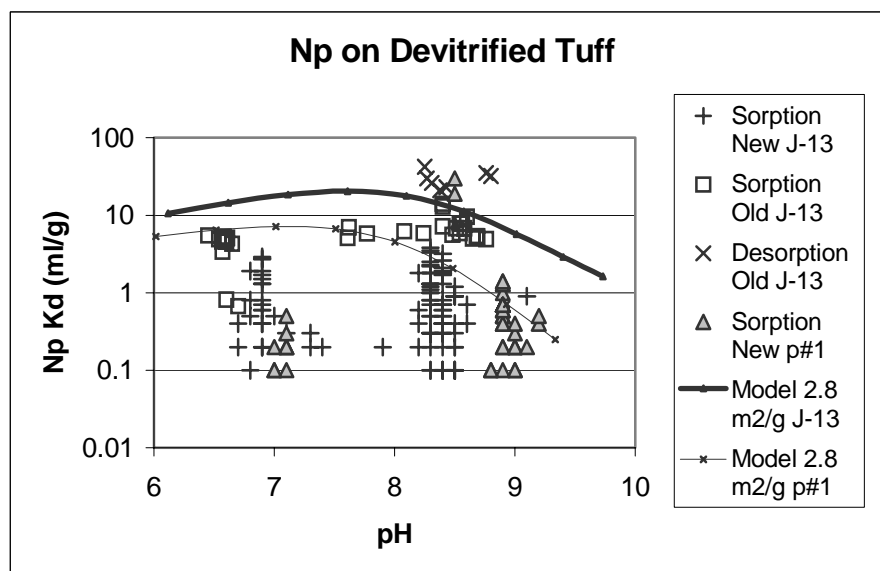
DTN: LA0010JC831341.007 [153319], LA0305AM831341.001 [163789], LA0309AM831341.004 [165525]

NOTE: PHREEQC model results for J-13 and p#1 waters are also plotted (DTN: LA0306AM831343.001. Data from
file output/Npsij13.pun).

Figure I-17. Neptunium Sorption Coefficients on Devitrified Tuff in J-13 and Synthetic p#1 Waters
Versus Solution pH in Sorption (Forward) and Desorption (Backward) Experiments

The neptunium sorption-coefficient probability distribution selected for devitrified tuff in the saturated zone is an exponential distribution with a range of 0 to 2 mL/g and a mean of 0.69 mL/g and a standard deviation of 0.707 mL/g. The low end of the chosen range is selected based on the minimum value obtained in short-term experiments (up to 21 days). The experiments on which this value is based do not appear in the graphs because the graphs use logarithmic coordinates. The upper end of the distribution was chosen as a minimum upper limit with a neptunium concentration near the solubility limit (Figure I-15) with emphasis on results from experiments with pH near 7.0. Experiments with pH near 7.0 were emphasized because the pH values of saturated zone waters in volcanic units downgradient from the repository cluster near 7.0 (BSC 2003 [162657] Table 5). It is acknowledged that a higher limit could be selected for the upper end of the distribution based on the available data.

I.8.3.2 Zeolitic Tuff

Sorption coefficients on zeolitic tuff are shown as a function of calculated final solution concentration in Figure I-18. Many of the experiments with J-13 water had final neptunium concentrations above 7.0×10^{-6} M/L. Thus, the results for these experiments should be discounted because the experiments could have been oversaturated with Np_2O_5. Many of the experiments with synthetic p#1 water had final neptunium solution concentrations close to or greater than 2.5×10^{-5} M/L. The results for these experiments must also be discounted.
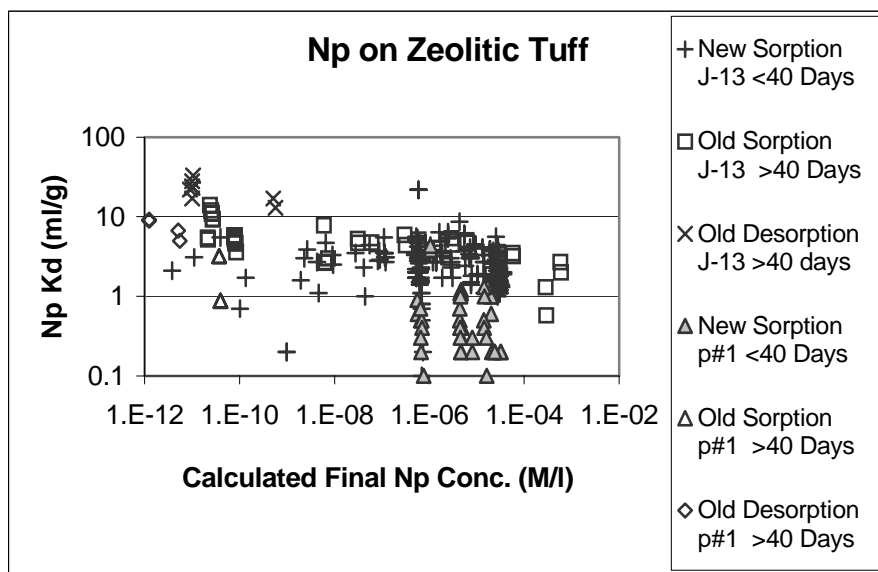
DTN: LA0010JC831341.007 [153319], LA0305AM831341.001 [163789], LA0309AM831341.004 [165525]

Figure I-18. Neptunium Sorption Coefficients on Zeolitic Tuff
Versus Calculated Final Neptunium Concentration in Solution

Removal of the oversaturated experiments from the data set results in Figure I-19. With these points removed, there is essentially no dependence of sorption coefficient on calculated final

solution concentration for J-13 experiments. However, it is clear that there is a dependence of sorption coefficient on water chemistry in the short-term experiments. If the solubility of neptunium in synthetic p#1 water is less than the solubility in actual p#1 water, this dependence on water chemistry may not be real.
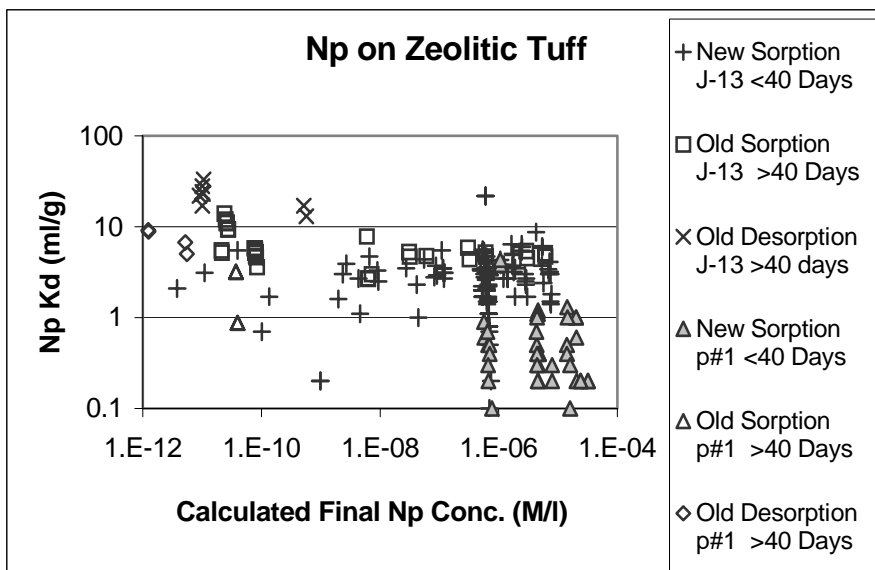
DTN: LA0010JC831341.007 [153319], LA0305AM831341.001 [163789], LA0309AM831341.004 [165525]

Figure I-19. Neptunium Sorption Coefficients on Zeolitic Tuff Versus Calculated Final Neptunium Concentration in Solution with Data from Oversaturated Experiments Removed

Neptunium sorption experiments carried out as a function of experiment duration are shown in Figure I-20. There is a significant difference between the results for "old" and "new" experiments with the "old" results generally having higher values than the "new" results. The most straightforward explanation is that the difference is due to the fact that the "old" results represent experiments with longer durations than the "new" results. Within the "old" data points, the sorption-coefficient values appear to reach a steady-state level after 42 days.

Figure I-20. Neptunium Sorption Coefficients on Zeolitic Tuff Versus Experiment Duration for Sorption (Forward) and Desorption (Backward) Experiments

DTN: LA0010JC831341.007 [153319], LA0305AM831341.001 [163789], LA0309AM831341.004 [165525]

NOTE: Oversaturated experiments have been omitted.

The impact of variations in pH on neptunium coefficients for sorption on devitrified tuffs is shown in Figure I-21. There is a lot of scatter in the "new" data, and there do not appear to be clear positive or negative trends among these data points. Nor does there appear to be much difference between the results for J-13 water and synthetic p#1 water. The "old" data points are more consistent and show very little dependence of the neptunium sorption coefficient on pH except at pH values less than 7.0.
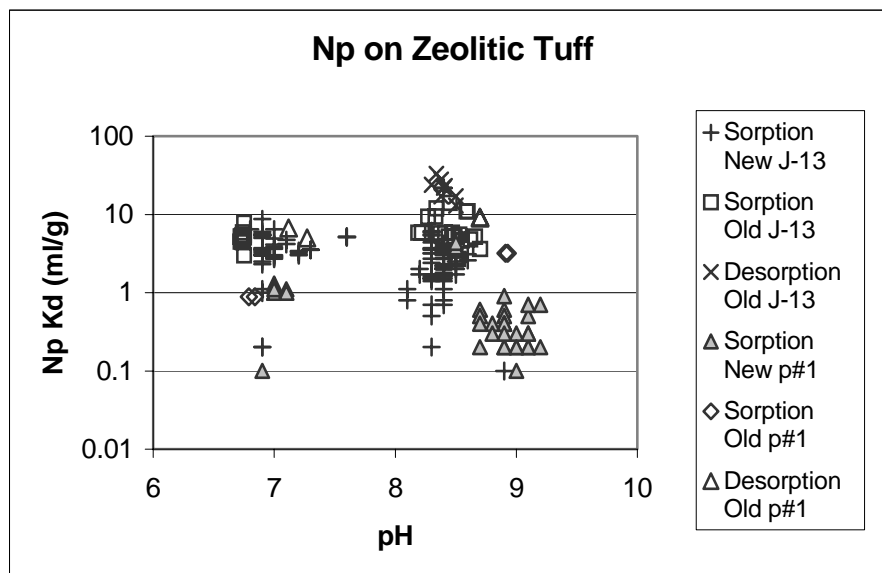
DTN: LA0010JC831341.007 [153319], LA0305AM831341.001 [163789], LA0309AM831341.004 [165525]

NOTE: Oversaturated experiments have been omitted.

Figure I-21. Neptunium Sorption Coefficients on Devitrified Tuff in J-13 Water and Synthetic p#1 Water Versus Solution pH in Sorption (Forward) and Desorption (Backward) Experiments

The neptunium sorption-coefficient probability distribution selected for zeolitic tuff in the saturated zone is a normal distribution with a range of 0 to 6 mL/g, a mean of 2.88 mL/g, and a standard deviation of 1.47 mL/g. The low end of the chosen range is selected based on the minimum value obtained in short-term experiments (up to 21 days). The upper end of the distribution was chosen as a minimum upper limit with a neptunium concentration near the solubility limit (Figure I-19) with emphasis on results from experiments at pH values near 7.0. It is acknowledged that a higher limit could be selected for the upper end of the distribution based on the available data.

I.8.3.3 Alluvium

Sorption coefficients have been measured in batch experiments from core obtained from three wells drilled into the alluvium (DTN: LA0302MD831341.003 [163784]): borehole NC-EWDP-10SA to the north, NC-EWDP-22SA in the middle, and NC-EWDP-19IM1A to the south, spaced between 4 to 5 km apart. Samples were taken below the water table from a 5-ft interval at two depths in wells NC-EWDP-19IM1A and NC-EWDP-10SA and at six depths in well NC-EWDP-22SA. For each core sample, batch experiments were run on three particle sizes: 500 to 2000 μm, 75 to 500 μm, and < 75 μm. The K_d values observed on the third particle size fraction were noticeably larger than the other two size fractions, probably because of mineral sorting effects. The K_d values for this size fraction were not considered further. Several replicates of each batch experiment were run so that a sample standard deviation could be obtained for each size fraction. Twelve of the 20 samples had a sample coefficient of variation < 0.1; six had a coefficient of variation < 0.22; and two had a coefficient of variation < 0.7.

The cell size in the three-dimensional FEHM model is 500 m x 500 m x ~10 m near the water table in the alluvium. Hence, the K_d parameter in the model represents a mean value, and the uncertainty distribution needs to represent the uncertainty about the mean on this large scale, not the local variance of the small-scale experiments. To avoid overly weighting the 12 samples from well 22SA, the mean K_d value was evaluated for each well (i.e., the K_d values obtained from any one well were similar and, thus, suggested some correlation). The coefficients of variation for these means were of the same order of magnitude as those for the samples (i.e., < 0.16), and so the small errors in any one experiment could be neglected. The three mean K_d values were taken to represent the best estimate of the K_d for any one cell in the FEHM model. According to the Law of Large Numbers, the means should be normally distributed; however, since the number of samples is small (i.e., 3), the Student-t distribution was used to correctly account for the error in estimating the standard deviation. The K_d value for Np were taken to be described by a t distribution with the following statistics: $\mu_{Np} = 6.3$ mL/g, $\sigma_{Np} = 0.81$ mL/g.

Although the t distribution was thought to correctly capture the spatial uncertainty, the question about the representativeness of the experiment does introduce a small amount of additional uncertainty. For example, other sources of uncertainty that may not have been completely represented in the experiments included potential competitive effects among radionuclides, different adsorption behavior between different oxidation states of the radionuclides, impact of climatic change, variability in water composition and rock types, and complexation by organic ligands. The probability that these uncertainties were not properly represented by the experiment was thought to be less than 10%. Nonetheless, to accommodate for this possibility, the tails of the distribution were extended from the approximate bounds of the t distribution ($\pm 3\sigma$) to the maximum and minimum experimental values observed. A 10% probability was assigned to these tails. This adjustment was implemented by using a piecewise-uniform cumulative distribution. For neptunium, the minimum experimentally observed value was 1.8 mL/g. Five percent probability was uniformly distributed between 1.8 mL/g and the lower bound of the t distribution at 4.0 mL/g. Since the t distribution had such little variation, it was reasonably represented by a uniform distribution; hence, 90% probability was uniformly distributed between 4.0 mL/g and the upper bound of the t distribution at 8.7 mL/g. The remaining 5% probability was uniformly distributed between 8.7 mL/g and the maximum experimentally observed value of 13 mL/g.
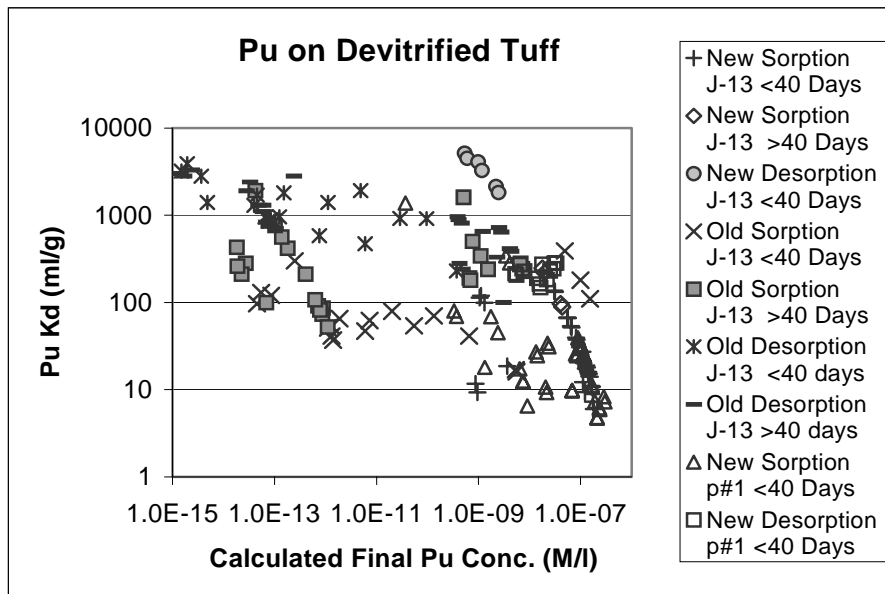
I.8.4 Plutonium

According to Nitsche et al. (1993 [155218], p. 54), the solubility of plutonium in J-13 water at 25°C and a pH of 8.4 is 2.9 ($\pm$ 0.8) x 10^{-7} M/L and is not very sensitive to pH over the range from 7.0 to 8.4. The solubility of plutonium in p#1 water at 25°C and a pH of 8.5 is 1.0 ($\pm$ 0.1) x 10^{-6} M/L and 4.5 ($\pm$ 0.4) x 10^{-7} M/L at 25°C and a pH of 7.0 according to Nitsche et al. (1995 [100163], p. 39). Thus, the solubility of plutonium in J-13 is somewhat lower than it is in p#1 water.

I.8.4.1 Devitrified Tuff

The experimentally derived sorption coefficients for plutonium on devitrified tuff are plotted against the calculated final plutonium concentrations of the experiments in Figure I-22. The data points are separated into groups on the basis of when the experiments were carried out (pre-1990 = "old" and post-1990 = "new"), water chemistry, experiment duration, and on whether the sorption coefficient was determined from a sorption or a desorption experiment. The plotted data indicate that the "new" and "old" data show similar ranges of K_d values, that the longer-term experiments generally yield higher sorption-coefficient values than the shorter-term experiments, and that desorption experiments yield higher sorption-coefficient values than sorption experiments. These points are discussed in greater detail in the following paragraphs.

The maximum calculated final plutonium concentration plotted in Figure I-22 is slightly less than the solubility determined by Nitsche et al. (1993 [155218], p. 54) for plutonium in J-13 water. Thus, the plutonium sorption coefficients plotted in Figure I-22 reflect solutions that were undersaturated with the solid plutonium phase precipitated in the experiments reported by Nitsche et al. (1993 [155218], p. 54).

The effect of the solution plutonium concentration on the sorption-coefficient value obtained is shown more clearly in Figure I-23. Data are plotted for two devitrified tuff samples that contain only trace amounts of secondary phases (e.g., clays, zeolites). In addition, plotted data are restricted to 21-day experiment durations and a pH value near 8.4. As is evident in the figure, within the errors of the analyses, the measured plutonium sorption coefficients are nearly independent of the final plutonium solution concentration.

DTN: LA0010JC831341.006 [153318], LA0305AM831341.001 [163789], LA0309AM831341.005 [165526]

Figure I-22. Plutonium Sorption Coefficients on Devitrified Tuff
Versus Calculated Final Plutonium Concentration in Solution
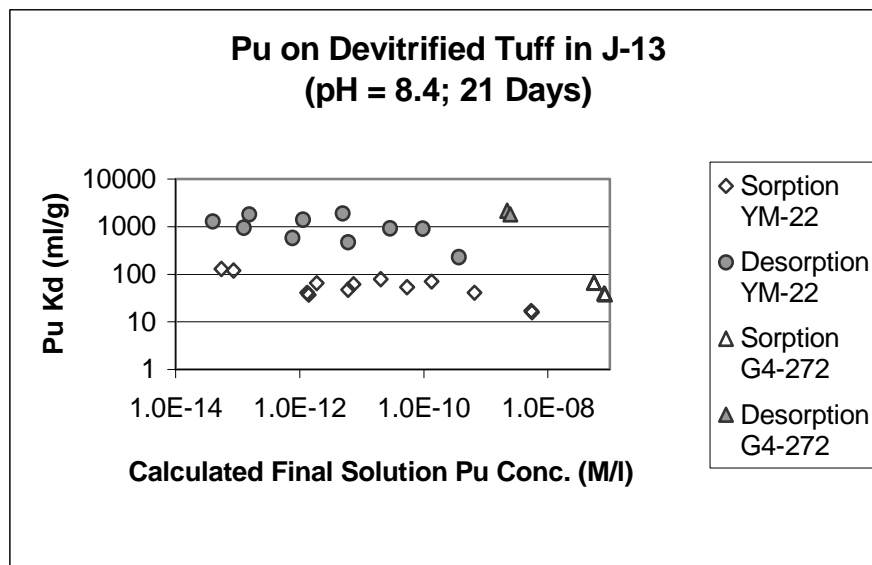
DTN: LA0010JC831341.006 [153318], LA0305AM831341.001 [163789]

Figure I-23. Plutonium Sorption Coefficients Versus Calculated Final Plutonium
Solution Concentration (M/L) for Experiments with Samples YM-22 and G4-272

The effect of experiment duration on the plutonium K_d value is shown in Figure I-24. As expected, the K_d values for sorption experiments increase with increasing duration, and the K_d values for desorption experiments decrease with increasing duration. However, the increase in the sorption values is much greater than the decrease in desorption values over the time frame of the experiments. This result may reflect the reduction of plutonium in the +5 and/or +6 oxidation states to plutonium in the +4 oxidation state on the mineral surfaces present in devitrified tuff, as discussed in greater detail below. The trends in the sorption and desorption data points suggest they would converge to values somewhere between 100 and 1,000 mL/g. Based on the data plotted, such convergence would require more than 100 days. Note that the "old" sorption data points exceeding 1,000 mL/g are for samples that contain significant amounts of clay or zeolite. For this reason, these data are discounted in the derivation of the sorption-coefficient probability distribution.
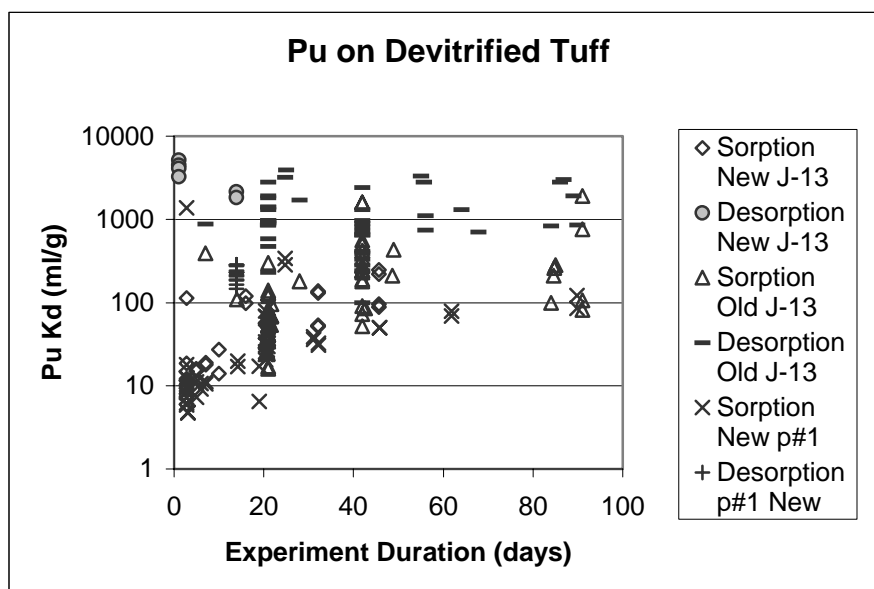
DTN: LA0010JC831341.006 [153318], LA0305AM831341.001 [163789], LA0309AM831341.005 [165526]

Figure I-24. Plutonium Sorption Coefficients on Devitrified Tuff Versus Experiment Duration for Sorption (Forward) and Desorption (Backward) Experiments

The impact of variations in pH on plutonium sorption coefficients on devitrified tuffs is shown in Figure I-25. There is a lot of scatter in the data, and there do not appear to be clear positive or negative trends in any of the data groupings.

The lack of clear trends is also evident when the results of short-term experiments (< 40 days) are removed from the data set. This outcome is shown in Figure I-26 in which only the longer-term data are plotted.

The impact of variations in the major ion composition of groundwaters is also shown in Figures I-25 through I-26. Although there is a limited set of experiments with synthetic p#1 water, the results are within the range of the results obtained in experiments with J-13 water. Thus, there is no clear evidence of an impact of water chemistry variations on plutonium sorption coefficients in devitrified tuff.

DTN: LA0010JC831341.006 [153318], LA0305AM831341.001 [163789], LA0309AM831341.005 [165526]

NOTE: Experiments lasting 40 days or more are plotted separately from experiments lasting less than 40 days.

Figure I-25. Plutonium Sorption Coefficients on Devitrified Tuff in J-13 Water and Synthetic p#1 Water Versus Solution pH in Sorption (Forward) and Desorption (Backward) Experiments
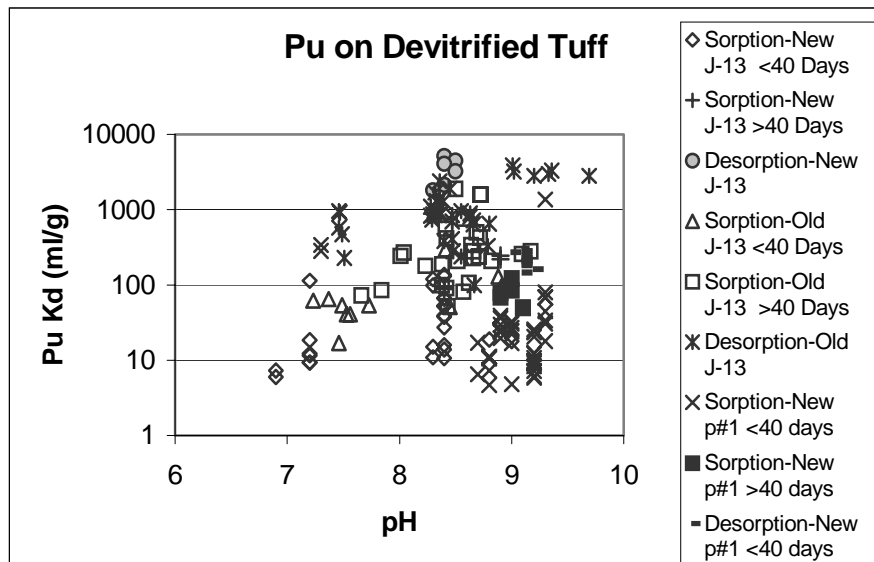
Pu on Devitrified Tuff
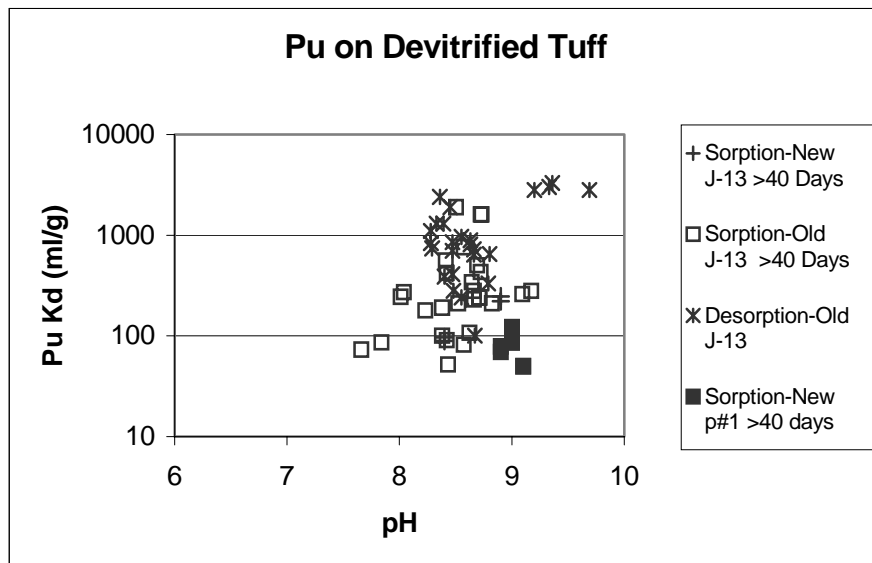
DTN: LA0010JC831341.006 [153318], LA0305AM831341.001 [163789], LA0309AM831341.005 [165526]

Figure I-26. Plutonium Sorption Coefficients on Devitrified Tuff in J-13 Water and Synthetic p#1 Water Versus Solution pH in Sorption (Forward) and Desorption (Backward) Experiments with Durations Greater than 40 Days

A major factor not explicitly accounted for in the experimental program is the impact of variations in the Eh of Yucca Mountain groundwaters on plutonium sorption coefficients. The laboratory experiments upon which the data discussed in this section are based were invariably conducted under oxidizing conditions because the waters used in the experiments contained dissolved oxygen and were in contact with the atmosphere. Nitsche et al. (1993 [155218], pp. 60–61) found that plutonium dissolved in J-13 water is present predominantly in the +5 and +6 oxidation states. If plutonium in the +5 and +6 oxidation states behaves similarly to neptunium +5 and uranium +6, respectively, as has been suggested by many investigators (e.g., Keeney-Kennicutt and Morse 1985 [106313], pp. 2577–2578), then small values (< 10 mL/g) would be expected for plutonium sorption coefficients under oxidizing conditions (see the sections on neptunium and uranium). The fact that plutonium sorption coefficients measured under oxidizing conditions are up to 2 to 3 orders of magnitude larger than expected (Figure I-26) suggests that either plutonium +5 and +6 do not behave like neptunium +5 and uranium +6 in sorption reactions or plutonium is reduced to the +4 oxidation state on rock/mineral surfaces. Data presented by Keeney-Kennicutt and Morse (1985 [106313], p. 2577) support the latter alternative.

To further pursue the latter alternative, a PHREEQC (V2.3, STN: 10068-2.3-00; BSC 2001 [155323]) model with the thermodynamic input data files LLNL.DAT (DTN: MO0309THDPHRLL.000 [165530]) and PHREEQC.DAT (DTN: MO0309THDPHRQC.000 [165529]) was developed to calculate plutonium sorption coefficients as a function of Eh. To develop this model, binding constants for neptunium +5 and uranium +6 species were used for

plutonium +5 and plutonium +6 species, respectively. For plutonium +4, binding constants were derived by fitting experimental data for plutonium sorption on quartz in artificial groundwater published by Allard (1982 [104512], p. 61). This water composition has somewhat reducing characteristics so that plutonium +4 would be expected to be sorbed onto the solid phase. The sorption coefficients calculated with this model using J-13 water are plotted as a function of Eh in Figure I-27. The curves plotted in that figure suggest that at Eh values less than 500 mV, plutonium is dominantly in the +4 oxidation state in the solution and on the solid phase. This Eh value is higher than the highest value measured in Yucca Mountain groundwater (DTN: LA0206AM831234.001 [160051] and LA0206AM831234.002 [163852]). This result implies that plutonium +4 will be the dominant oxidation state sorbed in most Yucca Mountain groundwaters. At higher Eh values, plutonium in solution will become progressively oxidized to plutonium +5 and eventually to plutonium +6. The end points of the curves (high Eh) plotted in Figure I-27 represent the Eh values expected when the water is in contact with the atmosphere. In the p#1 water composition, the lower ends of the curves are shifted downward somewhat to lower K_d values at a given Eh value (not shown).
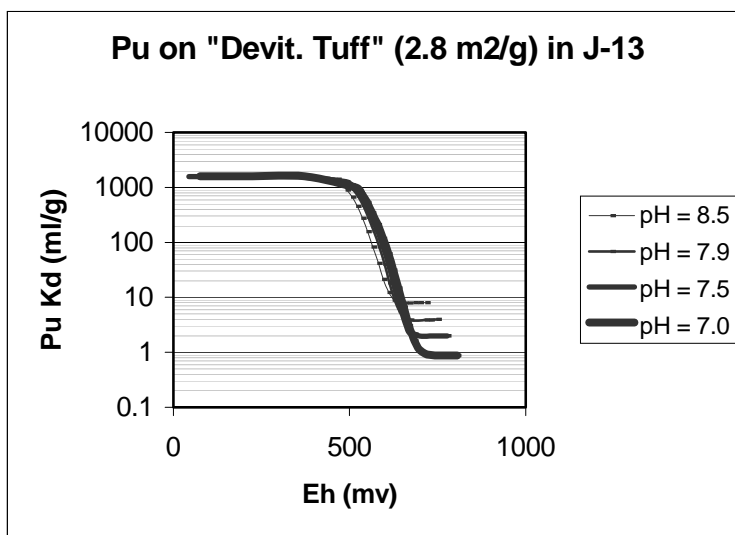
Output DTN: LA0306AM831343.001 files output/pudtfo70, pudt.fo75 pudtfo80 and pudtfo85

NOTES: PHREEQC V. 2.3 (BSC 2001 [155323]) was used. Separate curves are shown for different pH values.

Figure I-27. Plutonium Sorption Coefficients Versus Eh as Predicted by PHREEQC Model

The large range in plutonium sorption coefficients measured in devitrified tuffs (e.g., Figure I-26) could be explained if plutonium is present in more than one oxidation state on the rock/mineral surfaces in the devitrified tuffs. However, in the absence of definitive data on the oxidation state of plutonium on rock/mineral surfaces, the experimentally determined sorption-coefficient values will be used to derive the probability distributions.

The plutonium sorption-coefficient probability distribution selected for devitrified tuff in the saturated zone is a beta distribution with a range of 50 to 300 mL/g, mean of 100 mL/g, and a standard deviation of 15 mL/g. The low end of the chosen range is selected based on the minimum value observed in long-term experiments (> 40 days), but it also captures the potential impacts of variations in surface areas among samples used in the experiments, variations in water chemistry, and variations in plutonium concentrations up to the solubility limit. The upper end of the distribution was chosen as a minimum upper limit given the potential impacts of sorption kinetics in the long term. The fact that sorption coefficients derived from desorption experiments were, on average, greater in value than those obtained from sorption experiments (Figure I-26) indicates that equilibrium had not been reached. In longer time frames, the coefficients derived from desorption experiments may continue to decrease whereas the coefficients from sorption experiments continue to increase. The upper limit was selected in acknowledgement of this possibility. In addition, the impacts of variations in sample surface areas, waters chemistry, and plutonium solution concentrations were considered in choosing the upper limit value.

I.8.4.2 Zeolitic Tuff

The experimentally derived sorption coefficients for plutonium on zeolitic tuff are plotted against the calculated final plutonium concentrations in Figure I-28. As before, the data points are separated into groups on the basis of when the experiments were carried out (pre-1990 = "old" and post-1990 = "new"), water chemistry, experiment duration, and on whether the sorption coefficient was determined from a sorption or a desorption experiment. The plotted data indicate that there is no clear trend of plutonium K_d values with solution concentration. Most of the data from sorption experiments plot between sorption-coefficient values of 100 and 1,000 mL/g. A series of "old" experiments at concentrations between 10^{-7} and 10^{-9} M/L yielded sorption-coefficient values less than 100 mL/g. However, the same rock type, when used in "new" experiments, yielded a series of sorption-coefficient values > 100 mL/g. Why there is a difference of almost a factor of ten between these two sets of data is not known with certainty. Part of the answer lies in the fact that, on average, the "old" data points represent shorter duration experiments than the "new" data points. However, other factors are likely involved. For example, the oxidation state of plutonium in the starting solution may play a part.

As with devitrified tuffs, the plutonium sorption coefficients for zeolitic tuff plotted in Figure I-28 reflect solutions that were undersaturated, with the plutonium phase precipitated in the experiments conducted by Nitsche et al. (1993 [155218], p. 54; 1995 [100163], p. 39).
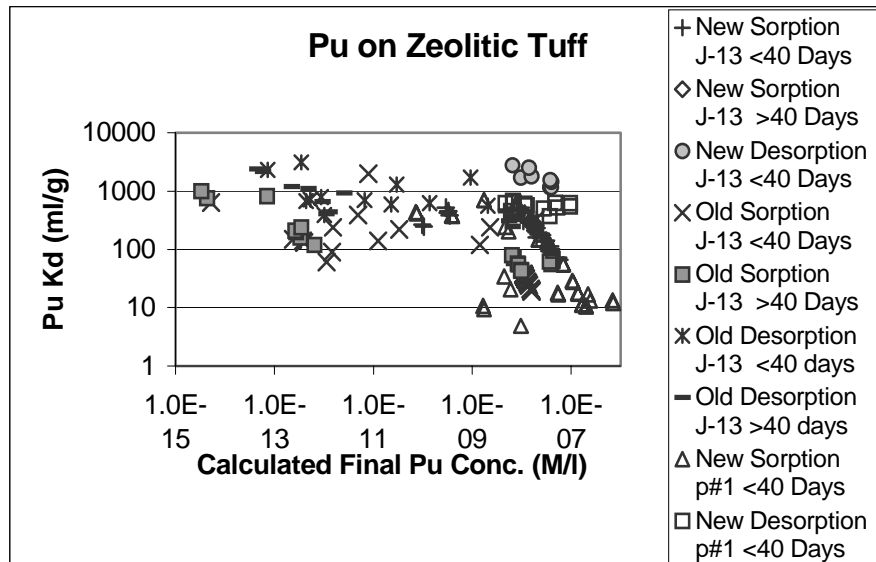
Pu on Zeolitic Tuff

Legend:
- + New Sorption J-13 <40 Days
- ◇ New Sorption J-13 >40 Days
- ⊙ New Desorption J-13 <40 Days
- ✕ Old Sorption J-13 <40 Days
- ▣ Old Sorption J-13 >40 Days
- ✳ Old Desorption J-13 <40 days
- ▬ Old Desorption J-13 >40 days
- △ New Sorption p#1 <40 Days
- ▢ New Desorption p#1 <40 Days

Y-axis: Pu Kd (ml/g), values 1, 10, 100, 1000, 10000
X-axis: Calculated Final Pu Conc. (M/l), values 1.0E-15, 1.0E-13, 1.0E-11, 1.0E-09, 1.0E-07

DTN: LA0010JC831341.006 [153318], LA0305AM831341.001 [163789, LA0309AM831341.005 [165526]

Figure I-28. Plutonium Sorption Coefficients on Zeolitic Tuff
Versus Calculated Final Plutonium Concentration in Solution

The effects of experiment duration on the plutonium K_d values for zeolitic tuff are shown in Figure I-29. As expected, the K_d values for sorption experiments increase with increasing duration and the values for desorption experiments decrease with increasing duration, at least in short-term experiments. Interestingly, the decrease in longer-term desorption experiments is not very pronounced. The trends in the sorption and desorption data points suggest they would converge to values somewhere between 100 and 1,000 mL/g. This result is similar to the range of values predicted for devitrified tuffs. Thus, the higher surface areas of zeolitic tuffs compared to devitrified tuffs (approximately 10 times) do not appear to result in higher sorption values. This effect was also observed by Pabalan et al. (1998 [162987], p. 113) in experiments with uranium sorption on zeolite. The cause for the large range of values obtained at a given value for experiment duration is not known but may be due largely to variations in the oxidation state of plutonium in the starting solutions. However, variations in surface areas and surface chemistry among the samples used in the experiments must also contribute to the range observed.

The impact of variations in pH on plutonium sorption coefficients on devitrified tuffs is shown in Figure I-30. Although there is a lot of scatter in the data, there do not appear to be clear positive or negative trends among any of the data groupings.

Figure I-29. Plutonium Sorption Coefficients on Zeolitic Tuff Versus Experiment
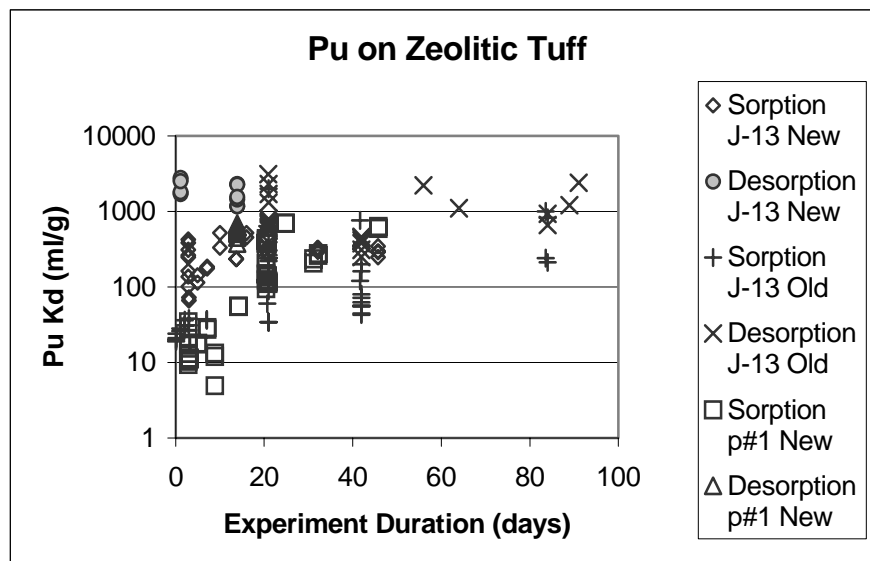Duration for Sorption (Forward) and Desorption (Backward) Experiments
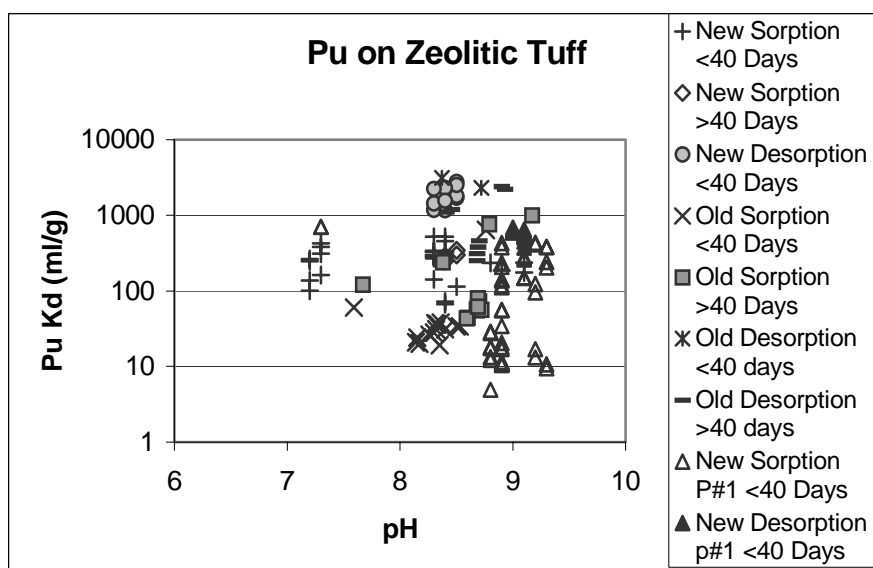
DTN: LA0010JC831341.006 [153318], LA0305AM831341.001 [163789], LA0309AM831341.005 [165526]

Figure I-30. Plutonium Sorption Coefficients on Zeolitic Tuff in J-13 Water
and Synthetic p#1 Water Versus Solution pH in Sorption (Forward) and
Desorption (Backward) Experiments with Durations Greater Than 40 Days

The impact of variations in the major ion composition of groundwaters is also shown in Figure I-30. Although there is a limited set of experiments with synthetic p#1 water, the results are largely within the range of the results obtained in experiments with J-13 water. Thus, there is no clear evidence of an impact of water chemistry variations on plutonium sorption coefficients in devitrified tuff.

The plutonium sorption-coefficient probability distribution derived for zeolitic tuff in the saturated zone is the same as the distribution derived for devitrified tuff because the experimentally derived sorption-coefficient values show similar ranges as a function of variations in surface areas among samples used in the experiments, variations in water chemistry, and variations in plutonium concentrations up to the solubility limit.

I.8.4.3 Alluvium

The probability distribution for devitrified tuff will be used as a default for the plutonium sorption-coefficient probability distribution in alluvium. Alluvium along the flow path is composed largely of disaggregated tuffaceous materials. Because it has been disaggregated, the surface area of alluvial material should be higher than that of devitrified tuff. In addition, clays and other secondary minerals are enriched in alluvial materials. These characteristics should result in higher sorption coefficients for plutonium in alluvial materials compared to intact devitrified tuff.

I.8.5 Protactinium

Protactinium is very insoluble in waters of the type found at Yucca Mountain. The best estimates of protactinium solubility in these waters range from 10^{-15} to 10^{-13} M/L (Berry et al. 1989 [144728], p. 346).

I.8.5.1 Devitrified Tuff

The oxidation state of protactinium is +5 in groundwaters of the type found at Yucca Mountain (Cotton and Wilkinson 1980 [101584], pp. 1092–1093). No sorption-coefficient data have been obtained for protactinium on devitrified tuffs from Yucca Mountain. Allard et al. (1983 [162982], p. 12) have reported protactinium sorption-coefficient data for experiments with a silica sample having a surface area similar to that measured for devitrified tuffs. The solution composition used in the experiments was 0.01 M/L NaClO$_4$. The initial protactinium concentration used in all experiments was 4.0×10^{-12} M/L. Allard's data indicate that protactinium sorption coefficients vary substantially (approximately 2 orders of magnitude) as a function of pH, as shown in Figure I-31. The cause for this variation in sorption coefficients with pH is unknown. Over the pH range expected in saturated-zone waters at Yucca Mountain (7-8.5), the sorption coefficients reported by Allard et al. (1983 [162982], p. 12) range from approximately 7,500 to 20,000 mL/g. The results for 6-hour experiments were similar to the results for experiments lasting up to 6 weeks. Thus, sorption kinetics for protactinium sorption reactions appear to be fast. Allard et al. (1983 [162982], p. 12) reported results for alumina that were very similar to the results they reported for silica.
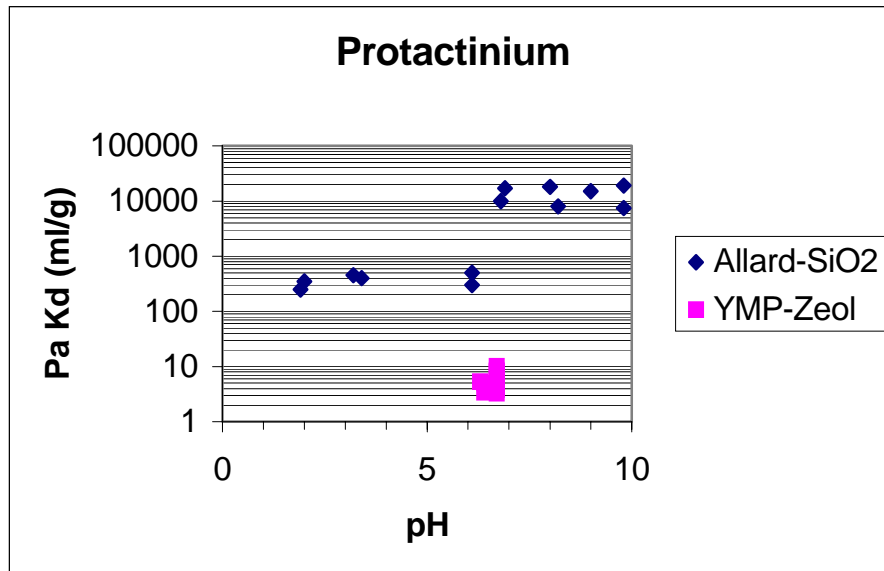
Protactinium

DTN: LA0305AM831341.001 [163789] and Allard et al. (1983 [162982] Figure 6])

Figure I-31. Protactinium Sorption Coefficients Versus pH

Hydrolysis reactions appear to dominate the solution chemistry of protactinium. The hydrolysis reactions of pentavalent protactinium in water are very complex even in relatively acidic solutions (Cotton and Wilkinson 1980 [101584], pp. 1091–1093). In near-neutral solutions, the hydrolysis behavior of protactinium is essentially unknown. However, because hydrolysis reactions appear to dominate the solution behavior of protactinium, changes in the major ion chemistry of groundwaters are not expected to impact the sorption behavior of protactinium. Unfortunately, insufficient thermodynamic data are available to model protactinium sorption behavior using a surface complexation model.

The sorption-coefficient range for americium was used as a default for protactinium (i.e., 1,000 to 10,000 mL/g). This range is well within the range reported by Allard et al. (1983 [162982], p. 12) for silica and alumina at values of pH > 7.0. As with americium sorption coefficients, a truncated normal distribution was selected with a mean of 5500 mL/g and a standard deviation of 1500 mL/g.

Corroboration of this range of sorption-coefficient values is provided by protactinium sorption experiments performed by Berry et al. (1989 [144728], p. 347). These authors report a range of 1,000 to 1,000,000 mL/g for protactinium sorption coefficients for rock samples, including sandstone, shale, granite, and clay in contact with natural groundwaters.

I.8.5.2   Zeolitic Tuff

Sorption coefficients for protactinium on zeolitic tuffs from Yucca Mountain in J-13 water were reported by Rundberg et al. (1985 [101355], p. 63). The reported sorption coefficients ranged from 3.3 to 10.1 mL/g (Figure I-31). The initial solution concentrations in the experiments ranged from 1 x 10^{-11} to 5 x 10^{-14}. The initial solution concentration used by Allard et al. (1983 [162982], p. 6) was in the low end of this range. Thus, initial solution concentration does not appear to explain the difference between the results of Allard et al. (1983 [162982], p. 12) and the results on Yucca Mountain samples. It is possible that the results on Yucca Mountain samples reflect oversaturation due to coprecipitation of protactinium with some other easily hydrolyzed species. This explanation requires that the precipitates were colloidal in size and, therefore, not efficiently removed from the final solutions.

The pH values of the final solutions in the experiments on Yucca Mountain samples were in the range of 6.3 to 6.7. These pH values are below the range expected in saturated-zone waters at Yucca Mountain. Thus, the reported sorption coefficients do not directly apply to conditions in the saturated zone at Yucca Mountain. As shown in Figure I-31, there appears to be an adsorption edge at a pH close to 6.8, and sorption coefficients increase by approximately 2 orders of magnitude at values of pH > 6.8. The cause for this increase is not known but is likely related to hydrolysis reactions.

Because zeolitic tuffs have greater surface area than devitrified tuffs, the sorption-coefficient distribution for devitrified tuff is used as a default for zeolitic tuff. This approach will lead to conservative predictions of protactinium transport rates.

I.8.5.3   Alluvium

The probability distribution for devitrified tuff will be used as a default for the protactinium sorption-coefficient probability distribution in alluvium. Alluvium along the flow path is composed largely of disaggregated tuffaceous materials. Because devitrified tuff makes up a major portion of the volcanic units exposed at the surface, it should be a major component in alluvium. In addition, clays and other secondary minerals are enriched in alluvial materials. The presence of these minerals should result in higher sorption coefficients in alluvial materials compared to intact devitrified tuff.

I.8.6   Radium

The chemistry of the element radium is very similar to that of the element barium (Cotton and Wilkinson 1980 [101584], p. 426). Because barium has a radioactive isotope that is more readily measured by gamma counting than the radium isotopes, barium was used to measure sorption coefficients for radium. A limited number of experiments were performed with radium to confirm its sorption behavior relative to barium.

Barite is the solubility-controlling solid for barium in Yucca Mountain groundwaters. The solubility of barite (barium sulfate) obtained from PHREEQC modeling (PHREEQC V2.3; BSC 2001 [155323]) with the thermodynamic input data files LLNL.DAT (DTN: MO0309THDPHRLL.000 [165530]) and PHREEQC.DAT (DTN:MO0309THDPHRQC.000 [165529]) in J-13 water at 25°C is 9.0 x 10^{-7} M/L (DTN: LA0306AM831343.001, File output/Usat.pun). The solubility of barite in p#1 water at 25°C is 2.0 x 10^{-7} M/L. At 25°C, the solubility of radium sulfate is 3.2 x 10^{-7} M/L in J-13 water (DTN: LA0306AM831343.001, File output/Usat.pun).

I.8.6.1 Devitrified Tuff

The experimentally derived sorption coefficients for barium on devitrified tuff are plotted against the calculated final barium concentrations of the experiments in Figure I-32. The data points are separated into groups on the basis of when the experiments were carried out (pre-1990 = "old" and post-1990 = "new"), water chemistry, experiment duration, and on whether the sorption coefficient was determined from a sorption or a desorption experiment.
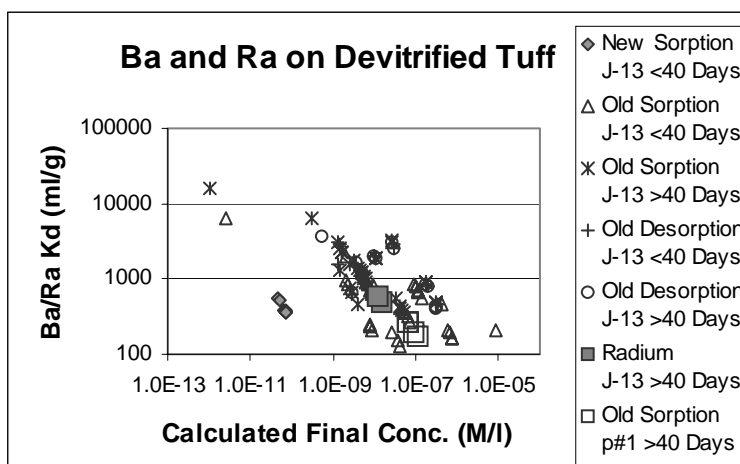
DTN: LA0305AM831341.001 [163789], LA0010JC831341.001 [162476], LA0309AM831341.002 [165523]

Figure I-32. Barium and Radium Sorption Coefficients on Devitrified Tuff Versus Calculated Final Barium or Radium Concentrations in Solution

The calculated final concentration of barium in the experiments with J-13 water was below saturation with barite in all but one experiment (Figure I-32). The results for this one experiment will be omitted from further consideration. The calculated final barium concentrations in experiments with p#1 water are all lower than the barite saturation value of 2.0 x 10^{-7} M/L. Thus, oversaturation was not an issue in the barium sorption experiments with p#1 water. Similarly, the radium solution concentrations were all lower than the radium sulfate saturation value in J-13 water. Thus, these experiments were undersaturated with radium sulfate.

The data plotted in Figure I-32 show a general increase in sorption coefficient with decreasing concentration. This result suggests the isotherms for barium sorption onto devitrified tuff are

nonlinear. The impact of this nonlinearity must be included in the sorption-coefficient probability distribution.

The effects of experiment duration on the barium K_d value for devitrified tuff are shown in Figure I-33. The large range in sorption coefficients obtained at a given duration reflects variations in grain size of the crushed-tuff samples used in the experiments, variations in solution concentrations, variations in surface chemistry, and analytical errors and artifacts. Experiments with crushed-tuff samples that include the fines (e.g., < 30 μm) often have sorption coefficients that are larger than samples from which the fines have been removed (e.g., 75–500 μm). This result is partly due to the higher surface area of samples with fines and partly due to mineral fractionation. Mineral fractionation can occur during the sieving process and cause the preferential concentration of very fine-grained minerals (e.g., clays) in the fine fraction.
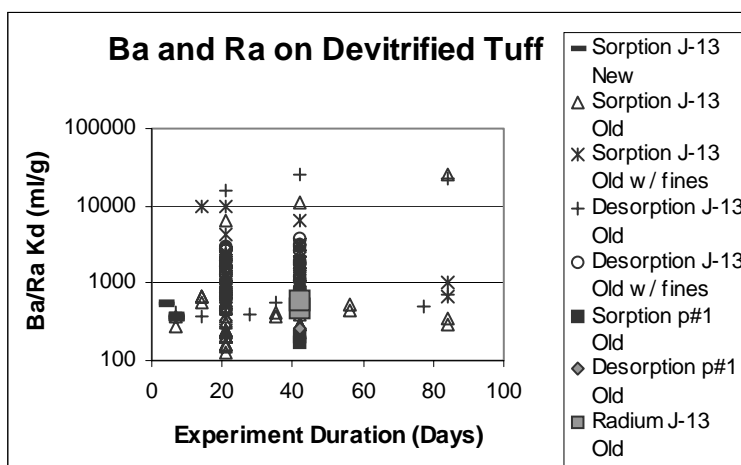
DTN: LA0305AM831341.001 [163789], LA0010JC831341.001 [162476], LA0309AM831341.002 [165523]

Figure I-33. Barium and Radium Sorption Coefficients on Devitrified Tuff Versus Experiment Duration for Sorption (Forward) and Desorption (Backward) Experiments

Figure I-34 shows the effects of experiment duration on sorption coefficients for samples with the fines removed. The few sorption coefficients with values near 10,000 mL/g represent experiments with very low solution concentrations (Figure I-34). For the remaining experiments, the total range of sorption-coefficient values is substantially reduced. Further, it appears likely the range would converge to a range between 100 and 1,000 mL/g with increasing duration. The horizontal trend among data points at durations other than 21 and 42 days suggests barium and radium sorption reactions are relatively fast.

Ba and Ra on Devitrified Tuff
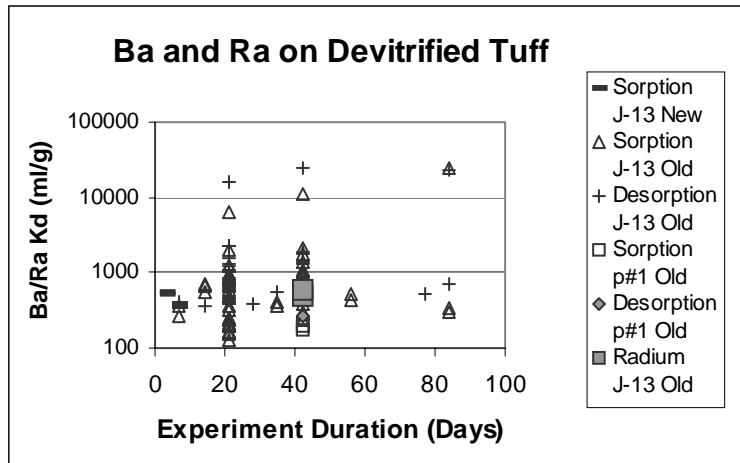
DTN: LA0305AM831341.001 [163789], LA0309AM831341.002 [165523]

Figure I-34. Barium and Radium Sorption Coefficients on Devitrified Tuff Versus Experiment
Duration for Sorption (Forward) and Desorption (Backward) Experiments

The impact of variations in the major ion composition of groundwaters is also shown in
Figures I-33 and I-34. Although there is a limited set of experiments with p#1 water, the
sorption coefficients obtained (at 42 days) fall at the low end of the range of results for J-13
water. Thus, there is some impact of water chemistry, although it is substantially less than an
order of magnitude.

The radium sorption-coefficient probability distribution derived for devitrified tuff in the
saturated zone is a uniform distribution with a range of 100 to 1,000 mL/g. The low end of the
chosen range was selected based on the minimum value observed in long-term experiments
(> 40 days) and potential impacts of variations in water chemistry and surface areas among
devitrified tuffs at Yucca Mountain. Because there are experiments within the data set that have
solution concentrations close to saturation with a barium/radium sulfate, the effect of nonlinear
isotherms is incorporated into the distribution. The upper end of the distribution was chosen as a
minimum upper limit given the potential impacts of sorption kinetics, radium solution
concentrations, and surface areas.

I.8.6.2 Zeolitic Tuff

The experimentally derived sorption coefficients for barium and radium on zeolitic tuff are
plotted against the calculated final barium or radium concentrations in Figure I-35. As before,
the data points are separated into groups on the basis of when the experiments were carried out
(pre-1990 = "old" and post-1990 = "new"), experiment duration, and on whether the sorption
coefficient was determined from a sorption or a desorption experiment. The plotted data indicate
that there is no clear trend of barium K_d values with solution concentration. Essentially all the
sorption coefficients exceed a value of 10,000 mL/g and some desorption experiments approach
values of 1,000,000 mL/g. The radium results are in the range of the results for barium,
confirming the similar sorption behavior of these two elements. As with devitrified tuffs, the
barium and radium sorption coefficients for zeolitic tuff plotted in Figure I-35 reflect solutions

that were undersaturated with barium and radium sulfate. The sorption coefficients obtained with p#1 water are well within the range defined by the experiments with J-13 water. Thus, there does not appear to be a clear impact of variations in groundwater chemistry.
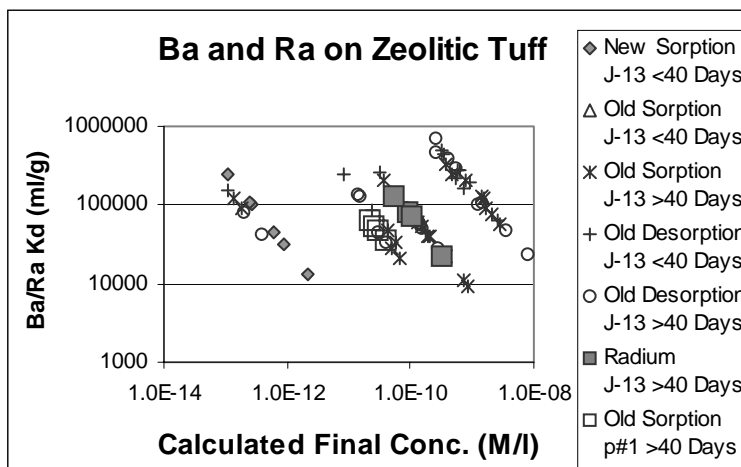
DTN: LA0305AM831341.001 [163789], LA0309AM831341.002 [165523]

Figure I-35. Barium and Radium Sorption Coefficients on Zeolitic Tuff Versus Calculated Final Barium or Radium Concentrations in Solution

The data plotted in Figure I-36 also indicate that there is no clear trend of barium K_d values with solution concentration. Data were obtained for a sorption isotherm on sample YM-38 (Figure I-36). As indicated by the exponent in the equation on the diagram, the calculated isotherm is essentially linear.

The effects of experiment duration on the barium K_d values for zeolitic tuff are shown in Figure I-37. The barium and radium sorption reactions are quite fast. This characteristic is indicated by the fact the range of values obtained in 6-day experiments (Figure I-37) is similar to the range of values obtained in 84-day experiments.
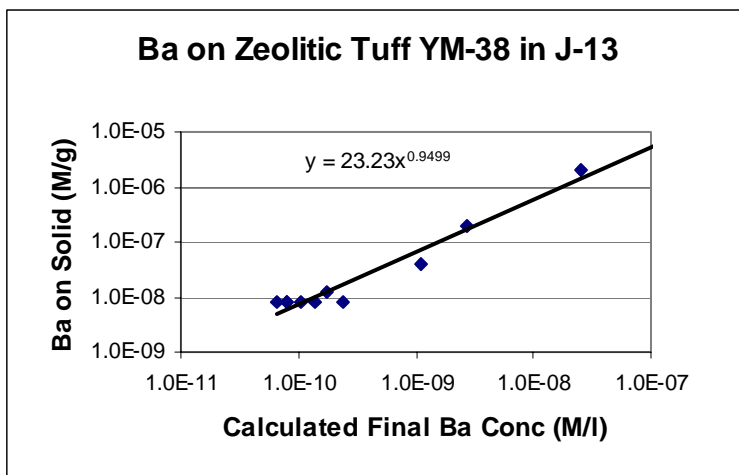
Figure I-36. Isotherm Diagram for Barium Sorption on Zeolitic Tuff Sample YM-38 in J-13 Water
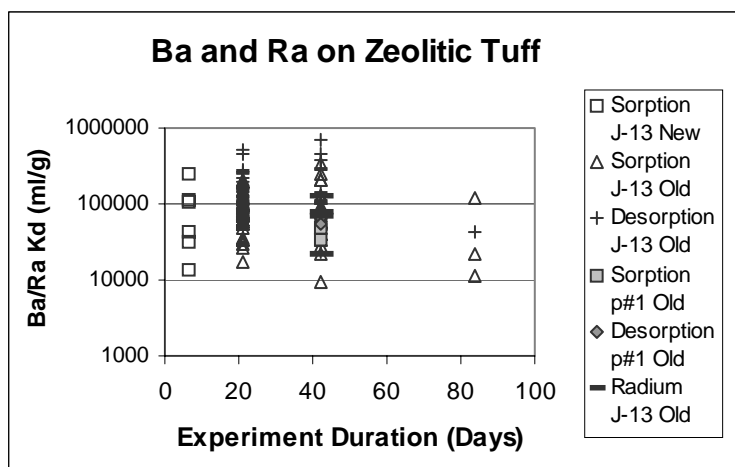
DTN: LA0305AM831341.001 [163789], LA0309AM831341.002 [165523]

Figure I-37. Barium and Radium Sorption Coefficients on Zeolitic Tuff in J-13 Water
Versus Experiment Duration for Sorption (Forward) and Desorption (Backward) Experiments

The impact of variations in the major ion composition of groundwaters is also shown in Figure I-37. Although there is a limited set of experiments with synthetic p#1 water, the results are largely within the range of the results obtained in experiments with J-13 water. Thus, there is no clear evidence of an impact of water chemistry variations on barium/radium sorption coefficients in zeolitic tuff.

The radium sorption-coefficient probability distribution derived for zeolitic tuff in the saturated zone is a truncated log-normal distribution with a range of 1,000 to 250,000 mL/g, a mean of 100,000 mL/g, and a standard deviation of 31,420 mL/g. The low end of the chosen range was selected based on the minimum value observed in long-term experiments (> 40 days) and potential impacts of variations in water chemistry and ion-exchange capacities among zeolitic tuffs at Yucca Mountain. The upper end of the distribution was chosen to address the potential for low radium solution concentrations and high ion-exchange capacities along the expected transport pathways.

Because zeolitic tuffs have greater surface area than devitrified tuffs, the sorption-coefficient distribution for devitrified tuff is used as a default for the radium sorption in the volcanic tuffs. This approach will lead to conservative predictions of radium transport rates.

I.8.6.3 Alluvium

The probability distribution for devitrified tuff will be used as a default for the radium sorption-coefficient probability distribution in alluvium. Alluvium along the flow path is composed largely of disaggregated tuffaceous materials. Because devitrified tuff makes up a major portion of the volcanic units exposed at the surface, it should be a major component in alluvium. In addition, clays and other secondary minerals are enriched in alluvial materials. The presence of these minerals should result in higher sorption coefficients in alluvial materials compared to intact devitrified tuff.

I.8.7 Strontium

The solubility of strontium obtained from PHREEQC modeling (PHREEQC V2.3; BSC 2001 [155323]) with the thermodynamic input data files LLNL.DAT (DTN: MO0309THDPHRLL.000 [165530]) and PHREEQC.DAT (DTN:MO0309THDPHRQC.000 [165529]) in J-13 water at 25°C ranges from 2.7×10^{-5} M/L at a pH of 7.1 to 1.4×10^{-6} M/L at a pH of 8.5 and the solubility controlling phase is strontianite (strontium carbonate). The solubility of strontianite in p#1 water at 25°C ranges from 2.4×10^{-5} M/L at a pH of 6.9 to 9.9×10^{-7} M/L at a pH of 8.6 (Output DTN: LA0306AM831343.001 file output/Usat.pun.).

I.8.7.1 Devitrified Tuff

The experimentally derived sorption coefficients for strontium on devitrified tuff are plotted against the calculated final strontium concentrations of the experiments in Figure I-38. The data points are separated into groups on the basis of when the experiments were carried out (pre-1990 = "old" and post-1990 = "new"), water type, and on whether the sorption coefficient was determined from a sorption or a desorption experiment. There are also data for a sorption isotherm on sample G1-2840.

Most of the calculated final solution concentrations for the sorption experiments are below saturation with strontianite in J-13. The data points with concentrations greater than 1.0×10^{-6} M/L reflect experiments that were oversaturated with strontianite. Thus, the sorption coefficients obtained in these experiments will not be used in the derivation of the strontium sorption-coefficient probability distribution. The calculated final strontium concentrations used in experiments with p#1 water are all lower than the saturation value. Thus, oversaturation was not an issue in the strontium sorption experiments with p#1 water.
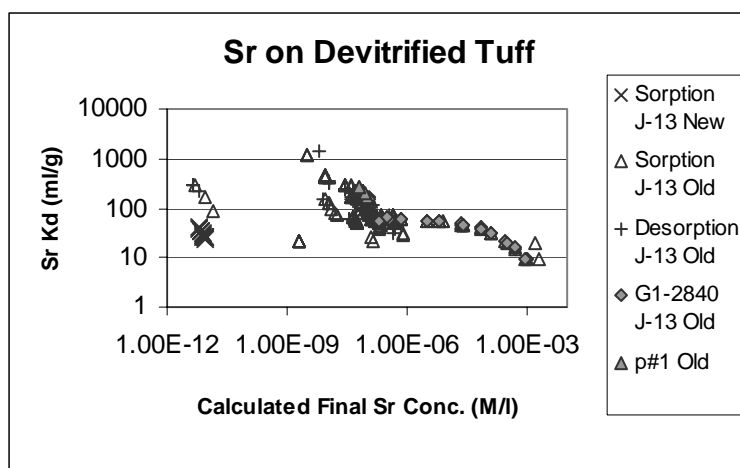
DTN: LA0305AM831341.001 [163789], LA0010JC831341.003 [153322], LA0309AM831341.006 [165527]

Figure I-38. Strontium Sorption Coefficients on Devitrified Tuff Versus Calculated Final Strontium Concentration in Solution

A sorption isotherm was obtained for sample G1-2840 in J-13 water. The isotherm is linear at concentrations below approximately 5×10^{-5} M/L as shown in Figure I-38. Further, the K_d value in the linear portion of the isotherm is at the low end of the range of strontium sorption coefficients obtained with J-13 and p#1 waters. Thus, the isotherms for the bulk of the samples would lie at higher K_d values compared to the isotherm for G1-2840. The sorption coefficients obtained in experiments with p#1 water fall in the middle of the range of values obtained for experiments with J-13 water. Thus, there is little or no impact of variations in water chemistry on strontium sorption coefficients on devitrified tuff.

The effects of experiment duration on values of the strontium K_d for devitrified tuff are shown in Figure I-39. The large range in sorption coefficients obtained at a given duration reflects variations in grain size of the crushed-tuff samples used in the experiments, variations in solution strontium concentrations, variations in surface chemistry, and analytical error and artifacts. Experiments with crushed-tuff samples that include the fines (e.g., particle size < 30 µm) usually

have sorption coefficients that are larger than samples from which the fines have been removed (e.g., particle sizes 75–500 µm). This result is partly due to the higher surface area of samples with fines and partly due to mineral fractionation. Mineral fractionation can occur during the sieving process and cause the preferential concentration of very fine-grained minerals (e.g., clays) in the fine fraction.
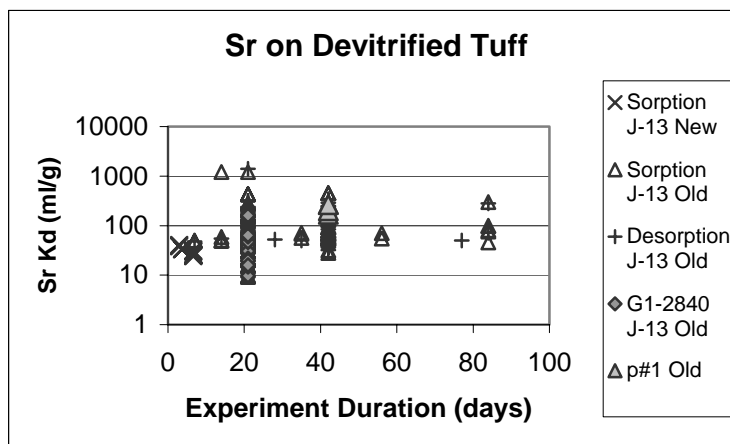
DTN: LA0305AM831341.001 [163789], LA0010JC831341.003 [153322], LA0309AM831341.006 [165527]

NOTE: Data points include experiments in which fines were not removed from the samples.

Figure I-39. Strontium Sorption Coefficients on Devitrified Tuff Versus Experiment Duration for Sorption (Forward) and Desorption (Backward) Experiments

Figure I-40 shows the effects of duration on sorption coefficients for crushed-tuff samples with the fines removed. The total range of sorption-coefficient values is reduced compared to Figure I-39. Further, it appears likely this range would converge to values between 50 and 500 mL/g with increasing duration. The horizontal trend among data points at durations other than 21 and 42 days suggests strontium sorption reactions are relatively fast.

The strontium sorption-coefficient probability distribution derived for devitrified tuff in the saturated zone is a uniform distribution with a range of 20 to 400 mL/g. The low end of the chosen range was selected based on the minimum value observed in long-term experiments (> 40 days) and potential impacts of variations in water chemistry and surface areas among devitrified tuffs at Yucca Mountain. Because there are experiments within the data set that have solution concentrations close to saturation with a strontium carbonate, the effect of nonlinear isotherms is incorporated into the distribution. The upper end of the distribution was chosen as a minimum upper limit given the potential impacts of strontium solution concentrations and surface areas.

NOTE: Samples containing fines fraction are removed from the figure.

Figure I-40. Strontium Sorption Coefficients on Devitrified Tuff Versus Experiment Duration for Sorption (Forward) and Desorption (Backward) Experiments with Reduced Range

I.8.7.2   Zeolitic Tuff

The experimentally derived sorption coefficients for strontium on zeolitic tuff are plotted against the calculated final strontium concentrations of the experiments in Figure I-41. The data points are separated into groups on the basis of when the experiments were carried out (pre-1990 = "old" and post-1990 = "new"), water type, whether or not the solid phase included fines, and whether the sorption coefficient was determined from a sorption or a desorption experiment.
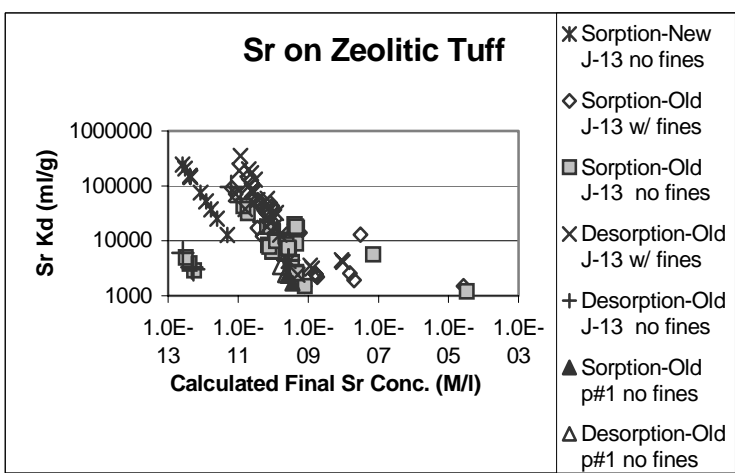
Figure I-41. Strontium Sorption Coefficients on Zeolitic Tuff Versus Calculated Final Strontium Concentration in Solution

All except two of the calculated final solution concentrations were below the saturation level with strontianite. The calculated final strontium concentrations used in experiments with p#1 water are all lower than the saturation value. Thus, oversaturation was not an issue in most of the strontium sorption experiments.

The few sorption coefficients obtained with p#1 water tend to lie at the low end of the range of values shown in Figure I-41. This result suggests variations in water composition will have an impact on the strontium sorption coefficient for zeolitic tuff.

Sorption experiments were carried out at a number of different starting concentrations to obtain an isotherm for sample YM-38. As shown in Figure I-42, the sorption coefficients obtained in these experiments are not consistent with a simple relationship between strontium concentration and sorption coefficient. Nonetheless, the sorption coefficients plotted in Figure I-42 were obtained over a range of strontium concentrations. Thus, the concentration dependence of the sorption coefficient is included in the data set.
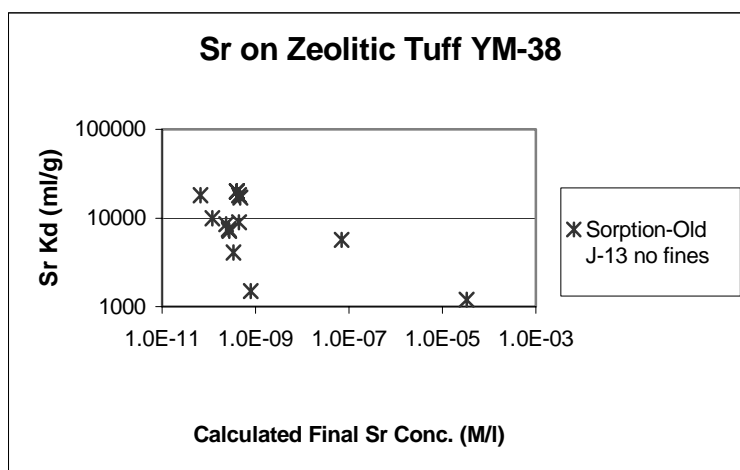
DTN: LA0305AM831341.001 [163789], LA0010JC831341.003 [153322], LA0309AM831341.006 [165527]

Figure I-42. Strontium Sorption Coefficients Versus Calculated Final Solution Concentration (M/L) for Sample YM-38 in J-13 Water

The effects of experiment duration on the values of strontium K_d for zeolitic tuff are shown in Figure I-43. The large range in sorption coefficients obtained at a given duration reflects variations in grain size of the crushed-tuff samples used in the experiments, variations in solution strontium concentrations, variations in surface chemistry, and analytical errors and artifacts. Experiments with crushed-tuff samples that include the fines (e.g., particle size < 30 µm) usually have sorption coefficients that are larger than samples from which the fines have been removed (e.g., particle sizes 75–500 µm). This result is partly due to the higher surface area of samples with fines and partly due to mineral fractionation. Mineral fractionation can occur during the sieving process and cause the preferential concentration of very fine-grained minerals (e.g., clays) in the fine fraction.
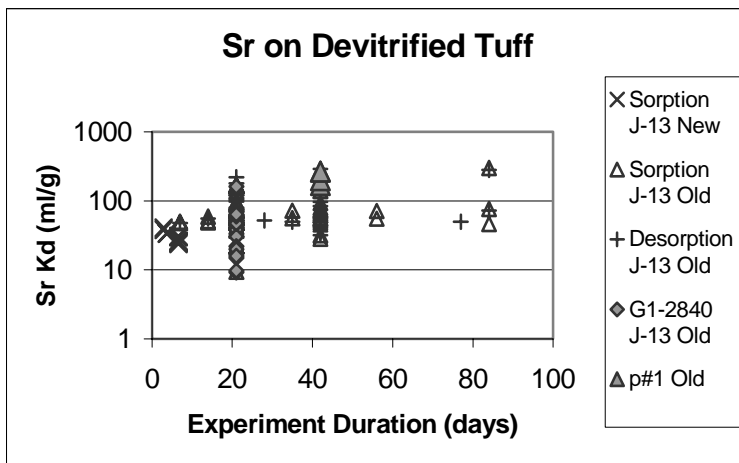
Figure I-43. Strontium Sorption Coefficients on Zeolitic Tuff Versus Experiment
Duration for Sorption (Forward) and Desorption (Backward) Experiments

Figure I-44 shows the effects of duration on sorption coefficients for crushed-tuff samples with the fines removed. The total range of sorption-coefficient values is reduced slightly compared to Figure I-43. The rather limited range of values at 84 days is likely due to the limited number of experiments carried out at this duration. There is no clear trend of sorption-coefficient value with duration. This result likely reflects fast sorption kinetics.
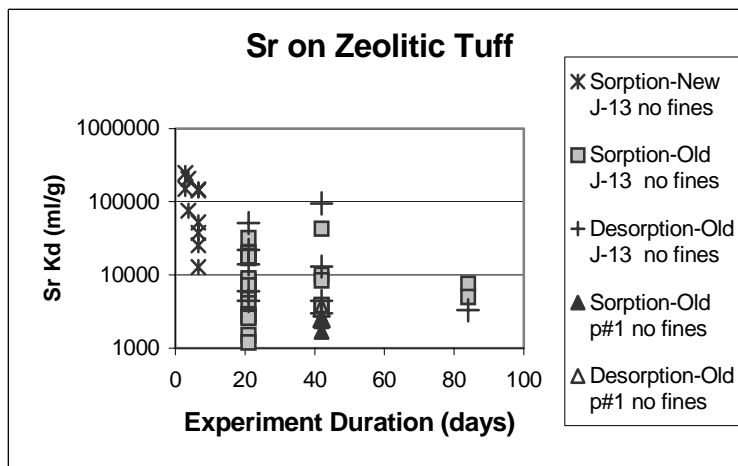
Figure I-44. Strontium Sorption Coefficients on Zeolitic Tuff With Fine Fraction Removed
Versus Experiment Duration for Sorption (Forward) and Desorption (Backward) Experiments

The strontium sorption-coefficient probability distribution derived for zeolitic tuff in the saturated zone is a cumulative distribution starting at 100 mL/g, with a value of 5,000 mL/g at 0.5 and a value of 90,000 mL/g at 1.0. The low end of the chosen range was selected based on the minimum value observed in long-term experiments (> 40 days) and potential impacts of variations in water chemistry and ion-exchange capacities among zeolitic tuffs at Yucca Mountain. Because there are experiments within the data set that have solution concentrations close to saturation with a strontium carbonate, the effect of nonlinear isotherms is included in the distribution. The upper end of the distribution was chosen as a minimum upper limit given the potential impacts of strontium solution concentrations and ion-exchange capacities.

I.8.7.3 Alluvium

The probability distribution for devitrified tuff will be used as a default for the strontium sorption-coefficient probability distribution in alluvium. Alluvium along the flow path is composed largely of disaggregated tuffaceous materials. Because devitrified tuff makes up a major portion of the volcanic units exposed at the surface, it should be a major component in alluvium. In addition, clays and other secondary minerals are enriched in alluvial materials. The presence of these minerals should result in higher sorption coefficients in alluvial materials compared to intact devitrified tuff.

I.8.8 Thorium

The solubility of thorium dioxide in waters such as the saturated-zone waters is estimated at 3.2×10^{-9} M/L at values of pH > 6.0 (Hummel et al. 2002 [161904], p. 377).

I.8.8.1 Devitrified Tuff

Experiments with Yucca Mountain tuffs were carried out with initial concentrations in the 1.0×10^{-7} to 6×10^{-8} M/L range. Thus, the experiments were initially oversaturated with thorium dioxide. The calculated final thorium concentrations shown in Figure I-45 indicate thorium sorption onto the rock sample brought the final solution concentrations below saturation with thorium dioxide in some cases but not all. The results of experiments oversaturated with thorium dioxide are of questionable value. For the remaining experiments, the sorption coefficients range from 1,213 to 23,800 mL/g. There are no data available for the effect of experimental duration on sorption-coefficient values for Yucca Mountain samples. However, Allard et al. (1983 [162982], p. 10) reported that, over experiment durations of 6 hours to 6 weeks, time had little influence on the measured sorption coefficients for thorium on silica in 0.01 M/L $NaClO_4$. Note that the starting concentrations reported by Allard et al. (1983 [162982], p. 6) were below the saturation level for thorium dioxide.

Th Sorption Coefficients in J-13
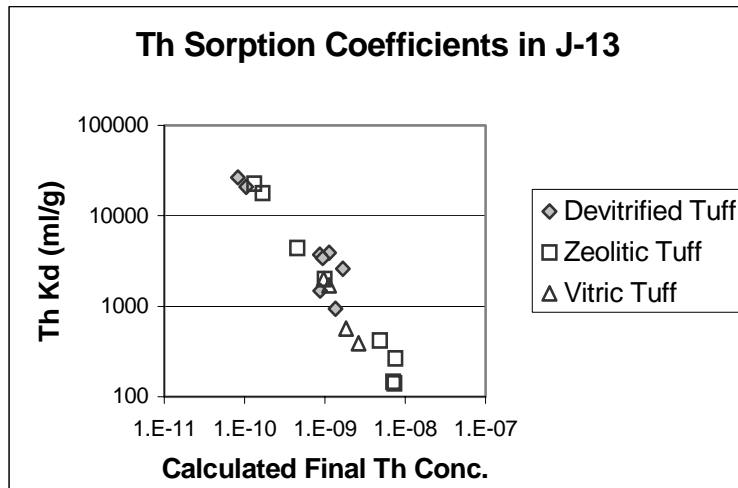
DTN: LA0305AM831341.001 [163789]

Figure I-45. Thorium Sorption Coefficients on Tuff Versus
Calculated Final Thorium Concentration in Solution

There are no data available to evaluate the impact of variations in water chemistry on thorium sorption coefficients. However, thorium forms primarily hydroxide complexes at near neutral pH in dilute solutions (Langmuir and Herman 1980 [147527], p. 1753). Therefore, water chemistry is expected to have very little influence on thorium sorption-coefficient values in Yucca Mountain groundwaters. However, water chemistry (i.e., pH) does impact the solubility of thorium dioxide. This effect is the reason some of the experiments in Figure I-45 were over-saturated with thorium dioxide. As shown in Figure I-46, the lowest sorption coefficients were obtained at near-neutral pH values where J-13 water was oversaturated with thorium dioxide.

Th Sorption Coefficients in J-13
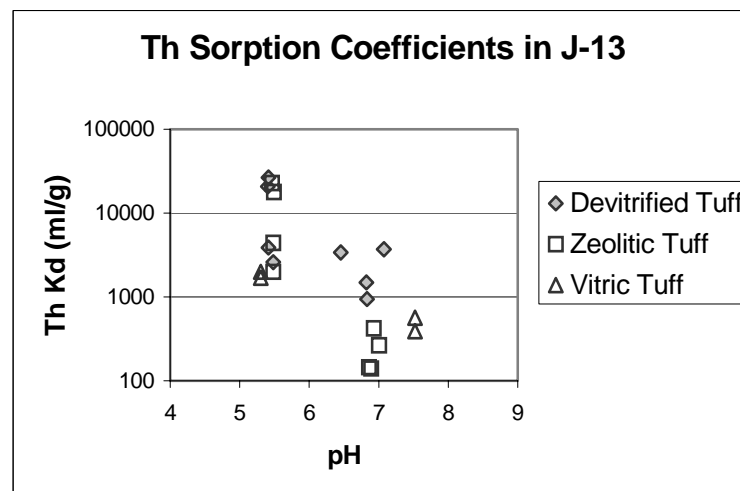
DTN: LA0305AM831341.001 [163789]

Figure I-46. Thorium Sorption Coefficients on Tuff Versus pH

On the basis of the experimental data in Figures I-45 and I-46, the range of thorium sorption coefficients expected for devitrified tuffs in the saturated volcanic section at Yucca Mountain is 1,000 to 10,000 mL/g. This range is intended to reflect the range in surface areas found in devitrified tuffs in the saturated zone and the range in thorium concentrations expected during saturated-zone transport. The lower end of the range reflects sorption coefficients at thorium concentrations near the solubility limit. The probability distribution type selected is a truncated normal distribution with a mean of 5500 mL/g and a standard deviation of 1500 mL/g.

I.8.8.2   Zeolitic Tuff

Sorption coefficient data for zeolitic tuff are also plotted in Figures I-45 and I-46. Based on the available data, zeolitic tuffs have sorption coefficients for thorium that are similar to those obtained for devitrified tuffs.

On the basis of the data plotted in Figures I-45 and I-46, the range of thorium sorption coefficients selected for zeolitic tuffs in the saturated volcanic section at Yucca Mountain is 1,000 to 10,000 mL/g. The upper end of this range was selected to reflect the higher surface areas of zeolitic tuffs relative to devitrified tuffs. The probability distribution selected is a truncated normal distribution with a mean of 5500 mL/g and a standard deviation of 1500 mL/g.

I.8.8.3   Alluvium

The probability distribution for devitrified tuff will be used as a default for the thorium sorption coefficient distribution in alluvium. Alluvium along the flow path is composed largely of disaggregated tuffaceous materials. Because it has been disaggregated, the surface area of alluvial material should be higher than that of devitrified tuff. In addition, clays and other secondary minerals are enriched in alluvial materials. These characteristics should result in higher sorption coefficients in alluvial materials compared to intact devitrified tuff.

I.8.9   Uranium

The solubility of uranium obtained from PHREEQC modeling (PHREEQC V2.3; BSC 2001 [155323]) with the thermodynamic input data files LLNL.DAT (DTN: MO0309THDPHRLL.000 [165530]) and PHREEQC.DAT (DTN: MO0309THDPHRQC.000 [165529]) in J-13 water under oxidizing conditions ranges from 1.8×10^{-4} M/L at a pH of 7.1 to 2.0×10^{-4} M/L at a pH of 8.5 (Output DTN: LA0306AM831343.001 file output/Usat.pun.). The solubility of uranium in synthetic p#1 water under oxidizing conditions ranges from 6.7×10^{-4} M/L at a pH of 6.9 to 9.9×10^{-4} M/L at a pH of 8.6 (Output DTN: LA0306AM831343.001 file output/Usatp1.pun.). The solubility-controlling solid in both waters is schoepite.

I.8.9.1   Devitrified Tuff

As shown in Figure I-47, the calculated final uranium concentrations in the sorption experiments were generally below saturation with schoepite. The sorption coefficients obtained in experiments with devitrified tuffs do not show a correlation with the calculated final uranium solution concentrations.
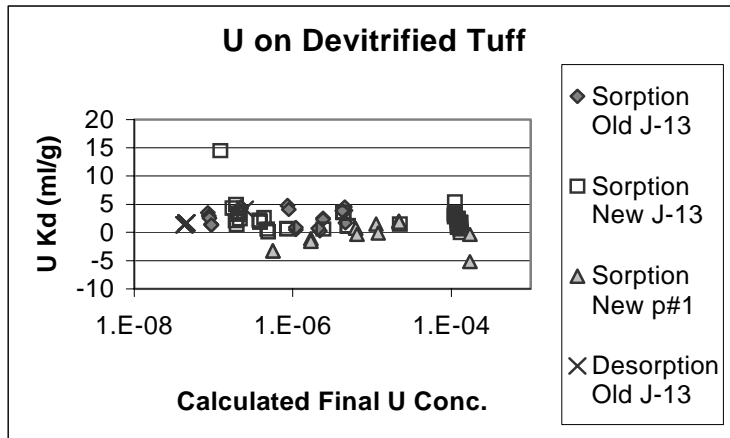
Figure I-47. Uranium Sorption Coefficients on Devitrified Tuff Versus
Calculated Final Uranium Concentration in Solution

Sorption experiments carried out as a function of time are shown in Figure I-48. Beyond approximately 3 days, there is no clear correlation between the sorption coefficients obtained and the duration of the experiments. The data imply that uranium sorption reactions on devitrified tuffs must be relatively fast (i.e., they reach steady state in a few days).
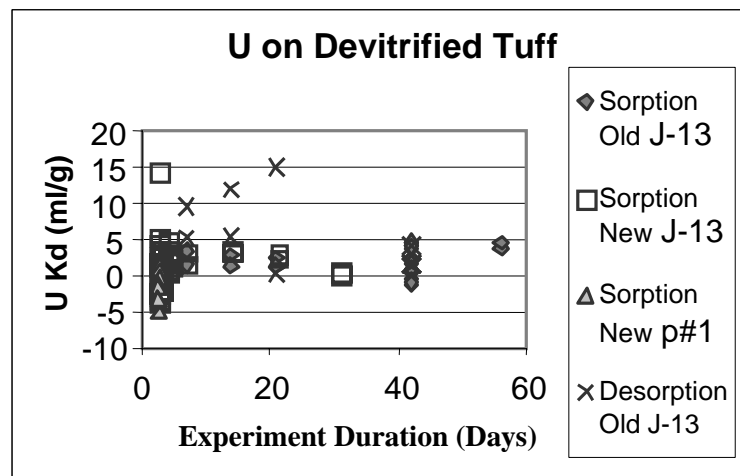
Figure I-48. Uranium Sorption Coefficients on Devitrified Tuff Versus Experiment
Duration for Sorption (Forward) and Desorption (Backward) Experiments

The dependence of the uranium sorption coefficient on water chemistry was tested with experiments using two water compositions (J-13 and synthetic p#1). The J-13 experimental data are shown as a function of pH in Figure I-49. The "old data" were obtained in the 1980s and the "new data" in the 1990s. The difference between the two data sets is not statistically significant. The range of values obtained at a given pH (e.g., 8.4) reflects experimental errors and natural variations in rock properties (e.g., surface area and mineral chemistry). It is not possible to discriminate between these possible causes with the available data. On the basis of the experimental data points, there does not appear to be a correlation between K_d values and pH. However, surface-complexation modeling with PHREEQC (V2.3; BSC 2001 [155323]), using binding constants derived by Pabalan et al. (1998 [162987], p. 124) for uranium on silica points to a clear pH dependence. As shown in Figure I-49, the two model curves reflect two different surface areas (2.8 and 5.6 m^2/g). The 2.8 m^2/g surface area is approximately an average value for devitrified tuffs at Yucca Mountain.

Uranium on Devit Tuff in J-13

DTN: LA0305AM831341.001 [163789], LA0010JC831341.005 [153320], LA0309AM831341.007 [165528]

NOTE: Model curves are from the PHREEQC surface-complexation model (Output DTN: LA0306AM831343.001 file output/Udt2j13.pun).

Figure I-49. Uranium Sorption Coefficients on Devitrified Tuff Versus pH

The sorption coefficients obtained in experiments with synthetic p#1 water are shown in Figure I-50. The data plotted have substantial experimental errors associated with them as indicated by the magnitude of some of the negative K_d values. These experimental errors result from counting statistics, the stability of counters over time, corrections made for adsorption to container walls, and the pH of the tracer solution added to the experiment. Taken at face value, the experimental data suggest a trend of increasing values of K_d with increasing pH. However, the surface complexation modeling predicts a decrease in the value of K_d with increasing pH, although the absolute K_d values are rather small.

Uranium on Devit Tuff in p#1(v)

DTN: LA0305AM831341.001 [163789], LA0010JC831341.005 [153320], LA0309AM831341.007 [165528]

NOTE: Model curve is from the PHREEQC surface-complexation model (Output DTN: LA0306AM831343.001 file output/Udtp1.pun).

Figure I-50. Uranium Sorption Coefficients on Devitrified Tuff in p#1 Water Versus pH

On the basis of the experimental data and model curves plotted in Figures I-49 and I-50, a normal distribution was selected for the uranium sorption-coefficient probability distribution for devitrified tuff in the saturated volcanic section with a range of 0 to 4 mL/g, a median of 2 mL/g, and a standard deviation of 0.6 mL/g.

I.8.9.2   Zeolitic Tuff

As shown in Figure I-51, the sorption coefficients obtained in experiments with zeolitic tuffs do not show a clear correlation with the calculated final uranium solution concentrations. The high end of the concentrations plotted is below saturation with a solid uranium phase.

Uranium sorption experiments on zeolitic tuffs carried out as a function of time are shown in Figure I-52. Beyond a period of approximately 3 days, there is no clear correlation between the sorption coefficients obtained and the duration of the experiments. These data imply that uranium sorption reactions on zeolitic tuffs are relatively fast (i.e., they reach steady state in a few days).

DTN: LA0305AM831341.001 [163789], LA0010JC831341.005 [153320], LA0309AM831341.007 [165528]
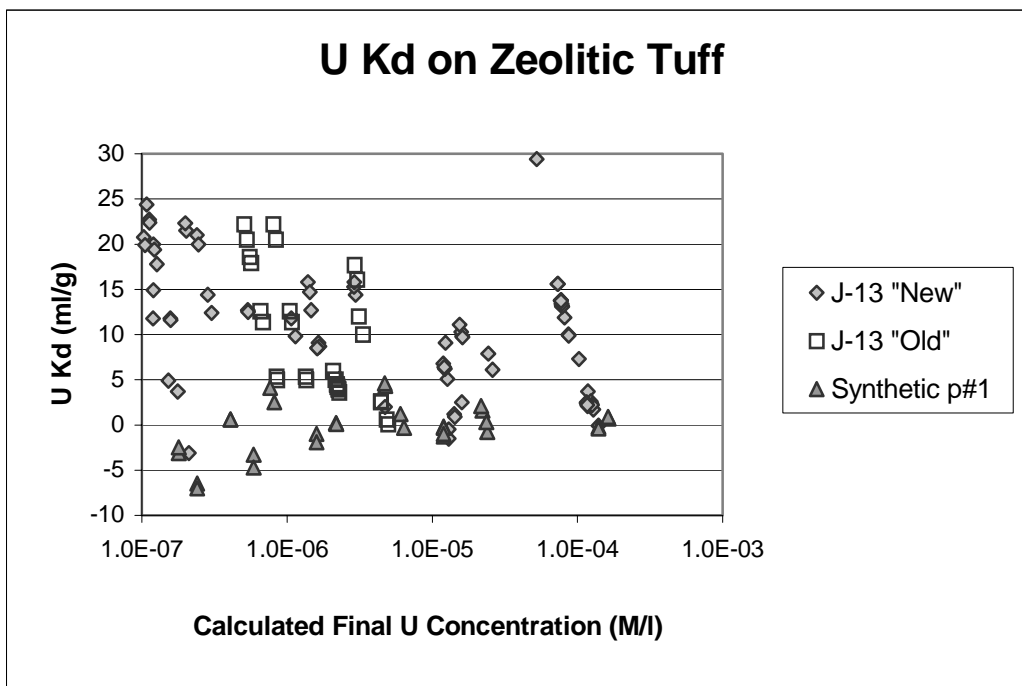
Figure I-51. Uranium Sorption Coefficients on Zeolitic Tuff Versus
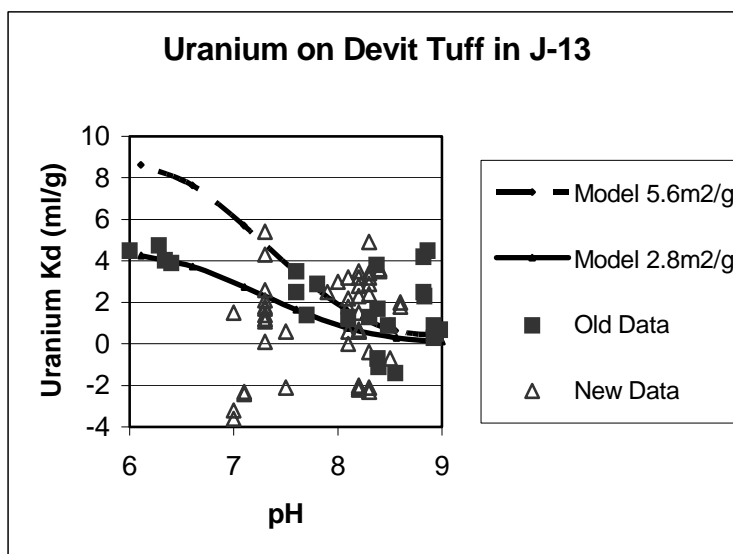Calculated Final Uranium Concentration in Solution

DTN: LA0305AM831341.001 [163789], LA0010JC831341.005 [153320], LA0309AM831341.007 [165528]
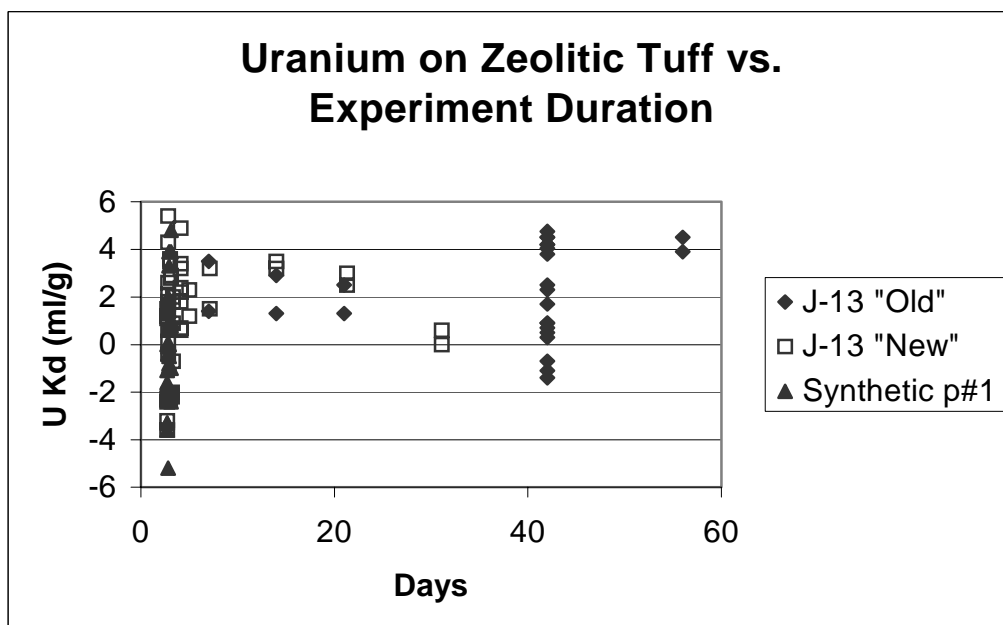
Figure I-52. Uranium Sorption Coefficients on Zeolitic Tuff as a Function of Experiment Duration

The dependence of the uranium sorption coefficient on water chemistry was tested with experiments using two water compositions (J-13 and synthetic p#1). The J-13 data are shown as a function of pH in Figure I-53. The "old data" were obtained in the 1980s and the "new data" in the 1990s. The difference between the two data sets is not statistically significant. The range of values observed at a given pH (e.g., 8.4) reflects variations in rock properties and experimental errors. The experimental errors result from such things as counting statistics, the stability of counters over time, the accuracy of corrections for adsorption to container walls, and other experimental artifacts. In some cases, the pH of the tracer solution added to the experiment seems to have an effect. Some of these errors are random (e.g., counting errors) and others (e.g., adsorption to container walls) may have a nonrandom bias. It is not possible to evaluate these errors separately with the available information. Note that the distribution of data points in Figure I-53 does not indicate a correlation between the values of K_d and pH.

Surface-complexation modeling was carried out with PHREEQC (V2.3; BSC 2001 [155323]) with the thermodynamic input data files LLNL.DAT (DTN: MO0309THDPHRLL.000 [165530]) and PHREEQC.DAT (DTN: MO0309THDPHRQC.000 [165529]) to provide a framework in which to interpret the experimental data. Binding constants for uranium on silica derived by Pabalan et al. (1998 [162987], p. 124) were used in the modeling. The modeling results show a clear pH dependence (Figure I-53). The two model curves reflect two different surface areas. A surface area of 28 m^2/g was used because it is approximately an average value for zeolitic tuffs and because it is an order of magnitude larger than the average value used for modeling devitrified tuffs. A surface area of 14 m^2/g was also used to show the impact of factor of 2 change in surface area.
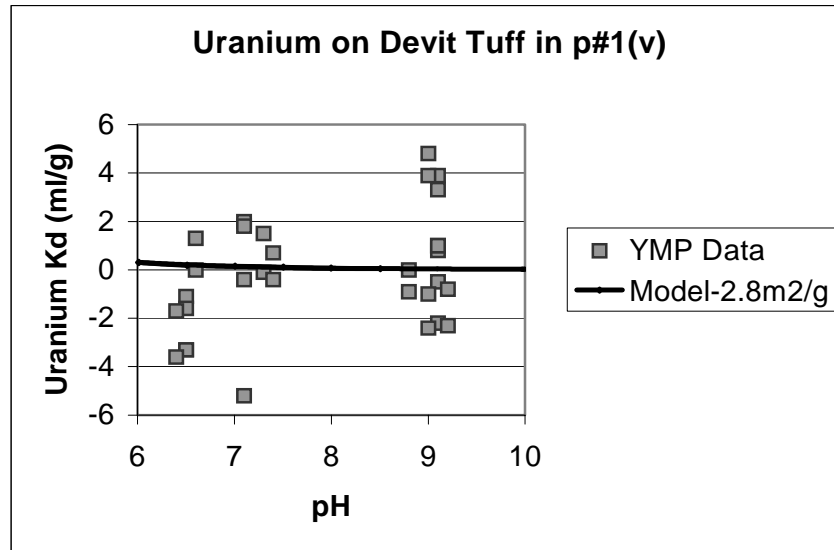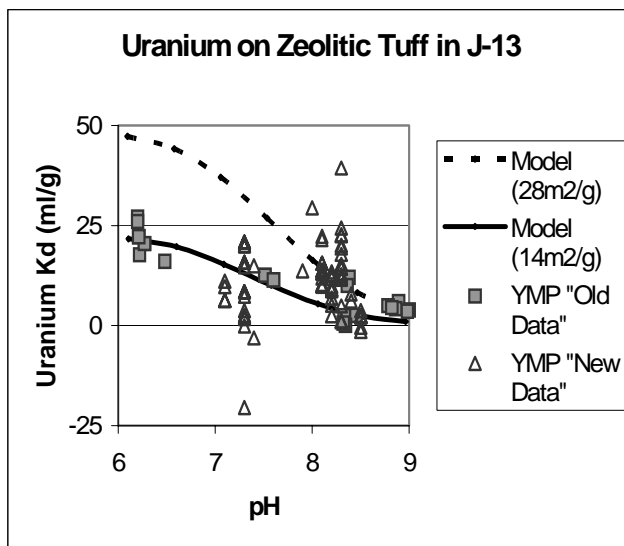

DTN: LA0305AM831341.001 [163789], LA0010JC831341.005 [153320], LA0309AM831341.007 [165528]

NOTE: Model curves derived with PHREEQC surface-complexation modeling are also shown (Output DTN: LA0306AM831343.001 file output/ Uzeoj13.pun).

Figure I-53. Uranium Sorption Coefficients for Zeolitic Tuff in J-13 Water Plotted as a Function of pH

The sorption coefficients obtained in experiments with synthetic p#1 water are shown in Figure I-54. The magnitudes of the negative K_d values plotted are similar to the magnitudes of the positive values plotted. Thus, the net values may be very close to zero. Taken at face value, the experimental data suggest a trend of increasing K_d values with increasing pH. However, the surface complexation modeling predicts an increase in K_d with decreasing pH, although the absolute K_d values are rather small in agreement with the net values obtained from the experimental data.
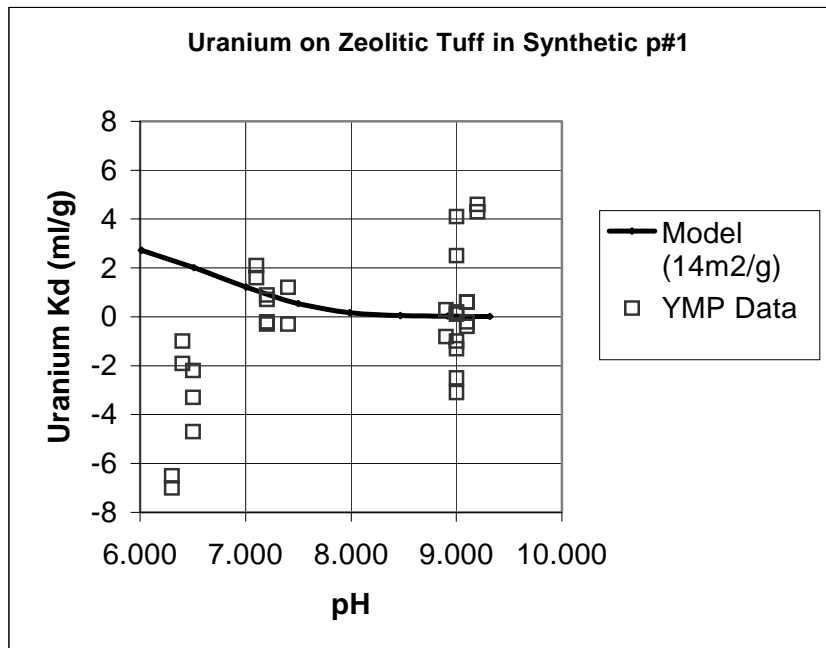
DTN: LA0305AM831341.001 [163789], LA0010JC831341.005 [153320]

NOTE: Model curves derived with PHREEQC surface-complexation modeling are also shown (Output DTN: LA0306AM831343.001 file output/ Uzeop1.pun)

Figure I-54. Uranium Sorption Coefficients for Zeolitic Tuff in Synthetic p#1 Water as a Function of pH

On the basis of the experimental data and model curves plotted in Figures I-53 and I-54, a normal distribution was selected for the uranium sorption-coefficient probability distribution for zeolitic tuff in the saturated volcanic section with a range of 5 to 20 mL/g, a median of 12 mL/g, and a standard deviation of 3.6 mL/g (Output DTN: LA0310AM831341.002). This distribution emphasizes the J-13 water chemistry over the p#1 water chemistry.

I.8.9.3 Alluvium

Sorption coefficients for uranium were measured in batch experiments on cores obtained from three wells (10SA, 22SA, and 19IM1A) drilled into the alluvium (DTN: LA0302MD831341.004 [163785]). Following a procedure identical to the that used for neptunium, described in Section I.8.3.3 of this report, the K_d values for uranium were taken to be described by a t distribution with the following statistics: $\mu_U = 4.6$ mL/g, $\sigma_U = 0.58$ mL/g.

Although the t distribution was thought to capture correctly the spatial uncertainty, the question about the representativeness of the experiment does introduce a small amount of additional uncertainty, as discussed for the case of neptunium in Section I.8.3.3 of this report. Hence a cumulative distribution was chosen for uranium. The minimum experimentally observed value was 1.7 mL/g. Five percent probability was uniformly distributed between 1.7 mL/g and the lower bound of the t distribution at 2.9 mL/g. Since the t distribution had such little variation, it was reasonably represented by a uniform distribution. Hence, 90% probability was uniformly distributed between 2.9 mL/g and the upper bound of the t distribution at 6.3 mL/g. The remaining 5% probability was uniformly distributed between 6.3 mL/g and the maximum experimentally observed value of 8.9 mL/g.

I.9 SUMMARY

Sorption-coefficient probability distribution functions were derived for the radionuclides of U, Cs, Np, Pu, Am, Th, Sr, Pa, and Ra. These are summarized in Table I-4. Experimental and modeling results were used to constrain the distributions. In general, the approach used in the derivation of the distributions tended to underestimate the range and median or mean. This approach was used to provide some conservatism in the derivation given potential scaling uncertainties in the application of these distributions to transport calculations at the Yucca Mountain site.

Table I-4. Small Scale Probability Distribution Functions for K_ds in the Saturated Zone Developed on the Basis of Laboratory Data from Core Samples

Species	Unit/Analysis	Distribution	Coefficients describing distribution (mL/g)
U	Zeolitic	Normal	range = 5 – 20; μ =12, σ = 3.6
	Devitrified	Normal	range = 0 – 4; μ=2, σ = 0.6
	Alluvium	Cumulative	(Kd, prob) (1.7, 0.) (2.9, 0.05) (6.3, 0.95) (8.9,1.0)
Np	Zeolitic	Normal	range = 0 – 6; μ =2.88, σ = 1.47
	Devitrified	Exponential	range = 0 – 2; μ=0.69, σ = 0.707
	Alluvium	Cumulative	(Kd, prob) (1.8, 0.) (4.0, 0.05) (8.7, 0.95) (13, 1.0)
Pu	Zeolitic	Beta	range = 50 – 300; μ =100, σ=15
	Devitrified	Beta	range = 50 – 300; μ =100, σ=15
	Alluvium	Beta	range = 50 – 300; μ =100, σ=15
Cs	Zeolitic	Exponential	range = 4,000 – 42,000; μ = 16,942: σ = 14,930.
	Devitrified	Normal	range =100 – 1,000; μ =728, σ = 464
	Alluvium	Cumulative	(Kd, prob) (100, 0.) (3700, 0.05) (7500, 1.0)
Am	Zeolitic	Truncated Norm	range = 1,000 – 10,000; μ =5,500, σ = 1500
	Devitrified	Truncated Norm	range = 1,000 - 10,000; μ =5,500, σ = 1,500
	Alluvium	Truncated Norm	range = 1,000 - 10,000; μ =5,500, σ = 1,500
Pa	Zeolitic	Truncated Norm	range = 1,000 - 10,000; μ =5,500, σ = 1500
	Devitrified	Truncated Norm	range = 1,000 - 10,000; μ =5,500, σ = 1,500
	Alluvium	Truncated Norm	range = 1,000 - 10,000; μ =5,500, σ = 1,500
Sr	Zeolitic	Cumulative	(Kd, prob) (100,0) (5000, 0.5) (90,000, 1.0)
	Devitrified	Uniform	range= 20 – 400
	Alluvium	Uniform	range= 20 – 400
Th	Zeolitic	Truncated Norm	range = 1,000 - 10,000; μ =5,500, σ = 1500 (for a symmetric distribution and a min and max at +/-3σ)
	Devitrified	Truncated Norm	range = 1,000 - 10,000; μ =5,500, σ = 1,500 (for a symmetric distribution and a min and max at +/-3σ)
	Alluvium (same as devitrified)	Truncated Norm	range = 1,000 - 10,000; μ =5,500, σ = 1,500 (for a symmetric distribution and a min and max at +/-3σ)
Ra	Zeolitic	Truncated Log-normal	range = 1,000 - 250,000; μ =100,000, σ = 31,420
	Devitrified	Uniform	range=100-1000
	Alluvium	Uniform	range=100-1000
C/Tc/I	Volcanics/Alluvium	Constant	zero

The following notations are used in this table:

μ = mean

σ = standard deviation

I.10 CORRELATIONS FOR SAMPLING OF SORPTION-COEFFICIENT PROBABILITY DISTRIBUTIONS

In the Total Systems Performance Assessment, saturated-zone transport calculations are carried out separately for each radionuclide. The sorption-coefficient probability distribution for each radionuclide could be sampled independently in each transport calculation. However, such independent sampling could potentially lead to dose dilution. That is, independent sampling of the distributions could cause radionuclides to travel at independent rates such that the calculated dose at the accessible environment is not representative of maximum possible doses. Similarities in the chemical dependencies of sorption coefficients for the various radionuclides suggest transport rates in the saturated zone are likely to be correlated for some radionuclides. These correlations are summarized in Table I-5.

Correlations for sampling sorption-coefficient probability distributions have been derived for the elements americium, neptunium, protactinium, plutonium, thorium, and uranium. The elements americium, protactinium, and thorium sorb primarily by surface-complexation mechanisms and generally have a high affinity for silicate surfaces. In Section I.8, the same sorption-coefficient probability distribution (K_d = 1,000–10,000 mL/g) has been chosen for all three of these elements. Thus, they are 100% correlated by definition. The elements carbon, iodine, and technetium are also 100% correlated in that the sorption coefficient is always zero for all three of these elements.

Separate sorption-coefficient probability distributions were derived for neptunium in volcanics and alluvium in Section I.8. However, controls on the sorption behavior of neptunium are likely to be similar in volcanics and alluvium, although not identical. A 75% correlation has been chosen for sampling of the neptunium sorption coefficients in volcanics and alluvium. The same arguments apply to uranium. Thus, a 75% correlation has also been chosen for sampling of the uranium sorption coefficients in volcanics and alluvium. The controls on the sorption behavior of neptunium and uranium are similar but not identical as discussed in Section I.8. To account for the similarities, a correlation of 50% was chosen for sampling sorption-coefficient distributions for neptunium and uranium. Finally, a correlation of 50% was chosen for sampling sorption-coefficient distributions for plutonium in volcanics and alluvium. In the volcanics, the applicable sorption-coefficient distribution is the composite distribution (Attachment III) whereas in the alluvium the sorption-coefficient probability distribution for devitrified tuff was chosen as a default in Section I.8.

Table I-5. Recommended SZ K_d Correlations

Species	Unit/Analysis	Correlation
U	Correlation	75% correlation Composite (Volcanics) / Alluvium and 50% correlation Np
Np	Correlation	75% correlation Composite (Volcanics) / Alluvium and 50% correlation U
Pu	Correlation	50% correlation Composite (Volcanics) / Alluvium
Cs	Correlation	None
Am/Th/Pa	Correlation	100%
Sr	Correlation	None
Ra	Correlation	None
C/Tc/I	Correlation	100%

Output DTN: LA0309AM831341.001

ATTACHMENT II. THE COLLOID-FACILITATED TRANSPORT OF REVERSIBLY-ATTACHED RADIONUCLIDES

The model presented here incorporates the main colloid-facilitated transport processes and is amenable to efficient computation in support of the Total Systems Performance Assessment. Radionuclides can sorb onto colloids either reversibly or irreversibly. The relative percentages of these radionuclides are obtained from an analysis of the near-field environment near the repository and the waste. In general, the majority of radionuclides that sorb to colloids are irreversibly sorbed, with a typical percentage being 90% irreversible and 10% reversible (BSC 2003 [161620], p. 16, pp. 53 to 58, pp. 94 to 97). Radionuclides that are irreversibly sorbed are typically embedded in the colloid or are so strongly sorbed onto the colloid that there is no possibility of detachment for typical transport time scales (thousands of years) through the saturated zone (SZ).   On the other hand, reversibly sorbed colloids have measurable desorption rates.

The SZ transport simulations of radionuclides that are irreversibly attached to colloids are conducted for radioisotopes of Pu and Am. Most radionuclides are taken to sorb onto colloids reversibly (that is, they have measurable desorption rates and can be entirely desorbed from colloids) (BSC 2003 [162729], Section 6.3). However, Pu and Am can sorb either reversibly or irreversibly onto colloids with the relative percentages of these obtained from an analysis of waste-form degradation and waste-package corrosion processes occurring in the repository near-field environment (BSC 2003 [162729], Section 6.3.).   In general, the majority of the Pu and Am sorbed to colloids is irreversibly sorbed, with a typical percentage being 90-99% irreversible and 1-10% reversible (BSC 2003 [161620], Section 6.3.3.2, p. 74). The irreversibly sorbed radionuclides are taken to transport in a manner identical to the colloids onto which they are sorbed. The colloid retardation factor distributions for irreversible colloids are developed in BSC (2003 [162729]), so only a brief description is provided here. The transport of the colloids is simulated using the advection-dispersion equation, and colloids are taken to not diffuse. Several field observations have suggested that a small percentage of colloids transport with essentially no retardation in ground water (Kersting et al. 1999 [103282], p. 56, 58; Penrose et al. 1990 [100811], p. 228), whereas the majority undergoes either reversible or irreversible filtration, which can be described by a retardation factor, R_{col}. In this analysis filtration is defined as the net effect of chemical sorption of the colloid onto the rock surface and the physical removal of colloids from the advective flow due to sieving and settling. The value of R_{col} is dependent on several factors such as colloid size, colloid type, and geochemical conditions (e.g., pH, Eh, and ionic strength). These factors are folded into the distribution of R_{col} that has been developed from field and experimental data collected under varying geochemical conditions with different colloid types and sizes.   Attachment rate constants, k_{att}, and detachment rate constants, k_{det}, of colloids to the rock matrix have been measured, and R_{col} distributions have been developed for the fractured volcanics and for the alluvium.   The relationship between R_{col}, k_{att}, and k_{det} is given by:

$$R_{col} = 1 + \frac{k_{att}}{k_{det}}$$
(Eq. II-1)

The attachment rate constant is also used to determine the fraction of the colloids that transport with no retardation. Specifically, colloids for which one over the attachment rate constant is smaller than the travel time through the system will transport with no retardation. The development of R_{col} distributions for the volcanics and the alluvium as well as the fraction of colloids that transport unretarded is documented in BSC 2003 [162729].

The SZ transport simulations of radionuclides that are reversibly attached to colloids are conducted for radioisotopes of Pu, Am, Th, Pa, and Cs (the rationale for selection of these radionuclides is given in BSC 2003 [161620], Section 6.3.3.1). Note that the Pu and Am inventories are split into reversibly and irreversibly sorbed fractions. For the reversibly sorbed transport simulations, radioisotopes of Pu are transported as one group, radioisotopes of Am, Th, and Pa are transported as a second group, and Cs is transported as a third group. Am, Th and Pa are being treated as a single group based on the similarity in their absorption characteristics–each of these three radionuclides are strongly sorbed to surfaces generally involving the OH group, and each of them displays a single valance state in solution and sorption (Allard et al. 1983 [162982] pp. 9, 10, and 12). The radionuclides that are reversibly absorbed onto colloids are modeled using the K_c model, which represents the equilibrium partitioning of radionuclides between the aqueous phase and the colloidal phase with the distribution coefficient K_c (Robinson et al. 1997 [100416], Equation 8-10, pp. 8-35). The K_c model is a simplified colloid transport model that applies under the following conditions:

1) The contaminant sorbs reversibly to the colloids in addition to interacting with the rock matrix and fractures.

2) The colloids are isolated to the fracture and possess dispersive properties equivalent to that of an aqueous solute.

3) The colloids interact reversibly with the rock surface.

4) Colloids exist throughout the flow system.

Under these conditions, a transport equation for contaminant attached to colloids can be written as

$$R_{\text{col}} \frac{\partial C_c}{\partial t} = D_z \frac{\partial^2 C_c}{\partial z^2} - v \frac{\partial C_c}{\partial z} \qquad \text{(Eq. II-2)}$$

where

$\quad C_c$ is the concentration of contaminants attached to colloids

$\quad R_{\text{col}}$ is a retardation factor that captures the details of colloid attachment/detachment and reversible filtration processes

$\quad v$ is the pore-water velocity

$\quad t$ is time

$\quad z$ is the spatial coordinate

D_z is the coefficient of longitudinal dispersion.

Note that Eq. II-2 represents a mass balance of solute sorbed to colloids, not to colloids alone.

The concentration of contaminants attached to the colloids is related to the aqueous contaminant concentration C using a linear relationship:

$$C_c = K_c C \qquad \text{(Eq. II-3)}$$

where K_c is the distribution parameter relating the concentrations. Since both C and C_c are expressed as moles contaminant per unit fluid volume, K_c is a dimensionless parameter expressing the ratio of contaminant mass residing on colloids to the mass present in aqueous form. In terms of more commonly defined and measured quantities, K_c is the product of the distribution coefficient for contaminant sorbing onto colloids ($K_{d(colloids)}$) and the concentration of colloidal material available for sorption-mass of colloids per unit fluid volume ($C_{collloids}$):

$$K_c = K_{d(colloids)} C_{colloids} \qquad \text{(Eq. II-4)}$$

Note that the $C_{colloids}$ term includes the concentration of colloids in the aqueous phase and sorbed to the rock. The transport equation for the contaminant transporting in the aqueous phase is given by

$$R_f \frac{\partial C}{\partial t} = D_z \frac{\partial^2 C}{\partial z^2} - v \frac{\partial C}{\partial z} \qquad \text{(Eq. II-5)}$$

where R_f is a retardation factor that captures details of radionuclide attachment/detachment. By combining Equations II-2 and II-3 and making use of Equation II-5, the concentration of the contaminant in the aqueous phase for the fracture can be obtained:

$$\left(\frac{R_f + K_c R_{col}}{1 + K_c} \right) \frac{\partial C}{\partial t} = D_z \frac{\partial^2 C}{\partial z^2} - v \frac{\partial C}{\partial z} \qquad \text{(Eq. II-6)}$$

The coupling between the fracture and matrix is identical to the case without colloids if there is no mobility of colloids into the rock matrix. Inspection of Equations II-5 and II-6 reveals that the forms of the transport equations are identical, with different constants in the accumulation loss term. Therefore, the solutions developed thus far need only be modified slightly to include colloid contaminant transport. To do this, a revised constant $\hat{R}_f$ is defined as follows:

$$\hat{R}_f = \frac{R_f + K_c R_{col}}{1 + K_c} \qquad \text{(Eq. II-7)}$$

Using $\hat{R}_f$ allows us to consider colloidal transport using the advection-dispersion equation.

ATTACHMENT III. DERIVATION OF COMPOSITE UPSCALED K_d DISTRIBUTIONS

This attachment provides details of the study performed to derive composite distributions applicable on the scale of the computational grid used in the SZ transport model for the radionuclides Cs, Np, Pu, U, Am, Th, Pa, Sr, and Ra. These distributions will be used to simulate transport of radionuclides in the saturated-zone site-scale model during the Total Systems Performance Assessment (TSPA) calculations. The distributions in alluvium for these radionuclides were taken to be the same as the small-scale distributions derived in Attachment I (Table I-4). Given the scope of the work presented here, simulations could not be carried out for all radionuclides, and a choice had to be made. The four radionuclides Cs, Np, Pu and Ra were chosen so as to approximately bracket the expected range of values. The distributions in volcanics for Am, Th, Pa, Sr, and Ra were taken to be the same as those in Table I-4. The distributions in volcanics for Cs, Np, Pu, and U were generalized using stochastic modeling (Section III-1 of this Attachment) to a scale of 500 m, and then modified to include additional uncertainties leading to composite distributions (Section III-2 of this Attachment) for use with the TSPA calculations.

In the TSPA calculations, radionuclide transport is modeled using a single value of K_d for grid blocks with dimensions 500 meters (m) x 500 m in the x and y directions. In the field, values of K_d are variable at a scale much smaller than 500 m. Thus, if a uniform single value of K_d is used to model sorption, it is important to use a value that effectively captures variability at smaller scale and results in the same sorption behavior as if all the small-scale processes were represented explicitly. The factors that affect the sorption behavior of the rock matrix include mineral composition, groundwater chemistry, and the type of radionuclide. Mineral composition and groundwater chemistry are spatially variable at a scale smaller than 500 m. The small-scale K_d distributions for these radionuclides were developed on the basis of laboratory data. This development is given in detail in Attachment I, and the small-scale K_d distributions are presented in Table I-4. The mineral compositions of the volcanic rocks show systematic variability, represented by the mineralogical data summarized in Tables III-1 through Table III-4. Hence, in the volcanics, the small-scale distributions were scaled to the 500-m grid size using stochastic modeling techniques. This development is presented in Section III.1 of this Attachment. The results of this scaling analysis are presented in Table III-11.

Although the scaled distributions are thought to correctly capture the spatial uncertainty, other sources of uncertainty such as potential fast pathways, reducing conditions along potential transport pathways, higher concentrations of radionuclides during transport in the SZ than the ranges included in the analysis, and competition among radionuclides for sorption sites may not be completely represented in these distributions. To incorporate these other sources of uncertainty, expert judgment was used to develop subjective estimates on the appropriate range of the K_ds and percentile points for the distribution. This process is described in Section III.2 of this attachment and the results are presented in Table III-14. The K_d distributions presented in this table are the ones recommended for use in TSPA analysis.

III.1   Stochastic Modeling For Upscaling Of K_d Distributions in the Volcanics

The stochastic approach used to calculate effective values of K_d for a 500-m grid block is discussed here. The effect of spatial heterogeneity in K_d values, the effect of upscaling, and the effect of mineralogy were incorporated.   The approach included generating spatially heterogeneous distributions of K_d at a scale much smaller than 500 m and using the heterogeneous distributions to calculate effective K_d values. The heterogeneous distributions were generated by incorporating the effect of spatial variability in rock mineralogy. A stochastic approach was used to generate distributions of effective K_d values, and multiple K_d realizations were used to calculate effective K_d values. The input data used to generate the heterogeneous K_d distributions were derived from experimental data described in Attachment I.

III.1.1   Definition of Effective K_d

Effective K_d was defined as the value of K_d that would result in a radionuclide sorption behavior that is similar to the sorption behavior resulting from a heterogeneous distribution of small-scale K_d values. This concept is shown schematically in Figure III-1, in which a two-dimensional (2-D) grid block with a uniform effective K_d produces radionuclide breakthrough behavior that is similar to that shown by the same grid block with four subgrid blocks with different K_d properties.

With the above definition, the following approach was used to compute an effective K_d. The retardation coefficient and K_d are related to each other by the following equation:

$$K_d = (\text{retardation coeff.} - 1) \frac{\text{Porosity}}{\text{Bulk Density}} \qquad \text{(Eq. III-1)}$$
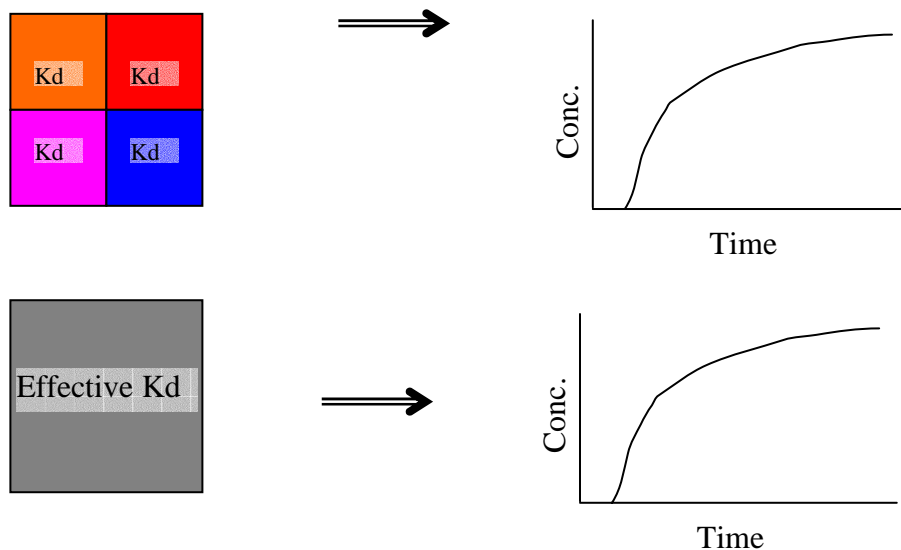
For illustration purposes only.

DNT: N/A

Figure III-1. A Schematic Representation of the Definition of Effective K_d

Thus, if the retardation behavior of a system is appropriately calculated, it can be used to calculate the effective K_d. Effective retardation behavior of a grid block for a particular radionuclide was determined by comparing two breakthrough curves for the same grid block under identical flow conditions. One breakthrough curve was calculated using a dual-porosity transport in which the radionuclide can diffuse from fracture to matrix and get retarded in the matrix (Figure III-2a). The second curve was calculated with identical diffusion behavior but using no retardation in matrix (Figure III-2b). In both calculations, retardation on fracture surface was neglected. Using these two curves, effective matrix retardation was calculated by comparing the breakthrough times for 50% relative concentration. This concept is further explained schematically in Figure III-3 where relative behavior of two breakthrough curves, with and without matrix sorption, is shown.

For illustration purposes only. DTN: N/A
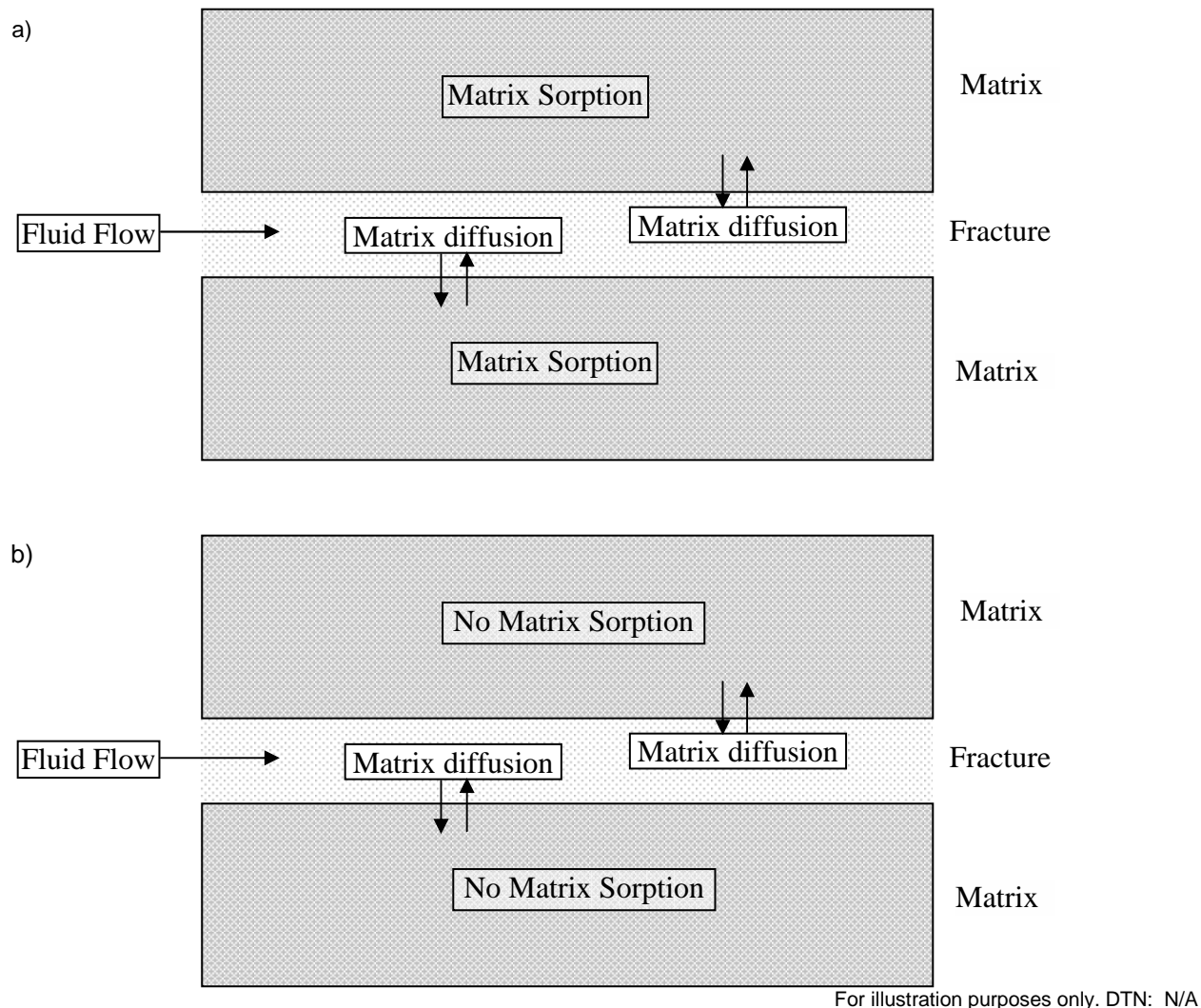
NOTE: (a) Transport with diffusion followed by matrix sorption.
(b) Transport with diffusion followed by no matrix sorption.

Figure III-2. The Processes During Transport of a Radionuclide in a Fractured Media
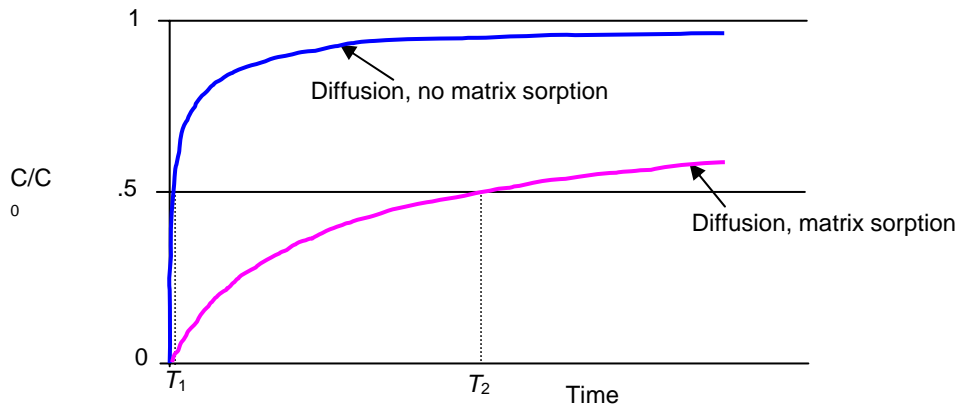
For illustration purposes only. DTN: N/A

Figure III-3. Representation of the Breakthrough Curves Used
to Calculate Effective Matrix Retardation Behavior

The breakthrough curve for the case with no matrix sorption is much steeper than that for the case with matrix sorption. The times at which 50% breakthrough takes place are marked as T_1 and T_2 for the cases without matrix sorption and with matrix sorption, respectively. The effective retardation coefficient was calculated as the ratio of these two times:

$$\text{Effective Retardation } (r_{\text{eff}}) = \frac{T_2}{T_1} \qquad \text{(Eq. III-2)}$$

This definition of effective retardation was used to calculate effective K_d values using Equation III-1. Multiple values of effective K_d were calculated using multiple spatially heterogeneous realizations of K_d and subsequently were used to generate statistical distribution of effective K_d. The heterogeneous K_d distributions were generated using a geostatistical approach. Before describing the approach, a brief discussion on the method used to perform transport calculations follows.

III.1.2   Transport Calculations

As mentioned earlier, a dual-porosity transport model was used to calculate the breakthrough curves. The calculations were performed using the streamline particle-tracking macro '*sptr*' in FEHM (Finite Element Heat and Mass Transport Code) V 2.20 (STN: 10086-2.20-00) [161725]. The dual-porosity transport model in the *sptr* macro is based on the analytical solution developed by Sudicky and Frind (1982 [105043]) for contaminant transport in a system of parallel fractures. This solution takes into account advective transport in the fractures, molecular diffusion from the fracture into the porous matrix, and adsorption on the fracture surface as well as within the

matrix. In this model all of the above mentioned processes except adsorption on the fracture surface are represented. The model includes the assumption that there is no sorption on fracture surfaces: see Table 5-1. Input files for the *sptr* macro were created using *cr8sptr.c* V2.0 (STN: 10927-2.0-00) [163836].

III.1.2.1 Stochastic Realizations of K_d

As mentioned before, the value of K_d is dependent on multiple factors, including rock mineralogy and water chemistry, as well as spatial location. This dependence was taken into account when developing K_d realizations. As mentioned in Section 6.3 of this model report, due to available data, it was not possible to take into account spatial variability of groundwater chemistry. However, groundwater chemistry was treated as a spatially random variable, and its effect on K_d values was incorporated in the K_d distribution used as input for generating stochastic realizations (Attachment I). A two-step process was used to capture dependence on rock mineralogy. First spatial distributions of mineralogically dependent rock types were generated. Data on mineral abundance in rock were available from x-ray diffraction (XRD) analysis of samples from multiple wells [Table III-1]. The mineral abundance data provided the content of the following minerals: smectites, zeolites, tridymite, cristobalite, quartz, feldspar, volcanic glass, analcime, mica and calcite.

Table III-1. List of Wells for Which Mineral Abundance Data Were Available

Data Description	DTN
Mineralogy, borehole UE-25 a#1	MO0101XRDDRILC.002 [163795]
Mineralogy, borehole UE-25 UZ#16	LA000000000086.002 [107144]; LAJC831321AQ98.005 [109004]
Mineralogy, borehole USW G-1	MO0101XRDMINAB.001 [163796]
Mineralogy, borehole USW G-2	MO0101XRDDRILC.002 [163795]
Mineralogy, borehole USW G-3/GU-3	MO0101XRDMINAB.001 [163796]
Mineralogy, borehole USW G-4	MO0101XRDMINAB.001 [163796]
Mineralogy, borehole USW SD-7	LADV831321AQ97.001 [107142]; LAJC831321AQ98.005 [109004]
Mineralogy, borehole USW SD-9	LADV831321AQ97.001 [107142]; LAJC831321AQ98.005 [109004]
Mineralogy, borehole USW SD-12	LADV831321AQ97.001 [107142]; LAJC831321AQ98.005 [109004]
Mineralogy, borehole USW WT-24	LASC831321AQ98.001 [109047]; LADV831321AQ99.001 [109044]
Mineralogy, borehole H-6	MO0106XRDDRILC.003 [163797]

These mineral abundance data were used to determine prevalent mineralogic rock types. The rock type was labeled as zeolitic if the zeolitic abundance was greater than 20%, as vitric if glass abundance was greater than 80%, and as devitrified otherwise. Only the data that were part of the saturated zone extending 200 m below the water table were used in the analysis. When mineralogic abundance data were converted to rock-type data with the above definition, it was observed that only zeolitic and devitrified rocks were present for the top 200 m of the saturated zone. The observed proportions of the rocks were 60% zeolitic and 40% devitrified. The data set also included information on the spatial location of rock samples. These data were used to

calculate spatial correlation information through indicator semivariograms. Two directional semivariograms were calculated: one in the horizontal direction and another in the vertical direction using *GSLIB V1.0GAMV3V1.201* (STN: 10398-1.0GAMV3V1.201-00 [153099]). The semivariograms were used to calculate the spatial correlation parameters. Next, the spatial correlation parameters were used to generate multiple realizations of spatial distribution of rock types. The geostatistical approach of sequential indicator simulations (*GSLIB V2.0MSISIMV2.0;* STN: 10098-2.0MSISIMV2.0-00) [149114] was used to generate the spatial distributions. Sequential indicator simulation is a powerful tool that can be used to generate stochastic realizations of parameters. It uses cumulative distribution functions (CDFs) of observed data as input and tries to estimate a discrete, nonparametric true CDF of a simulated parameter. An indicator is a variable used to show the presence or absence of any parameter qualitatively or quantitatively. For example, an indicator can be used to define the presence of a particular rock type at any spatial location. It can also be used to define whether the value of a parameter falls within a certain range of parameter values defined as cutoffs.

After the spatial distributions of rock types were generated, experimental data on K_d values (Attachment I) were used to generate spatial distributions of K_d values. The experimental data were analyzed to derive rock-type specific statistical distributions for K_d. The statistical distributions were used to derive the CDF for each radionuclide. Next, indicators were defined at four CDF cutoffs of 0.2, 0.4, 0.6, and 0.8. These cutoffs, along with the spatial correlation information, were then used to generate spatial distributions. Unlike mineral abundance data, spatial information on K_d observations was not available. As a result, no spatial correlation functions were available for K_d data. In the absence of any spatial correlation functions, the approach used was to generate spatial K_d distributions by varying the correlation length and to understand the impact of varying the correlation length on effective K_d calculations. Four different values were used for correlation length. This range covers the entire spectrum from completely uncorrelated to fully correlated. Four values were used to represent the entire spectrum while not making the number of simulations excessively large.

- Correlation length equal to a single grid block dimension (4 m) that represents spatially random realizations

- Correlation length equal to the correlation length used to generate permeability realizations (60 m)

- Correlation length equal to the large grid block length (500 m)

- Correlation length equal to the correlation length used to generate rock-type data (1000 m)

All of the above values represent the possible range of correlation lengths that K_d values can be expected to have. The spatial distributions of K_d realizations were generated using the sequential indicator simulation approach. These spatial distributions of K_d values were generated for individual rock types. Distributions for each rock type were generated independent of other rock-type distributions. Finally, the rock-type specific K_d distributions and rock-type distributions were used to generate integrated K_d distributions. The approach used is explained schematically below:

K_d distribution for rock-type '1': $K_{d1}^1, K_{d2}^1, K_{d3}^1, K_{d4}^1, K_{d5}^1, K_{d6}^1, K_{d7}^1, ..., K_{dn}^1$

K_d distribution for rock-type '0': $K_{d1}^0, K_{d2}^0, K_{d3}^0, K_{d4}^0, K_{d5}^0, K_{d6}^0, K_{d7}^0, ..., K_{dn}^0$

Rock-type distribution: 1, 0, 1, 1, 1, 0, 0,…, 1

Combined K_d distribution: $K_{d1}^1, K_{d2}^0, K_{d3}^1, K_{d4}^1, K_{d5}^1, K_{d6}^0, K_{d7}^0, ..., K_{dn}^1$, where n is the number of grid points.

The approach explained above incorporates the effect of spatial heterogeneity and rock mineralogy on the spatial distribution of K_d. Multiple realizations for the spatial distribution of K_d values were generated with this approach.

III.1.2.2 Stochastic Realizations of Permeability

Similar to the K_d distributions, spatial distributions of permeability were generated using the stochastic approach. The approach and data used were similar to that in CRWMS M&O (2000 [152259], Sections 5.2 and 6.1). The computer code gs2fehm.c V1.0 (STN: 10923-1.0-00) [163837] was used to create files for the "perm" macro needed as input to FEHM (Finite Element Heat and Mass Transport Code) V 2.20 (STN: 10086-2.20-00) [161725]. These permeability realizations represented continuum distributions of permeability for fractured rocks.

III.1.3 RESULTS

III.1.3.1 Stochastic Realizations of K_d

Figures III-4 and III-5 show the semi-variograms calculated from the rock-type data (converted from available mineral abundance data). The figures also show the correlation functions fit to the semi-variograms. There is scatter in the data, but the fits are considered reasonable. The parameters for the model fit are shown in Table III-2.

Table III-2. Spatial Correlation Parameters for Mineralogic Rock Type Data

Direction	Range (m)	Sill
Horizontal	1000	0.25
Vertical	75	0.35

Output DTN: LA0309RP831321.001

These correlation parameters were used to generate spatial distributions of rock types. The sequential indicator simulation algorithm SISIM (*GSLIB V2.0MSISIMV2.0;* STN: 100982.0MSISIMV2.0-00 [149114]), which is part of GSLIB, was used to generate these distributions. Five different rock-type realizations were generated using this approach. The proportions of zeolitic and devitrified rocks in the five output realizations are shown in Table III-3.
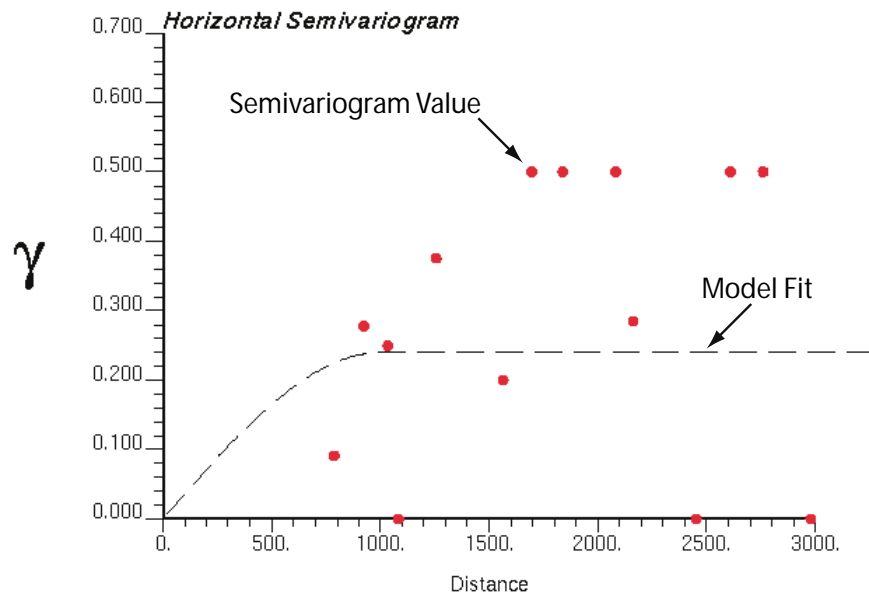
Figure III-4. Calculated Semivariogram and Model Fit in the Horizontal Direction
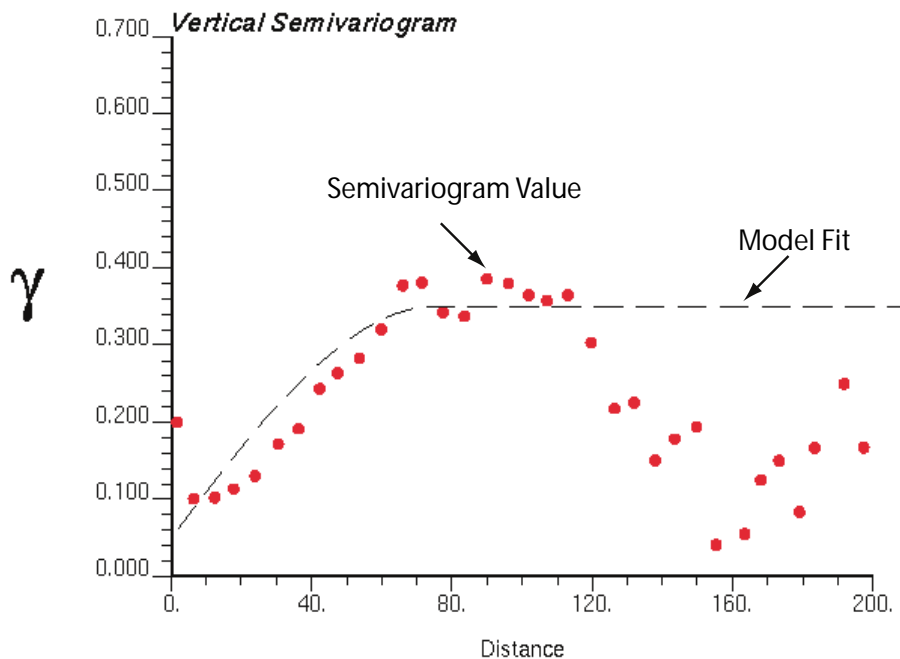
Figure III-5. Calculated Semivariogram and Model Fit in the Vertical Direction

Table III-3. Proportions of Zeolitic and Devitrified Rocks in Output Realizations

Realization	Zeolitic	Devitrified
1	0.6106	0.3894
2	0.5746	0.4254
3	0.6034	0.3966
4	0.5890	0.4110
5	0.6270	0.3730

Output DTN: LA0309RP831321.001

Spatial realizations for K_d were generated for four different radionuclides: uranium, neptunium, cesium, and plutonium. Neptunium is shown to be an important contributor to dose (TSPA-SR; CRWMS M&O 2000 [153246], Section 4.1.1) and neptunium to cesium covers the low to high K_d spectrum. The small-scale uncertainty distributions based on experimentally available data for these radionuclides (discussed in Attachment I) are given in Table III-4 (reproduced from Table I-4 for convenience).

Table III-4. Statistical Distributions of Experimentally Observed K_d Values

Radionuclide	Rock-type	Distribution	Mean (ml/g)	Standard Deviation (ml/g)	Minimum (ml/g)	Maximum (ml/g)
Uranium	zeolitic	Normal	12.0	3.6	5.0	20.0
	devitrified	Normal	2.0	0.6	0.0	4.0
Cesium	zeolitic	Exponential	16942.0	14930.0	4000.0	42000.0
	devitrified	Normal	728.0	464.0	100.0	1000.0
Neptunium	zeolitic	Normal	2.88	1.47	0.0	6.0
	devitrified	Exponential	0.69	0.707	0.0	2.0
Plutonium	zeolitic	Beta	100.0	15.0	50.0	300.0
	devitrified	Beta	100.0	15.0	50.0	300.0

SOURCE: Table I-4

These distributions were used to derive the CDFs for each radionuclide for each rock type using *calc_cdf.c* V1.0 (STN: 10924-1.0-00 [149117]). For each CDF, indicators were defined at four CDF cutoffs: 0.2, 0.4, 0.6, and 0.8. As mentioned earlier, in the absence of spatial data, correlation length was parameterized, and four different correlation lengths were used to generate stochastic realizations. This effect of correlation length was studied only for uranium. For other radionuclides, a correlation length of 500 m was used. Fifty different realizations were generated for each radionuclide and each rock type. Statistics of the output realizations were calculated and compared against the input data. The computer code calc_cdf.c V1.0 (STN: 10924-1.0-00 [149117]) was used to calculate the cumulative distribution function from the statistical realizations. Tables III-5 through III-8 compare the mean CDFs (calculated from 50 realizations) with the input CDFs for the four cutoffs.

Finally, these rock-type specific K_d distributions were combined to generate distributions that were conditioned to the realizations of rock types. The procedure for doing this was outlined in Section III.2.3.

Table III-5. Comparison of Input and Mean Output CDFs for Uranium

Zeolitic			Devitrified		
K_d (ml/gm) Cutoff	Input CDF	Output CDF	K_d (ml/gm) Cutoff	Input CDF	Output CDF
8.97	0.2	0.2047	1.49	0.2	0.2128
11.09	0.4	0.4014	1.84	0.4	0.4050
12.91	0.6	0.5964	2.15	0.6	0.5939
15.03	0.8	0.7918	2.50	0.8	0.7909

Output DTN: LA0309RP831321.001

Table III-6. Comparison of Input and Mean Output CDFs for Cesium

Zeolitic			Devitrified		
K_d (ml/gm) Cutoff	Input CDF	Output CDF	K_d (ml/gm) Cutoff	Input CDF	Output CDF
4929.3	0.2	0.2018	337.5	0.2	0.2026
9478.5	0.4	0.4058	610.5	0.4	0.4079
14613.3	0.6	0.5975	845.5	0.6	0.6012
24896.8	0.8	0.8058	1118.5	0.8	1.0

Output DTN: LA0309RP831321.001

Table III-7. Comparison of Input and Mean Output CDFs for Neptunium

Zeolitic			Devitrified		
K_d (ml/gm) Cutoff	Input CDF	Output CDF	K_d (ml/gm) Cutoff	Input CDF	Output CDF
1.65	0.2	0.2018	0.12	0.2	0.2018
2.51	0.4	0.4059	0.30	0.4	0.4059
3.26	0.6	0.5976	0.51	0.6	0.5976
4.12	0.8	0.8058	0.93	0.8	0.8058

Output DTN: LA0309RP831321.001

Table III-8. Comparison of Input and Mean Output CDFs for Plutonium

Zeolitic			Devitrified		
K_d (ml/gm) Cutoff	Input CDF	Output CDF	K_d (ml/gm) Cutoff	Input CDF	Output CDF
87.005	0.2	0.2054	87.005	0.2	0.2018
95.094	0.4	0.4229	95.094	0.4	0.4059
102.743	0.6	0.5852	102.743	0.6	0.5976
112.348	0.8	0.7855	112.348	0.8	0.8058

Output DTN: LA0309RP831321.001

III.1.3.2 Results of Breakthrough Curve Calculations Using the Particle-Tracking Algorithm

These multiple K_d realizations were used to compute breakthrough curves and model the sorption behavior of each radionuclide. A two-step approach was used. In the first step, steady-state flow fields were computed for fifty different permeability realizations. The properties used for these calculations are shown in Table III-9.

Table III-9. Values of Properties Used in Flow and Transport Calculations

Property	Value
Matrix Porosity	0.22 [1]
Rock Bulk Density	1997.5 [1] kg/m^3
Flowing Interval Porosity	0.001 [1]
Flowing Interval Spacing	19.49 [1] m
Hydraulic Gradient	2.9x10^{-4} [2]

[1] Value chosen to fall within the range given in Table 4-2 of this report.

[2] CRWMS M&O 2000 [152259], pp. 14, Sec. 5.2.

The steady-state flow fields were used in the particle-tracking calculations. In these calculations, 4000 particles were released along one face of the model and were allowed to move under the influence of the steady-state flow field. The locations of the particle releases were determined by a flux-weighted placement scheme. As mentioned in Section III.2.1, two sets of particle-tracking calculations were performed for each steady-state flow field. In the first set of calculations, the baseline breakthrough curve was calculated for transport with diffusion from fracture to matrix and no matrix sorption. In the second set of calculations, the breakthrough curve was calculated for transport with diffusion followed by sorption on the matrix. For these calculations, the stochastically generated K_d distributions were used. The values of the diffusion coefficient used for these calculations are shown in Table III-10.

Table III-10. Values of Diffusion Coefficients Used for the Particle-Tracking Calculations

Radionuclide	Diffusion Coefficient (m^2/s)
Anion (Uranium)	3.2 x 10^{-11}
Cation (Plutonium, Cesium, Neptunium)	1.6 x 10^{-10}

DTN: LA0003JC831362.001 [149557]

These breakthrough curves were used to calculate the effective K_d values using the procedure described in Section III.2.1. The procedure was repeated for 50 realizations of K_d. The statistics of the calculated effective K_d values are provided in Table III-11. These calculations of stochastic realizations of K_d were performed using a correlation length of 500 m. As can be seen

from the results, the effective K_d distributions are very narrow compared to the distributions of experimentally observed K_d values.

Table III-11. Statistics of Calculated Effective K_d Values

Radionuclide	Distribution	Mean	Standard Deviation	Minimum	Maximum
Uranium	Normal	6.61	0.61	5.39	8.16
Cesium	Normal	5188.72	941.55	3000.59	6782.92
Plutonium	Normal	110.17	7.45	89.90	129.87
Neptunium	Normal	1.48	0.23	0.99	1.83

Output DTN: LA0309AM831341.001

Output DTN: LA0309RP831341.001

Output DTN: LA0309RP831341.004

Output DTN: LA0309RP831341.002
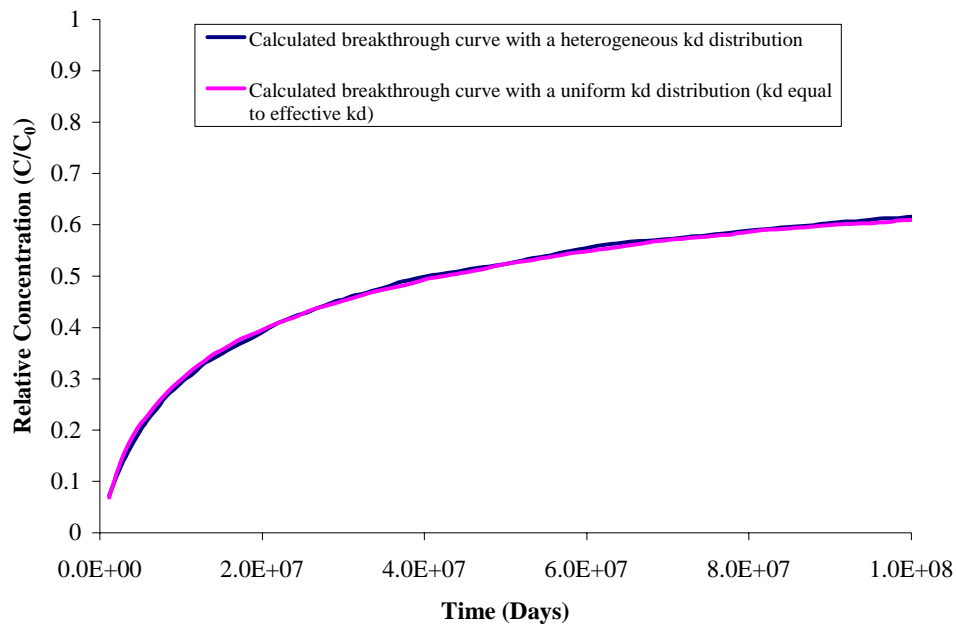
Output DTN: LA0309RP831341.003

Output DTN: LA0309RP831341.004

Figure III-6. Comparison of Breakthrough Behavior Predicted by the Calculated Effective K_d

A comparison was made as to how well the calculated effective K_d values predicted the particle breakthrough behavior with respect to the breakthrough behavior predicted by the heterogeneous K_d field (from which the effective value was calculated). In these calculations, a uniform value of K_d equal to the effective K_d value was used. Figure III-6 shows the two breakthrough curves for one of the K_d realizations. The effective value of K_d calculated for this realization was 7.32 (ml/g). As can be seen from the figure, the calculated effective K_d value captures the breakthrough behavior of the heterogeneous K_d field very well.

III.1.3.3 Effect of Correlation Length on Effective K_d Distributions of Uranium

As mentioned earlier, the correlation length used in generating the stochastic K_d realizations was parameterized because of the lack of the spatial information. The intent was to examine the effect of changes in correlation length on the distribution of effective K_d values. Once again, a similar procedure was followed to calculate effective K_d values. The heterogeneous K_d distributions generated by using different correlation lengths were used for these calculations. Table III-12 details the statistics of the calculated effective K_d values along with the correlation length used to generate the heterogeneous K_d distributions. As can be seen from the results, variation in the correlation length does not significantly affect the calculated statistics of effective K_d values.

Table III-12. Effect of Changes in Correlation Length on Effective K_d Distributions for Uranium

Correlation Length	Mean K_d (ml/gm)	Standard Deviation	Minimum	Maximum
4 meters	6.71	0.49	5.70	8.13
60 meters	6.79	0.47	5.42	8.14
500 meters	6.61	0.61	5.39	8.16
1000 meters	6.58	0.62	4.46	7.85

Output DTN: LA0309RP831341.004

III.1.3.4 Effect of Variability in the Hydraulic Gradient

The effect of variability in the hydraulic gradient on calculated effective K_d values was studied. These calculations were performed only for uranium and used K_d realizations generated with a correlation length of 500 m. Two different values of hydraulic gradient were used: 8.7×10^{-4} (3 times mean hydraulic gradient) and 0.967×10^{-4} (one-third of mean hydraulic gradient). Steady-state flow fields were calculated with these hydraulic gradients and were subsequently used to calculate particle breakthrough curves. The statistics of the resulting effective K_d values are compared with the ones for a mean hydraulic gradient of 0.14 in Table III-13. As can be seen from the results, a variability of three orders of magnitude in hydraulic gradient has not significantly affected the effective K_d distributions.

Table III-13. Statistics of Calculated Effective K_d Values for Uranium for Different Hydraulic Gradients

Hydraulic Gradient	Mean K_d (ml/gm)	Standard Deviation (ml/gm)	Minimum (ml/gm)	Maximum (ml/gm)
0.967×10^{-4}	6.55	0.59	5.13	7.53
2.9×10^{-4}	6.61	0.61	5.39	8.16
8.7×10^{-4}	6.27	0.56	4.97	7.65

Output DTN: LA0309RP831341.004

III.1.4 SUMMARY OF STOCHASTIC MODELING

This study was performed to calculate distributions of effective K_d for uranium, neptunium, cesium, and plutonium. The effective K_d distributions were calculated through a stochastic approach in which multiple values of effective K_d were calculated. The value of effective K_d was determined by calculating effective retardation resulting from a spatially heterogeneous K_d field. The spatially heterogeneous K_d fields were calculated using a geostatistical approach. The factors affecting the spatial distribution of K_d, such as rock mineralogy and spatial heterogeneity, were taken into account while generating the heterogeneous K_d fields. As spatial data on K_d were not available, the correlation length used to generate the fields was parameterized. The observations of the study were as follows:

- The calculated effective K_d values reproduced the sorption behavior of the heterogeneous K_d field very well, validating the approach used to determine the effective K_d values.

- The distributions of calculated effective K_d fields were much narrower than the distributions used as the input. This is to be expected because, in any upscaling study, as the scale gets larger, the variability in effective parameter values gets smaller.

- Variability in correlation length did not significantly affect the effective K_d distributions for uranium.

- Variability in hydraulic gradient did not significantly change the effective K_d distributions.

III.2 DEVELOPMENT OF COMPOSITE K_d DISTRIBUTIONS

As can be seen by comparing the Tables III-11 and I-4, the stochastically derived upscaled K_d distributions in the volcanics are narrow compared to the small-scale distributions. Although the scaled distributions are thought to correctly capture the spatial uncertainty, other sources of uncertainty may not be completely represented in these distributions. Other sources of uncertainty in the volcanics may include potential fast pathways (e.g., along faults) through devitrified tuff, the existence of reducing conditions along potential transport pathways, higher concentrations of radionuclides during transport in the SZ than the ranges included in the analysis, and competition among radionuclides for sorption sites.

To incorporate these other sources of uncertainty in the volcanics, the methods and approach for the development of parameter distributions documented in *Guidelines for Developing and Documenting Alternative Conceptual Models, Model Abstractions, and Parameter Uncertainty in the Total System Performance Assessment for the License Application* (BSC 2002, Section 4.2 [158794]) was implemented. In implementing this process, the Subject Matter Expert (SME) who developed the small-scale K_d distributions worked with the Parameter Team Lead (PTL) to assess the impact of these other sources of uncertainty on the recommended distributions. Because the observational data was limited, the SME worked with the PTL and several experts in uncertainty analysis to develop subjective estimates on the appropriate range of the K_ds and percentile points for the distribution.

The outcome of this process was that the SME judged that the scaled distributions did not completely capture the full-range of K_d uncertainty. In the SME's judgment the full range of the scaled distribution was extended to the minimum and maximum values of the small-scale distribution to create the range for the composite distribution. In this composite distribution 5% to 30% of the full distribution was assigned to the tails of the composite distribution. The resulting recommended composite distributions are piece-wise uniform distributions that incorporate both the scaled distributions and the small-scale distributions. Plots of these distributions are presented in BSC (2003 [164870], Figures 6-41 through 6-51). The following paragraphs detail the development of these distributions for U, Np, Pu, and Cs.

For uranium, the minimum small-scale value was 0 mL/g. Five percent probability was uniformly distributed between 0 mL/g and the lower bound of the scaled distribution at 5.39 mL/g. Since the scaled distribution had such little variation, it is reasonably represented by a uniform distribution; hence, 90% probability was uniformly distributed between 5.39 mL/g and the upper bound of the up-scaled distribution at 8.16 mL/g. The remaining 5% probability was uniformly distributed between 8.16 mL/g and the maximum small-scale experimentally observed value of 20 mL/g.

For neptunium, the minimum small-scale value was 0 mL/g. Five percent probability was uniformly distributed between 0 mL/g and the lower bound of the scaled distribution at 0.99 mL/g. Since the scaled distribution had such little variation, it is reasonably represented by a uniform distribution; hence, 85% probability was uniformly distributed between 1 mL/g and the upper bound of the up-scaled distribution at 1.83 mL/g. The remaining 10% probability was uniformly distributed between 1.83 mL/g and the maximum small-scale experimentally observed value of 6 mL/g.

For plutonium, the minimum small-scale value was 50 mL/g. Twenty-five percent probability was uniformly distributed between 10 mL/g and the lower bound of the scaled distribution at 89.9 mL/g. Since the scaled distribution had such little variation, it is reasonably represented by a uniform distribution; hence, 70% probability was uniformly distributed between 89.9 mL/g and the upper bound of the up-scaled distribution at 129.87 mL/g. The remaining 5% probability was uniformly distributed between 129.87 mL/g and the maximum small-scale experimentally observed value of 300 mL/g.

For cesium, the minimum small-scale value was 100 mL/g. Five percent probability was uniformly distributed between 100 mL/g and the lower bound of the scaled distribution at

3000.59 mL/g. Since the scaled distribution had such little variation, it is reasonably represented by a uniform distribution; hence, the remaining 95% probability was uniformly distributed between 3000.59 mL/g and the upper limit of the scaled distribution at 6782.92 mL/g.

Table III-14. Recommended Composite Distribution for K_ds In Volcanics and Alluvium

(NOTE: Development of the distributions given this table is based on Tables I-4 and III-11)
The following notation is used in this table:
μ = mean
σ = standard deviation)

Species	Unit/Analysis	Distribution	Coefficients describing distribution (mL/g)
U	Composite (Volcanics)	Cumulative	(K_d, prob) (0., 0.) (5.39, 0.05) (8.16, 0.95) (20, 1.0)
	Alluvium	Cumulative	(K_d, prob) (1.7, 0.) (2.9, 0.05) (6.3, 0.95) (8.9, 1.0)
Np	Composite (Volcanics)	Cumulative	(K_d, prob) (0, 0) (0.99, 0.05) (1.83, 0.90) (6, 1.0)
	Alluvium	Cumulative	(K_d, prob) (1.8, 0.) (4.0, 0.05) (8.7, 0.95) (13, 1.0)
Pu	Composite (Volcanics)	Cumulative	(K_d, prob) (10., 0.) (89.9, 0.25) (129.87, 0.95) (300, 1.0)
	Alluvium (Devitrified)	Beta	μ=100, range = 50 - 300, σ=15
Cs	Composite (Volcanics)	Cumulative	(K_d, prob) (100., 0.) (3000.59, 0.05) (6782.92, 1.0)
	Alluvium (Devitrified)	Truncated Norm	range = 100 – 1000 μ =728, σ = 464
Am/Th/Pa	Volcanics and Alluvium	Truncated Norm	range = 1,000 - 10,000 μ =5,500, σ = 1,500
Sr	Volcanics and Alluvium	Uniform	range= 20 - 400
Ra	Volcanics and Alluvium	Uniform	range=100-1000
C/Tc/I	Volcanics and Alluvium	Constant	zero

Output DTN: LA0309AM831341.001

ATTACHMENT IV. RADIONUCLIDE TRANSPORT THROUGH POROUS ROCK

To assess whether the sorption kinetics process needs to be included in the transport model, column test data, under flow rates pertinent to the Yucca Mountain flow system, are used to calculate Damköhler numbers to determine if kinetic effects are important (Triay et al. 1997 [100422]).   The Damköhler number can be used to determine whether the local equilbrium approach is valid. If valid, kinetic effects can be neglected, and equilibrium models that are computationally much more efficient can be used. Plutonium kinetics is examined in this analysis since plutonium sorption kinetics has been shown to be slower than the other radionuclides in the inventory (see Attachment I). Therefore, if the local equilibrium approach is valid for plutonium, it should be valid for the other radionuclides in the inventory.

The Damköhler number is defined as the rate constant, k (1/time), multiplied by a representative residence time, T,

$$Da = k * T \qquad\qquad \text{(Eq. IV-1)}$$

where k is a first order reaction rate constant.

In Equation IV-1, the rate constant quantifies the reaction timescale of the system whereas the residence time quantifies the transport timescale. By multiplying these parameters together, Da provides a basis for evaluating which timescale dominates a system. For cases in which the reaction timescale is much faster than the transport timescale, Da is large and the local equilibrium approach is valid.

Bahr and Rubin (1987 [144539], p. 440, Equation 12) demonstrate that the mass balance equation describing solute transport can be separated into an equilibrium and a kinetic component. The smaller the kinetic component, the more accurate are the retardation factors based on the local equilibrium approach.

Bahr and Rubin (1987 [144539], p. 450) found that equilibrium was well approximated when the sum of the two Damköhler numbers is greater than 100 and reasonably well estimated when the sum is greater than 10. For evaluation of sorption behavior, separate Damköhler numbers, Da_{att} and Da_{det}, can be computed for attachment and detachment of the sorbing contaminant using k_{att} and k_{det}, which are the attachment and detachment rate constants for plutonium sorbing onto the mineral surfaces. The magnitude of the kinetic component is inversely proportional to the total Damkohler number. As the sum of the two Damköhler numbers becomes larger, the equilibrium approximation becomes more appropriate.

Valocchi (1985 [144579], p. 813, Figure 2) had a similar result, although he used only the reverse rate k_{det} to compute a Damköhler number. Valocchi's approach is utilized in this study since a single first order rate best fit the column experiments. Since the Valocchi's approach utilizes one Damköhler number, which results in lower Da numbers than the Bahr and Rubin method, the Bahr and Rubin criteria of 10 and 100 can also be used with the Valocchi approach. Valocchi's approach is used in this study.

As seen from Equation IV-1, to estimate the Damkohler number for the saturated-zone transport model, the reaction rate constants for plutonium sorption must be determined. This determination is done by using laboratory data from column experiments. The general idea behind the calculation is to fit a first-order reaction rate constant to ^{239}Pu column data (DTN: LA0302HV831361.001 [163783]). This rate constant, along with a conservative travel time through the fractured volcanics, can be used to estimate a Damköhler number. The Damköhler number indicates whether kinetics are important in a system. A sample calculation is presented below.

1) Determine the pore volume *PV* of the column:

> The pore volume of the column is necessary to calculate the residence time of each column experiment. The pore volume can be calculated by determining the mean breakthrough time for tritium, which is a conservative tracer:

$$PV = 0.5 \text{ concentration breakthrough of tritium}$$

> *PV* for sample G4-268 devitrified tuff with J-13 well water and radionuclides ^{3}H and ^{239}Pu = 7 mL (DTN: LA0002JC831361.001 [147087]).

> With the pore volume and flow rate, the residence time *RT* for each column experiment can be calculated:

> *RT* of Each Column = *PV*/Flow rate:

>> Column 1: $RT = (7 \text{ mL})/(2.89 \text{ mL/hr}) = 2.42$ hr

>> Column 2: $RT = (7 \text{ mL})/(1.12 \text{ mL/hr}) = 6.25$ hr

>> Column 3: $RT = (7 \text{ mL})/(0.4 \text{ mL/hr}) = 17.5$ hr

2) Determine the steady-state concentrations of Pu in the column for the different flow rates:

> For each column experiment, the plutonium concentration plateaus. The value at which the concentration plateaus is needed to determine the kinetic sorption rate of plutonium.

> Steady-state concentrations of Pu at different flow rates:

>> Column 1: 2.89 mL/hr: $C/C_0 = 0.67$

>> Column 2: 1.12 mL/hr: $C/C_0 = 0.31$

>> Column 3: 0.8 mL/hr: $C/C_0 = 0.06$

3) Determine the kinetic rate constants that fit the Pu column data:

> The steady-state concentration versus residence time data was used to fit the first-order kinetic reaction rate constant. The first-order kinetic rate law (e^{-kt}) fit results in $k_{\text{for}} = 0.2$ hr^{-1}.

To calculate the Da number, a reverse kinetic rate is needed. Using the expected value of K_d for Pu in devitrified tuff of 100 cc/g (Section I.8.4.1 of this report), $k_{rev} = k_{for}/100 = 0.002$ hr^{-1} is obtained.

4) Estimate a travel time through the system:

Time to first breakthrough for Np reported in BSC 2001 ([157132], Figure 5) is less than 100 years. Hence a conservative value of 10 years is used for travel time through the fractured volcanics in the saturated zone.

5) Calculate the Damköhler number:

$$Da = k_{rev}RT = 175 \qquad \text{(Eq. IV-2)}$$

Valocchi (1985 [144579], p. 813, Fig. 2) found that equilibrium is well estimated for $Da > 100$.

Based on this analysis, the local equilibrium approach is valid for plutonium transport in the saturated zone of Yucca Mountain.

ATTACHMENT V. TRANSPORT SIMULATIONS WITH THE HIGHER WATER TABLE

Particle tracking simulations are conducted with the adapted Saturated Zone (SZ) Site-Scale Flow Model (with the higher water table grid) for a nonsorbing species and for neptunium. These simulations are performed for the estimated wetter, glacial climatic conditions in which the groundwater flux through the SZ is greater than present conditions by a factor of 3.9 (BSC 2003 [162649], Section 6.4.5). The higher groundwater flux rates are approximated by scaling up the recharge and the values of permeability for all hydrogeologic units by a factor of 3.9. The expected values for parameters associated with radionuclide transport are applied in these simulations.

The results of the transport simulation with the higher water table and estimated groundwater flow under future glacial climatic conditions for a nonsorbing species are shown with the solid line in Figure V-1. All of the simulated breakthrough curves presented in Figures V-1 and V-2 are for transport from beneath the proposed repository to the 18-km regulatory limit of the accessible environment. For comparison, the simulated breakthrough curve using the simplified approach utilized in the TSPA abstraction of radionuclide transport in the SZ (BSC 2001 [157132], Section 6.4.2) is shown with the dashed line in Figure V-1. Recall that this simplified approach uses the simulated breakthrough curve from the SZ Site-Scale Flow Model with the present water table configuration and scales that breakthrough curve to shorter transport times using the groundwater flux multiplier of 3.9 for future glacial climatic conditions. Similar results for the transport of neptunium using the two alternative approaches are shown in Figure V-2. Neptunium exhibits a small amount of sorption in the matrix of volcanic units and a moderate amount of sorption in the alluvium.

Differences in the simulated transport times for these alternative approaches to climate change in the SZ are primarily attributable to differences in the hydrogeologic units encountered along flow paths from beneath the repository. Flow paths in the SZ pass through a considerably longer length of the upper volcanic confining unit in the adapted SZ Site-Scale Model with the higher water table. The upper volcanic confining unit has significantly lower permeability than the underlying units of the Crater Flat Tuff, leading to longer transport times along these flow paths. In addition, the relatively slower groundwater flow rates in the upper volcanic confining unit allow greater matrix diffusion, leading, in turn, to even longer transport times. There is also greater flow path length through the porous alluvium near the water table to the south and east of the repository in the adapted model with the higher water table. The porous nature of the alluvium also leads to longer simulated transport times through this medium.

Comparison of the two approaches shown in Figures V-1 and V-2 indicates that the model with the higher water table results in longer simulated transport times for both the non-sorbing species and for neptunium. The simplified approach of scaling the breakthrough curves from the SZ Site-Scale Flow Model with the present water table elevations is thus a pessimistic representation of transport in the SZ under wetter glacial climatic conditions relative to the adapted model that incorporates water table rise associated with future conditions. Consequently, the results of these simulations tend to verify the assumption that the flux scaling approach to simulation of climate change is conservative with regard to radionuclide transport in the SZ, relative to the more realistic situation in which water table rise is included in the modeling.
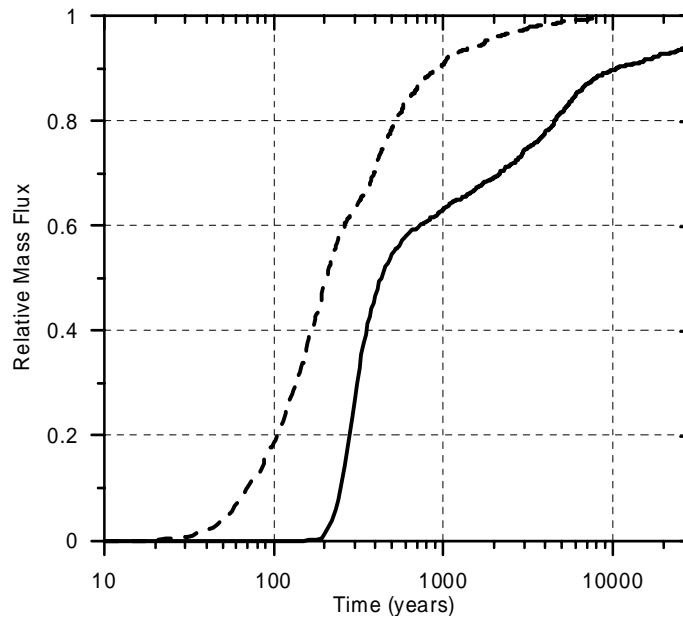
For illustration purposes only

NOTE: Dashed line is the SZ breakthrough curve at 18 km for future climatic conditions that has been scaled (by a factor of 3.9) from transport simulation for present conditions. The solid line is the SZ breakthrough curve at 18 km for future climatic conditions that has been simulated with the higher water table model. Breakthrough curves are for a constant source initiated at the water table beneath the repository at time equal to zero and do not include radioactive decay.

Figure V-1. Breakthrough Curves for Non-Sorbing Radionuclides for Future Glacial Climatic Conditions Using Two Alternative Approaches
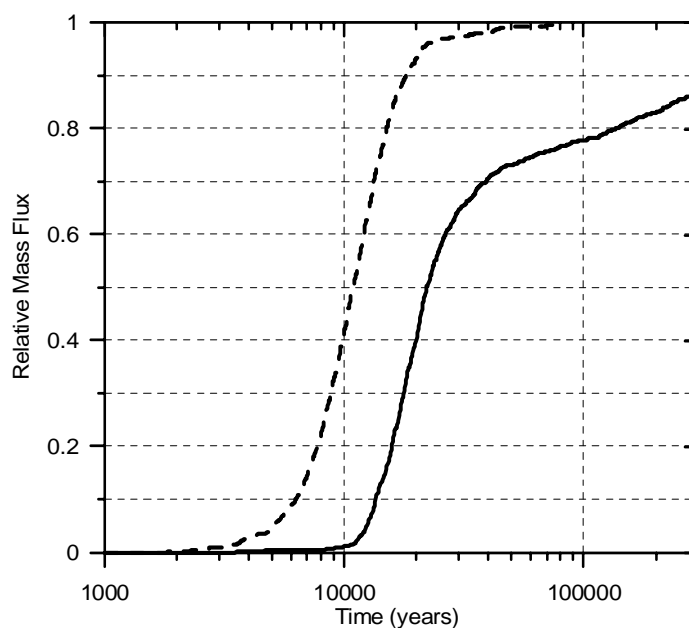
For illustration purposes only

NOTE: Dashed line is the SZ breakthrough curve at 18 km for future climatic conditions that has been scaled (by a factor of 3.9) from transport simulation for present conditions. The solid line is the SZ breakthrough curve at 18 km for future climatic conditions that has been simulated with the higher water table model. Breakthrough curves are for a constant source initiated at the water table beneath the repository at time equal to zero and do not include radioactive decay.

Figure V-2. Breakthrough Curves for Neptunium for Future Glacial Climatic Conditions Using Two Alternative Approaches